UNIVERSITY OF OKLAHOMA

GRADUATE COLLEGE

THREE-DIMENSIONAL FEM MODELING OF GEOTHERMAL RESERVOIR STIMULATION USING STOCHASTIC FRACTURE NETWORKS AND CONTINUUM DAMAGE MECHANICS

A DISSERTATION

SUBMITTED TO THE GRADUATE FACULTY

in partial fulfillment of the requirements for the

Degree of

DOCTOR OF PHILOSOPHY

By

XIAONAN WANG
Norman, Oklahoma
2014

THREE-DIMENSIONAL FEM MODELING OF GEOTHERMAL RESERVOIR STIMULATION USING STOCHASTIC FRACTURE NETWORKS AND CONTINUUM DAMAGE MECHANICS

A DISSERTATION APPROVED FOR THE
MEWBOURNE SCHOOL OF PETROLEUM AND GEOLOGICAL ENGINEERING

BY

_____
Dr. Ahmad Ghassemi, Chair

_____
Dr. Randy Keller

_____
Dr. Chandra Rai

_____
Dr. Deepak Devegowda

_____
Dr. Ahmad Jamili

Dedication

To my family and those who trusted and loved me

ACKNOWLEDGEMENTS

I would like to express my sincere gratitude to my advisor, Dr. Ahmad Ghassemi, for his constant guidance, inspiration and encouragement throughout my Ph.D. study. Dr. Ghassemi enlightened my horizons of geomechanics and enhanced my interest in reservoir rock mechanics, through providing me the opportunity to know, work with, learn from, and conference with a group of excellent experts in this field around the world. Without his support and supervising, the completion of this dissertation would not be possible.

Thanks are also due to my committee members: Dr. Chandra Rai, Dr. Randy Keller, Dr. Deepak Devegowda, and Dr. Ahmad Jamili at the University of Oklahoma, for their interests in guiding my work. Also, I thank my former committee members at Texas A&M University, Dr. Peter Volko, Dr. Charles Aubeny, and Dr. Eduardo Gildin, for their valuable advises in hydraulic fracturing and numerical methods in the first part of my Ph.D. study. Thanks also go to graduate programs in department of petroleum engineering at both TAMU and OU.

I also want to thank my officemates and group members, Kai Huang, Yawei Li, Dr. Jian Huang, Dr. Chakra Rawal, Dr. Sang-hoon Lee, Varahanaresh Sesetty,

and Qian Gao, for the many formal and informal technical discussions. Their suggestions and opinions speeded me up. Special thanks go to Jay Dosser for proofreading and grammar checking my text.

Finally, I would like to thank my family, my parents and two younger brothers, for their unconditional endless love and support. Away from home and not being able to stay with them for most of the time, their sweet and warm voice on the phone is one of my most important driving forces.

TABLE OF CONTENTS

LIST OF TABLES

LIST OF FIGURES

ABSTRACT

Unconventional reservoirs are gaining more and more attention in recently years. Pore pressure and temperature variations in unconventional reservoirs during stimulation are of great importance in reservoir exploration and development. Fluid injection is one of the most commonly used permeability enhancement technique, which induces significant changes in the stress, pore pressure and temperature fields of reservoir rock. Coupled thermo-hydro-mechanical (THM) processes are involved in those changes. In this work, three-dimensional finite element methods (FEM) are developed and applied to simulate the response of unconventional reservoirs to fluid injection. The FEM model is assisted with continuum damage mechanics and stochastic fracture network model, which simulates the intact rock failure process and natural fracture networks deformation during stimulation, respectively.

Numerical simulations using the current model are present in this dissertation, and applied to analyzing different aspect of reservoir response to fluid injection, such as, wellbore instability, intact rock failure, natural fracture deformation, permeability enhancement, and injection induced micro-seismicity. The results indicate the important roles of rock heterogeneity and natural fractures'

distribution in influencing the stimulation effect. The correlation among damaged zone, permeability enhanced volume, and induced MEQ distribution is shown in the results. The influences of injection plan, boundary conditions, and in-situ stress states on the stimulation results are also illustrated in the modeling examples.

Key words: natural fracture network; rock heterogeneity; stress dependent permeability; induced micro-seismicity; EGS.

1

INTRODUCTION

Unconventional reservoirs, in both petroleum and geothermal energy, are of great interest in recent years. One of the most important tasks for unconventional reservoir development is enhancing rock mass permeability and predicting its variation with reservoir development. When external forces, for example, mechanical loading, fluid injection and production, and heating, are applied to the rock mass, it will deform and pore fluid diffusion and heat transport will occur. These physical processes in the reservoir will result in changes of state, e.g. the resultant stress distribution, induced pore pressure and temperature fields. All of these state variables are inter-related and need to be considered simultaneously. Change of the stress state can lead to rock failure, fracture slippage, and changes of behavior of both fluid and heat flow, which are critical issues when planning the exploration strategy. Rock failure, fracture slippage, and heating/cooling induced permeability development and rock degradation have significant impact on reservoir behavior during injection and production.

Reservoir rock has complex properties. All rocks in earth's crust are fractured to some extent. In addition, intact rock usually has heterogeneous poroelastic modulus, strength, permeability, and thermal conductivity. The existence of natural fractures and heterogeneity significantly influence the reservoir response to injection and production. The analysis of fractured rock behavior generally contains three components, namely: 1) fracture network and rock heterogeneity characterization; 2) stress and failure analysis of fractured rock in response to the stimulation; 3) stress dependent permeability and rock damage evolution. This process involves identification and modeling of fractures and elemental rock properties, thermal-poroelastic analysis of the response of rock, fluid flow, and heat transfer in the heterogeneous and fractured rock mass (Figure 1.1).

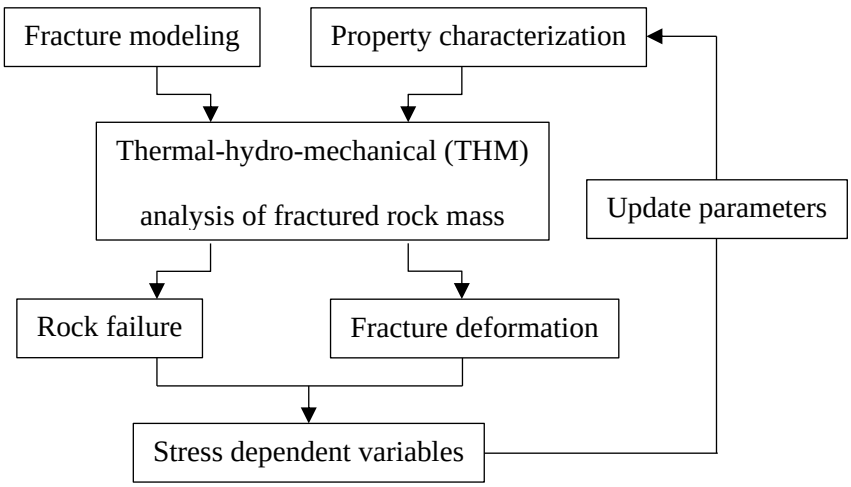

Figure 1.1 Work flow of the fully coupled THM model

A fundamental step in understanding and predicting natural fracture performance is identifying and characterizing fractures. The literature on various methods of treating fracture networks is extensive. These approaches can be summarized into two categories based on how they represent the fractures: 1) deterministic fracture network models locate fractures (or major fractures) explicitly (Hicks et al. 1996; Kolditz and Clauser 1998; Ghassemi and Kurma 2007; Safari and Ghassemi 2011); 2) stochastic fracture network models determine the types of patterns or the fracture's statistical properties (Cladhuous et al. 2011; Bruel et al. 1994; Willis-Richards et al. 1996; Tezuka et al. 2005). According to the simulation approaches of fluid flow in the fracture systems, the previous models can also be described as equivalent continuum model (Carrera et al. 1990) or discrete fracture network model (DFN) (Hudson and La Pointe 1980; Long et al. 1982; Dershowitz 1984; Smith and Schwartz 1984). In this thesis, a hybrid method is developed by using the discrete stochastic networks in building a continuum approximation.

Similarly to modeling natural fractures, the stochastic approach has also been applied to rock heterogeneity study. There are different stochastic functions have been proposed in the literature to describe the distribution of rock properties. In this work, Weibull's distribution function (Weibull 1961) is used for heterogeneity distribution, such as the distribution of young's modulus, strength, Poisson's ratio and permeability.

Stress and failure analysis of reservoir has been gaining extensive attention, and laboratory and numerical models have been developed and utilized in reservoir engineering practice for decades. From the geomechanical point of view, the deformation of fractures and rock mass and the variation of pore pressure and temperature, in response to the fluid injection, are key factors in reservoir stimulation design and control. In previous models for fractured rocks, the thermo-poroelastic coupling process has been either neglected or simplified to empirical correlations (Cladhuous et al. 2011; Bruel 2002; Willis-Richards et al. 1996). Three-dimensional coupled thermo-poroelastic (THM) models have been developed and applied to reservoir stimulation, development, and well bore stability analysis. However, the reservoir rock mostly has been treated as continuous with possibly a few major fractures (Zhou and Ghassemi 2009; Lee and Ghassemi 2011; Huang and Ghassemi 2011).

This work develops a fully coupled thermal-poroelastic FEM model with stochastic fracture networks to address the impact of the presence of a fracture network on stimulation results. In this dissertation, after coupled finite element analysis, updated stress, pore pressure and temperature are obtained from model results, which are used next for rock failure and fracture deformation analysis. Continuum damage models, on the basis of the stress-strain behavior of rocks in experimental test, are used for intact rock failure analysis. On the other hand, for

fracture deformation, joint model and penny-shaped fracture model are used to study the fracture aperture change. Rock failure and increase of fracture aperture are related to permeability enhancement and induce micro-seismicity (Figure 1.1). Thereafter, rock properties such as elastic modulus, poroelastic coefficients and permeability, and fracture geometry are updated and applied to the finite element analysis for the next time step. Induced micro-seismic events obtained at the end of every time step is used to estimate the growth of stimulated volume and stress reorientation, since they reflect the released earthquake energy where failure takes place. Since the FEM formula used in this work is non-linear, a convergence check is conducted at the end of every time step, in order to confirm that the updated rock and fracture properties are matched with the stimulation results at current time step.

1.1. Motivation and objectives

Predicting the response of a heterogeneous fractured rock to injection is challenging. Rock heterogeneity and natural fractures add complexity to the mechanical and flow responses of the reservoir rock. In addition, the mechanical and flow responses are coupled and need to be simultaneously solved. Given the complexity of the problem, an advanced numerical is needed to able to consider the influence of rock heterogeneity and natural fractures on rock deformation and fluid and heat flow. It should also be able to simulate the thermal-hydro-

mechanical (THM) interactions and their impact on damage evolution and thus, permeability change of the reservoir rock. The model should show be capable of estimating stimulation result, such as stimulated reservoir volume, permeability enhancement and improved fracture connectivity. Induced micro-seismicity is one of the promising approaches for indicating the growth of stimulated reservoir volume and the evolution of rock damage. In addition, extensive induced seismicity is not desirable in reservoir development operations. Therefore, a real-time distribution of induced micro-seismicity events is desirable. These important issues are addressed in this work with emphasize on the influence of rock heterogeneity and natural fracture properties on the stimulation results.

1.2. Dissertation outline

This dissertation will first introduce and explain the theoretical foundations of the work with respect to four sub-models: 1) discrete fracture network model; 2) rock heterogeneity model and continuum damage model; 3) fully coupled geomechanics model (thermo-poroelasticity theory); and 4) the three-dimensional Finite Element model. Then, three categories of numerical simulations are given to illustrate the model application on predicting different aspect of reservoir responses due to fluid injection for heterogeneous and

naturally fractured reservoirs. These three cases represent different reservoir conditions and scales.

Chapter 2 first provides a general review of the state-of-the-art of fracture network models, including the physical characteristics of fracture patterns and development of conceptual and mathematical models. Then physical properties and fundamental process in fractures and of fractured rock mass are addressed, including the mechanical and hydraulic properties of fractured rock, and the features of fracture flow model used in this work.

Chapter 3 states the current research on rock heterogeneity distribution, based on which, the continuum damaged model is applied to capture the rock failure process owing to change of stresses during fluid injection. A brief introduction to Weibull's distribution and Weibull damage development theory is presented, and then the continuum elastic damage model based on Weibull theory and lab tests is reviewed. Scenario of how to relate Weibull theory with lab test results to determine the heterogeneity distribution parameters is also explained.

Chapter 4 contains the basic theories of thermo-poroelasticity applied in the subsequent chapters for the numerical modeling of reservoir stimulation. This chapter briefly illustrates the derivation of governing equations of thermo-poro-elastic processes in the reservoir during stimulation. Modifications are made according conditions and assumptions of problems studied in this dissertation.

The necessary modifications for developing field equations which are suitable for Finite Element analysis are also discussed.

Chapter 5 explains the procedure of developing a Finite Element model which can simulate the fully coupled thermo-poroelastic processes, taking into account natural fracture networks and rock heterogeneity. The Finite Element model used in this dissertation also considers the non-linearity of the rock properties during the THM process so that elastic modulus, hydraulic parameters, and poroelastic parameters are made stress dependent in this model.

Chapter 6 provides the results of near wellbore rock failure analysis during well operation. Mohr-Coulomb failure criterion is used to determine the instability status of the rock near wellbore. Common failure zone shapes of a vertical borehole under different in-situ stress state and well conditions are illustrated; Influence of stress reorientation, well pressure, and cooling effect on wellbore failure mode are pointed out. Recommendations of wellbore stabilization are provided also.

Chapter 7 presents the simulation results of the fully coupled FEM analysis of heterogeneous reservoirs considering rock damage and permeability enhancement. Two simulation examples are provided, the first aims to study the near well-bore during stimulation, and the second shows the large scale reservoir

response due to a point source injection. The important role of rock heterogeneity is emphasized in this chapter.

Chapter 8 consists of application of the current model to predicting the geothermal reservoir stimulation results. In this chapter, stochastic fracture networks are introduced to the geothermal reservoir system, and fracture flow and deformation models are embedded into the Finite Element model. Similarly to Chapter 7, near well-bore response and the larger scale reservoir response are studied. The influence of natural fractures and their deformation to stimulation results are addressed.

Finally, in chapter 9, a summary of the studies conducted in this dissertation is given, and the major contributions of this work are outlined. Based on the current study, recommendations and discussions are proposed on potentially important future work.

2

NATURAL FRACTURE NETWORK MODEL

All rocks in earth's crust are fractured to some extent and these fractures are important in oil/gas, geothermal, and ground water reservoirs. Fractures serve as fluid flow paths, and play important roles in the stability of wellbores, as well as occurrence of seismicity. The presence of natural fractures in the reservoir poses challenges in exploration, evaluation, stimulation, and modeling of the reservoir. Major challenges for numerical modeling include but are not limited to: 1) identifying and characterizing natural fractures; 2) quantifying flow and transport through them; and 3) predicting and controlling changes in fracture systems. These challenges are dealt with in this work by 1) developing a conceptual model to represent the geometry of the fracture network; 2) developing a mathematical model to represent fluid flow and solute transport in fractured media; 3) building a hydro-mechanical model which can analyze the coupled fluid and solid response, and simulate the fracture deformation and porous rock response simultaneously.

2.1. Natural fracture network models

There are generally two classes of fracture models, stochastic fracture models (Cladhuous et al. 2011; Bruel et al. 1994; Willis-Richards et al. 1996; Tezuka et al. 2005) and deterministic models (Kolditz and Clauser 1998; Ghassemi et al. 2007; Safari and Ghassemi 2011). On the cases of the treatment of fluid flow through fracture systems, fracture models can also be classified in to equivalent continuum models (Carrera et al. 1990) and discrete fracture models (Hudson and La Pointe 1980; Long et al. 1982). In this work a hybrid method is developed, using discrete stochastic networks to build a continuum approximation.

In a conventional equivalent continuum model, the induced rock heterogeneity by fractures is modeled using sub-regions with different local properties. Individual fractures are not explicitly present unless their scale is large enough to be considered separately as a determined unit in the model. Each sub-region has uniform properties, such as poro-mechanical parameters and permeability, which are resulted from the volume-averaged behavior of many fractures inside the sub-region. For example, flow through a sub-region is calculated in every direction and is used to form the equivalent permeability tensor for the sub-region. In this work, a sub-region is viewed as one finite element in the FEM (Finite Element Method). For instance, each element in the simulated domain

has its own elemental properties tensors, which is calculated using equivalent continuum technique that will be discussed later in this chapter.

If the properties for the equivalent continuum are known with certainty, the model is deterministic. If the properties and coefficients are viewed as randomly distributed with a probability, the model is stochastic (Long et al. 1982; Robinson 1984; Dershowitz 1984; Hudson and LaPointe 1980). In the stochastic framework, fractures are reproduced only in a statistical sense to capture the overall connectivity of the entire region, but not to represent the local in-situ connectivity. In other words, the model is developed to simulate the overall behavior of the entire reservoir, such as predicting the injection rate vs. pressure profile, estimating stimulated reservoir volume, and anticipating induced micro-seismicity. However, the stochastic fracture model is not aimed to accurately approximate the local properties of a sub-region, such as the permeability of a particular element or the local connectivity of several fractures. It is important to note that, in order to approximate the conductive fracture geometry (the inner connection between fractures), interference testing and tracer testing is critical to see how the system is interconnected in the field (National Research Council 1996).

2.2. Stochastic fracture network models

In a stochastic fracture network model, the fracture network consists of series of penny-shaped fractures, the distributions of which is determined by the statistical descriptions of fracture density, size, and orientation. The stochastic distribution functions of fracture network properties can be fitted from field survey data or experience. In this work, the fracture network generation approach is adopted from Cacas et al. (1990). The fracture density, size, and orientation are described by Poisson distribution, log-normal distribution, and Fisher-von Mises distribution, respectively. Parameters for these three distributions are obtained from field data. However, slight modification can be made to the distribution function on a case-by-case basis. For example, AltaRock (2011) suggested an elliptical Fisher distribution fits better for field data from Newberry site. The initial fracture aperture is related to the fracture size (r) with a coefficient β (Tezuka and Watanabe 2000) :

$$\alpha = \beta r^n \tag{2.1}$$

where α is the initial aperture. β equals 0.004, estimated from average virgin permeability (Willis-Richards 1996). β is a field dependent factor and requires careful evaluation. We use n = 0.5, which is adopted from Tezuka and Watanabe 2000.

A fracture network with five hundred penny-shaped fractures is shown in Figure 2.1. The geometry algorithms for the visualization of 3D penny-shaped fractures network is presented in the Appendix.

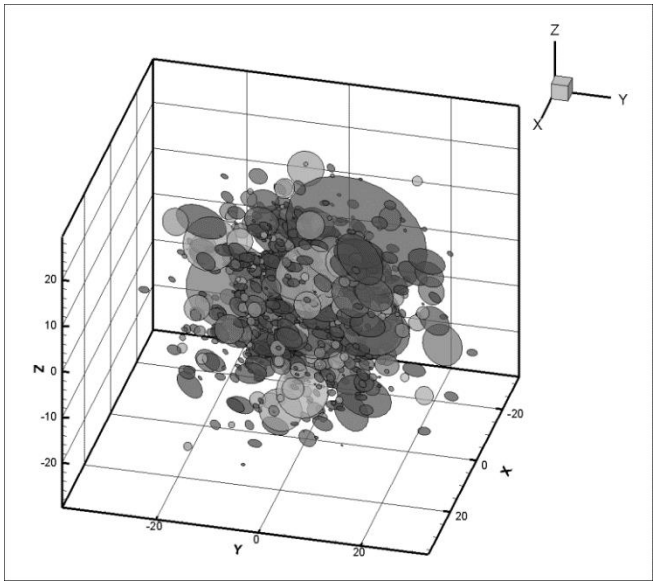

Figure 2.1 A stochastic fracture network with 500 penny-shaped fractures.

2.2.1. Fracture locations (density)

The distribution of fracture centers follows Poisson distribution (Equation 2.2) in this work. Poisson distribution is a discrete probability distribution that describes the probability of a given number of events occurring in a fixed domain (time or space). In this work, the expected value (EX = λ for Poisson process) of x in Equation (2.2) is the expected number of fractures in our modeling domain, i.e. the fracture density (Cacas et al. 1990; Bruel 2002).

$$f(x;\lambda) = \frac{\lambda^x e^{-\lambda}}{x!} \tag{2.2}$$

Fracture location can be obtained by randomly generating center coordinates following Equation (2.2). Figure 2.2 shows examples of fracture center distributions with different density parameters in a $500 \times 500 \times 500$ m^3 volume.

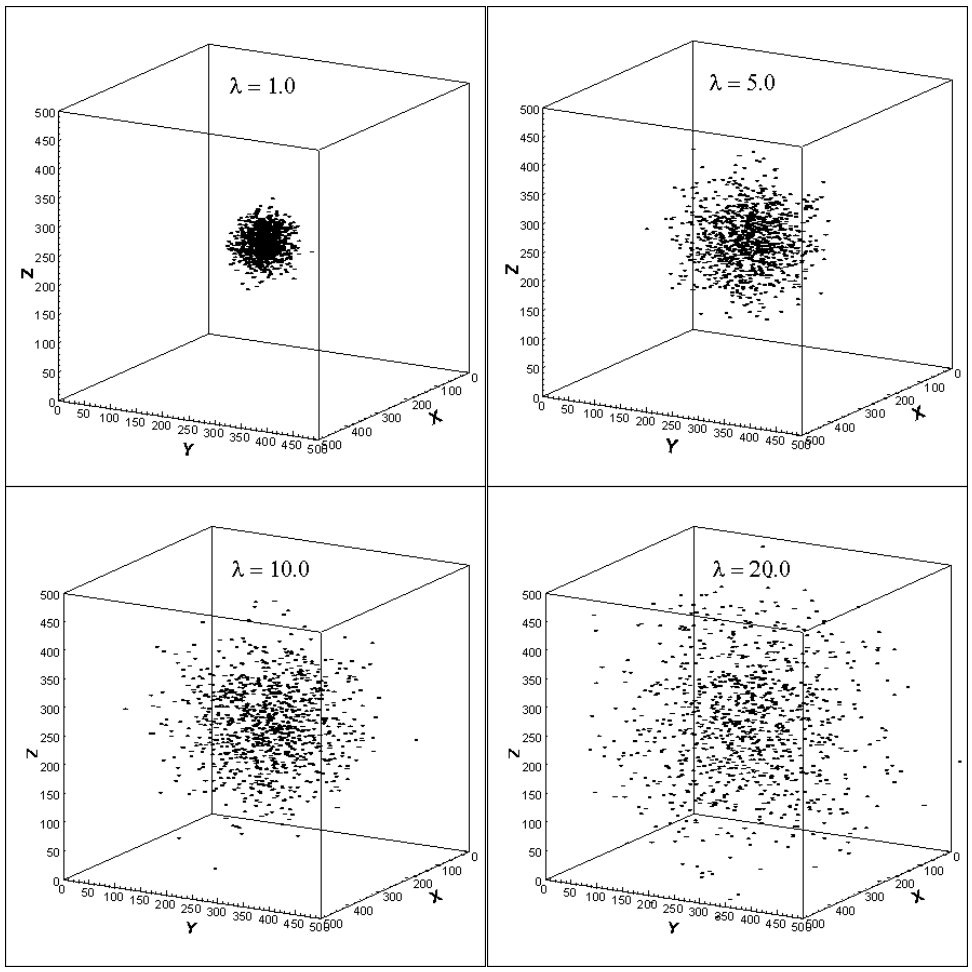

Figure 2.2 Fracture center distributions with different density parameters.

The density parameter (λ), from logging, well-imaging, or other methods, usually indicates one dimensional fracture density, i.e., number of fractures per length. In this work, three random arrays, representing *x*-, *y*-, *z*- coordinates of the centers, are generated simultaneously using the same parameter (λ), by assuming the fracture distribution has the same density in *x*-, *y*-, and *z*-directions. More realistic three-dimensional distribution can be obtained by well correlation (Kelkar and Perez 2002), which is not considered in this study.

2.2.2. Fracture size

In this work, fracture sizes are generated following log-normal distribution. The two parameters of the log-normal distribution are the mean (μ) and standard deviation (σ) of the fracture radius's natural logarithm. We assume the sizes of all fractures in the simulated domain follow one single distribution with one set of parameters. However, sub-sets or different distributions can always be applied using similar algorithms, when suggested by field data (Cacas et al. 1996). Figure 2.3 shows examples of penny-shaped fractures having same location (λ = 10) and orientation (k = 2.8) but different size distribution.

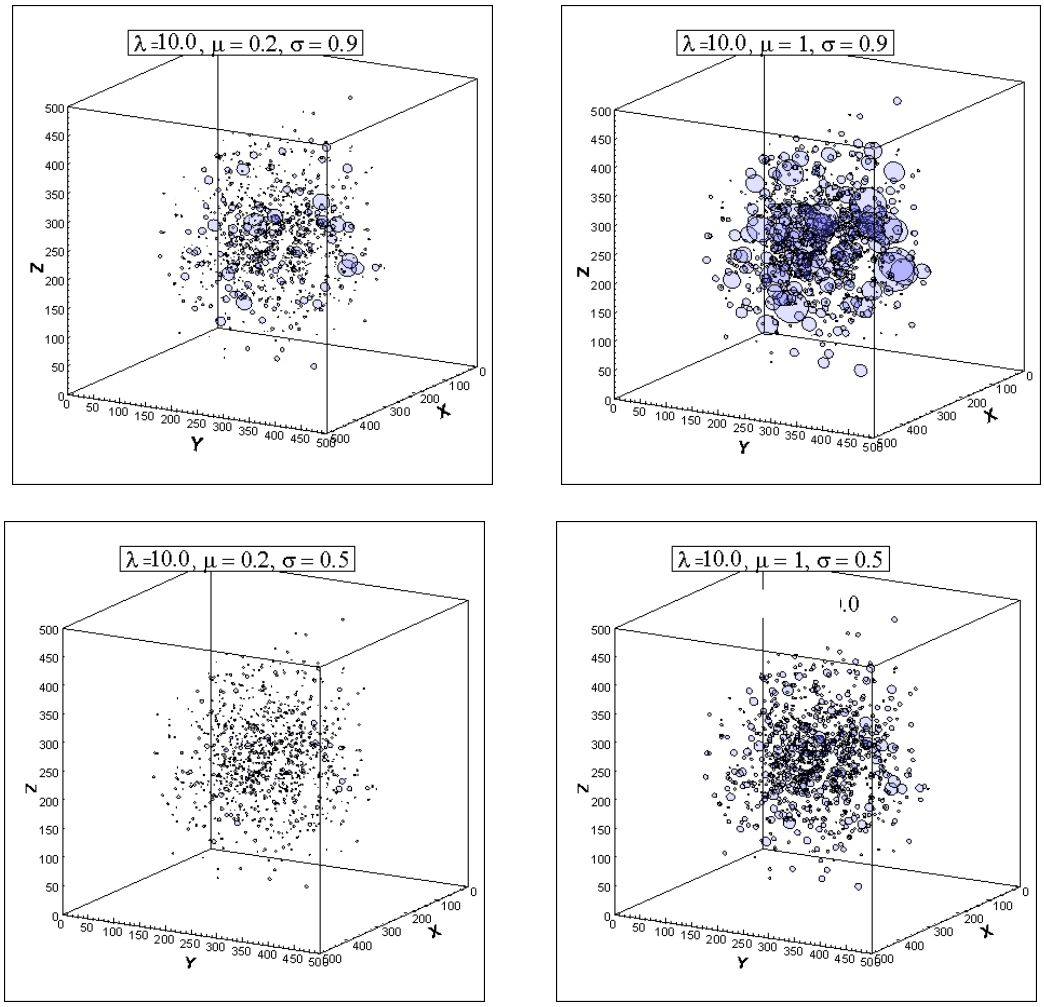

Figure 2.3 Fracture networks with different size parameters.

2.2.3. Fracture orientation

Fisher von Mises distribution is usually used in directional statistics to describe the distribution of directions on a sphere (Mardia 1999). Figure 2.4 shows examples of Fisher von Mises distribution with mean direction at (-1, 1, 1) and different ***k*** parameters.

In this work, modified Fisher von Mises distribution (Equation 2.3) is used (Cacas et al. 1990).

$$f(\alpha) = \frac{k}{2sh(k)} \exp(k\cos(\alpha))\sin(\alpha) \tag{2.3}$$

where α is the angle between fracture normal and the mean direction. First, an array of direction angles is generated randomly. Then, these values are substituted into Equation 2.3, converting to the fracture orientations. Finally, direction angles that fall outside the range of fracture orientations are eliminated. Figure 2.5 shows comparisons of fracture networks with different orientation distribution parameters.

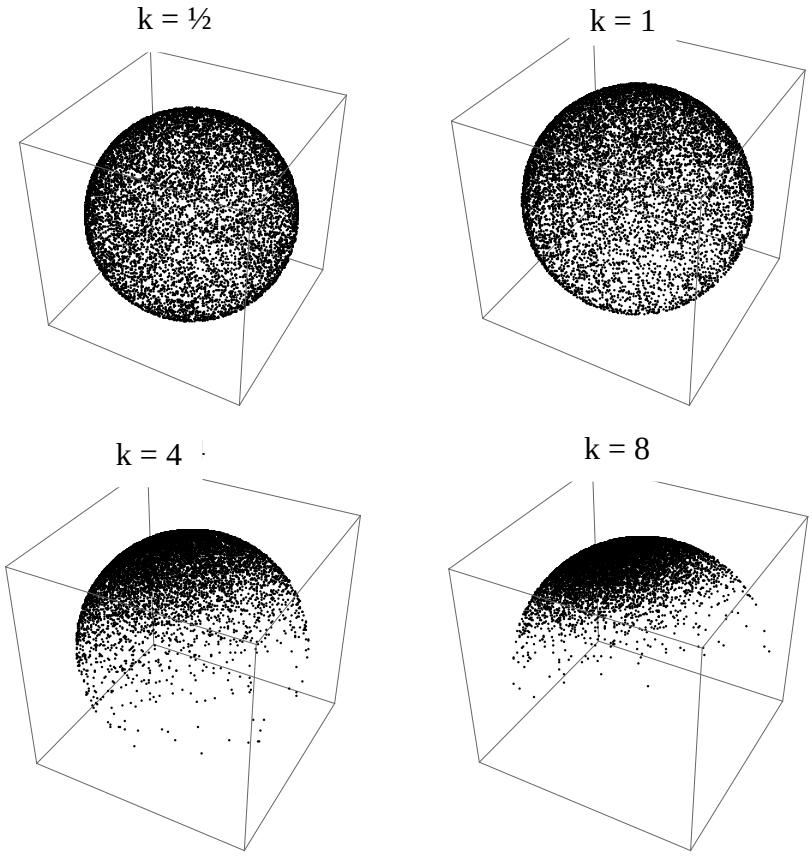

Figure 2.4. Fisher von Mises distributions with mean direction at (-1, 1, 1) and k = ½, 1, 4, and 8.

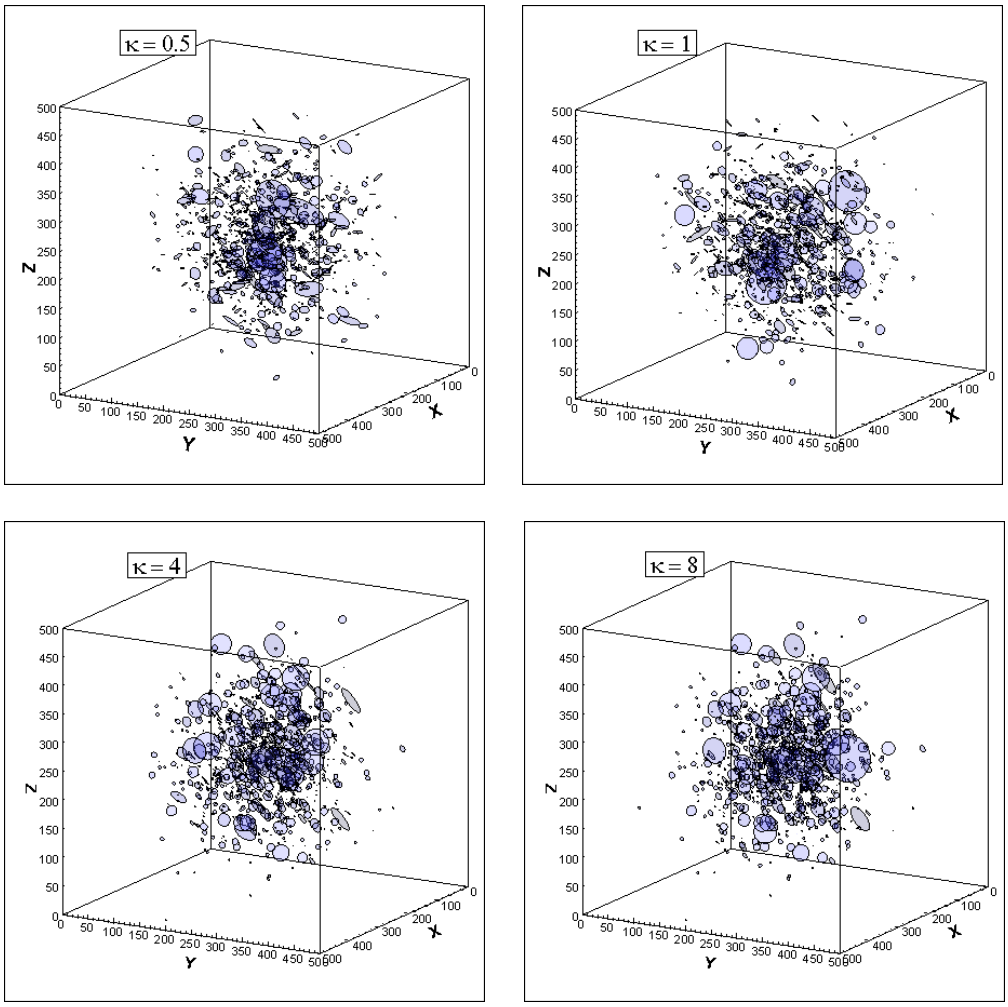

Figure 2.5 Fracture networks with different orientation distributions.

2.3. Hydraulic properties of fractured rock

The rock blocks contain natural fractures are convert into a continuum media, the permeability of which is equivalent to the fractured rock. The fracture flow model is based on the assumptions that fluid moves through the reservoir body within an interconnected fracture network, and that leakage from fractures to the

rock matrix is negligible in comparison with the flow in the fracture (Figure 2.6). Therefore, within one elemental volume, we consider fracture flow and matrix flow separately, and superpose these two parts together at the end of elemental evaluation. In this finite element model, local equivalent permeability is evaluated at element interfaces (indicating the connectivity between elements, Figure 2.6), using the conservation of directional volumetric flow rate (e.g. x-directional flow in Figure 2.6) through the interface (Equation 2.4 – 2.8).

$$Q = Q_f + Q_m \tag{2.4}$$

We use Darcy's law for matrix flow calculation:

$$Q_m = \frac{k_m}{\mu} A_m \nabla p \tag{2.5}$$

The fluid flow in the parallel-wall fracture (Figure 2.6) is assumed to be governed by the cubic law (Witherspoon et al. 1980):

$$Q_f = \frac{a^3 l}{12\mu} \nabla p \tag{2.6}$$

Therefore, Equation (2.4) can be written as:

$$Q = \frac{k_m A_m + a^3 l / 12}{\mu A} A \nabla p \tag{2.7}$$

In above equations, Q is the volumetric flow rate in m^3/s, l is the length of intersection line between fracture and element interface in meter; a is the aperture of the fracture in meter; μ is the fluid viscosity in Pa s; ∇p is the pressure gradient in Pa/m. A is the interface area in m^2. The equivalent permeability at interface A is obtained from Equation (2.7):

$$\bar{k} = \frac{kA_m + (a^2/12)A_f}{A} \tag{2.8}$$

In numerical simulations, the reservoir block is divided into small elements as shown in Figure 2.7. Each element usually contains more than one fracture (n >1). Each fracture in the element has apertures (a_i) and an intersection length (l_i). The directional conductivity (e.g. x- direction) of the element can be expressed in the following way (Rahman et al. 2002):

$$\bar{k}_x = k_{mx} + \sum_{i=1}^{n} \frac{a_i^3 l_i}{12A_x} - \frac{k_m \sum_{i=1}^{n} a_i l_i}{A_x} \tag{2.9}$$

In this work, the rock matrix's permeability is very low, i.e. several orders (10^4-10^6) lower than the fracture permeability. And the fracture cross-section area A_f (in mm^2) is much smaller than the area of the element interface A_x (in m^2). Therefore, the last term in Equation (2.9) is a higher order term and ignored in this work.

Geometry algorisms for calculation intersections between penny-shaped fractures and element faces can be found in the Appendix at the end of this dissertation.

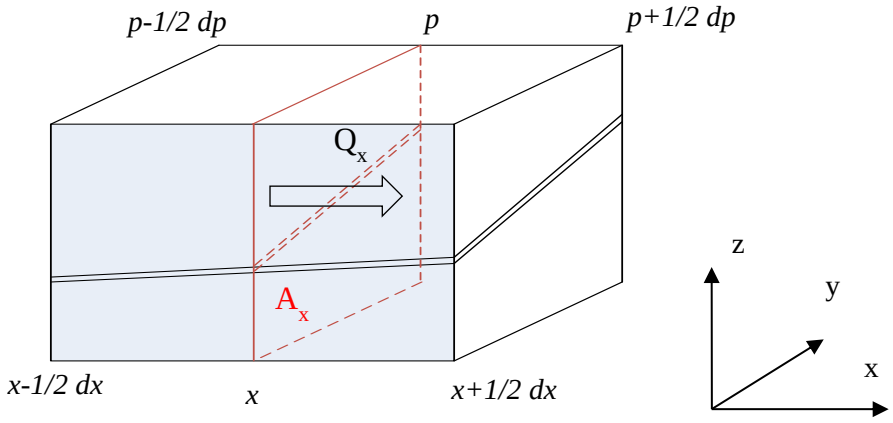

Figure 2.6 Illustration of x- directional flow through an interface.

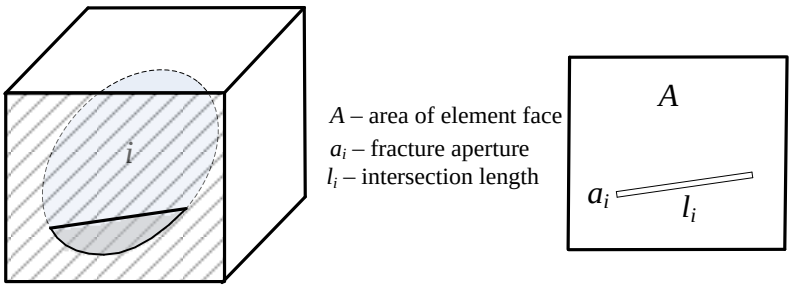

(a) Fracture *i* intersects element x-interface

(b) Notations used in Eq. 2.9

Figure 2.7 Conversion of fracture permeability into equivalent permeability of FEM element.

The equivalent permeability technique converts fracture networks into a continuum media with an equivalent permeability. The conductivity of the

resulting continuous media is dramatically influenced by the connectivity of the fracture network, and is also affected by the finite element mesh selection. An example is shown here to analyze the parameter sensitivity of fractures connectivity and to test the mesh sensitivity of the equivalent permeability technique. In the following example, a network of 500 fractures is created within the domain matrix block using different fracture orientation parameters, i.e. Fisher von Mises distribution (used in this study) vs. random distribution (used in Rhaman et al. 2002). Three different sizes of finite element mesh were used to investigate the impact of the mesh.

Figure 2.8A-D shows the influence of fracture orientations on the fracture network directional conductivities. The blue color shows the connectivity of fracture networks whose orientations are derived using the Fisher von Mises distribution (FVM) (group I) and the random distribution (group II). We can see that the fracture network with random orientations has a higher conductivity in x- and y- directions and a lower conductivity in the z- direction when compared with Fisher von Mises distributed fracture networks. Considering the geometric average conductivity (Figure 2.8D), group (II) fractures also show higher values than group (I). These two groups have the same number of fractures, and the same size distributions. The finite element meshes are the same as well. By comparison, we can see the connectivity of fracture networks is significantly influenced by the fracture orientations.

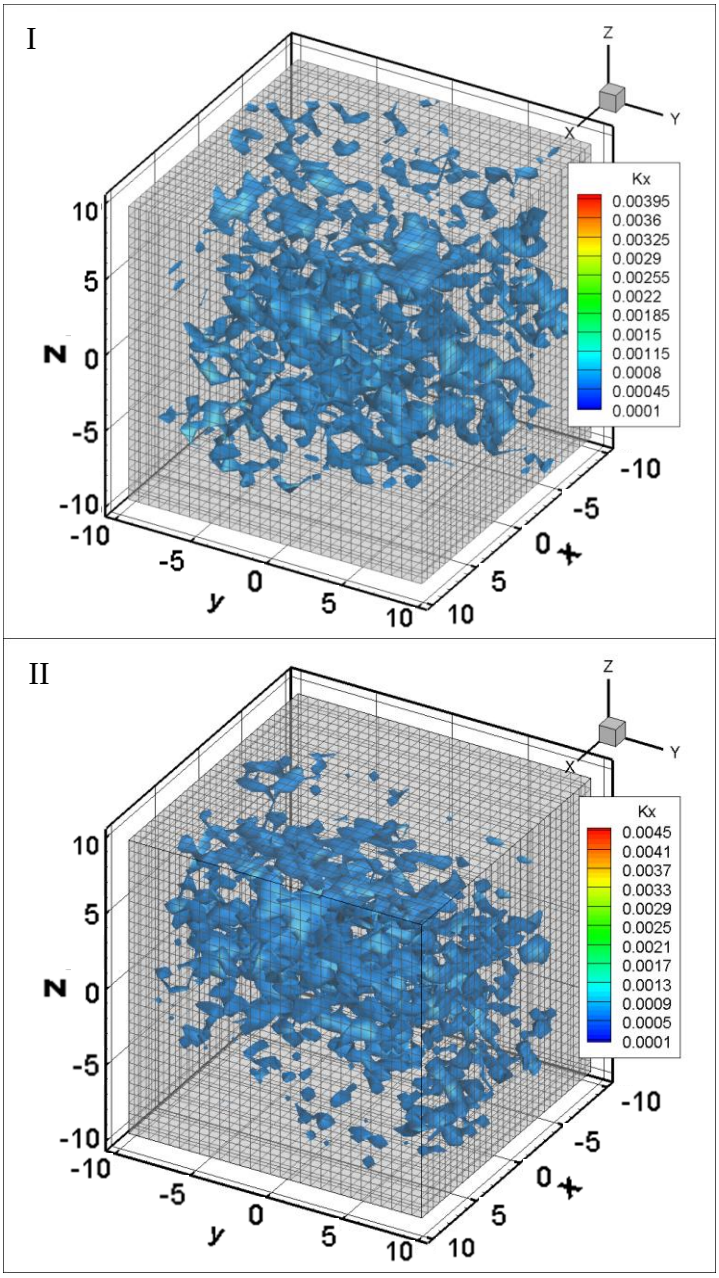

Figure 2.8A The equivalent x- directional connectivity on FEM mesh of networks with Fisher von Mises (above, $\boldsymbol{k}$ = 2.8) and random orientation distribution (below).

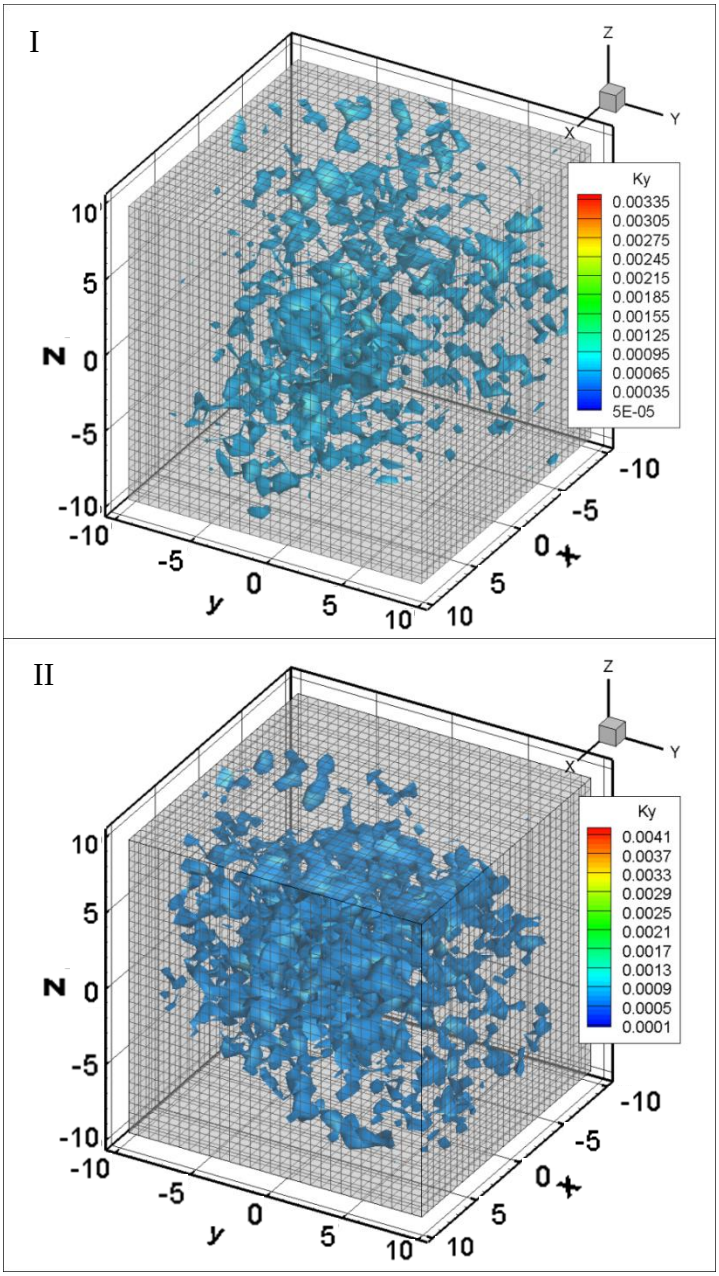

Figure 2.8B The equivalent y- directional connectivity on FEM mesh of networks with Fisher von Mises (above, $\boldsymbol{k}$ = 2.8) and random orientation distribution (below).

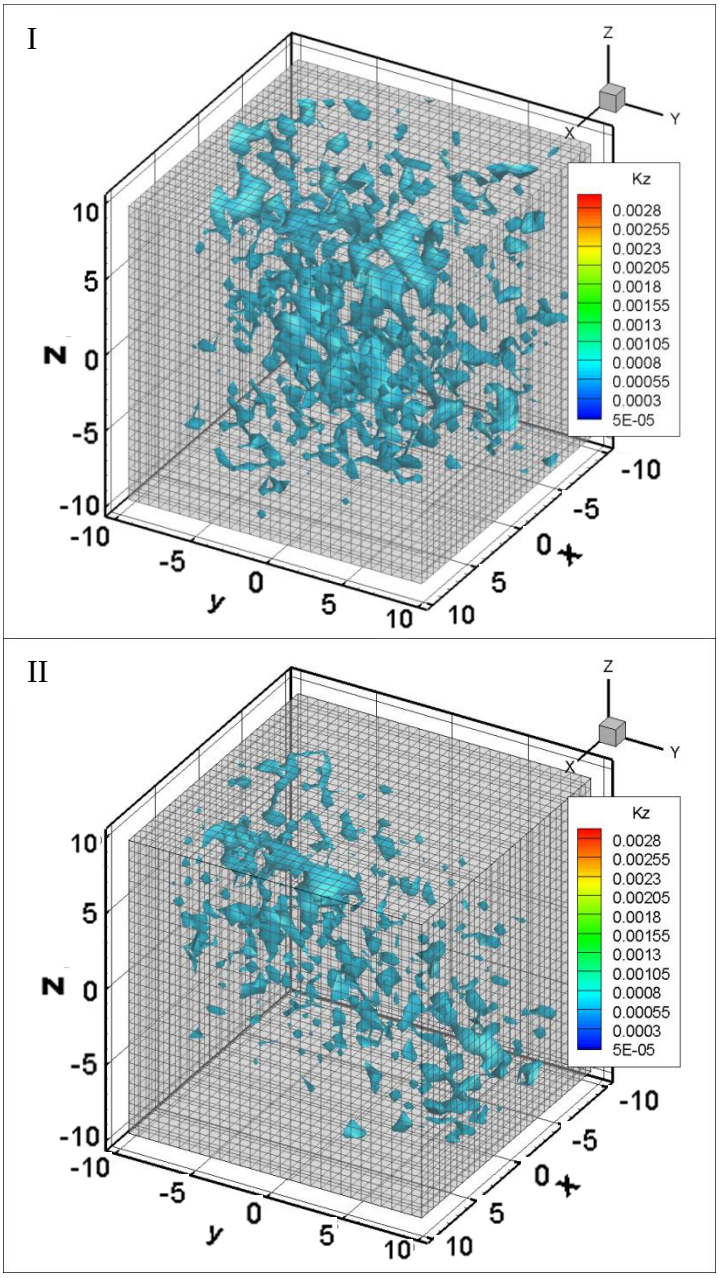

Figure 2.8C The equivalent z- directional connectivity on FEM mesh of networks with Fisher von Mises (above, $\boldsymbol{k}$ = 2.8) and random orientation distribution (below).

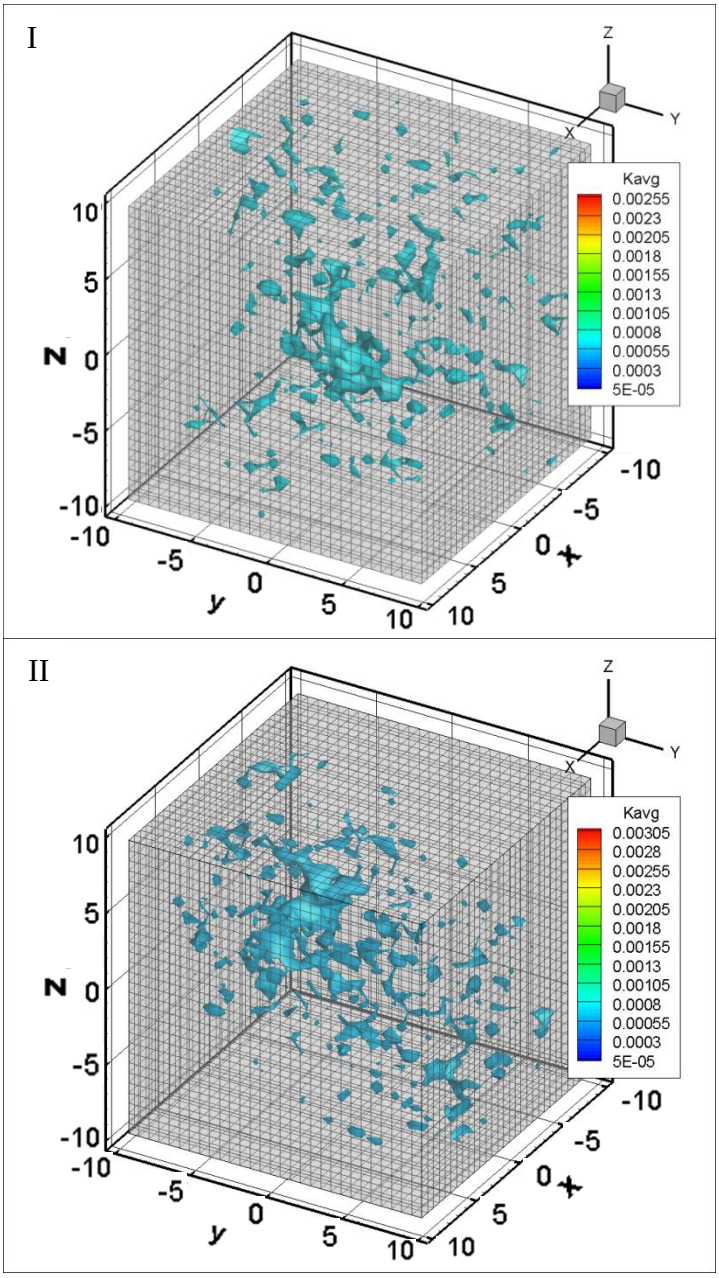

Figure 2.8D The equivalent elemental average connectivity on FEM mesh of networks with Fisher von Mises (above, $\boldsymbol{k}$ = 2.8) and random orientation distribution (below).

The equivalent permeability is evaluated on each element's surfaces. Figure 2.9A-B shows the effect of mesh size on the permeability evaluation. The same two fracture groups as above are used. The matrix block is discretized in to 1000, 8000, and 27000 elements for three test cases, respectively (I, II, III series in Figure 2.9A and B). We can see that after the fractures and the matrix elements are converted to a continuous media, the patterns of heterogeneity of the element conductivity are similar in all three cases (I, II, III) with different mesh sizes. However, as the mesh becomes finer, connectivity deteriorates. For the mesh with 27000 elements, most of the high conductivity zones are isolated. The isolated high conductivity zones will negatively impact fluid flow and heat transfer in the model. Comparing plots in Figure 2.9A (Fisher von Mises distribution) with those in Figure 2.9B (random distribution), we can see that the randomly distributed cases have higher connectivity for all three mesh sizes.

I

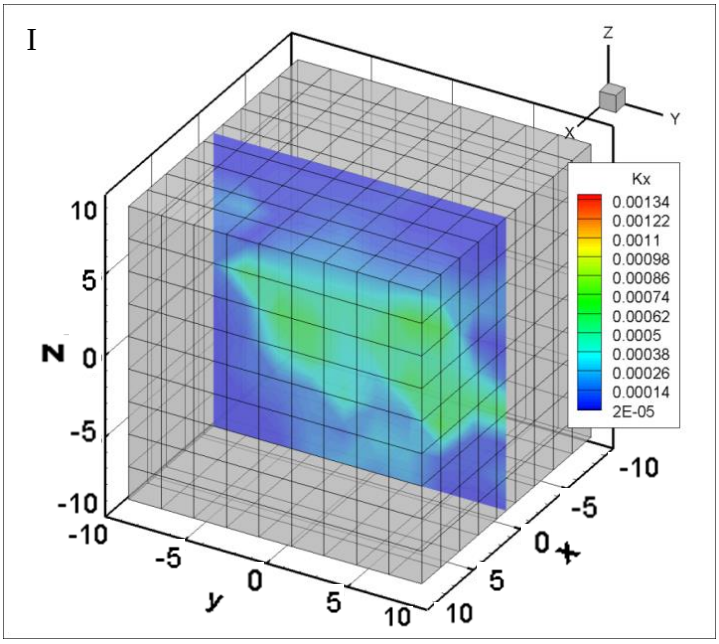
Z
Y
X
Kx
0.00134
0.00122
0.0011
0.00098
0.00086
0.00074
0.00062
0.0005
0.00038
0.00026
0.00014
2E-05
10
5
0
-5
-10
N
-10
-5
0
5
10
y
-10
-5
0
5
10
x

II

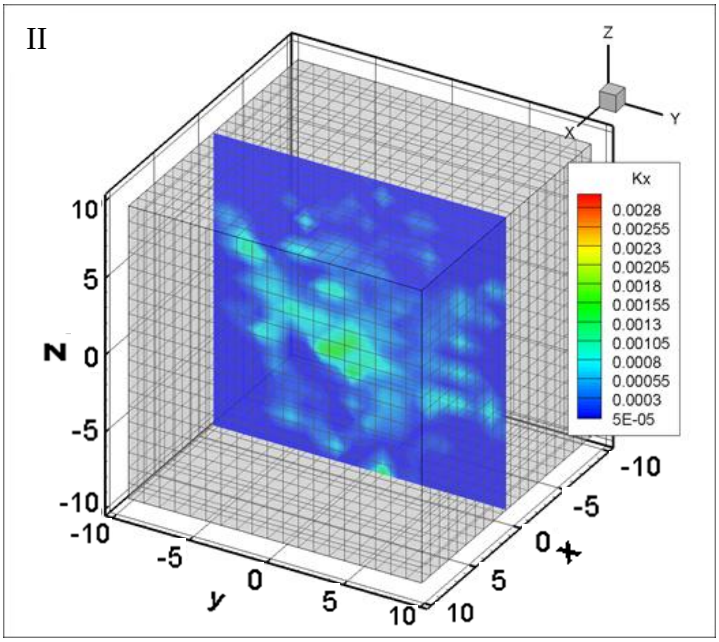
Z
Y
X
Kx
0.0028
0.00255
0.0023
0.00205
0.0018
0.00155
0.0013
0.00105
0.0008
0.00055
0.0003
5E-05
10
5
0
-5
-10
N
-10
-5
0
5
10
y
-10
-5
0
5
10
x

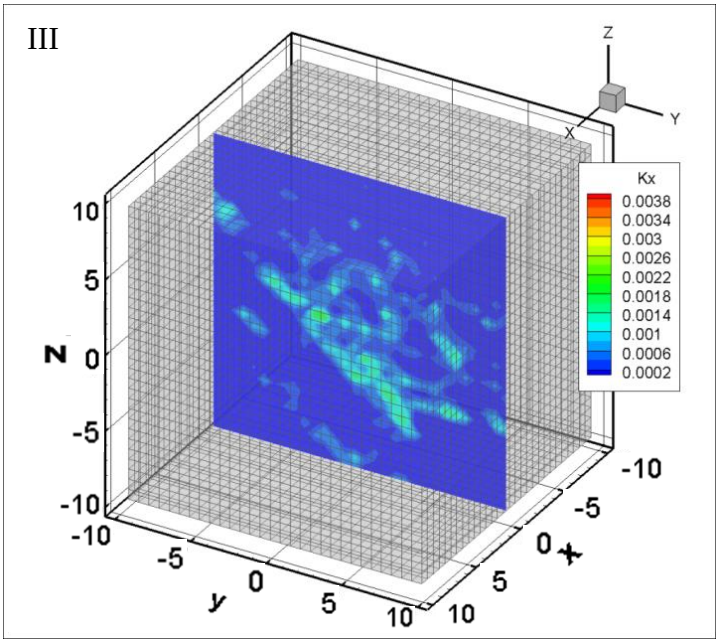

Figure 2.9A The equivalent fracture connectivity on different mesh sized of networks with Fisher von Mises orientation distribution (***k*** = 2.8).

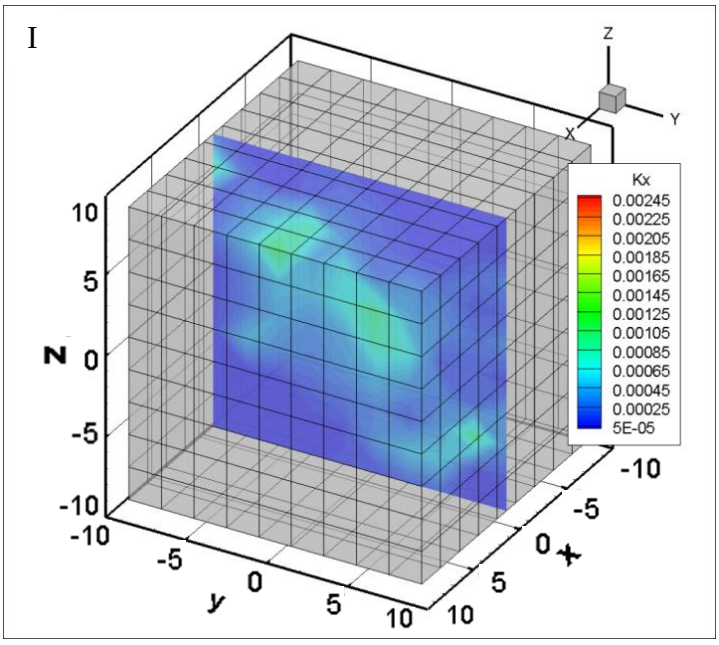

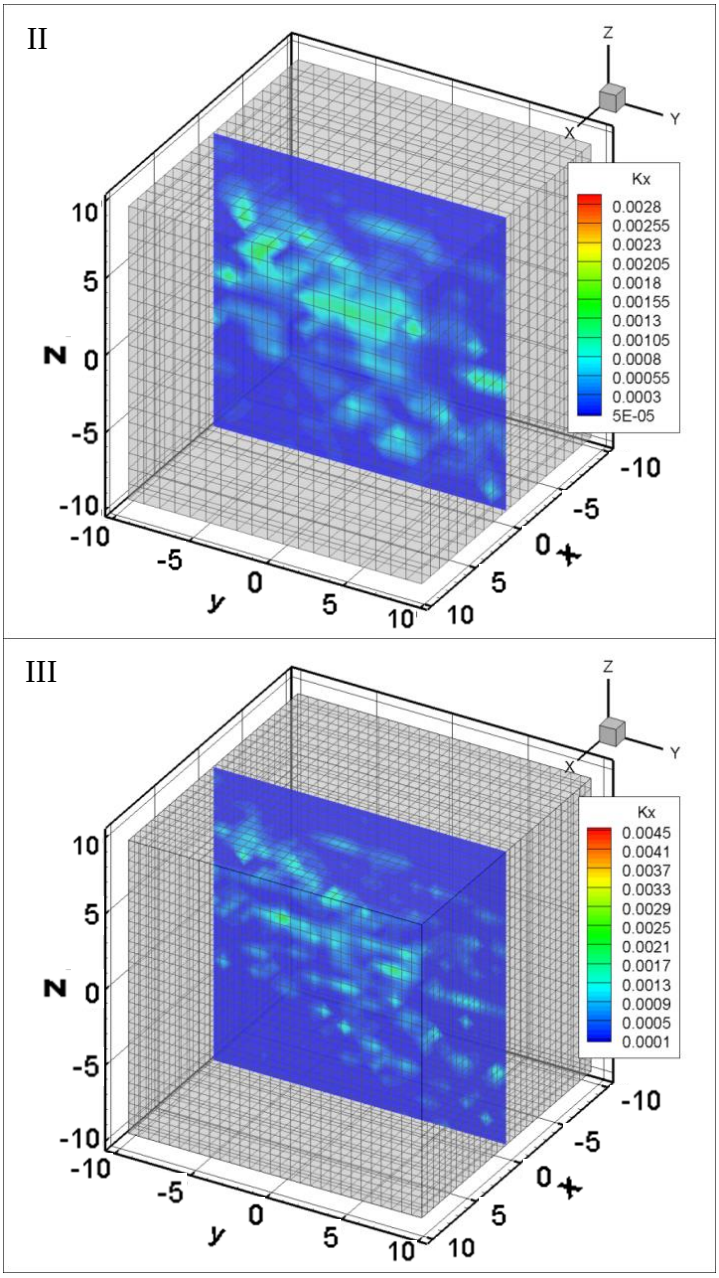

Figure 2.9B The equivalent fracture connectivity on different mesh sized of networks with random orientation distribution.

The average permeability of the entire reservoir is used to evaluate the mesh size effect on fracture connectivity. Harmonic mean, geometric mean, and arithmetic mean are commonly used for permeability averaging of a heterogeneous reservoir. In practice, harmonic mean is used to obtain the effective permeability for layered-vertical flow (Henritte et al. 1989; Amyx et al. 1960). For a system with log-normal permeability distribution, the geometric mean approximation is better than harmonic or arithmetic averages (Warren and Price 1961). However, some studies suggested that the effective permeability of 3D composite is a 1/3 power average (Equation 2.10) for log-normal system (Neotinger 1994; Hristopulos and Christokos 1999):

$$\overline{K} = \left(\frac{1}{n_{els}} \sum_{i=1}^{n_{els}} (K_i)^{1/3}\right)^3 \tag{2.10}$$

where K_i is the variable of each elements, n_{els} is the total number of elements.

We use the 1/3 power average to approximate the average permeability of the entire block, and to quantify the mesh size effect on fracture connectivity. Figure 2.10 shows the correlation between mesh size and effective permeability of the entire reservoir. Two fracture networks with same stochastic parameters as in group (I) of Figure 2.8 are analyzed (fracture network with FVM orientation distribution). As the mesh becomes finer, the average permeability decreases and converges to some smaller value. Also, the curves for the two stochastic

fracture networks in Figure 2.10 show that the horizontal permeability (x- and y-directions) is slightly higher than the vertical permeability (z- direction), which is consistent with the results from Figure 2.8.

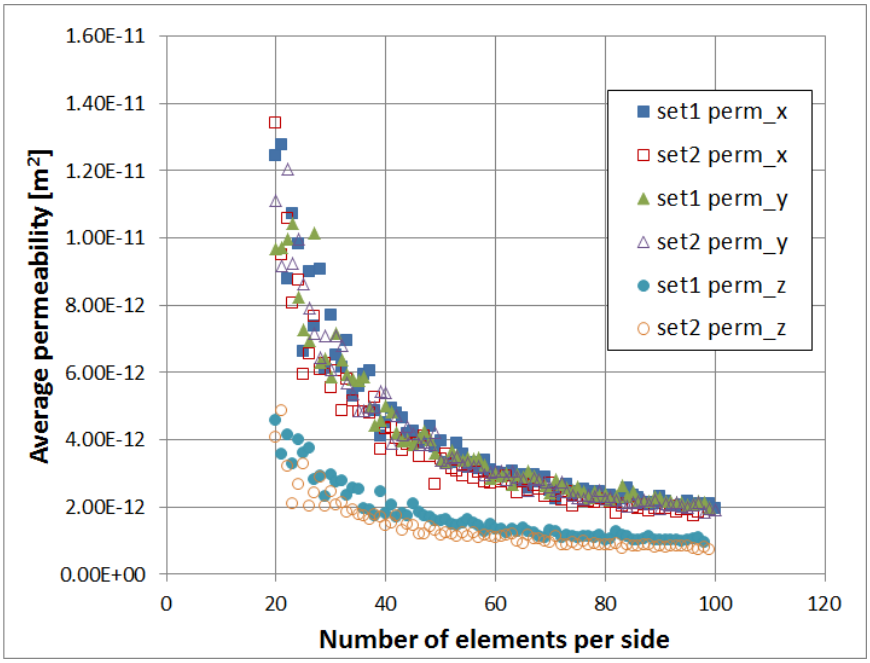

Figure 2.10 Change of overall average permeability with mesh size.

2.4. Mechanical properties of fractured rock

In simulations, the simulated domain is discretized into finite elements (meshing). Each element is required to have its individual properties input to the model, such as Young's modulus, Poisson's ratio, and permeability, etc. In modeling of rock heterogeneity (Chapter 3), we statistically distribute the local properties into individual elements. In some cases when rock mass with natural

fractures are considered, it is necessary to calculate the equivalent elemental mechanical properties of the elements that contain fracture(s) before conducting Finite Element analysis. In this work, for intact rock, we assume isotropic Young's modulus and Poisson's ratio, and the variation of Poisson's ratio after fracturing is small for isotropic material. Therefore, Poisson's ratio is kept constant in this model. In the following, equivalent technique for Young's modulus of a fractured sample is presented. As conservation of flow rate is used in permeability conversion, the balance of displacement is used accordingly for the equivalent Young's modulus. The overall displacement of the fractured rock is equal to the displacement of converted continuum mass with equivalent Young's modulus under the same external loading. Rosso 1976 illustrated correlations among joint stiffness, axial and transverse strains of rock sample, and Young's modulus of intact rock during a triaxial test (Figure 2.11):

Average joint displacement: $d_s = \dfrac{(\varepsilon_3 - \varepsilon_2)D + d_n \cos\theta}{\sin\theta}$

Average joint closure: $d_n = \left[\left(\varepsilon_1 L - \dfrac{\sigma_1}{E} L\right) - (\varepsilon_3 - \varepsilon_2) D \cot\theta\right] \sin\theta$

Joint shear stiffness: $K_s = \dfrac{\tau}{d_s}$

Joint normal stiffness: $K_n = \dfrac{\sigma_n}{d_n}$

Shear stress: $\tau = (\sigma_1 - \sigma_3)\sin\theta\cos\theta$

Normal stress: $\sigma_n = \sigma_3 + (\sigma_1 - \sigma_3)\sin^2\theta$

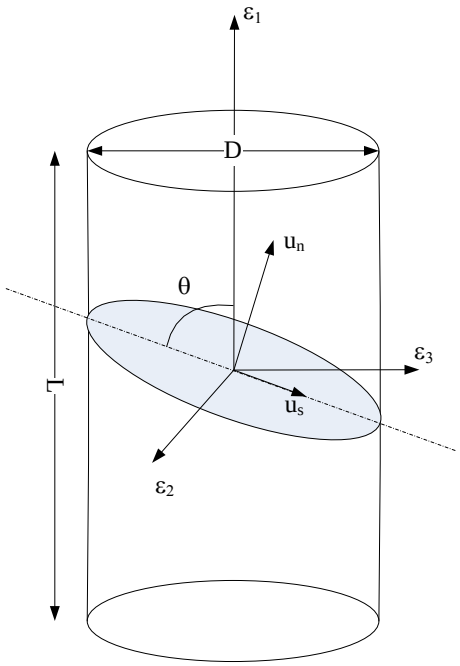

Figure 2.11 Illustration of relations between variables in triaxial test of a fractured specimen.

In above correlations and Figure 2.11, ε_1 is axial strain; ε_2 is small transverse strain; ε_3 is large transverse strain; D is sample diameter; θ is angle between the joint surface and the sample axis; L is sample length; E is elastic modulus determined from the competent specimen; σ_1 is axial stress; σ_3 is confining pressure.

From above relations, we can derive an expression of vertical equivalent Young's modulus in terms of properties of intact rock and fracture.

$$\frac{\sigma_d}{E'} = \frac{\sigma_d \sin^3\theta}{K_n L} + \frac{\sigma_3 \sin\theta}{K_n L} - \frac{\sigma_d}{K_s L}\sin\theta\cos^2\theta + \frac{\sigma_1}{E} \tag{2.11}$$

where deviatory stress $\sigma_d = \sigma_1 - \sigma_3$; E' is equivalent Young's modulus of the fractured sample; and other parameters are same as defined above. Here we assume the fracture properties and intact rock properties are known. Figure 2.12 shows the comparison between lab test result and calculated result using Equation (2.11). We can see that that equation approximates the lab test result well in elastic part.

Equation (2.11) is an approximation of Young's modulus in axial direction for an element which contains only one cut-through fracture, for example, elements in simulation case presented in Chapter 8.3, which are cut by a single hydraulic fracture (Figure 8.18). When more than one fracture are included in one element, fracture interactions need to be examined, which are not considered in this dissertation. The cutting-through angle θ in equation 2.11 is subject to change when the Young's modulus of other direction is calculated, which indicates that the fractured element may have anisotropic Young's modulus after equivalent continuum conversion.

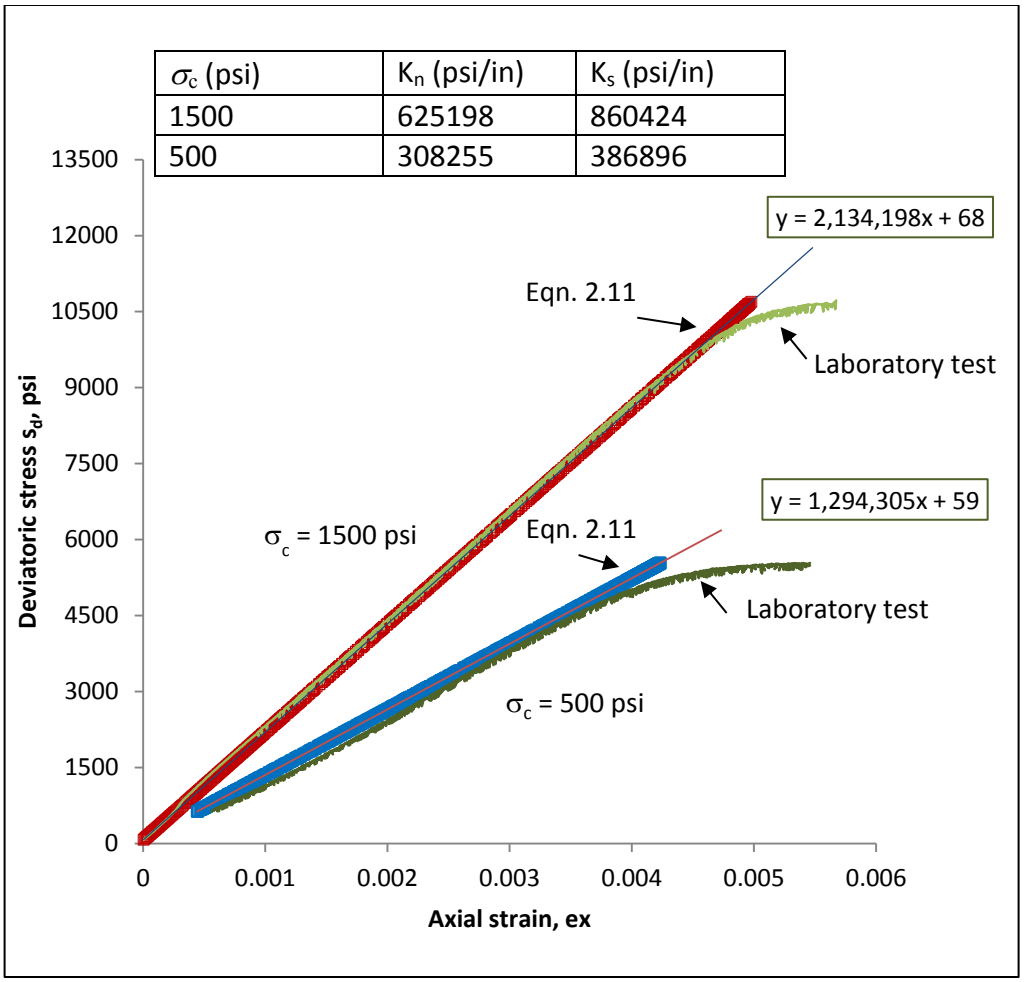

Figure 2.12 Comparison between Equation 2.11 results with laboratory data.

2.5. Heat transfer via fracture flow

In some cases, heat transfer can be de-coupled from mechanical response analysis. For example, heat flow (convection) in interconnected fracture network takes place so rapidly that the convection from adjacent rock to fracture can be ignored during the simulation time. The heat transfer model includes two parts:

1) 1D linear heat conduction from adjacent rock matrix into the fracture; and 2) 1D linear heat convection through channels formed by interconnected fractures (Figure 2.13; Equation 2.12). In this model, it is assumed that 1) fluid flow (heat convection) primarily occurs in channels within fractures; 2) heat conduction develops perpendicular to the fracture face; and 3) no heat is retained by the volume of fluid with in the fractures (Bruel 2002). In decoupled heat transfer calculations, the water flow through the rock matrix is ignored; therefore, the heat convection is confined within the interconnected fracture network. The energy conservation is obtained (Bruel 2002) at each fracture center by balancing the heat convection (via fluid flow) and heat conduction between adjacent rock mass and the fluid in the fracture (Figure 2.13; Equation 2.12).

$$\Delta E_i + \sum_{j}^{in} \rho_f C_f q_{ij} T_{fj} \Delta t = \sum_{k}^{out} \rho_f C_f q_{ik} T_{fk} \Delta t \qquad (2.12)$$

Where $\Delta E_i = k_m S_i (\frac{dT_m}{dy})_{y=0} \Delta t$ denotes the energy from the heat flux at fracture walls which is governed by conduction (diffusive equation, Equation 2.13). q_{ij} and q_{ik} represents the fluxes flow in a given fracture *i*, from fracture *j* and flow out to fracture *k* with temperature T_{fj} and T_{fi}, respectively (Figure 2.13). The fluid exits to the fracture *k* having the same temperature as the current temperature in fracture *i*. Similarly, fluid flows from fracture *j* to fracture *i* having the same temperature as the current temperature in fracture *j*.

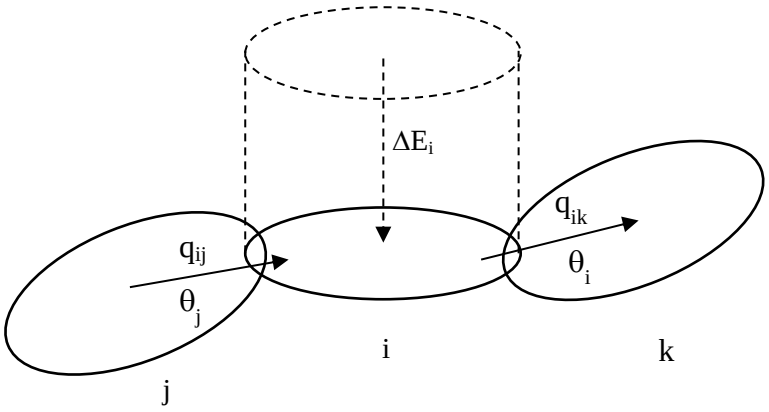

Figure 2.13 Energy conservation of fracture i.

The heat exchange across the fracture face can be described as (Bruel 2002):

$$dE_i = \Phi_i S_i dt$$

$$\Phi_i = k_m (dT_m / dy)_{y=0}$$

$$\alpha \nabla T_m = \frac{\partial T_m}{\partial t} \tag{2.13}$$

The above diffusive equation is solved using the finite difference method. Given the fracture temperature at time *t*, the solution will return the temperature distribution from the fracture face to the other end of the rock cylinder. After that, the heat flux Φ_i can be obtained and the energy exchanged (ΔE_i) calculated. At each fracture center, one energy balance equation is set up, and the set of equations is solved for q_{fi} at each time step. Parameters that appear in the above

equations are ρ_f and ρ_m are the fluid and rock density respectively, C_m is the solid heat capacity, α_m is the heat diffusivity of rock mass, S_i is the fracture face area, and k_m is the heat conductivity of rock mass.

The shape of the heat source rock block is assumed to be cylindrical with a radius equal to the fracture radius (Figure 2.14). The length of the cylinder is chosen so that the temperature on the other end of the cylinder remains unchanged during stimulation (Marin 2010). The results show that the temperature changes will not develop at a long distance within test time period. Therefore, the cylinder to cylinder interaction and the thermal stress effects are ignored at this stage. According to characteristic length definition (Marin 2010), the characteristic length of a cylinder of rock with a heat diffusivity of 1.15×10^{-6} m^2/s, is approximately 12 m/year. This length ensures the temperature on the opposite end of the matrix block is unchanged during one year of heat transfer. The 1D heat diffusive equation (2.12) for heat conduction can be written as

$$\frac{k_m}{\rho_m C_m}\frac{\partial T_m^2}{\partial y^2} = \frac{\partial T_m}{\partial t} \tag{2.14}$$

Defining $\alpha_m = \frac{k_m}{\rho_m C_m}$, then equation (2.13) becomes:

$$\alpha_m \frac{\partial T_m^2}{\partial y^2} = \frac{\partial T_m}{\partial t} \tag{2.15}$$

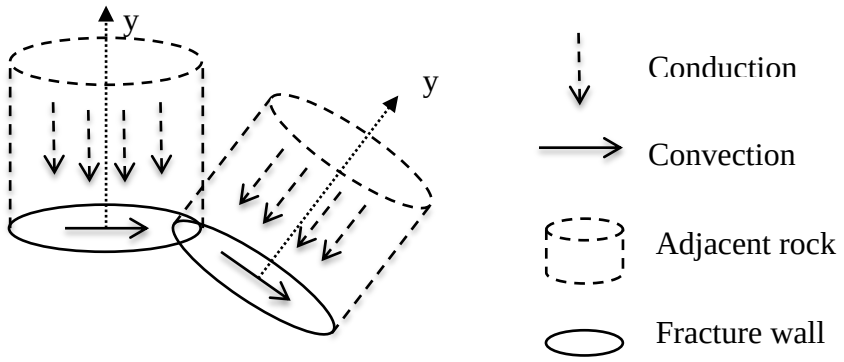

Figure 2.14 Heat transfer in interconnected fracture network.

It is easier to solve above equation using Finite Difference Method (FDM) than using FEM. The right hand side can be discretized in y- coordinate direction as

$$\frac{\partial T_m^2}{\partial y^2} = \frac{T_m(i+1) - 2T_m(i) + T_m(i-1)}{(\Delta y_i)^2} \tag{2.16}$$

The one dimensional heat conduction takes place in a cylinder which has a cross section area of $A = \pi r^2$. Therefore, the volume of each element (i) has a volume of $V_i = \pi r^2 \Delta y_i$. We can then write the discretized form of Equation (2.14) as

$$\frac{\alpha_m A}{\Delta y_i}\left[T_m(i+1) - T_m(i)\right] + \frac{\alpha_m A}{\Delta y_i}\left[T_m(i-1) - T_m(i)\right] = V_i \frac{T_m(t1) - T_m(t0)}{\Delta t} \tag{2.17}$$

If we use uniform element size, i.e. Δy = *const.*, then according to central differentiation, we can denote the coefficients as

$$K_T(i+) = K_T(i-) = \frac{\alpha_m}{(\Delta y)^2} \tag{2.18}$$

And finally the diffusion equation can be written in matrix form as

$$(1 - K_T \Delta t) T_m(t1) = T_m(t0) \tag{2.19}$$

The temperature distribution ($T_m|_y$) in the rock cylinder at time t can then be calculated. The temperature gradient dT_m / dy at fracture wall is needed in the heat convection calculation as the heat gain of the fracture from adjacent rock. In this model it is approximated by $(T_{m1}\text{-}T_{m0})|_t / \Delta y$.

For uncoupled heat transfer analysis, we assume the fluid flow is confined within the connected fracture networks. Therefore, it is necessary to find out the inter-connected fractures. A search algorithm is used to determine the connectivity. Every fracture is checked whether or not it belongs to a connected flow path. Then, dead ends and isolated fractures are removed. An iterative analysis is employed to do the searching (Appendix).

In order to solve the system of equation for heat transfer, the fluid flow in fracture network need to be solved first. As explained in the equivalent permeability section (2.3) fluid flow is confined within fracture networks. Fluid flow in fractures is assumed to be similar to that of parallel surfaces. Then the

cubic law provides the volumetric flux (m^3/s) through a fracture with aperture a and length l:

$$Q = \frac{-a^3 l}{12\mu}\frac{dp}{dl} \tag{2.20}$$

The flow network considers each connected fracture as a 1D pipe linking the centers of adjacent fractures (Figure 2.15). Let k_i and k_j represent the conductivity of fracture i and j, and let p_i and p_j be the pore pressure at each fracture center. L_i and L_j are the channel length in fracture i and j, respectively. The volumetric flow rate between fractures i and j can be write as (Cacas et al. 1990):

$$Q_{ij} = k_{ij}\frac{p_i - p_j}{L_i + L_j};\ k_{ij} = \frac{L_i + L_j}{L_i / k_i + L_j / k_j} \tag{2.21}$$

Conductivity of each fracture can be obtained from the modified cubic law:

$$k_i = \frac{-a_i^{\,3} L_i}{12\mu} \tag{2.22}$$

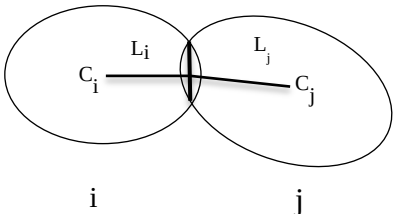

Figure 2.15 Flow channel between two connected fractures. C_i and C_j are centers of fractures i and j, L_i and L_j are the channel lengths in fractures i and j, respectively.

The system of equation for solving fluid flow between fractures can be generalized as following using the fact flow-in equals to flow-out

$$\sum_i Q_{ij} + source = 0 \tag{2.23}$$

$$[K_T][[p] = [Q] \tag{2.24}$$

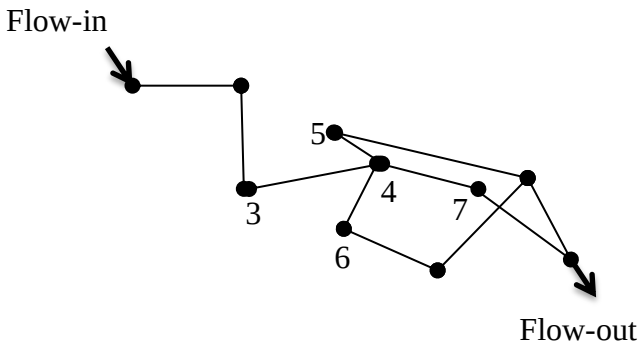

Figure 2.16 An example of pipe model for interconnected fracture network.

Taking node 4 in Figure 2.16 as an example, the above matrix equation can be expanded as

$$\begin{bmatrix} & & & & & & & & & \\ & & & & \vdots & & & & & \\ & & & & \vdots & & & & & \\ 0 & 0 & \frac{K_{34}}{L_{34}} & -\sum\frac{K_{ij}}{L_{ij}} & \frac{K_{45}}{L_{45}} & \frac{K_{46}}{L_{46}} & \frac{K_{47}}{L_{47}} & 0 & 0 & 0 \\ & & & & \vdots & & & & & \\ & & & & \vdots & & & & & \end{bmatrix} [p_i] = \begin{bmatrix} \vdots \\ \vdots \\ Q_4 \\ \vdots \\ \vdots \end{bmatrix} \quad (2.25)$$

where $\sum\frac{K_{ij}}{L_{ij}} = \frac{K_{34}}{L_{34}} + \frac{K_{45}}{L_{45}} + \frac{K_{46}}{L_{46}} + \frac{K_{47}}{L_{47}}$;

$[p_i] = [p_1, p_2, p_3, p_4, p_5, p_6, p_7, p_8, p_9, p_{10}]$;

$[Q_i] = [q_{in}, 0, 0, 0, 0, 0, 0, 0, 0, q_{out}]$.

After obtaining the nodal pore pressure, using Equation (2.21) we can find out the q_{ij} terms in Equation (2.12). And finally we can solve for the temperatures in each fracture. Figure 2.17 shows the result of a 2D pipe network example, and Figure 2.18 shows the result of a 3D pipe network example. All interconnected fractures are represented as pipes.

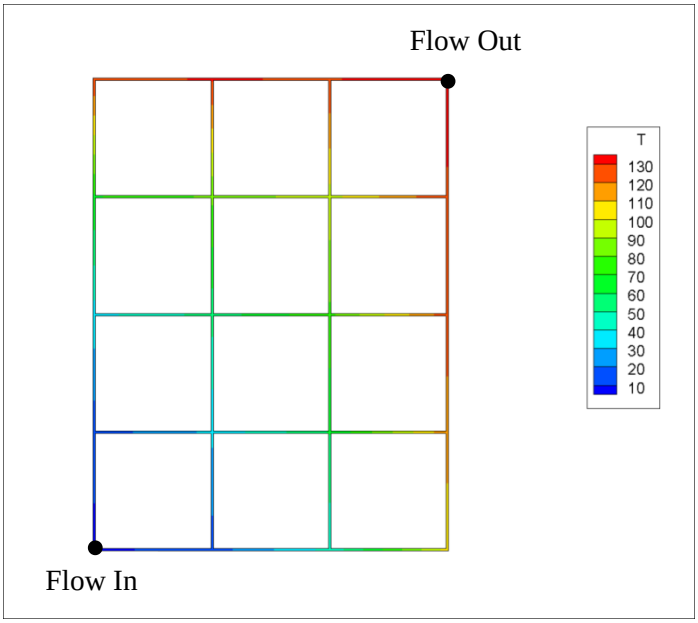

Figure 2.17 Temperature distribution in 2D channels formed by 1D pipes.

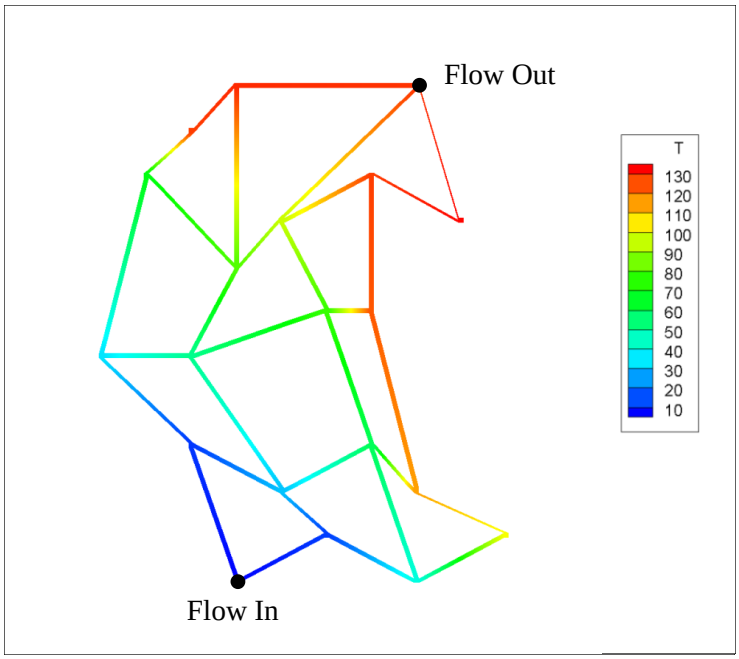

Figure 2.18 Temperature distribution of a 3D pipe network.

3

DISTRIBUTION OF ROCK HETEROGENEITY IN NUMERICAL MODELS

In general, all materials are more or less non-homogeneous because of the existence of micro-defects, such as pores, micro-cracks, different mineral grains, flaws, etc. These heterogeneities significantly affect the mechanical and flow behaviors of the material. In some cases, it is critical to take heterogeneities into consideration when the conventional homogeneous model is not sufficient to explain physical processes for the macro-scale heterogeneous materials, such as the strain-softening process of some rock. In this work, it is assumed that the initial distributions of the material properties are heterogeneous, which is described by Weibull distribution function whose parameters are obtained through comparing numerical stress-strain curves with laboratory test results. Three-steps are followed to produce the numerical stress-strain curve: 1) build a heterogeneous numerical sample in which the elemental properties' distribution follow Weibull distribution; 2) Derive the stress-strain curves (find initial Young's modulus, peak strength, threshold strain, residual stress and strain, etc.) of each element using it's elemental properties on the basis of continuum

damage model; 3) Use the FEM model to compute the stress-strain behavior of the entire numerical sample (Liang 2005). Applications of Weibull distribution and the continuum damage model, and the correlation between these two theories are introduced and explained in this chapter.

3.1. Weibull distribution

Weibull distribution (Weibull 1961) is widely used for modeling reliability and residual life data. Weibull models have been used to describe various types of observed failures of components and phenomena (Hallinan 1993; Johnson et al. 1994; Murthy et al. 2003). However, the Weibull distribution was initially used to model the distribution of breaking strength of materials (Weibull 1939). Weibull distribution has been modified and justified to be more applicable for the degradation of geo-materials in its later applications (Krajcinovic and Silva 1982; Chen et al. 2003; Cao et al. 2004; Wong et al. 2006). In the strength model, the distribution describes that the stress is a function of strain, similar as the time-life correlation in reliability models. In this situation, the probability density function (PDF) of two-parameter Weibull distribution of material strength (T) can be written as:

$$f(T) = \frac{m}{T_0}\left(\frac{T}{T_0}\right)^{m-1} \exp\left[-\left(\frac{T}{T_0}\right)^{m}\right] \tag{3.1}$$

And the cumulative distribution function (CDF), which can be viewed as damage ratio (the ratio between the numbers of damaged element and total element), is:

$$F(T) = 1 - \exp[-(\frac{T}{T_0})^m] \tag{3.2}$$

In above, the parameters of two-parameter Weibull distribution are: *m* the shape parameter and T_0 the characteristic material strength. Figure 3.1 and 3.2 give the PDF and CDF of two-parameter Weibull distribution for different parameters, from which one can get a sense of the physical meaning of *m* and T_0. The shape factor *m* controls the distribution of variables around the characteristic material strength T_0, which is the threshold strain at peak stress.

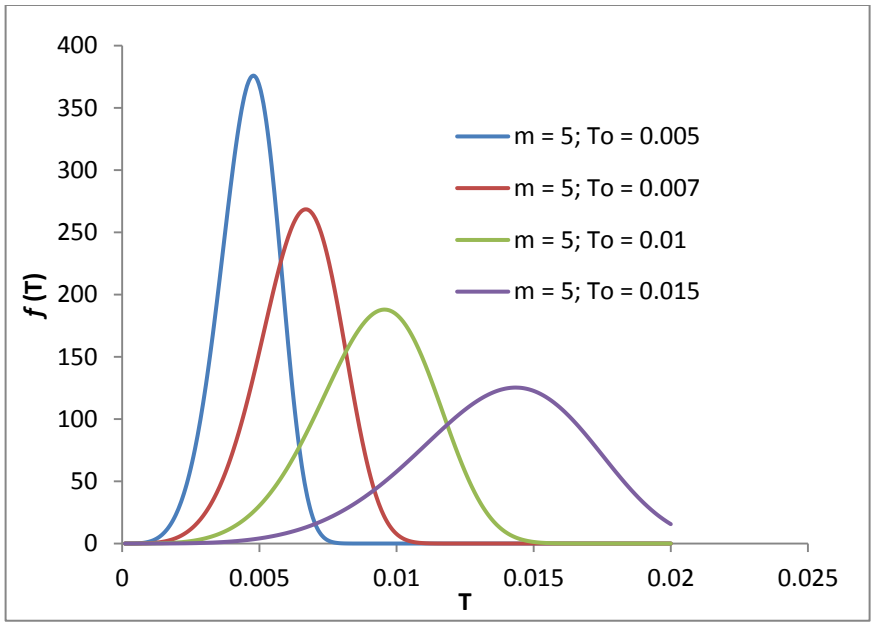

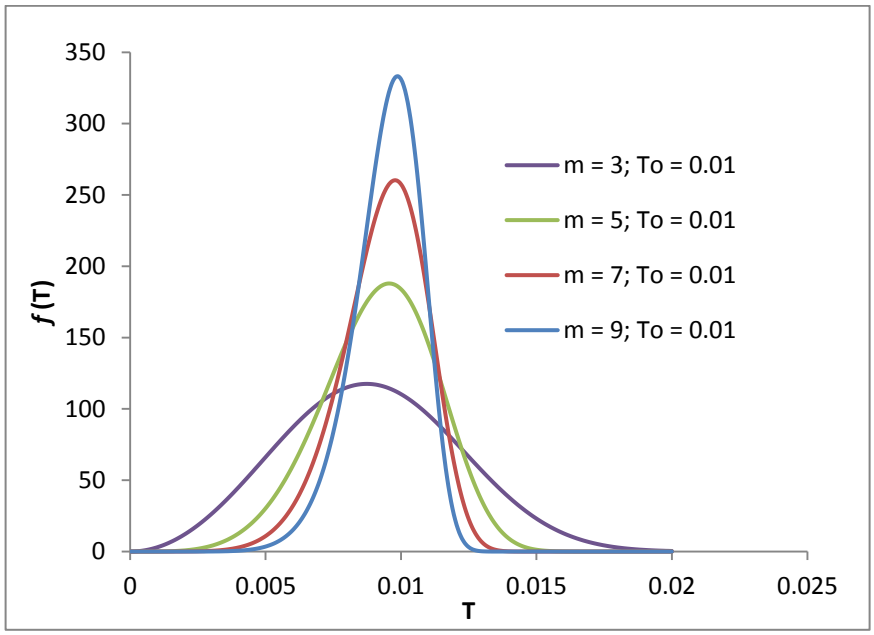

Figure 3.1 PFD of 2-parameter Weibull distribution.

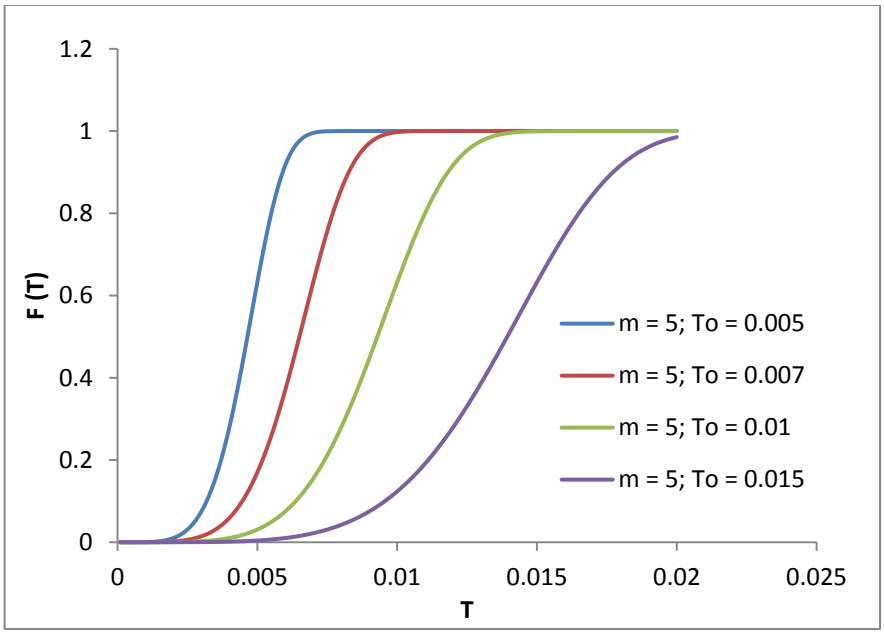

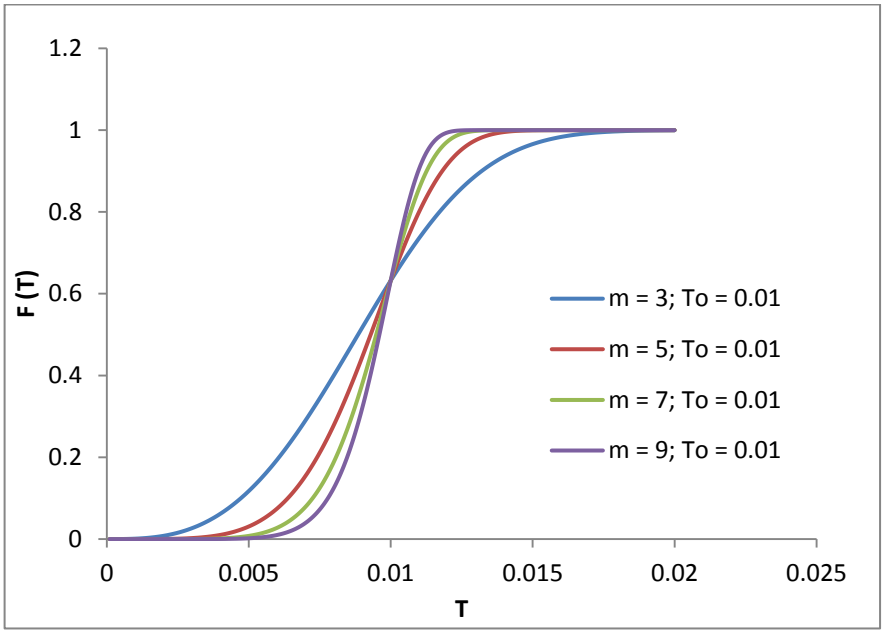

Figure 3.2 CFD of 2-parameter Weibull distribution.

3.2. Continuum damage mechanics and its illustration in uniaxial constitutive laws

Continuum damage mechanics has been developed continuously since it was first proposed by Kachanov (1958) and Rabotonov (1969). Various models have been reported in the literature, based on different concepts of damage measurement (Krempl 1977; Murakami and Ohno 1980; Lemaitre 1985). Generally, continuum mechanics is accepted to describe the undamaged (elastic) stress-strain constitutive relation of a heterogeneous material, even if the pre-existing micro-void, grains, and micro-defects makes the material not really continuum. The degradation process of most geo-materials consists of the initiation of micro-cracks, stress-strain concentration around micro-defects, and dislocation of grains, is considered irreversible even in generally considered elastic period. The progressive material degradation is caused by local damages, which initiate micro-fractures. Kachanove (1958) brought out the remarkable concept of macroscopic damage variable *D* as a measurement of damage of the entire structure (Figure 3.3A). Duvaut (1976) introduce the concept of measuring the material damage through the change in the mechanical behavior of the material, which can be interpreted through the "effective stress" concept (not to be confused with Terzaghi/Biot effective stress) is the stress (σ^{eff}), with higher than average (σ) value acting on the undamaged cross-section area (Figure 3.3B).

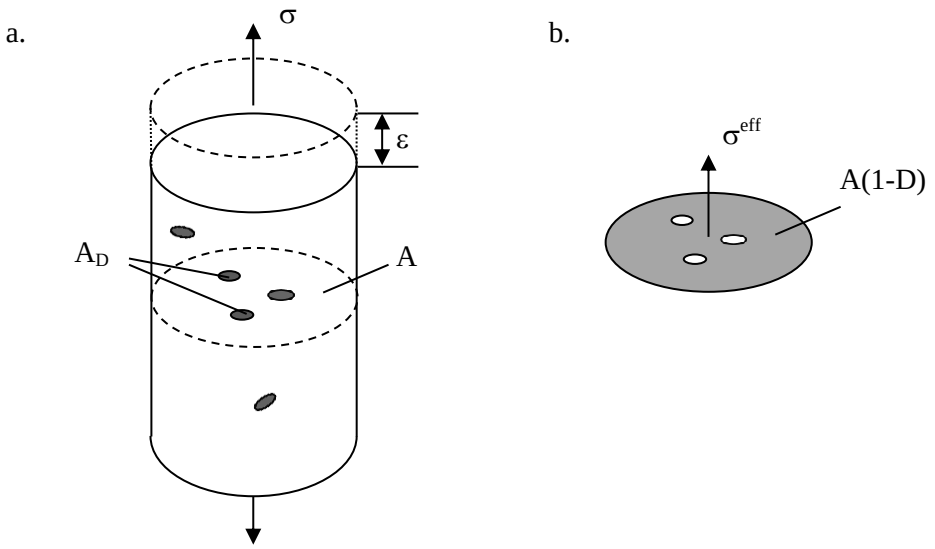

Figure 3.3 Schematic of a) area reduction due to damage; b) effective stress on un-damaged area A(1-D).

$$D = \frac{A_D}{A} \tag{3.3}$$

$$\sigma^{eff} = \frac{\sigma}{1-D}; \qquad 0 \le D < 1 \tag{3.4}$$

From the effective stress concept, for ductile material, the damage variable can be considered as the degradation of the material elastic modulus (Lemaitre 1985).

$$\text{Since } \frac{\sigma^{eff}}{E_d} = \frac{\sigma}{E}, \text{ then } D = 1 - \frac{E_d}{E} \tag{3.5}$$

D ranges from zero for the undamaged rock to one for ultimately damaged rock. Figure 3.4 shows the theoretical uniaxial stress-strain curve with both compressive and tensile behavior. According to the definition of damage variable *D* (Equation 3.5), after peak strength, the degraded material will have a lower Young's modulus, E_d, and lower strength, σ (Figure 3.4). In this work, it is assumed that the curve will go back to initial state with a slope of E_d when unloading (Li et al. 2012). According to Equation (3.5), the damage variable can also be expressed in terms stress of undamaged material and stress of damaged material:

$$D = 1 - \frac{\varepsilon E_d}{\varepsilon E} \tag{3.6}$$

Applying Equation (3.6) onto the constitutive relation (Figure 3.4):

1) If damage occurs as compressive failure, the damage variable, *D*, can be expressed in terms of strain, peak stress (uniaxial compressive strength), and residual compressive strength of the sample (Figure 3.4):

$$\begin{cases} D = 0; & \varepsilon < \varepsilon_c \\ D = 1 - [(\dfrac{\sigma_r - \sigma_c}{\varepsilon_r - \varepsilon_c})(\varepsilon - \varepsilon_c) + \sigma_c] / E_0 \varepsilon; & \varepsilon_c < \varepsilon < \varepsilon_r \\ D = 1 - \sigma_r / E_0 \varepsilon; & \varepsilon > \varepsilon_r \end{cases} \tag{3.7-1}$$

where σ_r and ε_r are the residual compressive strength and strain, and σ_c and ε_c are the compressive stress and strain at peak. ε is the current compressive axial strain. E_0 is the undamaged Young's modulus.

2) In tensile loading, the damage variable can be written as (Figure 3.4):

$$\begin{cases} D = 0; & \varepsilon < \varepsilon_t \\ D = 1 - \dfrac{\sigma_t}{E_0 \varepsilon}; & \varepsilon > \varepsilon_t \end{cases} \tag{3.7-2}$$

where, similar as compressive damage, σ_t and ε_t are the tensile stress and strain at peak. ε is the current tensile axial strain. E_0 is the undamaged Young's modulus.

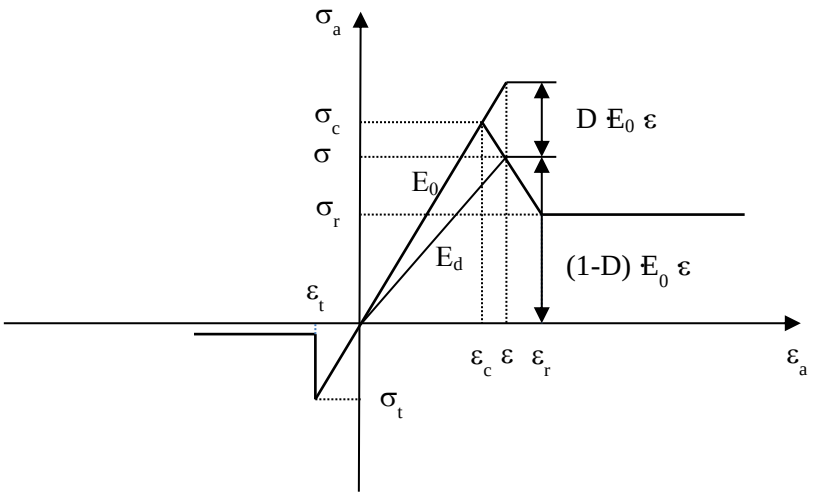

Figure 3.4 Constitutive law of uniaxial test.

3.3. Combination of continuum damage mechanics and Weibull failure theory

As a load is applied to a rock sample, the stresses gradually increase and an individual element may fail when the local stress reaches the elemental strength. First, it is assumed that each element is homogeneous and will be completely failed (i.e. elemental damage variable D_e = 1) when elemental stress reaches the ultimate strain, i.e. no residual strength (Figure 3.6). The distribution of elemental strengths follows the Weibull probability density function (Chen et al. 2006):

$$f(x) = \frac{m}{\varepsilon_0}\left(\frac{\varepsilon}{\varepsilon_0}\right)^{m-1} \exp\left[-\left(\frac{\varepsilon}{\varepsilon_0}\right)^{m}\right] \tag{3.8}$$

where m is a shape parameter related to the material homogeneity, ε_0 is a scale parameter related to the average local uniaxial strength, and x is the uniaxial strain strength for an individual element.

The damage variable D of the entire sample, indicating the ratio of the number of damaged FEM elements to the total number of elements in this study, is the cumulative density function (CDF) of Weibull distribution (Equation 3.2):

$$D = \int_0^{\varepsilon_1} f(x)dx \tag{3.9}$$

ε_1 is the current uniaxial strain of the rock specimen. Combining Equation (3.8) and (3.9) provides:

$$D = 1 - \exp[-(\frac{\varepsilon_1}{\varepsilon_0})^m] \tag{3.10}$$

For uniaxial test, $\varepsilon_1 = \sigma_1 / E(1-D)$. Therefore, the uniaxial constitutive equation can be written as:

$$\sigma_1 = E\varepsilon_1 \exp[-(\varepsilon_1 / \varepsilon_0)^m] \tag{3.11}$$

Figure 3.5 shows a typical theoretical stress-strain curve of a uniaxial test. At peak load, the derivative of above equation with respect to strain equals zero, yielding:

$$\frac{d\sigma_1}{d\varepsilon_1} = E \exp[-\left(\frac{\varepsilon_1}{\varepsilon_0}\right)^m][1 - m\left(\frac{\varepsilon_1}{\varepsilon_0}\right)^m] = 0 \tag{3.12}$$

At the peak point, the stress and strain are given by the uniaxial strength (σ_c) and threshold strain (ε_c) from laboratory test curve. Then it can be shown that (Chen et al. 2006):

$$m = \frac{1}{\ln(E_o / E_c)}; \text{ and } \varepsilon_0 = m^{1/m}\varepsilon_c \tag{3.13}$$

where E_0 and E_c are the initial tangent modulus and the secant modulus of rock in uniaxial compression stress-strain curve. Finally, with parameters obtained from laboratory test curve (Equation 3.13), the theoretical stress-strain curve calculated using Weibull theory (Equation 3.8) for the heterogeneous rock

sample is plotted in Figure 3.5. It can be observed that the theoretical curve fits well with the pre-peek part of the lab curve. In order to better approximate the post peak softening behavior, the post peak behavior of each individual element needs to be modified.

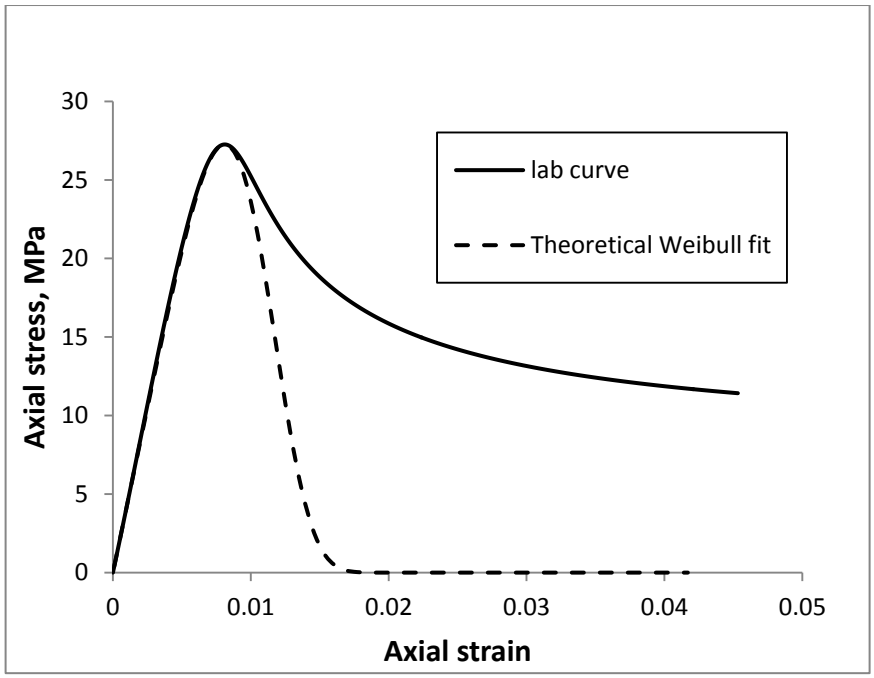

Figure 3.5 Typical complete stress-strain curve of a stress softening rock and the theoretical Weibull fit of the curve.

In the theoretical damage constitutive law derivation, the damaged element is assumed to have complete failure and has no residual strength. However, damaged element in the sample still has some strength, due to the confinement of surrounding elements. Therefore, in order to approximate the post peak behavior, we modify the post peak constitutive relation by assigning residual

strength (stress) to each element; hence change the elemental constitutive law from Figure 3.6 to Figure 3.7. The value of residual strength is determined by trial and error as shown in Figure 3.8.

After this modification, we can produce better fitted stress-strain curves (Figure 3.8) by combining continuum damage mechanics and Weibull distribution. For instance, in the heterogeneity modeling, four steps are followed: 1) use Weibull's distribution Equation (3.8), with parameters calculated from constitutive correlation of continuum damage mechanics (Equation 3.13), to assign the heterogeneous properties to each element. 2) at each load increment, apply modified constitutive correlations (Figure 3.7) to each element for elemental failure analysis, by calculating elemental damage variables (Equation 3.7), and hence obtain the degraded material properties for next load increment; 4) at the end of loading process, plot the complete stress-strain curve of the entire sample; 5) compare to laboratory test curve, make adjustment to constitutive correlations if necessary until satisfactory fit, i.e., adjust the value of elemental residual strength and ultimate strain. In Figure 3.8 the numerical stress-strain curves with different residual strengths and ultimate strains (post peek behavior) are plotted. The parameter m (shape factor) for heterogeneous distribution is 4.5; the average undamaged Young's modulus, uniaxial strength, and Poisson's ratio are 4.2 GPa, 27 MPa, and 0.2, respectively. One can find that

the curve with 40% residual strength and 2.5ε_c ultimate strain gives a good match to the laboratory test curve.

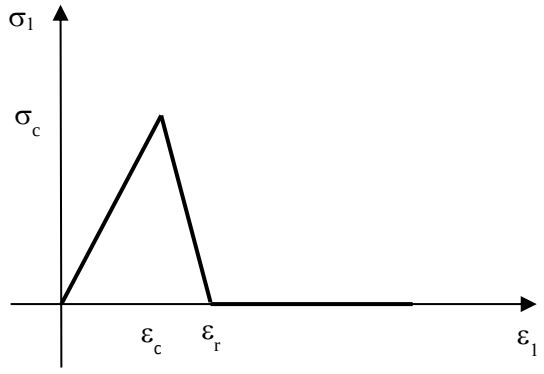

Figure 3.6 Schematic of uniaxial constitutive law with no residual strength.

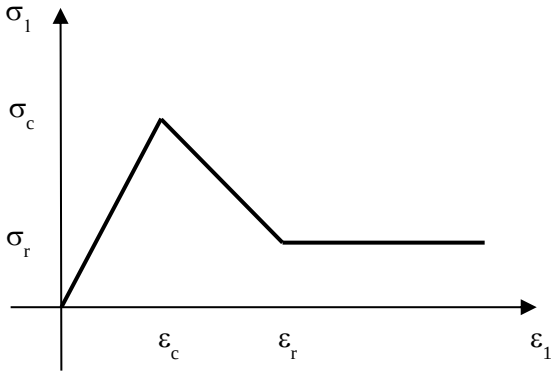

Figure 3.7 Schematic of uniaxial constitutive law with residual strength.

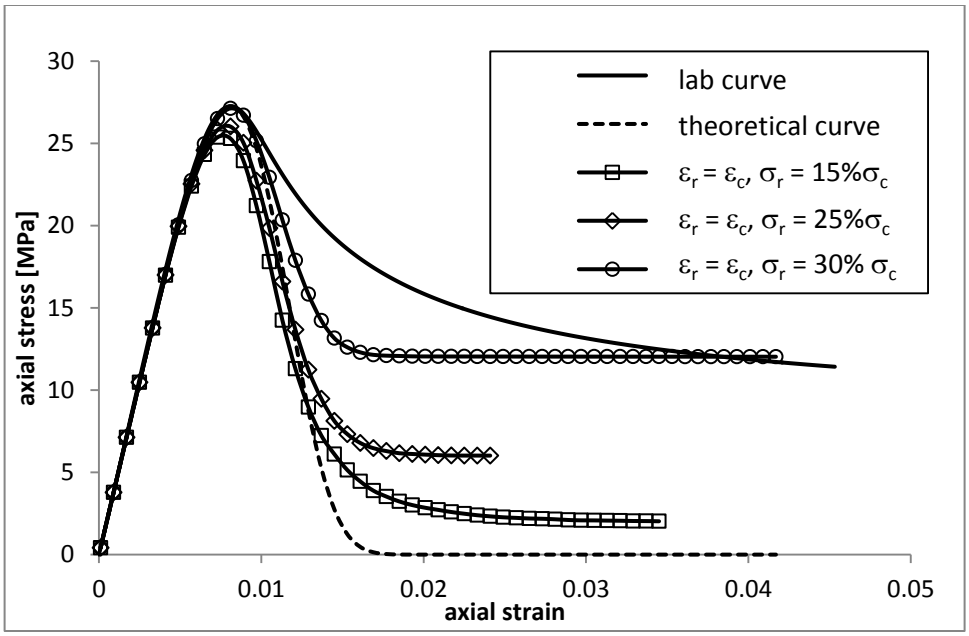

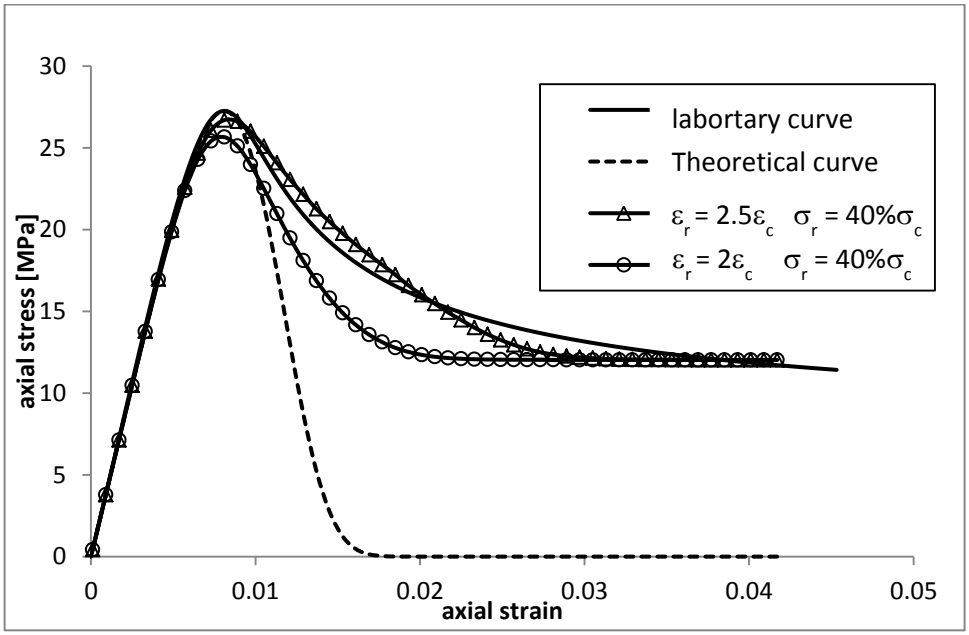

Figure 3.8 Numerically fitting lab test stress-strain curve using Weibull Theory and continuum damage mechanics.

4

THERMO-POROELASTICITY

Governing equations for coupled rock deformation-fluid flow problems have been developed and improved for decades. Terzaghi (1923) proposed the concept of effective stress considering the pore pressure effect on soil consolidation. Biot (1941) systematically developed the fundamental poroelastic theory, or Biot theory, that illustrates the coupling effect between fluid and solid. Rice and Cleary (1976) reformulated Biot theory by using more familiar elastic constants. More recently, thermal-poroelastic theory has been extended from Cleary theory (McTigue 1986; Kurashige 1989). These theories are extensively used nowadays in research and application. Extensions according to problem definitions have also been made, for example, effect of chemical potential on rock deformation has been studied and thermal-chemo-poroelastic formulation has been developed (Mody and Hale 1993; Heidug and Wong 1996; Ghassemi and Diek 2003). In this thesis, Kurashige's formulation of thermo-poroelasticity is adopted which considers the coupling effect among mechanical stress, fluid pressure and thermal stress, and the coupling between fluid flow and heat transfer. *The sign convention is tension positive*.

4.1. Constitutive equations

The coupling between solid and fluid is reflected in the interaction between rock deformation and pore fluid diffusion, in other words, the change of pore pressure causes rock deformation and also rock could deformed by fluid flow. Similarly, temperature change causes rock deformation and fluid diffusion, and fluid flow lead to heat convection. In this work, the thermal effect of rock deformation and fluid compression is ignored. The 3D constitutive equations of the fluid saturated thermoelastic porous material can be written as:

$$\varepsilon_{ij} = C_{ijkl}\sigma_{kl} + B_{ij}p + \alpha_{ij}^{Tl}T \tag{4.1}$$

$$\Delta\phi = B_{kl}\sigma_{kl} + Dp + \alpha_{p}^{T}T \tag{4.2}$$

Equations (4.1 - 4.2) show the influences of stresses, pressure and temperature on the deformation of solid phase and fluid phase. For instance, tensile stress, increase of pore pressure, and increase of temperature will cause expansion of the solid phase. Similarly, compression, decreasing pore pressure, and cooling of pore fluid will lead to shrinkage of the pore space.

For isotropic materials:

$$C_{ijkl} = \frac{1}{4G}(\delta_{ik}\delta_{jl} + \delta_{il}\delta_{jk} - \frac{2}{1+\upsilon}\delta_{ij}\delta_{kl}) \tag{4.3}$$

$$B_{ij} = \frac{3(\upsilon_u - \upsilon)}{2GB(1+\upsilon)(1+\upsilon_u)}\delta_{ij} \tag{4.4}$$

$$D = \frac{1}{B}(\frac{1}{K} - \frac{1}{K_s^{'}}) - \frac{\phi}{K_f} \tag{4.5}$$

$$K = \frac{2G(1+\upsilon)}{3(1-2\upsilon)} \tag{4.6}$$

$$\alpha_{ij}^{Tl} = \alpha_m^{Tl}\delta_{ij} \tag{4.7}$$

Where, ϕ, G, K, ν, and α_m^{Tl} are the porosity, shear modulus, bulk modulus, Poisson's ratio, and the linear thermal expansion coefficient of the rock, respectively. And ν_u is the corresponding undrained Poisson's ratio. K_f is the bulk modulus of pore fluid; $K_s^{'}$ is the effective bulk modulus of the solid constituent. α_p^T is the volumetric thermal expansion coefficient of the pore space. B in Equation (4.5) is Skempton's pore coefficient, and is related to Biot's coefficient α as:

$$B = \frac{3(\upsilon_u - \upsilon)}{\alpha(1-2\upsilon)(1+\upsilon_u)} \tag{4.8}$$

With above expressions, equation (2.1) and (2.2) can be rewrite as:

$$\sigma_{ij} = 2G\varepsilon_{ij} + (K - \frac{2G}{3})\varepsilon_{kk}\delta_{ij} - \alpha p\delta_{ij} - \frac{2G(1+\upsilon)}{3(1-2\upsilon)}\alpha_m^T T\delta_{ij} \tag{4.9}$$

$$\Delta\phi = \frac{1}{2G}\frac{\alpha(1-2\upsilon)}{(1+\upsilon)}\sigma_{kk} + (\frac{1}{B}(\frac{1}{K} - \frac{1}{K_s^{'}}) - \frac{\phi}{K_f})p + \alpha_p^T T \tag{4.10}$$

α_m^T is the volumetric thermal expansion coefficient of the rock, assuming $\alpha_m^{Tl} = \alpha_m^T / 3$. If the pores expand with their shapes remaining similar, as the pours matrix expands thermally, coefficient α_p^T can be expressed as $\alpha_m^T\phi$. For thermal expansion, we assume the same temperature increment for both rock and pore fluid because local heat

change between both components may be rapid enough in comparison with global heat and fluid diffusions (Kurashige 1989).

For a unit bulk volume, the mass content of pore fluid can be expressed as:

$$m = \rho_f \phi \tag{4.11}$$

Therefore, the change of fluid mass content for the unit volume of material is:

$$\Delta m = \rho_f \Delta\phi + \Delta\rho_f \phi \tag{4.12}$$

In above expressions, ρ_f is the fluid density. The change in fluid density due to pore pressure and temperature variation can be expressed as:

$$\frac{\Delta\rho_f}{\rho_f} = \frac{p}{K_f} - \alpha_f^T T \tag{4.13}$$

where α_f^T is the volumetric thermal expansion coefficient of the pore fluid. Substituting (4.10) and (4.13) into (4.12) yields:

$$\frac{\Delta m}{\rho_f} = \frac{1}{2G}\frac{\alpha(1-2\upsilon)}{(1+\upsilon)}\sigma_{kk} + \frac{1}{B}\left(\frac{1}{K} - \frac{1}{K_s^{'}}\right)p + (\alpha_p^T - \alpha_f^T\phi)T \tag{4.14}$$

Presenting (4.14) in terms of the change of fluid volume content per unit reference volume ζ, yields:

$$\zeta = \frac{1}{2G}\frac{\alpha(1-2\upsilon)}{(1+\upsilon)}\left(\sigma_{kk} + \frac{3}{B}p\right) + (\alpha_p^T - \alpha_f^T\phi)T \tag{4.15}$$

by applying the following relation between material properties and (4.8):

$$\frac{1}{B}\left(\frac{1}{K} - \frac{1}{K_s^{'}}\right) = \frac{9(\upsilon_u - \upsilon)}{2GB^2(1+\upsilon_u)(1+\upsilon)} \tag{4.16}$$

Equations (4.9) and (4.15) are convenient versions of the constitutive relations for thermo-poroelastic analysis. Next, the constitutive relations associated with the heat and fluid diffusion are considered. As noted by to Cleary 1976, by identifying the consequence of positive entropy production as implied by existing relationship between the fluxes and their driving forces, the following coupled Fourier-Darcy laws (Kurashige 1989):

$$q_i = -\rho_f \kappa_{ij} p_{,j} + L_{ij} T_{,j} \tag{4.17}$$

$$h_i = -\kappa_{ij}^T T_{,j} + L'_{ij}\, p_{,j} \tag{4.18}$$

where h_i and q_i are the heat flux and fluid flux, respectively. L_{ij} and L'_{ij} are the cross-effect coefficients, which are neglected in this work because they are generally much smaller than the first terms in the right hand side of (4.17) and (4.18). Therefore, the constitutive relations for mass and heat diffusion in this work can be simplified as:

$$q_i = -\rho_f \kappa_{ij} p_{,j} \tag{4.19}$$

$$h_i = -\kappa_{ij}^T T_{,j} \tag{4.20}$$

where κ_{ij} and κ_{ij}^T are hydraulic and thermal conductivity, respectively.

4.2. Conservation laws

There are three conservation laws used to solve stress, pressure and temperature field, namely,

1) The equilibrium equation:

$$\sigma_{ij,j} = 0 \tag{4.21}$$

2) The fluid mass conservation equation:

$$\frac{\partial \Delta m}{\partial t} = -q_{i,i} \tag{4.22}$$

Substituting (4.19) into (4.22), one obtains:

$$\frac{\partial \Delta m}{\partial t} = \rho_f \kappa p_{,jj} \tag{4.23}$$

or:

$$\frac{\partial \zeta}{\partial t} = \kappa p_{,jj} \tag{4.24}$$

3) The energy conservation equation:

$$\rho_t C_t \frac{\partial T}{\partial t} = -h_{i,i} - C_f T q_{i,i} \tag{4.25}$$

where ρ_t and C_t are the total mass density and specific heat for the bulk material, and C_f is the specific heat of pore fluid. The first term on the right hand side represents the conductive heat transfer through the porous material, and the second term represents the convective heat transfer via the pore fluid

flow. Similarly as thermal expansion, we assume same temperature increment for both rock and fluid. This is based on an assumption that the fluid velocity in the porous medium is low enough to maintain the equality of temperature between fluid and solid phase in an elementary volume (Li 1996). The occurrence of significant temperature differences between the two phases are possible when the fluid velocity is high, which will be discussed in heat transfer of fracture flow later.

4.3. Field equations

4.3.1. Deformation field equation

Substituting compatibility equation (4.26) for small deformations into (4.9), the Navier's equation for displacements (4.27) is obtained:

$$\varepsilon_{ij} = \frac{1}{2}(u_{i,j} + u_{j,i}) \tag{4.26}$$

$$Gu_{i,jj} + (K + \frac{G}{3})u_{j,ji} - \alpha p_{,j} - \gamma_1 T_{,j} = 0 \tag{4.27}$$

in which:

$$\gamma_1 = \frac{2G(1+\upsilon)}{3(1-2\upsilon)}\alpha_m^T \tag{4.28}$$

4.3.2. Fluid diffusion field equation

Differentiating (4.15) with respect to time, one obtains:

$$\frac{\partial}{\partial t}\zeta = \frac{1}{2G}\frac{\alpha(1-2\upsilon)}{(1+\upsilon)}\left(\frac{\partial \sigma_{kk}}{\partial t} + \frac{3}{B}\frac{\partial p}{\partial t}\right) + (\alpha_p^T - \alpha_f^T \phi)\frac{\partial T}{\partial t} \tag{4.29}$$

Using the following relation between material properties and (4.24):

$$\frac{2GB^2(1+\upsilon)(1+\upsilon_u)}{9(\upsilon_u - \upsilon)} = \frac{2G(1+\upsilon)}{1-2\upsilon}\cdot\frac{1}{\alpha}\cdot\frac{B}{3} \tag{4.30}$$

Equation (4.29) can be rewritten as:

$$\begin{aligned}\frac{B}{3}\frac{\partial \sigma_{kk}}{\partial t} + \frac{\partial p}{\partial t} + \frac{2GB^2(1+\upsilon)(1+\upsilon_u)}{9(\upsilon_u - \upsilon)}(\alpha_p^T - \alpha_f^T \phi)\frac{\partial T}{\partial t} \\ - \frac{2GB^2(1+\upsilon)(1+\upsilon_u)}{9(\upsilon_u - \upsilon)}\kappa p_{,jj} = 0\end{aligned} \tag{4.31}$$

Differentiating (4.9) with respect to time yields:

$$\frac{\partial \sigma_{kk}}{\partial t} = 2G\frac{1+\upsilon}{1-2\upsilon}\frac{\partial \varepsilon_{kk}}{\partial t} - 3\alpha\frac{\partial p}{\partial t} - \frac{2G(1+\upsilon)}{(1-2\upsilon)}\alpha_m^T\frac{\partial T}{\partial t} \tag{4.32}$$

Substituting (4.32) back into (4.31), then rearranging, one obtains:

$$\alpha\frac{\partial \varepsilon_{kk}}{\partial t} + \beta\frac{dp}{dt} - \kappa p_{,jj} - \gamma_2\frac{dT}{dt} = 0 \tag{4.33}$$

Where:

$$\beta = \frac{\alpha^2(1-2\upsilon)(1-2\upsilon_u)}{2G(\upsilon_u - \upsilon)} \tag{4.34}$$

$$\gamma_2 = (\alpha\alpha_m^T + \alpha_f^T\phi - \alpha_p^T) \tag{4.35}$$

4.3.3. Thermal diffusion field equation

Substituting (4.19) and (4.20) into (4.25), one obtains:

$$\rho_t C_t \frac{\partial T}{\partial t} = k^T T_{,jj} + (\rho_f \kappa C_f T p_{,i})_{,i} \tag{4.36}$$

Rearranging (4.36) and defining the following, one can get the thermal diffusion field equation as (4.39):

$$c^T = \frac{k^T}{\rho_t C_t} \tag{4.37}$$

$$\kappa^T = \kappa \frac{\rho_f C_f}{\rho_t C_t} \tag{4.38}$$

$$\frac{\partial T}{\partial t} - c^T T_{,jj} - (\kappa^T T p_{,i})_{,i} = 0 \tag{4.39}$$

Three field equations we obtained previously are summarized as follows:

$$G u_{i,jj} + (K + \frac{G}{3}) u_{j,ji} - \alpha p_{,j} - \gamma_1 T_{,j} = 0 \tag{4.40}$$

$$\alpha \frac{\partial \varepsilon_{kk}}{\partial t} + \beta \frac{dp}{dt} - \kappa p_{,jj} - \gamma_2 \frac{dT}{dt} = 0 \tag{4.41}$$

$$\frac{\partial T}{\partial t} - c^T T_{,jj} - (\kappa^T T p_{,i})_{,i} = 0 \tag{4.42}$$

From the above field equations, it can be seen that in this work the displacement field is completely coupled with the pore pressure and temperature fields. Also, pore pressure is coupled with displacement and temperature fields.

The above fully coupled thermo-poroelastic field equations are derived for continuum fields of homogeneous and isotropic material. Extension of these equations for the usage in heterogeneous anisotropic rock will be discussed later in next chapter (Chapter 5) by applying finite element method (FEM).

5

FINITE ELEMENT METHOD AND ITS APPLICATIONS IN GEOMECHANICS PROBLEMS

Governing equations for thermo-poroelasticity are a set of partial differential equations with respect to space and time. Analytical solutions exist for relatively simple geometries and material properties, and are generally subjected to many strict assumptions (homogeneous, continuum, simple boundary, etc.). When realistic physical conditions such as heterogeneity, nonlinearity, and complex geometries are considered, numerical solutions have to be sought. There are few numerical methods available for solving a set of partial differential equations. Finite element method (FEM) and Finite difference method (FDM) are among the most popular numerical methods. Comparing to traditional FDM, FEM is better in dealing with arbitrary geometries, and has greater capability for higher order boundary conditions.

5.1. Fundamental aspects of PDE discretization in FEM

The finite element method is a technique for solving partial differential equations (PDE) by first discretizing these equations in their space domain

(discretization) and to a system of elemental equations. The representative small regions are called the finite elements, which has simple but irregular geometry with finite number of degree of freedom. In order to solve equations over large regions, the discretized matrix equations for the smaller sub-region (elemental equation) can be summed node by node, resulting in global matrix equations (assemble).

In the finite element method, continuous spatial variables in these PDEs such as displacement *u*, pore pressure *p*, and temperature *T* can be approximated by interpolation functions (*u(x, y, z)*, *p(x, y, z)*, and *T(x, y, z)*) in terms of their nodal values ($\widetilde{u}_i$, $\widetilde{p}_i$, and $\widetilde{T}_i$) respectively by assigning appropriate coefficients N_i (shape functions) to each node value. For example, considering a three-dimensional brick element (8 nodes) (Figure 5.1), the interpolation functions can be written as:

$$u = \sum_{i=1}^{8} N_i \widetilde{u}_i \tag{5.1}$$

$$p = \sum_{i=1}^{8} N_i \widetilde{p}_i \tag{5.2}$$

$$T = \sum_{i=1}^{8} N_i \widetilde{T}_i \tag{5.3}$$

where u , p , and T are the polynomial interpolations of continuous displacement, pore pressure and temperature functions. N_i is the interpolation coefficient and is generally referred to as shape function where subscript denotes the corresponding node. $\tilde{u}_i$, $\tilde{p}_i$, and $\tilde{T}_i$ denote the function values on corresponding nodes.

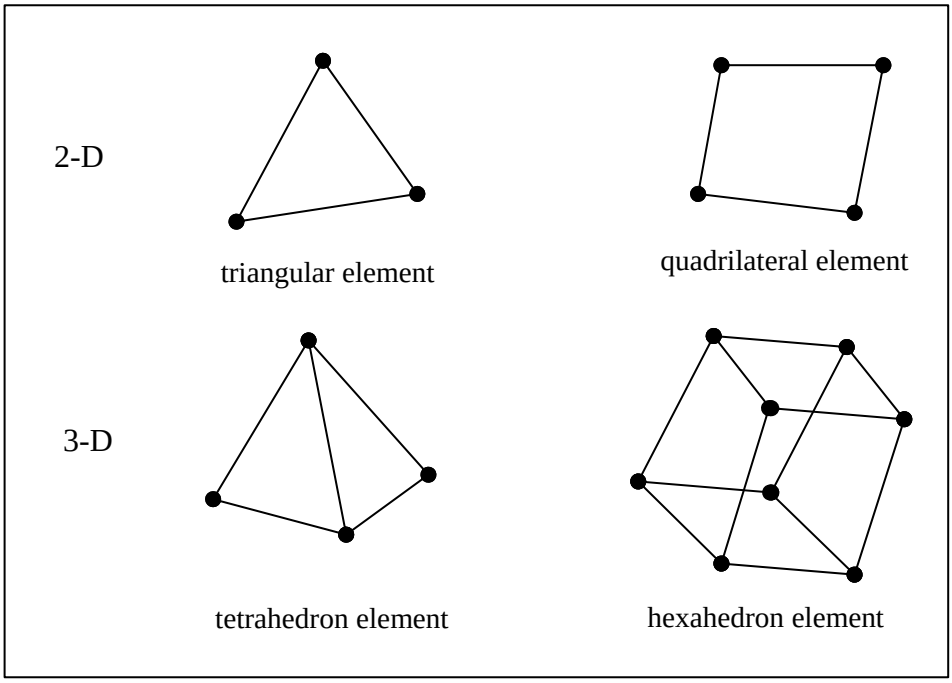

Figure 5.1 Commonly used 2D and 3D FEM Elements

The accuracy of the finite element solution depends on the order of interpolation error and is generally called *residual*. Many methods could be used to minimize the residual, for example collocation, subdomain, Galerkin, and least square technique (Griffiths and Smith 1991). Of these, Galerkin's method is the most

widely used in finite element work. For illustration simplicity, the following example for Galerkin's method considers a one-dimensional rod element (Figure 5.2).

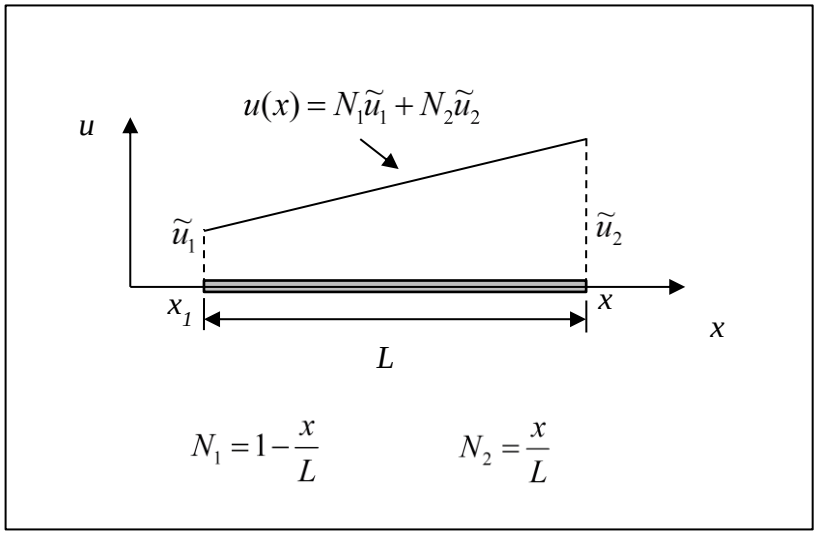

Figure 5.2 Example for interpolation of continuous displacement using nodal variable and shape function in 1D FEM element.

Figure 5.2 shows a 1D solid element with end nodes 1 and 2. The element has length *L* and a cross sectional area *A*, and Young's modulus of *E*. u is the longitudinal displacement which is a function of space variable (*x* in this case). The differential equation for displacement of this element under external force *F* can be written as (Smith and Griffiths 2004):

$$EA\frac{d^2u}{dx^2} + F = 0 \tag{5.4}$$

After discretization, Equation (5.4) becomes:

$$EA\frac{d^2}{dx^2}[N_1 \quad N_2]\begin{Bmatrix}\tilde{u}_1\\ \tilde{u}_2\end{Bmatrix}+F=R \tag{5.5}$$

where $N_1=1-\frac{x}{L}$, $N_2=\frac{x}{L}$, $R=$ *residual* (5.6)

In the Galerkin's method or so the called weighted residual method the values of u_1 and u_2 are widely selected to minimize the residual. The process basically consists of multiplying the residual by each shape function in turn, integrating over the element and equating to zero. Thus:

$$\int_0^L \begin{Bmatrix}N_1\\ N_2\end{Bmatrix} EA\frac{d^2}{dx^2}[N_1 \quad N_2]dx\begin{bmatrix}\tilde{u}_1\\ \tilde{u}_2\end{bmatrix}+\int_0^L \begin{Bmatrix}N_1\\ N_2\end{Bmatrix} Fdx=\begin{Bmatrix}0\\ 0\end{Bmatrix} \tag{5.7}$$

In the present example, since linear shape functions are used, double differentiation would lead them to vanish. But typically, by applying Green's theorem (integration by parts) integrals terms with double differentiation can be calculated as:

$$\int N_i\frac{\partial^2 N_j}{\partial x^2}dx=-\int\frac{\partial N_i}{\partial x}\frac{\partial N_j}{\partial x}dx \; + \textit{boundary terms} \tag{5.8}$$

Therefore, assuming E, A, and F are not functions of x for this element, Equation (5.7) becomes:

$$-EA\begin{bmatrix} \frac{1}{L} & -\frac{1}{L} \\ -\frac{1}{L} & \frac{1}{L} \end{bmatrix}\begin{Bmatrix} \tilde{u}_1 \\ \tilde{u}_2 \end{Bmatrix} + F\begin{Bmatrix} \frac{L}{2} \\ \frac{L}{2} \end{Bmatrix} = \begin{Bmatrix} 0 \\ 0 \end{Bmatrix} \tag{5.9}$$

The resulted $\{\tilde{u}\}$ from above equation full fill the minimal residual. Typically, the discretized elastic differentiation equation will take the form of Equation (5.9), and can be write using matrix notation as:

$$[K]\{\tilde{u}\} = \{\tilde{f}\} \tag{5.10}$$

where $[K]$ is the element stiffness matrix, $\{\tilde{u}\}$ is the element nodal displacement vector, and $\{\tilde{f}\}$ is the element nodal force vector.

5.2. Shape functions and their mathematical properties

With the knowledge of Galerkin's formulation, the key part of discretization is the differentiation and integration of shape functions with respect to space variables Equation (5.8). Therefore, before discretization, it is necessary to study the shape function of different finite elements and their mathematical properties of the in terms of differentiation and integration. The following table gives commonly used finite elements and their shape functions (Table 5.1) (Smith and Griffiths 2004; Dhondt 2004). Shape functions have the property that they equal to one at a specific node and zero at all others.

Table 5.1 Shape functions for commonly used FEM elements

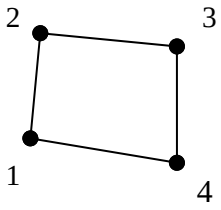

$$N_1 = \frac{1}{4}(1-\xi)(1-\eta)$$
$$N_2 = \frac{1}{4}(1-\xi)(1+\eta)$$
$$N_3 = \frac{1}{4}(1+\xi)(1+\eta)$$
$$N_4 = \frac{1}{4}(1+\xi)(1-\eta)$$

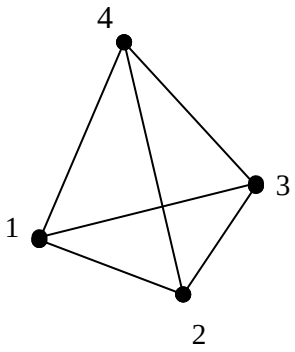

$$N_1 = 1-\xi-\eta-\zeta$$
$$N_2 = \xi$$
$$N_3 = \eta$$
$$N_4 = \zeta$$

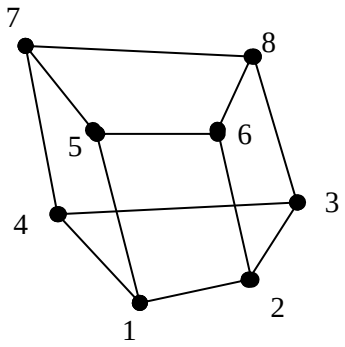

$$N_1 = (1-\xi)(1-\eta)(1-\zeta)/8$$
$$N_2 = (1+\xi)(1-\eta)(1-\zeta)/8$$
$$N_3 = (1+\xi)(1+\eta)(1-\zeta)/8$$
$$N_4 = (1-\xi)(1+\eta)(1-\zeta)/8$$
$$N_5 = (1-\xi)(1-\eta)(1+\zeta)/8$$
$$N_6 = (1+\xi)(1-\eta)(1+\zeta)/8$$
$$N_7 = (1+\xi)(1+\eta)(1+\zeta)/8$$
$$N_8 = (1-\xi)(1+\eta)(1+\zeta)/8$$

Previously, it was shown that integral of double differentiation of variables to be discretized would result in a product of two first order differentiations of shape functions when applying Galerkin's technique (Equation 5.8). In practice, higher order of differentiation is present at times, e.g. second order differentiation of a linear shape function. Green's theorem is used to avoid the difficulty of the vanishing of shape function under higher order of differentiation. By doing so, Table 5.2 gives general remarks on the discretization process.

Table 5.2 Typical resulting term in matrix equation from term in differential equation (Smith and Griffiths 2004)

Term in differential equation	Typical term in matrix equation
u	$\int N_i N_j dx$
$\frac{du}{dx}$	$\int N_i \frac{dN_j}{dx} dx$
$\frac{d^2u}{dx^2}$	$-\int \frac{dN_i}{dx}\frac{dN_j}{dx} dx$
$\frac{d^4u}{dx^4}$	$-\int \frac{d^2N_i}{dx^2}\frac{d^2N_j}{dx^2} dx$

5.3. Discretization of three-dimensional thermo-poroelasticity equations

Writing out again the field equations of thermo-poroelasticity used in this work (tension positive):

$$Gu_{i,jj} + (K + \frac{G}{3})u_{j,ji} - \alpha p_{,j} - \gamma_1 T_{,j} = 0 \tag{5.11}$$

$$\alpha \frac{\partial \varepsilon_{kk}}{\partial t} + \beta \frac{dp}{dt} - \kappa p_{,jj} - \gamma_2 \frac{dT}{dt} = 0 \tag{5.12}$$

$$\frac{\partial T}{\partial t} - c^T T_{,jj} - (\kappa^T T p_{,i})_{,i} = 0 \tag{5.13}$$

The above equations are to be discretized in the solution domain. In this section, the generally used 8-node finite brick element is used to illustrate the discretization process. From Equations (5.1), (5.2), and (5.3), the numerical interpolation of displacement, pore pressure, and temperature in the above PDEs can be expressed as

$$u = [N_u][\tilde{u}] \tag{5.14}$$

$$p = [N_p][\tilde{p}] \tag{5.15}$$

$$T = [N_T][\tilde{T}] \tag{5.16}$$

where $u = \{u_x \quad u_y \quad u_z\}^T$, p, and T are displacement, pore pressure, and temperature field variables.

$$[\tilde{u}] = [\tilde{u}_x^1 \quad \tilde{u}_y^1 \quad \tilde{u}_z^1 \quad ... \quad \tilde{u}_x^8 \quad \tilde{u}_y^8 \quad \tilde{u}_z^8]^T \tag{5.17}$$

$$[\tilde{p}] = [\tilde{p}^1 \quad ... \quad \tilde{p}^8]^T \tag{5.18}$$

$$[\tilde{T}] = [\tilde{T}^1 \quad ... \quad \tilde{T}^8]^T \tag{5.19}$$

are nodal values of displacement, pore pressure, and temperature.

$$[N_u] = \begin{bmatrix} N_u^1 & 0 & 0 & ... & N_u^8 & 0 & 0 \\ 0 & N_u^1 & 0 & ... & 0 & N_u^8 & 0 \\ 0 & 0 & N_u^1 & ... & 0 & 0 & N_u^8 \end{bmatrix} \tag{5.20}$$

$$[N_p] = [N_p^1 \quad ... \quad N_p^8] \tag{5.21}$$

$$[N_T] = [N_T^1 \quad ... \quad N_T^8] \tag{5.22}$$

are shape function matrices.

According to Table 5.2, after discretization, double and single differentiation of variables can be expressed as:

$$\{\varepsilon\} = [B_u]\{\tilde{u}\} \tag{5.23}$$

$$\{p_{,j}\} = [B_p]\{\tilde{p}\} \tag{5.24}$$

$$\{T_{,j}\} = [B_T]\{\tilde{T}\} \tag{5.25}$$

While double differentiations will take the following form:

$$\{p_{,jj}\} = -[B_p]^T [B_p]\{\tilde{p}\} \tag{5.26}$$

where $[B]$ calculate the derivatives of shape functions:

$$[B_u] = \begin{bmatrix} N^1_{u,x} & 0 & 0 & \dots & N^8_{u,x} & 0 & 0 \\ 0 & N^1_{u,y} & 0 & \dots & 0 & N^8_{u,y} & 0 \\ 0 & 0 & N^1_{u,z} & \dots & 0 & 0 & N^8_{u,z} \\ N^1_{u,x} & N^1_{u,y} & 0 & \dots & N^8_{u,x} & N^8_{u,y} & 0 \\ 0 & N^1_{u,y} & N^1_{u,z} & \dots & 0 & N^8_{u,y} & N^8_{u,z} \\ N^1_{u,x} & 0 & N^1_{u,z} & \dots & N^8_{u,x} & 0 & N^8_{u,z} \end{bmatrix} \tag{5.27}$$

$$[B_p] = \begin{bmatrix} N^1_{p,x} & \dots & N^8_{p,x} \\ N^1_{p,y} & \dots & N^8_{p,y} \\ N^1_{p,z} & \dots & N^8_{p,z} \end{bmatrix} \tag{5.28}$$

$$[B_T] = \begin{bmatrix} N^1_{T,x} & \dots & N^8_{T,x} \\ N^1_{T,y} & \dots & N^8_{T,y} \\ N^1_{T,z} & \dots & N^8_{T,z} \end{bmatrix} \tag{5.29}$$

Thus, after discretization, Equations (5.11), (5.12), and (5.13) become (Li 1998; Zhou and Ghassemi 2009; Smith and Griffiths 2004):

$$K_u \tilde{u} - C_{up}\tilde{p} - C_{uT}\tilde{T} = F_u \tag{5.30}$$

$$C_{pu}\frac{d\tilde{u}}{dt} + K_p\tilde{p} + C_{pp}\frac{d\tilde{p}}{dt} - C_{pT}\frac{d\tilde{T}}{dt} = -F_{qout} \tag{5.31}$$

$$C_{TT}\frac{d\tilde{T}}{dt}+K_{cdT}\tilde{T}+K_{cvT}\tilde{T}=-F_{hout} \tag{5.32}$$

where F_u, F_q, and F_h are the external force, fluid and heat sink/source terms.

$$K_u=\int_{V_e}B_u^T D B_u dV\ ;\ C_{up}=\int_{V_e}B_u^T \alpha I N_p dV\ ;\ C_{uT}=\int_{V_e}B_u^T \gamma_1 I N_T dV \tag{5.33}$$

$$K_p=\int_{V_e}B_p^T \kappa B_p dV \quad ; \quad C_{pu}=C_{up}^T \quad ; \quad C_{pT}=\int_{V_e}N_p^T \gamma_2 N_T dV \quad ; \quad C_{pp}=\int_{V_e}N_p^T \beta N_p dV$$

(5.34)

$$K_{cdT}=\int_{V_e}B_T^T C^T B_T dV\ ;\ K_{cvT}=\int_{V_e}B_T^T \kappa^T B_p \tilde{p} N_T dV\ ;\ C_{TT}=\int_{V_e}N_T^T N_T dV \tag{5.35}$$

$$[\mathbf{D}]=\frac{E(1-\nu)}{(1+\nu)(1-2\nu)}\begin{bmatrix} 1 & \frac{\nu}{1-\nu} & \frac{\nu}{1-\nu} & 0 & 0 & 0 \\ \frac{\nu}{1-\nu} & 1 & \frac{\nu}{1-\nu} & 0 & 0 & 0 \\ \frac{\nu}{1-\nu} & \frac{\nu}{1-\nu} & 1 & 0 & 0 & 0 \\ 0 & 0 & 0 & \frac{1-2\nu}{2(1-\nu)} & 0 & 0 \\ 0 & 0 & 0 & 0 & \frac{1-2\nu}{2(1-\nu)} & 0 \\ 0 & 0 & 0 & 0 & 0 & \frac{1-2\nu}{2(1-\nu)} \end{bmatrix} \tag{5.36}$$

$$I=\begin{bmatrix}1 & 1 & 1 & 0 & 0 & 0\end{bmatrix}^T \tag{5.37}$$

Differentiating both sides of Equation (5.30) with time and rearranging, the system of equations can be expressed in matrix form as:

$$\begin{bmatrix} K & -C_{up} & -C_{uT} \\ C_{pu} & C_{pp} & -C_{pT} \\ 0 & 0 & C_{TT} \end{bmatrix} \begin{bmatrix} \frac{d\tilde{u}}{dt} \\ \frac{d\tilde{p}}{dt} \\ \frac{d\tilde{T}}{dt} \end{bmatrix} + \begin{bmatrix} 0 & 0 & 0 \\ 0 & K_p & 0 \\ 0 & 0 & K_{cdT} + K_{cvT} \end{bmatrix} \begin{bmatrix} \tilde{u} \\ \tilde{p} \\ \tilde{T} \end{bmatrix} = \begin{bmatrix} \dot{F}_u \\ F_{qin} \\ F_{hin} \end{bmatrix} \tag{5.38}$$

Since the problem of interest is also time dependent, we need both spatial and temporal discretization. In this work, the Crank-Nicolson type of approximation is used to discretize the temporal domain (Crank and Nicolson 1947).

$$\frac{dp}{dt} = \frac{\theta p_t + (1-\theta) p_{t-\Delta t}}{\Delta t} \tag{5.39}$$

where θ is a scalar parameter which can vary between 0.5 and 1.0.

Applying Equation (5.39) onto (5.38) and multiply both side with Δt, one obtains:

$$\begin{bmatrix} K & -C_{up} & -C_{uT} \\ C_{pu} & C_{pp} & -C_{pT} \\ 0 & 0 & C_{TT} \end{bmatrix} \begin{bmatrix} \Delta u \\ \Delta p \\ \Delta T \end{bmatrix} + \begin{bmatrix} 0 & 0 & 0 \\ 0 & \Delta t K_p & 0 \\ 0 & 0 & \Delta t(K_{cdT} + K_{cvT}) \end{bmatrix} \begin{bmatrix} u_{t-\Delta t} + \theta \Delta u \\ p_{t-\Delta t} + \theta \Delta p \\ T_{t-\Delta t} + \theta \Delta T \end{bmatrix} = \begin{bmatrix} \Delta t \dot{F}_u \\ \Delta t F_{qin} \\ \Delta t F_{hin} \end{bmatrix} \tag{5.40}$$

Finally, the FEM matrix formula used in this work can be written as (Zhou and Ghassemi, 2009; Lee and Ghassemi 2011):

$$\begin{bmatrix} K & -C_{up} & -C_{uT} \\ C_{pu} & C_{pp}+\Delta t\theta C_{pp} & -C_{pT} \\ 0 & 0 & C_{TT}+\Delta t\theta(K_{cdT}+K_{cvT}) \end{bmatrix} \begin{bmatrix} \Delta u \\ \Delta p \\ \Delta T \end{bmatrix} = \begin{bmatrix} \Delta t\dot{F}_u \\ \Delta tF_{qin}-\Delta tK_p p_{t-\Delta t} \\ \Delta tF_{hin}-\Delta t(K_{cdT}+K_{cvT})T_{t-\Delta t} \end{bmatrix} \quad (5.41)$$

In Equation (5.41), Δu , Δp , and ΔT are primary unknowns we need to solve, which are the increments of displacement, pore pressure, and temperature between successive steps. Δt denotes the time step size.

5.4. FEM modeling of heterogeneous and fractured reservoir

In the modeling of a heterogeneous and/or fractured reservoir, elemental properties are assigned in the first place. Equation (5.41) represents a set of 40 equations for one element, which includes 3 equations for displacement (u_x, u_y, and u_z), 1 equation for pore pressure (p), and 1 equation for temperature (T) for each of the eight nodes. Matrix equation of each element, each node, and each degree of freedom in the FEM mesh can be written out explicitly. FEM discretizes the simulation domain into elements, and elemental matrix equation is formulated explicitly. Hence, it is capable of assigning different properties (heterogeneity distribution) element by element using previously described Weibull's distribution (Chapter 3). Similarly, natural fractures are mapped to the FEM mesh element by element too using equivalent continuum conversion

(Chapter 2). Coefficient matrices composited by elemental properties, such as Young's modulus (E), drained and undrained Poisson's ratio (υ and υ_u), Biot's coefficient (α),and hydraulic and thermal conductivities, in the left side of Equation (5.41) can be anisotropic as needed, since they are represented as tensors in the formula. After elemental properties are distributed and obtained from heterogeneity and fracture characterization, coefficient matrices are formed using Equation (5.33 – 5.35). Next, Boundary conditions, such as injection pressure/rate, far field boundary pressure and stress, and drainage condition, and initial conditions, such as in-situ stresses, initial pressure, and initial temperature are imposed to the FEM model. As explained previously, the primary results from FEM analysis are Δu , Δp , and ΔT . At each time step, rock failure analysis and fracture deformation analysis are conducted after FEM analysis finds the unknowns.

In the numerical calculations of this dissertation, the damage variable (as discussed in Chapter 3 and Chapter 7), is computed after each time step of the coupled FEM analysis. However, the equation system (Equation 5.41) is nonlinear and the coefficient matrix is subject to change according to damage evolution and fracture deformation. Therefore, an iterative method is used to solve the non-linear system of equations. In each iteration step within a given time step, the value of coefficient matrix from the last time step is used as the

initial guess (Equation 5.41) to obtain an initial damage variable, d_i. The initial damage variable is used to evaluate the current coefficient matrix and to obtain the new damage variable d_{i+1}. The iteration continues until d is close enough to those obtained in last iteration within a prescribed tolerance (0.01 in this work, as in chapter 7), i.e.:

$\left\| \frac{d_{i+1} - d_i}{(1 - d_i)} \right\| < \varepsilon$ where i = number of iteration step. (1-d_i) is used in the denominator due to the fact that d can be zero at some data points. The solution then advances to the next time step and is repeated for as many steps as needed.

Different from failure analysis of the intact rock, which is an integral part of the FEM solution, the fracture deformation is carried out as a post-processing step at each time step, *and solution convergence is not checked for fracture deformation (permeability change)*. Therefore, the fracture deformation is not coupled with the FEM analysis in this work. In other words, the fracture deformation analysis (Chapter 8) is a sequential process after FEM analysis and as such it does not impact stress distribution in the FEM analysis.

The fracture deformation analysis consists of three steps: for fractured element at each time step, 1) the effective stress applied on fracture surface is solved from the FEM analysis, 2) fracture deformation (aperture change) is calculated using effective stresses, 3) the fracture permeability enhancement is obtained

from aperture change, and converted to equivalent elemental permeability for next finite element solution step. The fracture deformation is decoupled from finite element displacement calculation. For simplicity, and given that the aperture change (~ 10^{-4} m) is much smaller than the element size (~10^{1} m), *the fracture dilation induced elemental strain is ignored in this work*. Only fracture permeability is updated at the end of fracture deformation analysis. Sophisticated fracture deformation and propagation models (e.g. Huang et al. 2011) can simulate the coupling between fracture deformation and element strain in detail, which is not considered in the current study. The implementation of this model in heterogeneous fractured reservoir simulation is illustrated in Chapters 7 and 8.

5.5. Applications of FEM model in geomechanics problems

5.5.1. Transient problems (Uncoupled)

Uncoupled first order transient problems must be analyzed in many physical processes, for example in the case of Terzaghi “consolidation”, transient flow (heat or fluid) analysis, or mode II loading in wellbore problem. In this section, the usage of Finite Element Method to solve transient equation has been verified by compared to analytical solutions of Terzaghi 1-D consolidation theory. The governing diffusion equation of above mentioned problems can take a generalized form as:

$$c\nabla^2 p = \frac{\partial p}{\partial t} \tag{5.42}$$

The discretized matrix form used in FEM is:

$$[k_c]\{p\} + [m]\{\frac{dp}{dt}\} = \{q\} \tag{5.43}$$

where $\{p\}$ represents the pore pressure, $\{q\}$ is the source/sink term, $[k_c]$ is the matrix of coefficient of consolidation or diffusivity matrix as $[K_{cdT}]$ in Equation (5.32), and $[m]$ is the matrix resulted from discretization of variable p on to nodes, taking the same form as $[C_{TT}]$ in Equation (5.32).

$$[m] = \int_V [N]^T [N] dV \tag{5.44}$$

$$[k_c] = \int_V [\nabla N]^T c[\nabla N] dV \tag{5.45}$$

Considering a time step size Δt from t_0 to t_1, the matrix equation can be written at time "0" and "1" as follows:

$$[k_c]\{p\}_0 + [m]\{\frac{dp}{dt}\}_0 = \{q\}_0 \tag{5.46}$$

$$[k_c]\{p\}_1 + [m]\{\frac{dp}{dt}\}_1 = \{q\}_1 \tag{5.47}$$

And Crank-Nicolson method is used in this work for discretization in time domain, thus:

$$\{p\}_1 = \{p\}_0 + \Delta t((1-\theta)\{\frac{dp}{dt}\}_0 + \theta\{\frac{dp}{dt}\}_1) \tag{5.48}$$

Multiply (*1-*θ) to Equation (5.46), multiply θ to Equation (5.47), and sum them up to eliminate $\{\frac{dp}{dt}\}_0$ and $\{\frac{dp}{dt}\}_1$, yields:

$$([m]+\theta\Delta t[k_c])\{p\}_1 = ([m]-(1-\theta)\Delta t[k_c])\{p\}_0 + \theta\Delta t\{q\}_1 + (1-\theta)\Delta t\{q\}_0 \tag{5.49}$$

If fully implicit method (θ = 1) is used in the time domain, and assuming no sink/source for the moment, Equation (5.48) becomes:

$$([m]+\Delta t[k_c])\{p\}_1 = [m]\{p\}_0 \tag{5.50}$$

The analytical solution of surface displacement of Terzaghi 1D consolidation is (Jaeger et al. 2007):

$$w(0,t) = w_\infty\left[1-\sum_{n=1,3,\ldots}^{\infty}\frac{8}{n^2\pi^2}\exp\left(\frac{-n^2\pi^2 c_v t}{4h^2}\right)\right] \tag{5.51}$$

where c_v is the vertical consolidation coefficient, and h is the drainage length (thickness), w_∞ is the ultimate surface settlement. The average degree of consolidation (U) as a function of time (t) can be expressed as:

$$U(t) = \frac{w(0,t)}{w_\infty} = 1 - \sum_{n=1,3,\ldots}^{\infty} \frac{8}{n^2\pi^2} \exp\left(\frac{-n^2\pi^2 c_v t}{4h^2}\right) \tag{5.52}$$

1D finite element (rod element) is used to represent a horizontal layer in this 1D consolidation problem. The model setup is shown in Figure 5.3. For validation purpose, parameters have been normalized by defining time factor $T = \frac{c_v t}{h^2}$. As can be seen from Figure 5.3, the consolidation coefficient (c_v) takes a unit value of 1.0 m^2/s. Drained length (h) (single side drain) is also unit and equals to one meter, and is uniformly divided in to 10 line elements (0.1 m each). Time step size $\Delta T = 0.001$, and there are 2000 steps. The initial pore pressure in the domain is set to be 100 Pa. The surface pore pressure is set to be 0 Pa when the simulation begins and is kept at 0 Pa during the entire simulation (the surface is a drained boundary and bottom is an undrained boundary). It can be seen from Equation (5.50) that the primary variable resulted from Finite Element Analysis (FEA) is pore pressure at every node. The relation between average degree of consolidation and pore pressure is:

$$U(t) = 1 - \frac{\int_0^h p(z,t)dz}{\int_0^h p_0 dz} \tag{5.53}$$

Therefore, after FEA a numerical integration of pore pressure over drained length is conducted. In above equation, *p (z, t)* is the value of pore pressure at a

location at time *t*. p_0 is the initial pore pressure which is uniform and given. After post-processing, the FEA result of *U(t)* can be obtained. Analytically, we can calculate the average degree of consolidation using Equation (5.53) at each T. Figure 5.4 shows comparison between analytical solution and FEA, showing excellent agreement. The pore pressure distribution along the depth at T = 1 is also plotted out and compared with analytical solution, as shown in Figure 5.5.

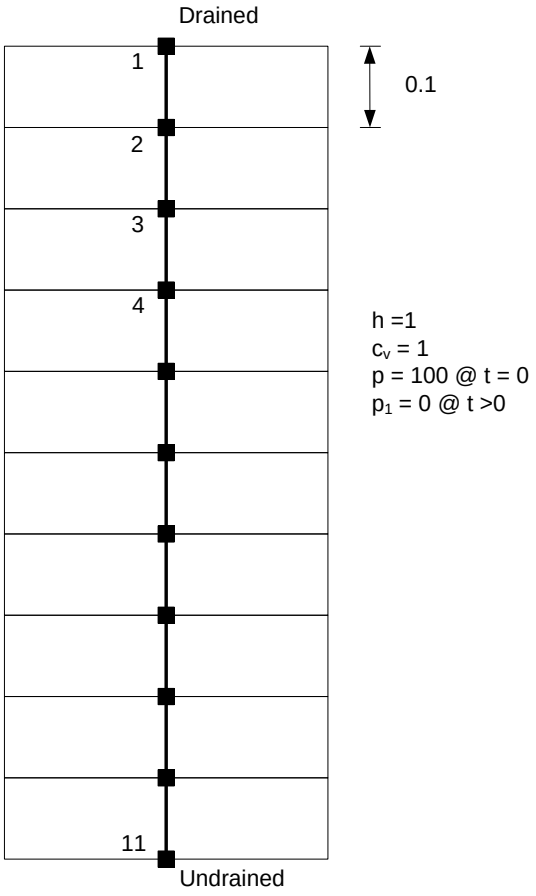

Figure 5.3 Mesh and model setup for FEA of Terzaghi's consolidation.

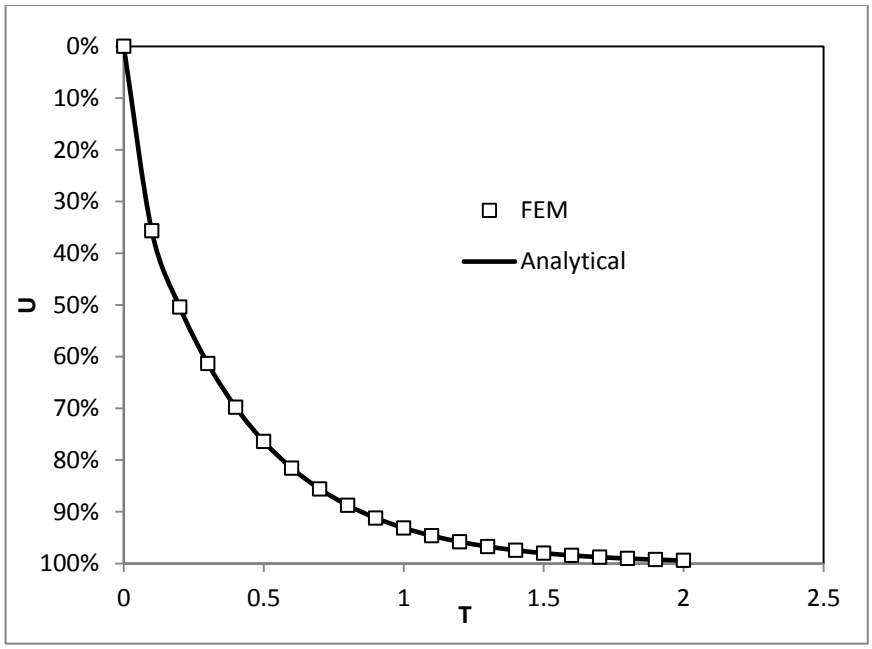

Figure 5.4 Comparison of FEA results with Terzaghi's consolidation theory (*U*).

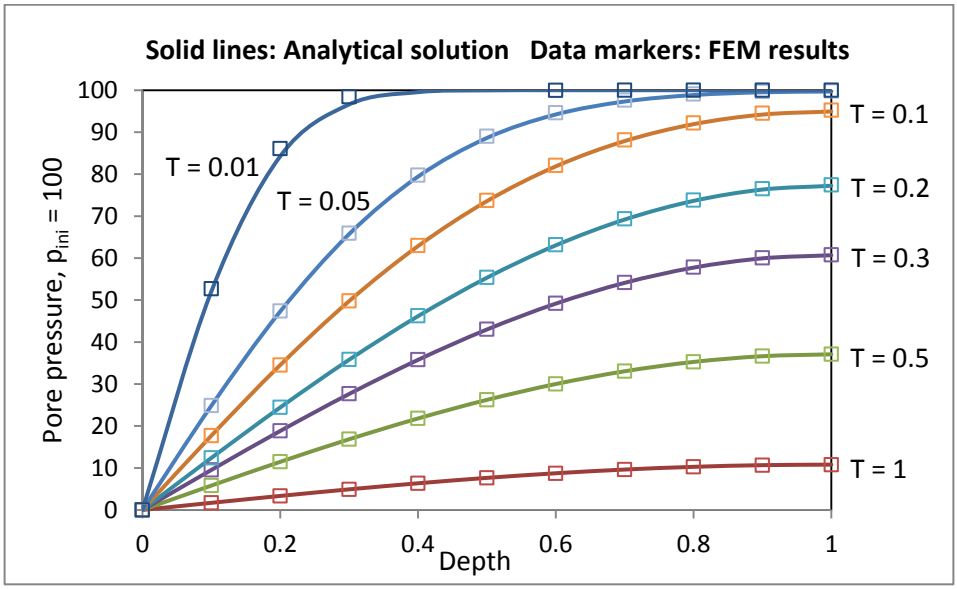

Figure 5.5 Comparison of FEA results with Terzaghi's consolidation theory (*p*).

5.5.2. Mandel's problem (Poroelastic)

Mandel's problem (normal mode) has been used as a standard problem to validating numerical codes. The initial problem solved by Mandel considers a poroelastic sample between two rigid impermeable plates under constant compressive force (Figure 5.6). The original Mandel's problem assumes incompressible fluid and solid grain, and gives the pore pressure solution (Mandel 1953). Later Cheng and Detournay (1988) extended the solution to all field quantities, and generalized to the compressible solid case. The following is the pore pressure and displacement solution provided by Cheng and Detournay:

$$p(x,t)=\frac{2FB(1+\upsilon_u)}{3a}\sum_{i=1}^{\infty}\frac{\sin\alpha_i}{\alpha_i-\sin\alpha_i\cos\alpha_i}(\cos\frac{\alpha_i x}{a}-\cos\alpha_i)\exp(-\alpha_i^2 ct/a^2) \tag{5.54}$$

$$\begin{aligned}u_x(x,t)=&\left[\frac{F\upsilon}{2Ga}-\frac{F\upsilon_u}{Ga}\sum_{i=1}^{\infty}\frac{\sin\alpha_i\cos\alpha_i}{\alpha_i-\sin\alpha_i\cos\alpha_i}\exp(-\alpha_i^2 ct/a^2)\right]x\\&+\frac{F}{G}\sum_{i=1}^{\infty}\frac{\cos\alpha_i}{\alpha_i-\sin\alpha_i\cos\alpha_i}\sin\frac{\alpha_i x}{a}\exp(-\alpha_i^2 ct/a^2)\end{aligned} \tag{5.55}$$

$$u_y(y,t)=\left[-\frac{F(1-\upsilon)}{2Ga}+\frac{F(1-\upsilon_u)}{Ga}\sum_{i=1}^{\infty}\frac{\sin\alpha_i\cos\alpha_i}{\alpha_i-\sin\alpha_i\cos\alpha_i}\exp(-\alpha_i^2 ct/a^2)\right]y \tag{5.56}$$

where, $\tan\alpha_i=\frac{1-\upsilon}{\upsilon_u-\upsilon}\alpha_i$. The average degree of consolidation for Mandel's problem can be expressed as:

$$U(t) = \frac{u_x(a,t) - u_x(a,0)}{u_x(a,\infty) - u_x(a,0)} \tag{5.57}$$

where $u_x(a,\infty) = F\upsilon / 2G$, and $u_x(a,0) = F\upsilon_u / 2G$

The average degrees of consolidation for x- and y- direction are proved to be identical (Cheng and Detournay, 1988).

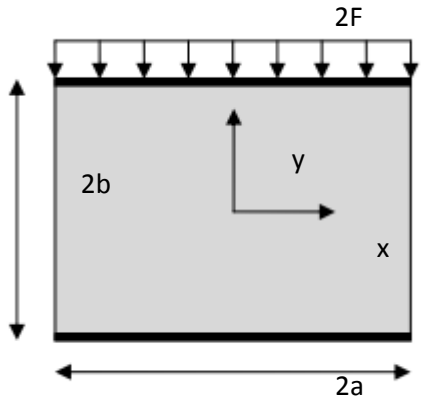

Figure 5.6 Mandel's problem for normal mode.

Finite element analysis of poroelastic equations (5.58 - 5.59) is to solve a system of matrix equations (5.60) as explained previously.

$$\sigma_{ij} = 2G\varepsilon_{ij} + (K - \frac{2G}{3})\varepsilon_{kk}\delta_{ij} - \alpha p\delta_{ij} \tag{5.58}$$

$$\zeta = \frac{1}{2G}\frac{\alpha(1-2\upsilon)}{(1+\upsilon)}(\sigma_{kk} + \frac{3}{B}p) \tag{5.59}$$

$$\begin{bmatrix} K & -C_{up} \\ C_{pu} & K_p + \Delta t\theta C_{pp} \end{bmatrix} \begin{bmatrix} \Delta u \\ \Delta p \end{bmatrix} = \begin{bmatrix} \Delta t \dot{F}_u \\ \Delta t F_{qin} - \Delta t C_{pp} p_{t-\Delta t} \end{bmatrix} \tag{5.60}$$

In above Equation (5.58) - (5.60), all parameters and matrices are as defined previously in the context.

The Finite Element mesh set up for numerical analysis of Mandel's problem is shown in Figure 5.7.

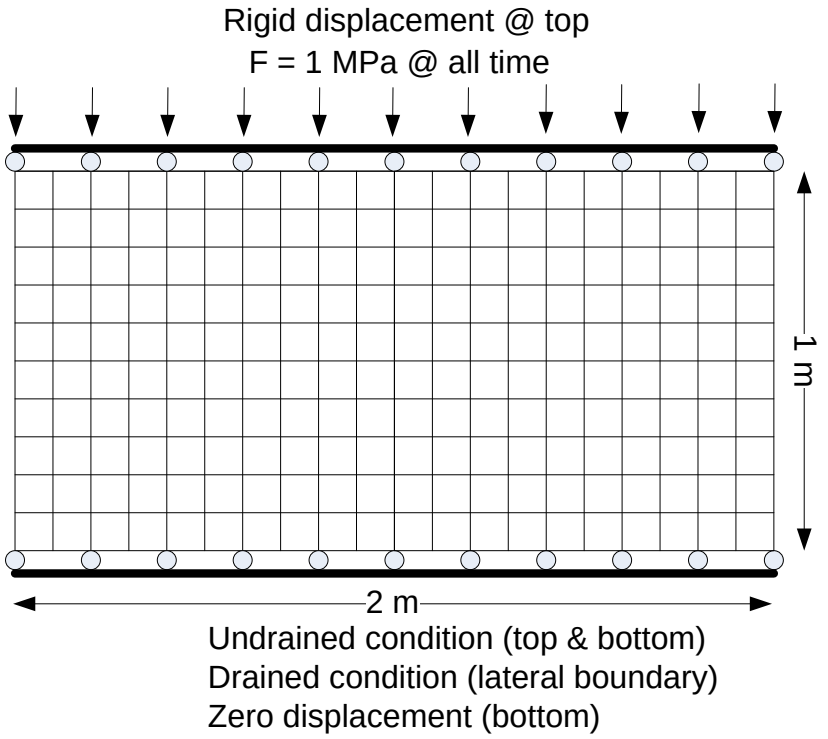

Figure 5.7 Finite Element mesh and model set up for Mandel's problem.

Table 5.3 Parameters used in Mandel's problem

Shear modulus, G	12 GPa
Poisson's ratio υ	0.15
Undrained Poisson's ratio, υ_u	0.29
Boit's coefficient, α	1
Permeability, k	0.005 md
Fluid viscosity, μ	3.0×10^{-4} Pa s

Figure 5.8 and Figure 5.9 show comparisons between analytical solution and FEA results, showing excellent agreement. Table 5.3 gives parameters used in calculation.

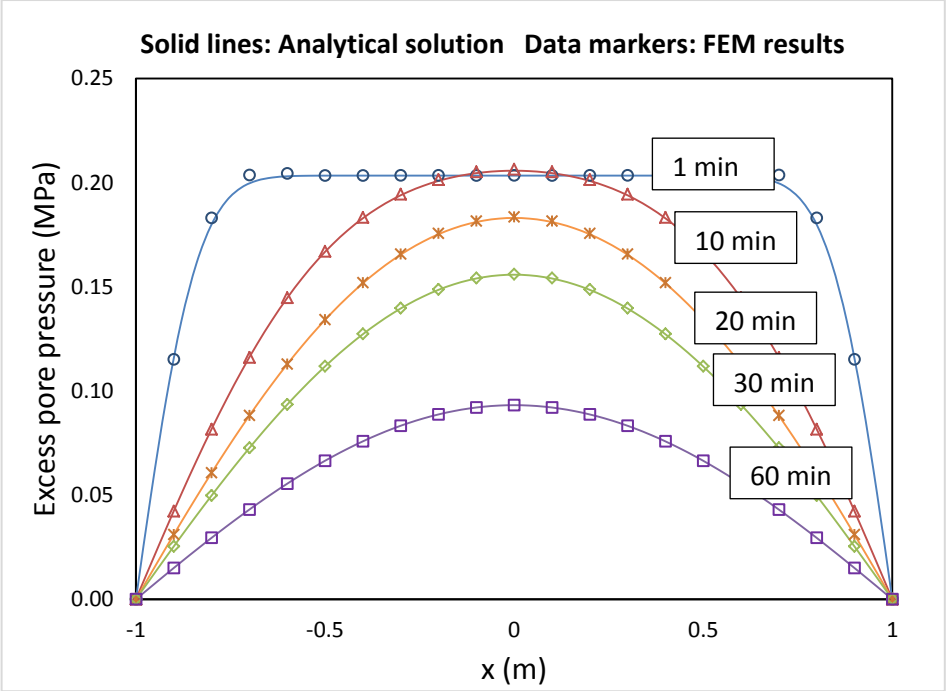

Figure 5.8 Comparison of pore pressure results from FEA with Mendel's solution.

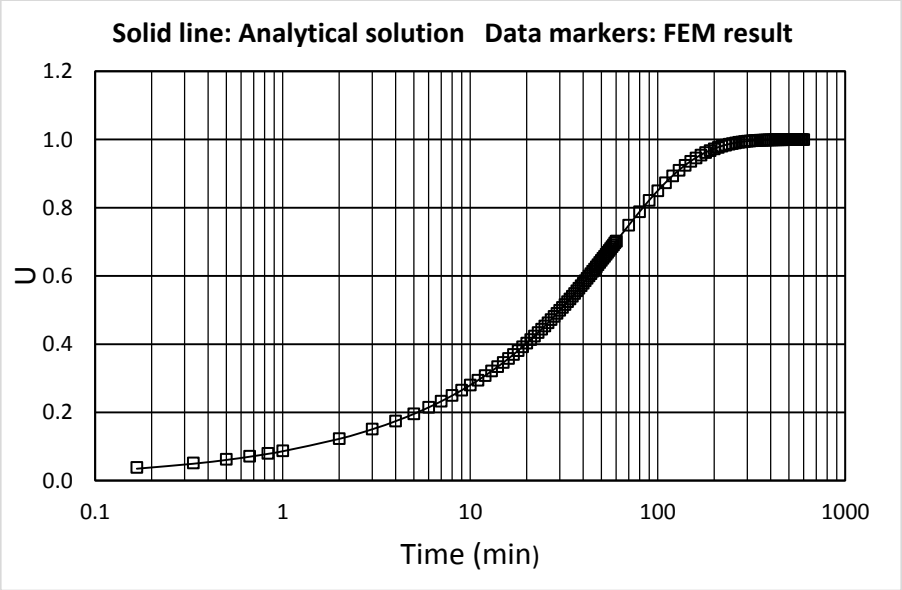

Figure 5.9 Comparison of average degree of consolidation results from FEA with Mendel's solution.

5.5.3. Three-dimensional stress field around a penny-shape crack

When the solution of fracture-rock interaction is being pursued using the FEM part of the numerical model, it is important to know the capability of the model in calculating stress distribution in the vicinity of a penny shape fracture. As analytical solution, Sneddon's solution (1946) is explained in this part for an internal penny shape crack under pressure, and Westmann's (1965) solution is used for a fracture under surface shear. At the end, comparison is made between analytical solution and results from 3D Finite Element model.

5.5.3.1. Analytical solutions of stress field around a penny-shape crack

Sneddon (1946) provided the analytical solution of 3D stress distribution of a circular fracture under uniform loading, which is similar to the Boussinesq problem of a cylinder footing on a semi-infinite half space (Sneddon 1946). In Sneddon's work, he defined new variables (ζ and ρ) in cylindrical coordinate system due to the axisymmetric of the problem. And three un-vanished stresses (σ_z, σ_r, and σ_θ) can be expressed in terms of these two variables, as follows. Definition of $\boldsymbol{C}$ and $\boldsymbol{S}$ terms in Sneddon's solution (Equation 5.62-5.64) can be found in Appendix.

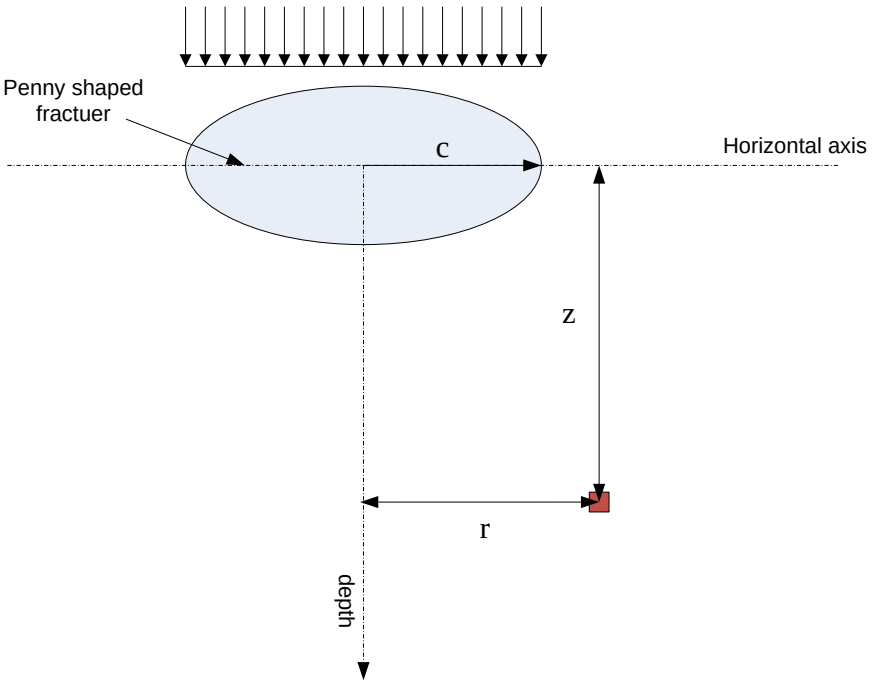

Figure 5.10 Illustration of Sneddon 1946 problem.

$$\zeta = z/c\,;\ \rho = r/c \tag{5.61}$$

$$\sigma_z = \frac{2p_0}{\pi}[C_1^0 - S_0^0 + \zeta C_2^0 - \zeta S_1^0] \tag{5.62}$$

$$\sigma_r + \sigma_\theta + \sigma_z = \frac{4(1+\sigma)}{\pi} p_0[C_1^0 - S_0^0] \tag{5.63}$$

$$\sigma_\theta - \sigma_r = \frac{2p_0}{\pi}[(1-2\sigma)[C_1^2 - S_0^2 - \zeta(C_2^2 - S_1^2)] \tag{5.64}$$

In Westmann 1965, a half-space is considered on which the surface interior to the circle $r = a$ is subjected to a uniform shearing stress S in the $\theta = \pi$ - direction (Figure 5.11). Exterior to the circle the surface displacements u, v are zero; the entire surface is assumed to be free from normal tractions (pure shear).

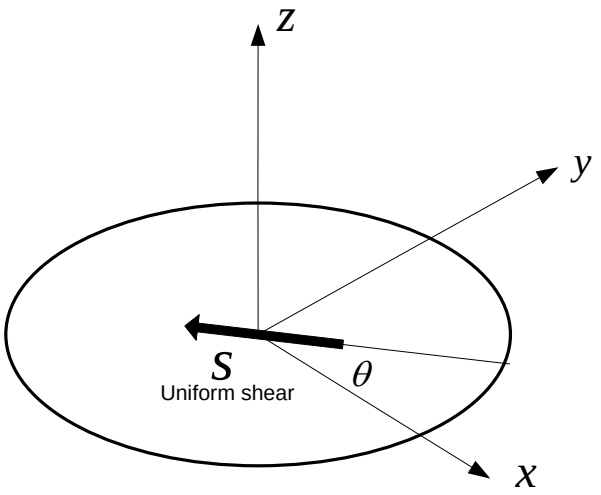

Figure 5.11 Illustration of Westmann 1965 problem.

The solution for stresses in cylindrical coordinates when $z \neq 0$ is:

$$\frac{\sigma_r}{S} = \frac{4}{\pi}\frac{1}{2-\nu}[2I_1^1 - \frac{z}{a}(I_2^1 - \frac{1}{r/a}I_1^2)]\cos\theta \tag{5.65}$$

$$\frac{\sigma_\theta}{S} = \frac{4}{\pi}\frac{1}{2-\nu}[2\nu I_1^1 - \frac{z}{a}\frac{1}{r/a}I_1^2]\cos\theta \tag{5.66}$$

$$\frac{\sigma_z}{S} = \frac{4}{\pi}\frac{1}{2-\nu}\frac{z}{a}I_2^1\cos\theta \tag{5.67}$$

$$\frac{\sigma_{r\theta}}{S} = \frac{4}{\pi}\frac{1}{2-\nu}[-(1-\nu)I_1^1 + \frac{z}{a}\frac{1}{r/a}I_1^2]\sin\theta \tag{5.68}$$

$$\frac{\sigma_{\theta z}}{S} = \frac{2}{\pi}\frac{1}{2-\nu}[-\nu I_1^2 - (2-\nu)I_1^0 + \frac{z}{a}(I_2^2 + I_2^0)]\sin\theta \tag{5.69}$$

$$\frac{\sigma_{zr}}{S} = \frac{2}{\pi}\frac{1}{2-\nu}[-\nu I_1^2 + (2-\nu)I_1^0 + \frac{z}{a}(I_2^2 - I_2^0)]\cos\theta \tag{5.70}$$

Definition of ***I*** terms in Westmann's solution can be found in Appendix.

When z = 0, adopting Heaviside step function *H(x)*:

$$H = \begin{cases} 0 & x < 0 \\ \frac{1}{2} & x = 0 \\ 1 & x > 0 \end{cases} \tag{5.71}$$

$$\frac{\sigma_r}{S} = \frac{8}{\pi}\frac{1}{2-\nu}\frac{(r/a)H(1-r/a)}{[1-(r/a)^2]^{\frac{1}{2}}}\cos\theta \tag{5.72}$$

$$\frac{\sigma_\theta}{S} = \frac{8}{\pi}\frac{\nu}{2-\nu}\frac{(r/a)H(1-r/a)}{[1-(r/a)^2]^{\frac{1}{2}}}\cos\theta \tag{5.73}$$

$$\sigma_z = 0 \tag{5.74}$$

$$\frac{\sigma_{r\theta}}{S} = -\frac{4}{\pi}\frac{(1-\nu)}{2-\nu}\frac{(r/a)H(1-r/a)}{[1-(r/a)^2]^{\frac{1}{2}}}\sin\theta \tag{5.75}$$

$$\begin{aligned}\frac{\sigma_{\theta z}}{S} = -\{H(1-\frac{r}{a}) + \frac{2}{\pi}(&\frac{-1}{[(r/a)^2-1]^{\frac{1}{2}}} + \sin^{-1}(\frac{a}{r}) \\ &+ \frac{\nu}{2-\nu}\frac{1}{(r/a)^2[(r/a)^2-1]^{\frac{1}{2}}})H(\frac{r}{a}-1)\}\sin\theta\end{aligned} \tag{5.76}$$

$$\begin{aligned}\frac{\sigma_{zr}}{S} = \{H(1-\frac{r}{a}) + \frac{2}{\pi}(&\frac{-1}{[(r/a)^2-1]^{\frac{1}{2}}} \\ &+ \sin^{-1}(\frac{a}{r}) - \frac{\nu}{2-\nu}\frac{1}{(r/a)^2[(r/a)^2-1]^{\frac{1}{2}}})H(\frac{r}{a}-1)\}\cos\theta\end{aligned} \tag{5.77}$$

5.5.3.2. Numerical modeling of stress field in the vicinity of a penny-shape fracture

A pressurized circular crack of r = 80 m in an elastic and homogeneous domain of 800 m × 800 m ×350 m has been simulated (Figure 5.12). The elastic modulus of the domain are E = 10 GPa, ν = 0.219. In the Finite Element mesh (224,000 FEM brick elements), the fracture is approximated using elements

which are fully included (all four nodes are with-in the 80 m radius) in the circular area (Figure 5.12). Fluid pressure inside fracture is p_{net} = 10 MPa.

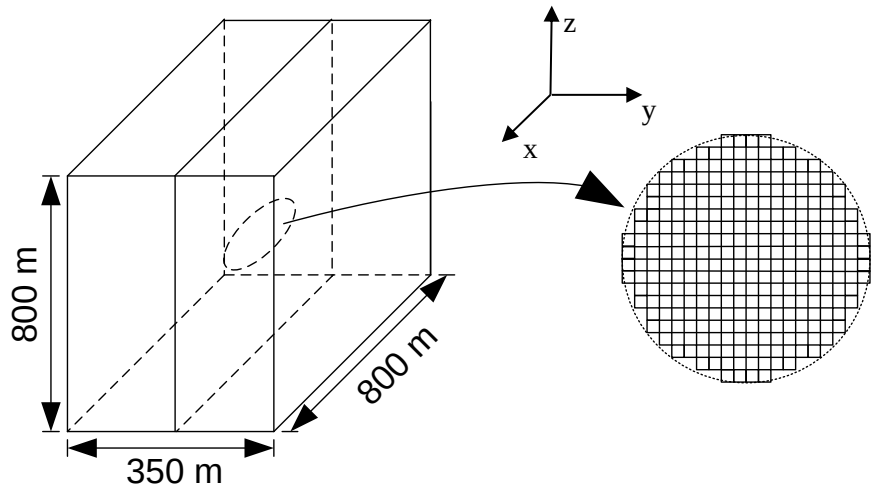

Figure 5.12 FEM set up for stress distribution calculation around a pressurized penny shape fracture.

Figure 5.13 shows a slice from the 3-D stress fields. The slice is made on z = 400 m plane through the fracture center. Figure 5.14 and Figure 5.15 compare the analytical solution and numerical results of the stress distribution on lines located arbitrarily in the stress filed, showing excellent agreement.

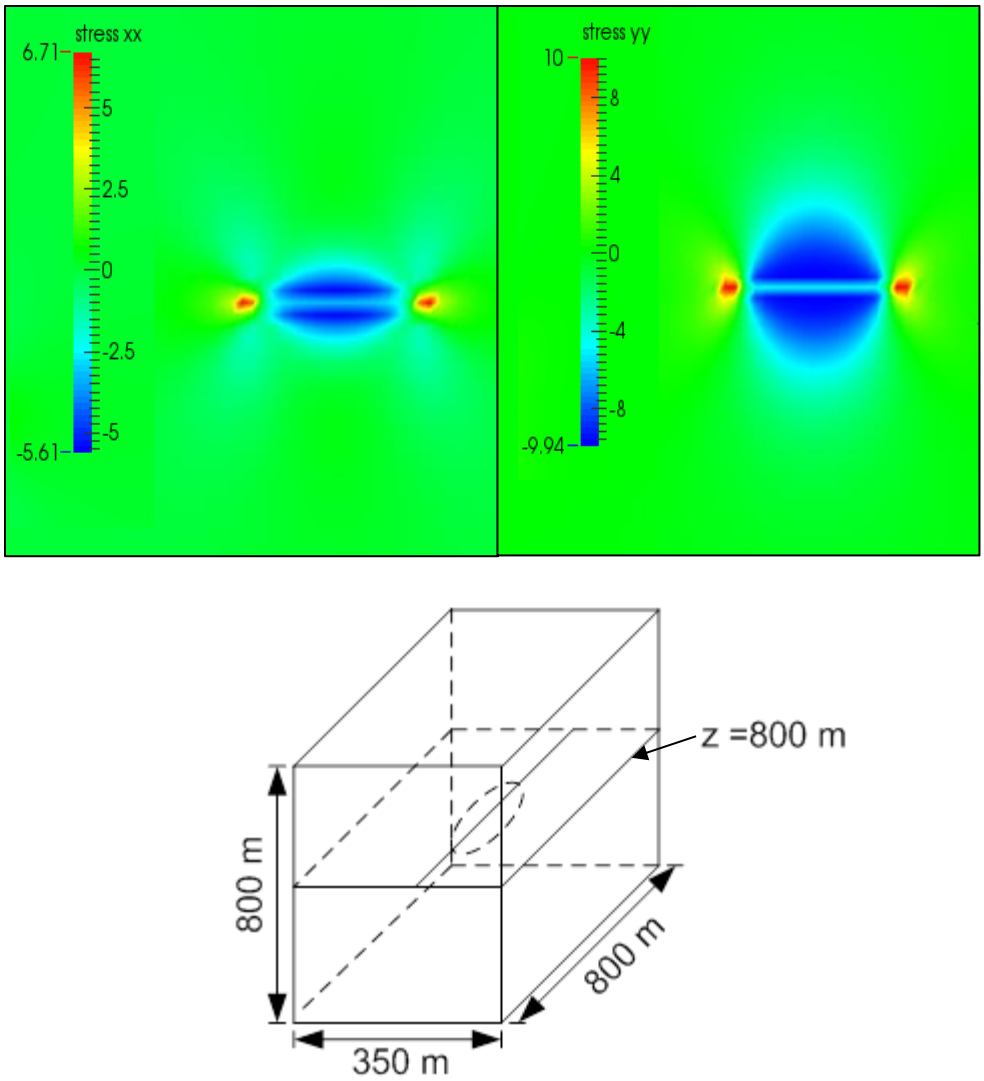

Figure 5.13 Three-dimensional stress fields in the vicinity of a penny shape fracture. Slices are made at z = 400 m, perpendicular to the crack plane.

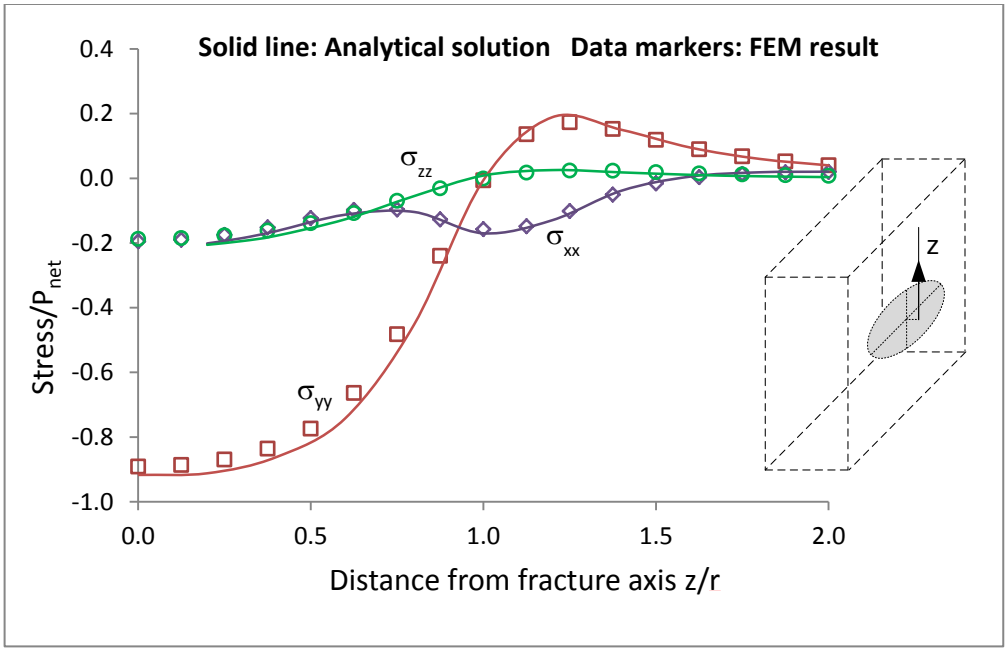

Figure 5.14 Comparison of analytical solution and numerical results of the stress distribution on line parallel to fracture plane.

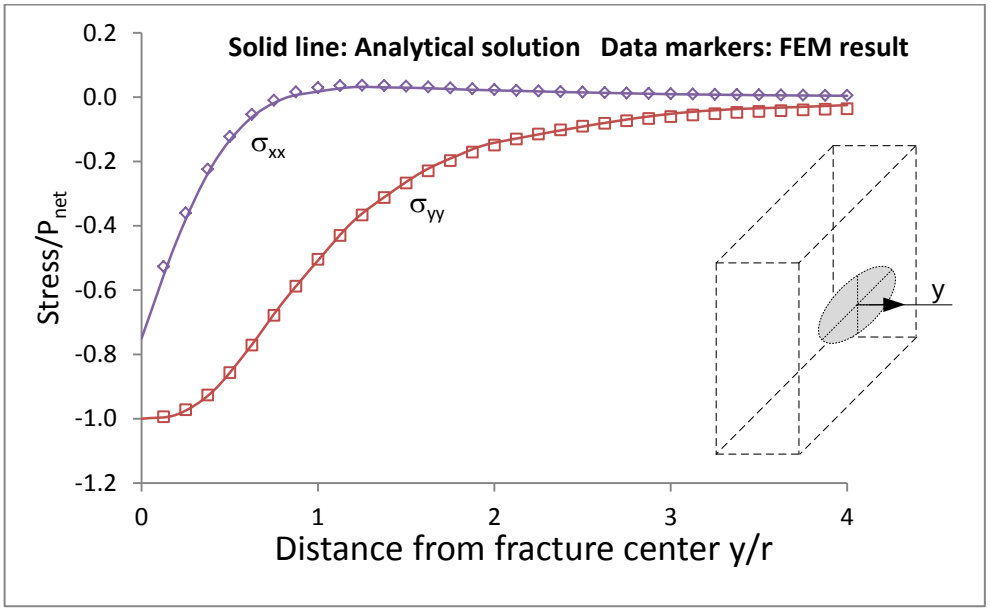

Figure 5.15 Comparison of analytical solution and numerical results of the stress distribution on line perpendicular to fracture plane.

6

NEAR WELLBORE ROCK FAILURE ANALYSIS USING FEM MODEL

During the operation of an oil or gas well, the orientation and magnitude of rock stresses are alternated. Short-term and long-term stress and pore pressure analysis need to be carried out, accounting for undrained or drained poroelastic effects and isothermal or non-isothermal conditions. Another important factor of wellbore stability analysis is the thermal effects, especially when dealing with tight reservoirs where thermal conductivity is significantly higher than hydraulic conductivity. The rotation and relative magnitude of three principal stresses are critical when determining the failure mode and failure planes. In this work, three-dimensional THM (thermal-hydro-mechanical) analysis of instability around a wellbore during drilling and production under different in-situ stress conditions is carried out using a 3D FEM.

There have been research studies on the effect of horizontal stress anisotropy on wellbore stability (Detournay and Cheng 1988; Li et al. 1998), and suggestions have been made to ensure wellbore stability under different conditions (Maury

and Sauzay 1987). Two-dimensional analytical solutions for simple poroelastic well conditions are available (Carter and Booker 1982; Detournay and Cheng 1988). Analytical solutions are obtained using strong assumption and strict boundary conditions that will not always be satisfied. When more complicated problem, for example, transient state, poroelastic effect, thermal effect, and rock heterogeneity are considered, numerical simulation is necessary. Two dimensional numerical analysis of wellbore stability have been study extensively (Zhou and Ghassemi 2009; Ghassemi et al. 1999). Stress concentration due to anisotropic horizontal stresses is a well-known phenomenon. Thermal-mechanical and chemo-mechanical interaction have also been studied (Ghassemi and Diek 2003; Ekbote and Abousleiman 2006). However, quantitative studies on the extension of failure zone and extent of wellbore rock damage, especially the three-dimensional layout of failure planes have seldom been done. According to Mohr-Coulomb failure criterion, the shear failure plane is parallel to the intermediate principal stress (σ_2) direction and perpendicular to σ_1 - σ_3 plane. It is known those three principal stress axes in the rock surrounding the wellbore are subject to rotation during well operation. Therefore, a rigorous calculation is necessary to obtain the three-dimensional geometry of failure zone.

Simulation result shows that the reorientation of principal stresses due to excavation mostly controls the failure plane orientation. The pressure and temperature difference between well and formation have significant influence on wellbore stability. Also the anisotropy of in-situ lateral stresses will affect the shape of failure zone as does the wellbore, and the formation flow conditions. The heterogeneity of rock property will locally alter the shape of failure zone.

This chapter systematically studies the wellbore instability under different in-situ stress and well pressure/temperature conditions and provides reference to field operations. Elastic, poroelastic, and thermo-poroelastic simulation are presented. The simulation cases illustrate the capability of the fully coupled 3D FEM model in predicting the mechanical, fluid flow and thermal responses of the reservoir rock to external load, and the coupling between them.

6.1. Model setup

The simulation domain is 16 m × 16 m × 2 m, and has been divided into 40,000 hexahedron finite elements (Figure 6.1). There are 80 elements in the tangential direction and 50 elements in the radial direction. There are 10 layers of elements in the vertical direction. A vertical wellbore with radius r = 0.125 m is located at the center of the domain, and the horizontal extension of the domain is 50 times of well radius. And the vertical dimension is 16 times of wellbore radius, which is selected according to experience to minimize the boundary effects on stress

distribution near the center part of the borehole, without adding extensive computation time. For all simulation cases, the far field boundary conditions are zero displacement, and zero fluid and heat flow. Top and bottom of the domain are constant stress boundaries, and in-situ vertical stress is applied on top and bottom surface of the model. For homogenous rock analysis, the rock properties are listed in Table 6.1.

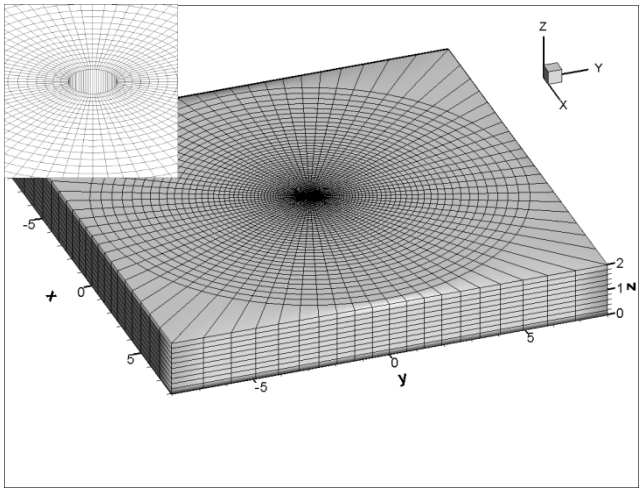

Figure 6.1 Finite element mesh used in the computation.

Table 6.1 Rock properties used in the instable zone computation.

Young's modulus	10 GPa
Poisson's ratio	0.219 (υ); 0.461(υ_u)
Skempton's coefficient	0.915
Thermal expansion coefficient of solid	1.8×10^{-5} K^{-1}
Thermal expansion coefficient of fluid	3.0×10^{-4} K^{-1}
Thermal diffusivity	1.6×10^{-6} m^2/s
Permeability	10^{-7} darcy
Porosity	0.2989
Internal friction angle	30 °
Uniaxial compressive strength (unconfined)	50 MPa
Uniaxial tensile strength	5 MPa

6.2. Elastic analysis

In elastic analysis, only mechanical components of the governing equation (Equation 4.40) are considered. Wellbore mechanical loading can be decomposed into mean stress (σ_m) loading and deviatory stress (σ_d) loading. The applied traction boundary condition on wellbore for elastic simulation can be written as follows (Equation 6.1) (tension positive). t_x and t_y are applied uniform forces on wellbore elements surface. θ is the angle between the vector of element center and x axis (counter clock wise positive).

$$\begin{aligned} t_x &= (\sigma_m - \sigma_d \cos 2\theta)\cos\theta - \sigma_d \sin 2\theta \sin\theta \\ t_y &= (\sigma_m - \sigma_d \cos 2\theta)\sin\theta + \sigma_d \sin 2\theta \cos\theta \end{aligned} \tag{6.1}$$

Both isotropic and anisotropic horizontal stresses states have been simulated. The in-situ stresses for isotropic case are $\sigma_v = \sigma_y = \sigma_x = 15$ MPa ($\sigma_m = 15$ MPa, $\sigma_d = 0$ MPa). And for anisotropic case, $\sigma_v = 15$ MPa, $\sigma_y = 12$ MPa, and $\sigma_x = 8$ MPa (($\sigma_m = 10$ MPa, $\sigma_d = 2$ MPa). Magnitude (compression positive) and direction of principal stresses of both cases have been calculated and plotted in Figure 6.2 - 6.4. For isotropic stress case, after removing the radial support from the wellbore wall, the principal stresses become radial (σ_3), vertical (σ_2) and tangential (σ_1) stresses. The radial stress (σ_3) at wellbore wall is zero (Figure 6.4A). For anisotropic case, a rotation of principal stress orientation occurs near wellbore. Due to high stress concentration at and near the wellbore wall in the minimum in-situ stress direction (x- direction), there are out of plane rotation of σ_1 and σ_2. In the stress concentration zone, local σ_1 gradually rotate from lateral to vertical; and local σ_2 gradually rotate from vertical to lateral accordingly from x-direction to y-direction. Outside the stress concentration zone, σ_2 has in-plane rotation from tangential to y-direction, and σ_3 has in-plane rotation from radial to x-direction. Figure 6.5 shows the contour of Mohr-Coulomb function value (f_{mc}) and the normal directions of maximum shear planes. The magnitude of f_{mc} represents the failure tendency of the element. Positive f_{mc} indicates failure. According to Mohr-Coulomb theory there are two possible failure planes for one element. The normal of failure planes has an angle of $\pm (45^\circ + \phi/2)$ from σ_1

direction on σ_1-σ_3 plane, and failure planes are parallel to σ_2 direction. Therefore, comparing Figure 6.5 to Figure 6.3, we can see two crossing normal direction lines on x-y plane in zones where σ_2 is vertical, indicating the maximum shear planes are vertical. Therefore, for isotropic case, all maximum shear planes are vertical, and for anisotropic case, maximum shear plane in stress concentration zones are vertical. Elsewhere except the compression zone (x-direction) in Figure 6.5B, the projections of two normal direction lines on x-y plane are collinear indicating σ_2 is coplanar with x-y plane, as is proved in Figure 6.3B. For each element, the intersection line of the maximum shear plane and x-y plane should be perpendicular to the collinear projection lines shown in Figure 6.5B. Knowing this, sketches of failure planes for above two situations are presented in Figure 6.6. Figure 6.7 illustrates the wellbore deformation for both isotropic and anisotropic cases. The wellbore has a uniform radial inward displacement of 0.0225 cm under 15 MPa of isotropic horizontal in-situ stresses. For anisotropic case, the wellbore becomes elliptic, with a radial inward displacement of 0.0087 cm in x-direction (σ_h) and 0.0214 cm in y-direction (σ_H). One should notice that in Figure 6.7 the wellbore displacements have been magnified 100 times for illustration purpose.

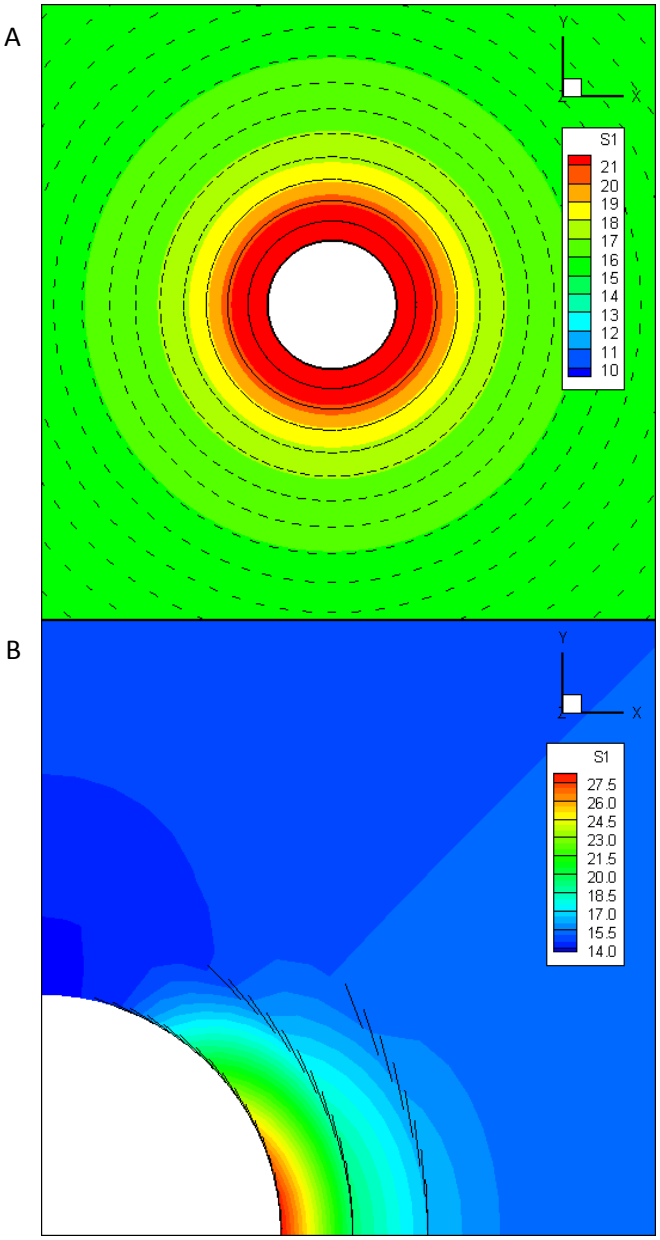

Figure 6.2 Magnitude and orientation of maximum principal stresses (σ_1). A) Isotropic horizontal stress case. B) Anisotropic horizontal stress case.

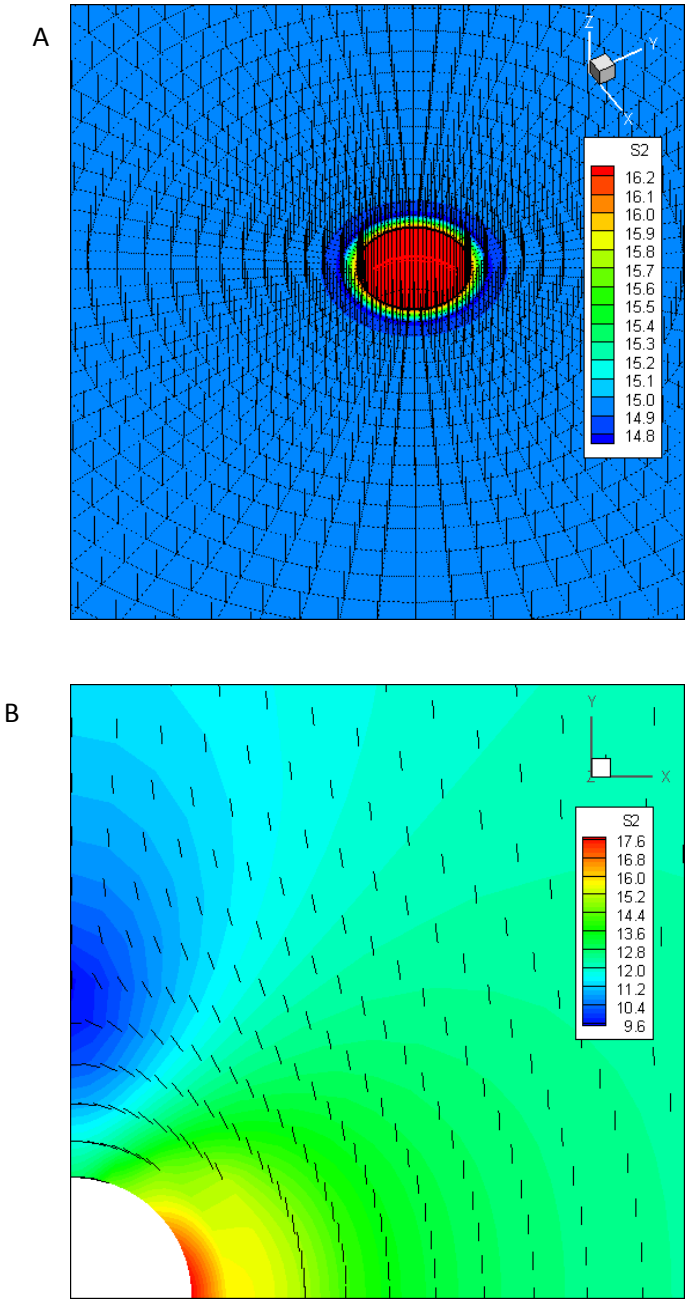

Figure 6.3 Magnitude and orientation of intermediate principal stresses (σ_2). A) Isotropic horizontal stress case. B) Anisotropic horizontal stress case

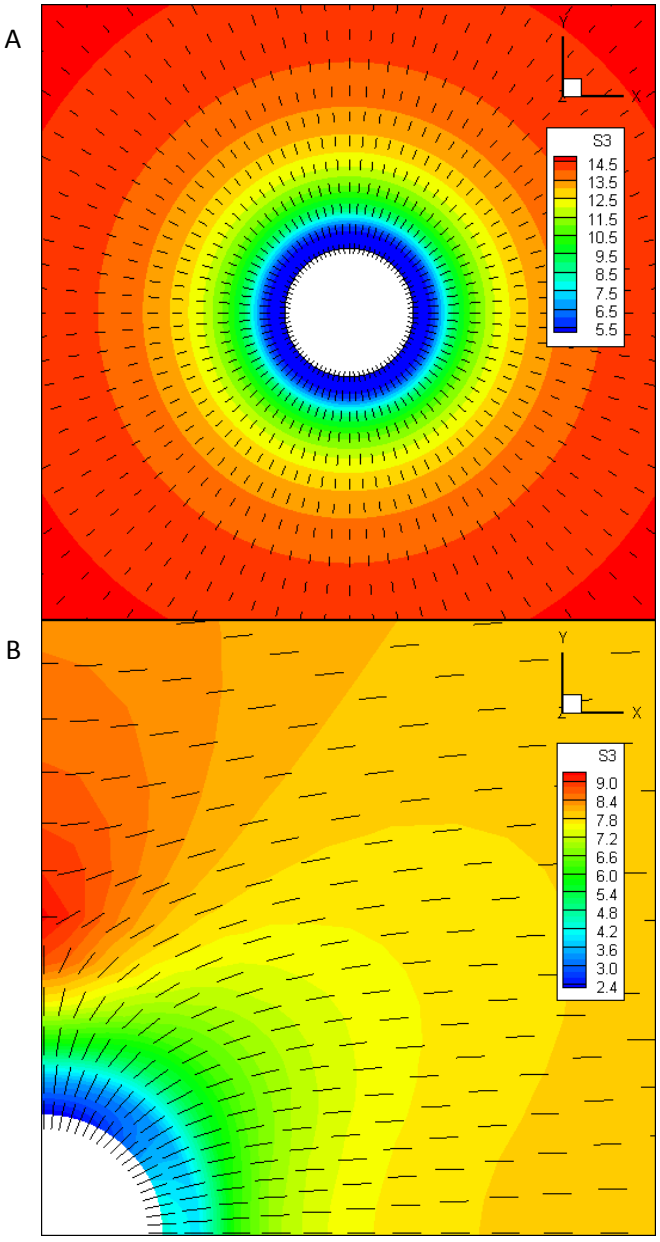

Figure 6.4 Magnitude and orientation of minimum principal stresses (σ_3). A) Isotropic horizontal stress case. B) Anisotropic horizontal stress case.

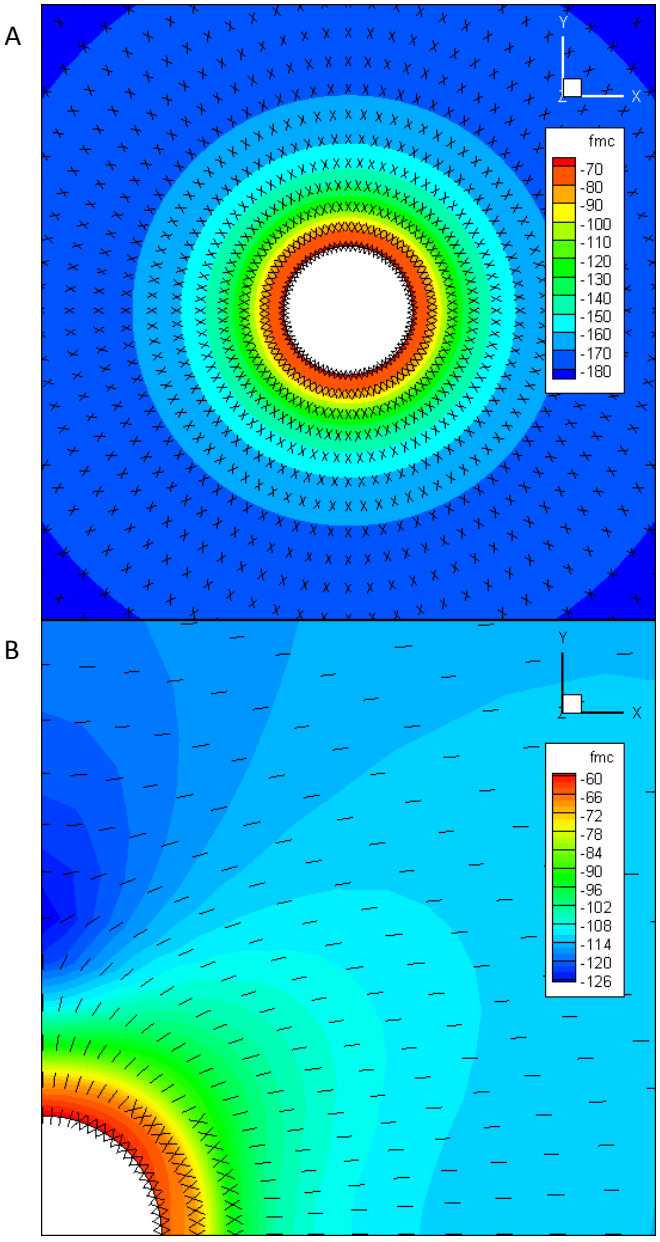

Figure 6.5 Value of Mohr-Coulomb function and orientation of potential failure planes ($\beta = \pm 30°$ from σ_1). A) Isotropic horizontal stress case. B) Anisotropic horizontal stress case.

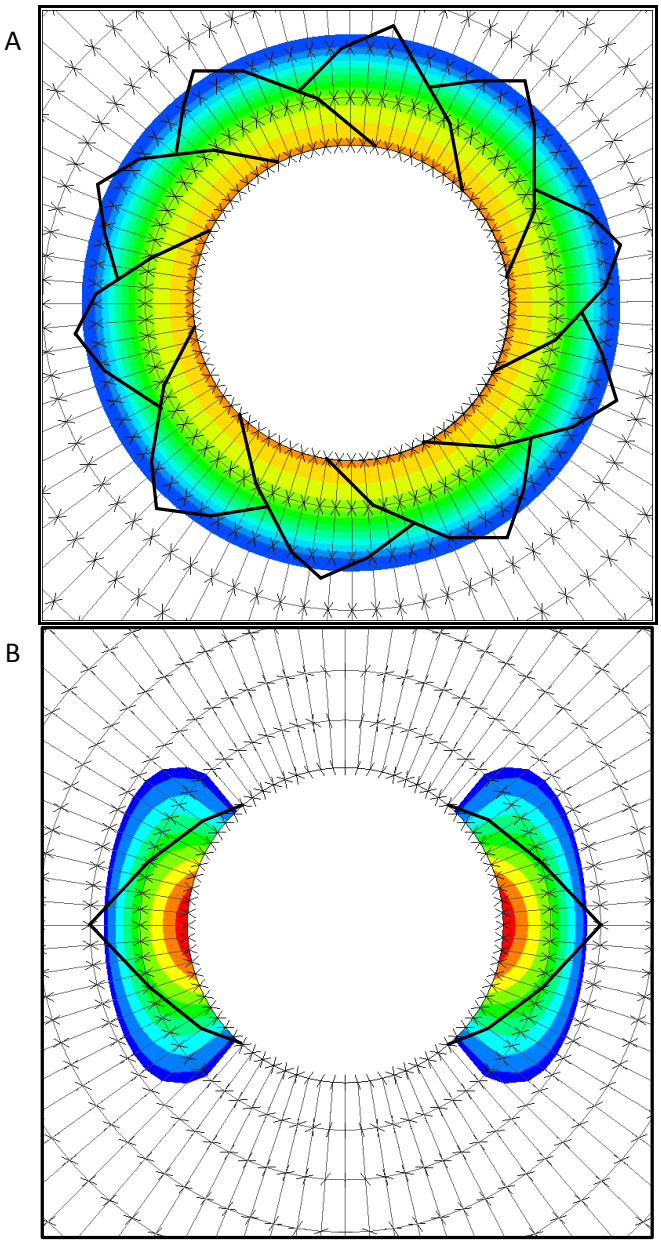

Figure 6.6 Sketches of vertical failure planes. A) σ_v = 30MPa, σ_H = 25 MPa, σ_h =25 MPa; B) σ_v = 30MPa, σ_H = 40 MPa, σ_h =10 MPa. Color zones indicating $f_{mc} > 0$.

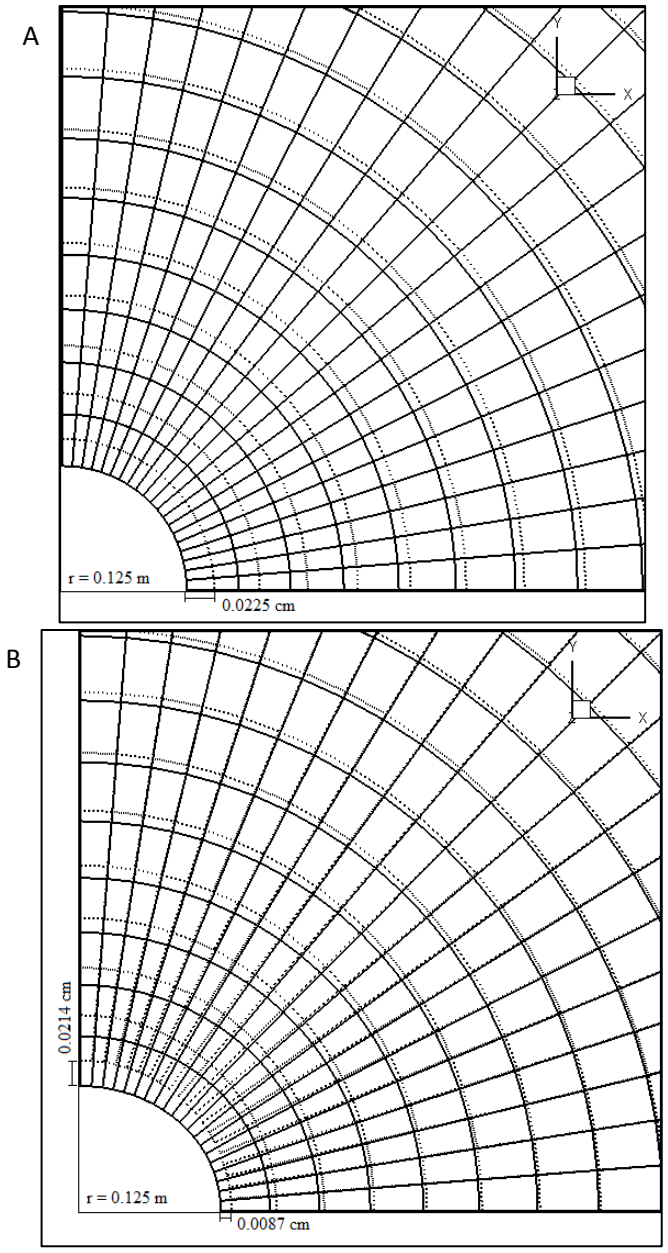

Figure 6.7 Illustration of the wellbore deformation. The borehole has radial shrinkage after drilling. Dotted mesh is before drilling, and solid mesh is after drilling. A) Isotropic horizontal stress case. B) Anisotropic horizontal stress case. The wellbore displacements have been magnified 100 times for illustration purpose.

Failure tendency of stress conditions with σ_d = 2 MPa, 5 MPa, 10 MPa, and 13 MPa are calculated. Contour plots of failure tendency (value of f_{mc}) are shown in Figure 6.8. As deviatory stress increases, failure zones appear at the top and bottom of the wellbore (y-direction). The development of failure tendency with the increasing horizontal stress anisotropy can be observed. One should notice that, the stress state of the simulation case for σ_d = 13 MPa is reverse faulting regime (σ_v = 15 MPa, σ_H = 28 MPa, σ_h =2 MPa). The cross-section shape of the failure zone for the reverse faulting stress regime does not show significant difference from the one of normal faulting stress regime. However, as discussed in Figure 6.6, the failure planes orientation is noticeably different between these two situations. Therefore, the three-dimensional shape for failure zones of different stress regimes are different as summarized later in Figure 6.18. There are tensile and compressive failure types in the failure zones, as shown in Figure 6.9. For the given stress condition and rock type, compressive failure occurs approximately 30 °- 50 ° between the direction of σ_H and σ_h, and tensile failure occurs in the direction of σ_H. The angle of failure range on wellbore is 67.5 ° as observed from Figure 6.9. Regarding the influence of horizontal stress anisotropy on wellbore deformation, Figure 6.10 shows the comparison among five different simulation cases presented in this section. Relative wellbore displacement and corresponding stress states are also stated in the figure. The deformed wellbore is more elliptic under higher horizontal stress anisotropy. It

should be noted that the relative displacement has been magnified 100 times for illustration purpose. The mesh shows the undeformed wellbore.

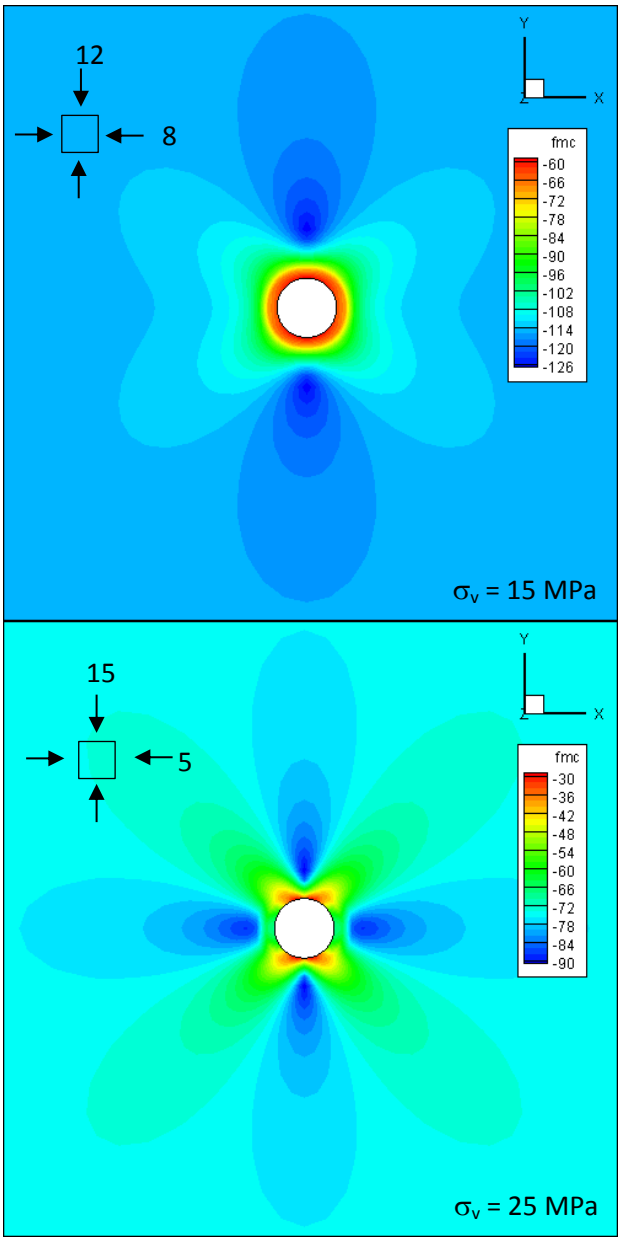

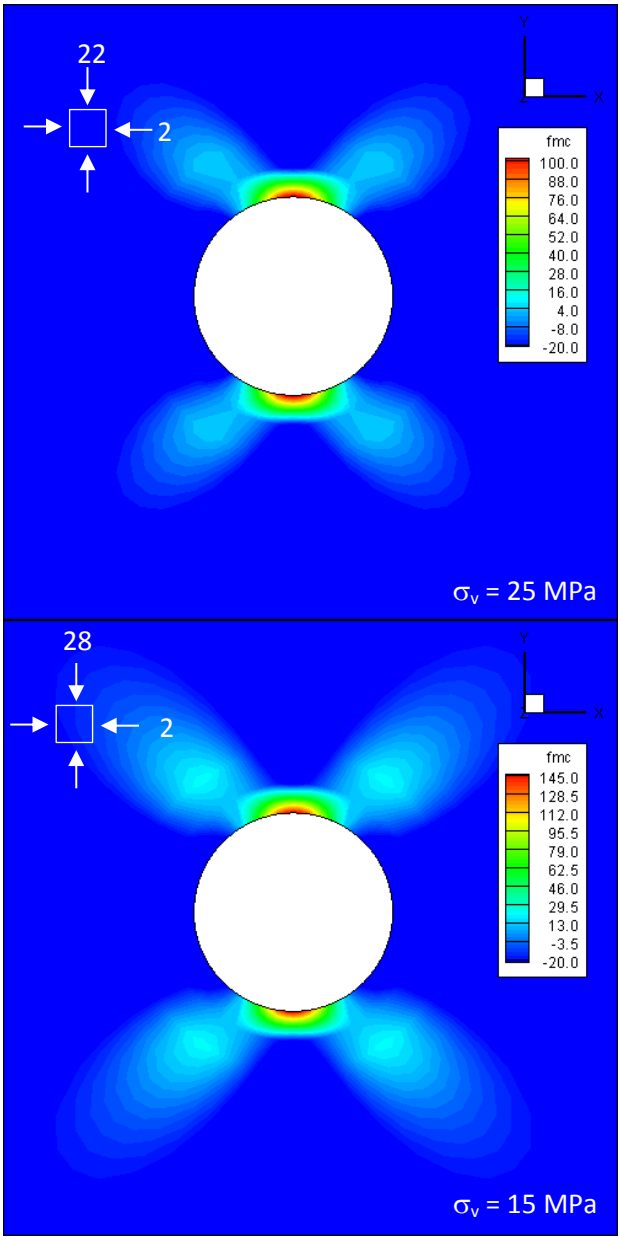

Figure 6.8 Elastic analysis of failure zones under different in-situ stresses. f_{mc} is the value of Mohr-Coulomb failure function. Positive value indicates failure.

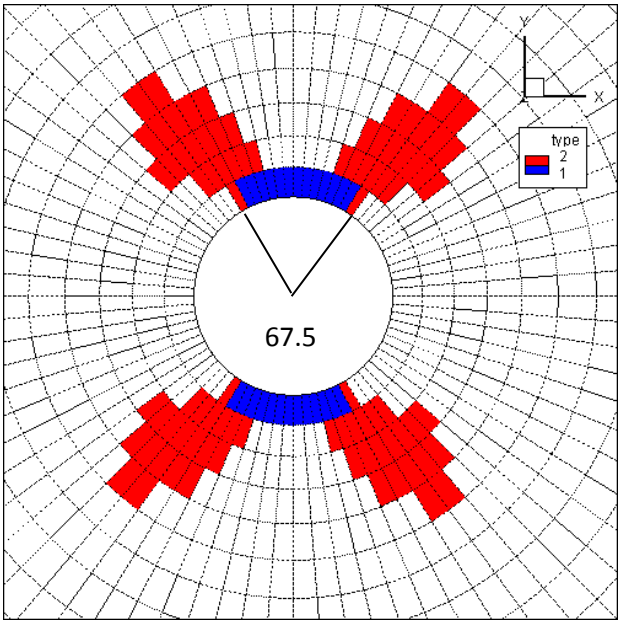

Figure 6.9 Failure types. σ_v = 15MPa, σ_H = 28 MPa, σ_h =2 MPa. Red zones represent compressive failure and blue zones represent tensile failure.

Relative displacement (r = 0.125m)
1: u_x = 0.0087cm; u_y = 0.0214cm
2: u_x = 0.0225cm; u_y = 0.0225cm
3: u_x = -0.0007cm; u_y = 0.0308cm
4: u_x = -0.0135cm; u_y = 0.0497cm
5: u_x = -0.0185cm; u_y = 0.0637cm

In-situ stress states
1: σ_x = 8MPa; σ_y = 12MPa; σ_v = 15MPa;
2: σ_x = 15MPa; σ_y = 15MPa; σ_v = 15MPa;
3: σ_x = 5MPa; σ_y = 15MPa; σ_v = 25MPa;
4: σ_x = 2MPa; σ_y = 22MPa; σ_v = 25MPa;
5: σ_x = 2MPa; σ_y = 28MPa; σ_v = 15MPa;

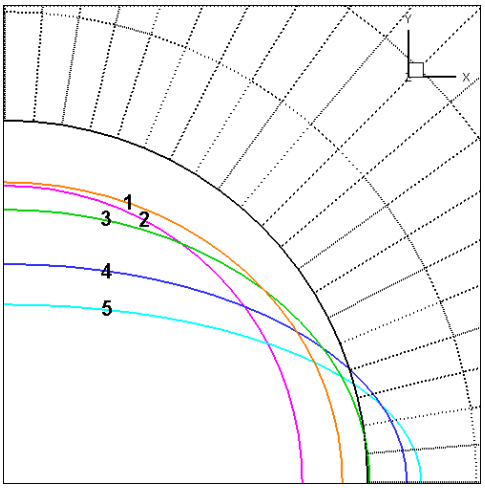

Figure 6.10 Wellbore deformation under different in-situ stresses. The wellbore displacements have been magnified 100 times for illustration purpose.

6.3. Poroelastic analysis

In poroelastic analysis, first two governing equation (Equation 4.40-4.41) are solved, neglecting the thermal effect terms. When pore pressure effect is considered, the wellbore boundary condition can be written in terms of in-situ total stress, initial pore pressure and mud pressure, as follows:

Mechanical force boundary condition:

$$\begin{aligned} t_x &= (p_{mud} + \sigma_m - \sigma_d \cos 2\theta)\cos\theta - \sigma_d \sin 2\theta \sin\theta \\ t_y &= (p_{mud} + \sigma_m - \sigma_d \cos 2\theta)\sin\theta + \sigma_d \sin 2\theta \cos\theta \end{aligned} \tag{6.2}$$

Fluid boundary condition:

$$p = p_{mud} - p_{ini} \tag{6.3}$$

The fluid-rock coupled response in 34 hours after drilling is analyzed, and results are shown in Figure 6.11-13. Two conditions with different mud-pressures are calculated for same in-situ stress states of σ_z = 15 MPa, $\sigma_{y(H)}$ = 12 MPa, $\sigma_{x(h)}$ = 8 MPa, and initial pore pressure p_{ini} = 6 MPa. Plots in left side of Figure 6.11 - 6.13 represent condition with p_{mud} = 0 MPa, while right side plots represent condition with p_{mud} = 8 MPa. The drilling induced wellbore deformation with p_{mud} = 0 MPa is larger than that with p_{mud} = 8 MPa. The problem is assuming instantaneous drilling of the wellbore. The deformation of wellbore during 34 hours after drilling is insignificant for both cases, as can be

seen from Figure 6.11, the maximum incremental displacement 34 hours after drilling is 0.0012 cm. It is noticed that the wellbore has small elongation at minimum horizontal stress direction for p_{mud} = 8 MPa case. From Figure 6.12, a short term release of stress concentration at minimum horizontal stress direction is observed when increasing the mud weight. However, tensile stress concentration occurs at maximum horizontal stress direction for higher mud pressure case. After 34 hours of fluid diffusion, two cases show different development pattern. The stress concentration zones for zero mud pressure disappear after 34 hours of drainage ($p_{mud} < p_{ini}$). But the failure tendency for p_{mud} = 8 MPa becomes more significant after 34 hours of injection ($p_{mud} > p_{ini}$). High failure tendency zones show similar shape as those in Figure 6.8.

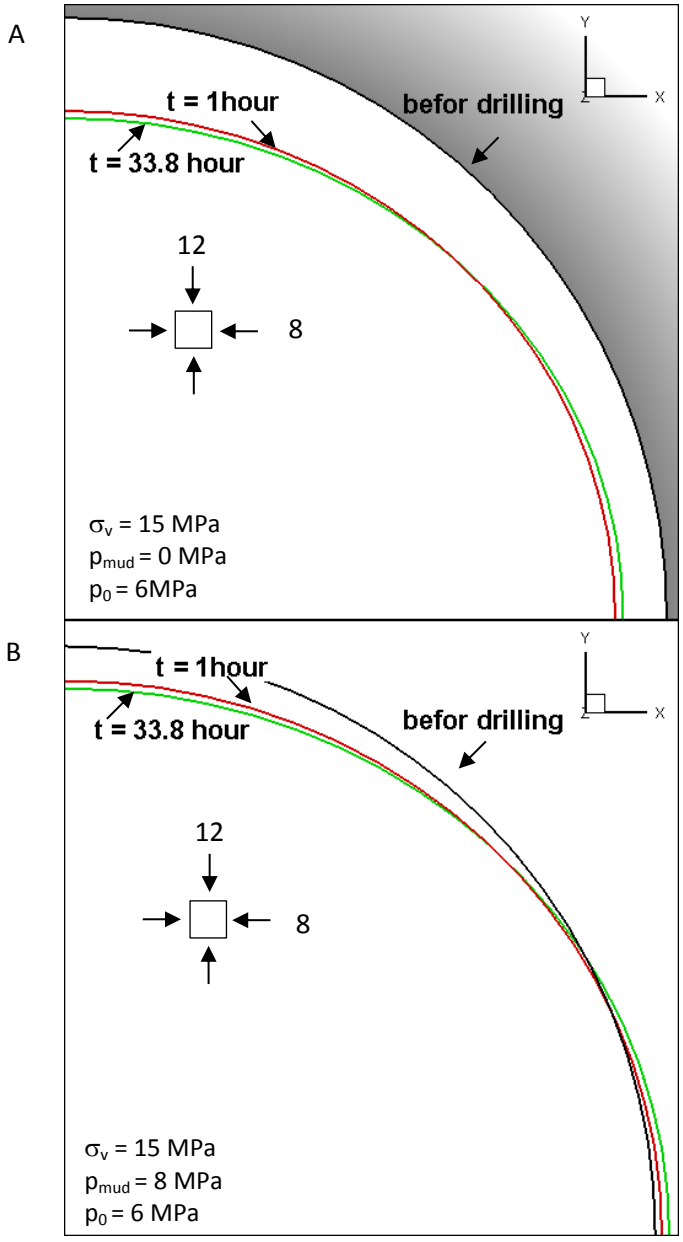

Figure 6.11 Poroelastic analysis: Illustration of wellbore deformation in 34 hours after drilling. p_{ini} = 6 MPa. A) p_{mud} = 0 MPa. B) p_{mud} = 8 MPa,

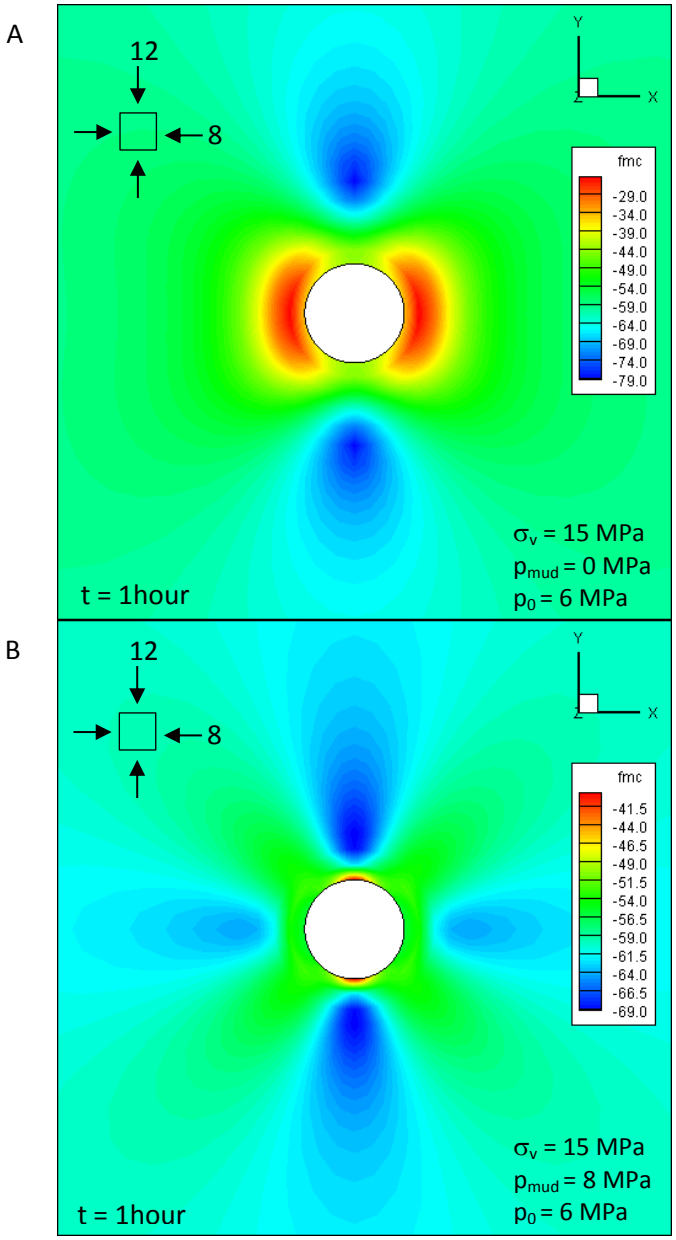

Figure 6.12 Poroelastic analysis: Development of failure tendency at 1 hour after drilling. A) p_{mud} = 0 MPa. B) p_{mud} = 8 MPa. f_{mc} is the value of Mohr-Coulomb failure function. Positive value indicates failure.

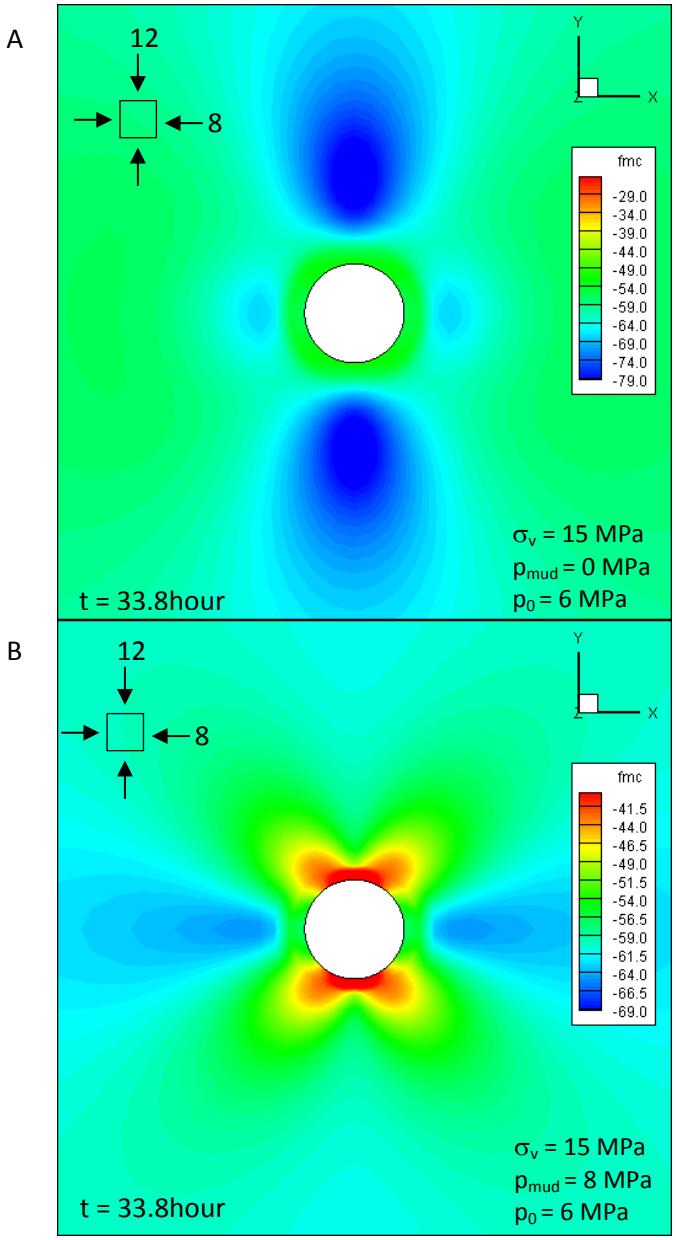

Figure 6.13 Poroelastic analysis: Development of failure tendency at 33.8 hour after drilling. A) p_{mud} = 0 MPa. B) p_{mud} = 8 MPa. f_{mc} is the value of Mohr-Coulomb failure function. Positive value indicates failure.

In order to study the influence of well condition and stress state on well instability, comparison analyses have been done for 6 simulation examples as shown in Figure 6.14 - 6.15. Slight differences are shown between normal faulting stresses regime (Figure 6.14 series I) and reverse faulting stress regime (Figure 6.14 series II) regarding the failure zone shapes. The series I of plots have slight higher f_{mc} value than those of series II in Figure 6.14. However when examine the failure plane orientation, significant differences have been noticed between two stress regimes (Figure 6.15). As described previously in this paper, directions shown in Figure 6.15B (reverse faulting regime) represents vertical failure planes. And directions shown in Figure 6.15A (normal faulting regime) indicates failure planes that intersect with x-y plane at some angle and distribute symmetrically with z-axis.

Plots in Figure 6.14 are the result for three different well conditions. Shapes of failure zones for drained and undrained conditions are similar. Undrained condition results in higher failure tendency, which is consistent to previous simulation example. The drainage of pore fluid can reduce the stress concentration at minimum horizontal stress direction. However, failure zones for uncoupled analysis (Figure 6.14 I-3 and II-3) are more similar to the elastic results (Figure 6.8), and showing failure zone at y-direction. Uncoupled analysis is calculated by assuming no excess pore pressure is generated by applied mechanical force.

I-1

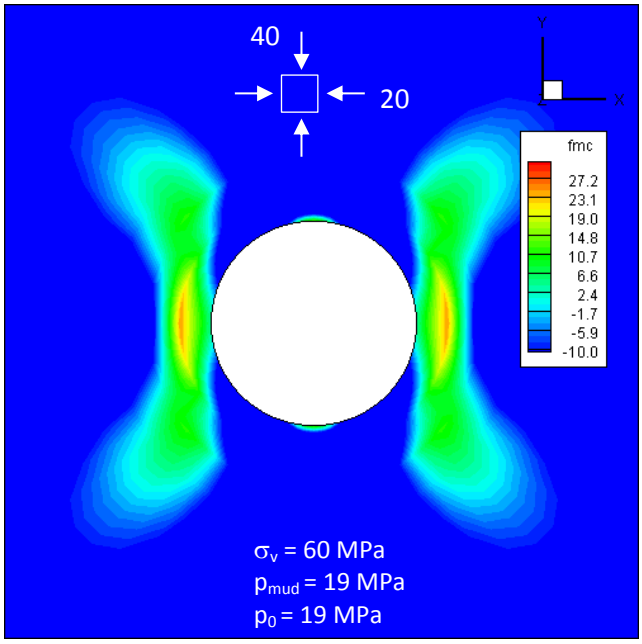
40
20
Y
X
fmc
27.2
23.1
19.0
14.8
10.7
6.6
2.4
-1.7
-5.9
-10.0
σv = 60 MPa
pmud = 19 MPa
p0 = 19 MPa

II-1

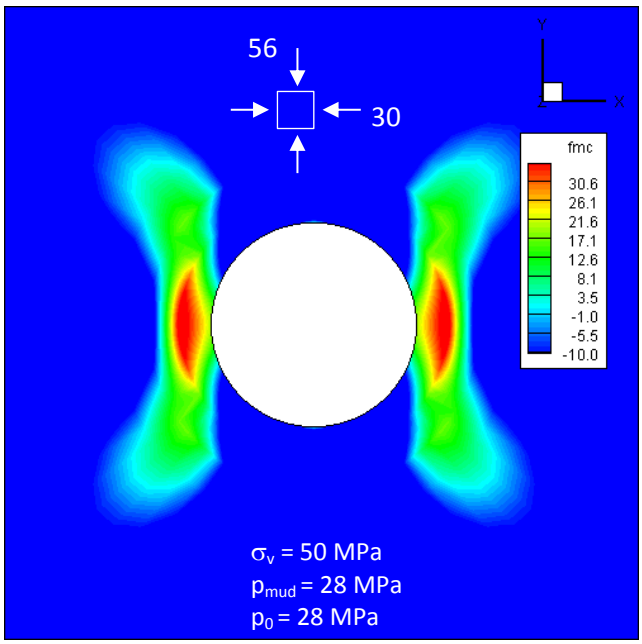
56
30
Y
X
fmc
30.6
26.1
21.6
17.1
12.6
8.1
3.5
-1.0
-5.5
-10.0
σv = 50 MPa
pmud = 28 MPa
p0 = 28 MPa

I-2

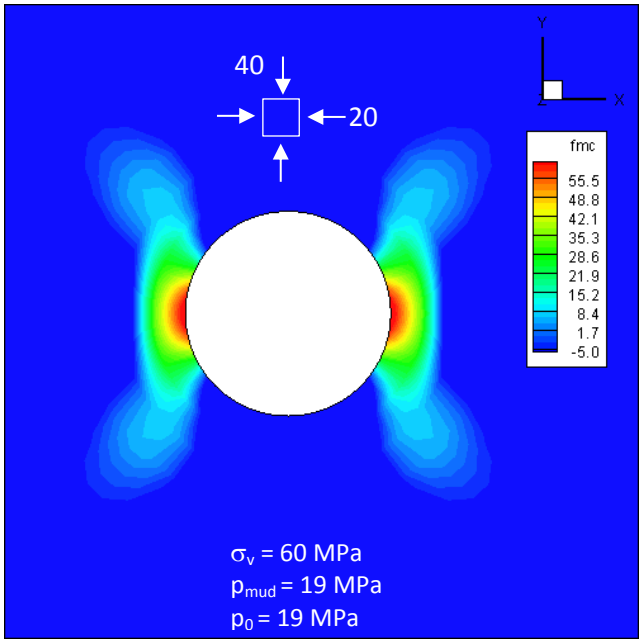
40
20
Y
X
fmc
55.5
48.8
42.1
35.3
28.6
21.9
15.2
8.4
1.7
-5.0
σv = 60 MPa
pmud = 19 MPa
p0 = 19 MPa

II-2

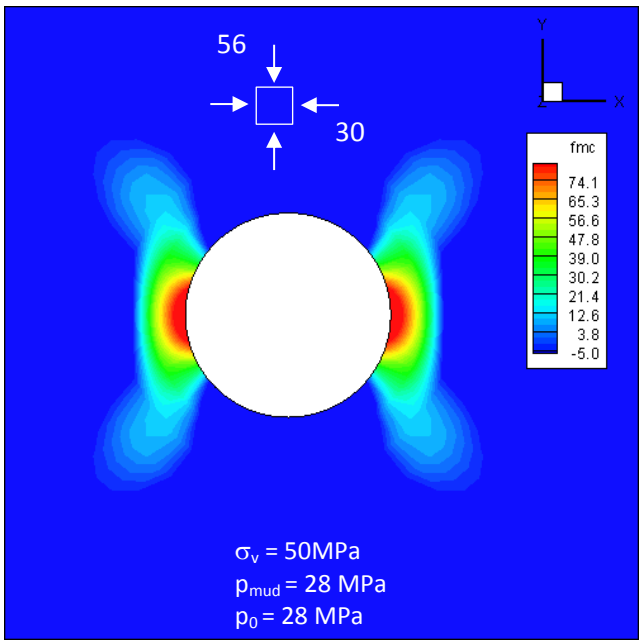
56
30
Y
X
fmc
74.1
65.3
56.6
47.8
39.0
30.2
21.4
12.6
3.8
-5.0
σv = 50MPa
pmud = 28 MPa
p0 = 28 MPa

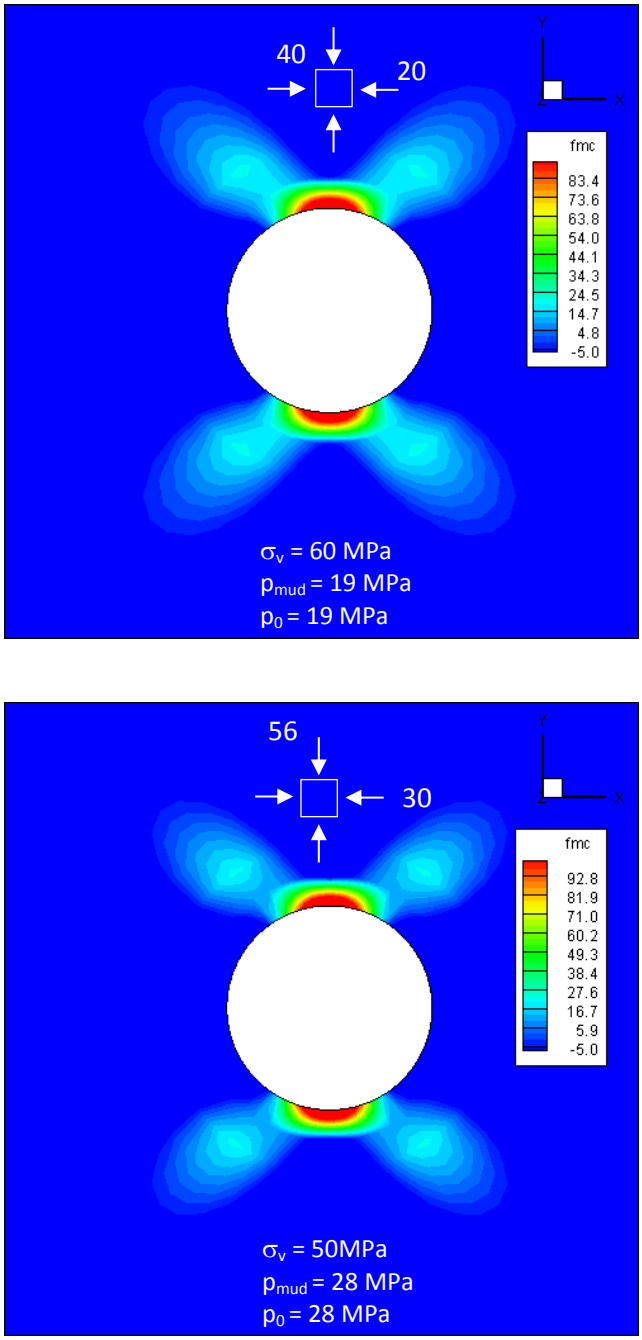

Figure 6.14 Failure zones under normal (I) and reverse (II) faulting stress regimes, from drained at 1 minute (I-1 and II-1), undrained (I-2 and II-2), and uncoupled analysis (I-3 and II-3).

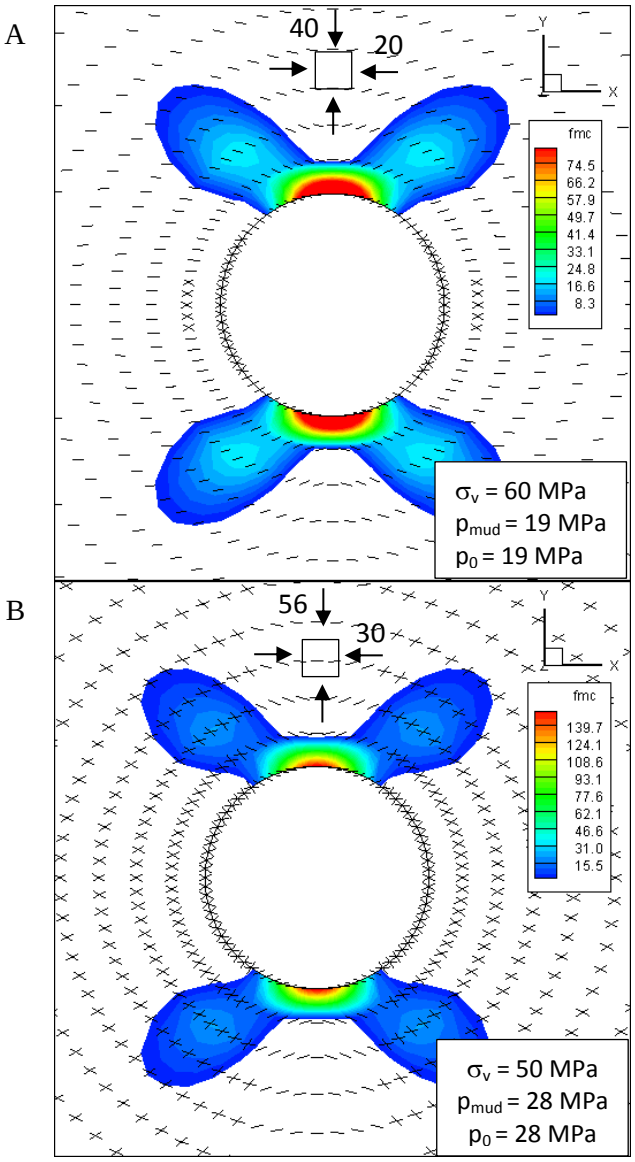

Figure 6.15 Potential failure planes of normal (A) and reverse (B) stress regimes from uncoupled analysis. Color zones represent failure zones. f_{mc} is the value of Mohr-Coulomb failure function.

When excess pore pressure is considered and well pressure present, different failure modes can occur. Modes shown in Figure 6.6 happen at conditions that well pressure is low or neglectable and the vertical stress is the intermediate principal stress after drilling. Failure mode shown in Figure 6.6A will occur at isotropic horizontal stress situation. And failure mode shown in Figure 6.6B will occur at anisotropic horizontal stress situation. When well pressure is extremely high, the wellbore will fail as hydraulic fracturing perpendicular to minimum horizontal stress direction. Otherwise, basic modes for cases with medium well pressure are shown in Figure 6.16 and Figure 6.17. Comparing Figure 6.16, 6.17 and Figure 6.6, we can find that same failure zones can have different failure mode and shear planes. Failure zone cross-sections in Figure 6.6A and Figure 6.16 have similar symmetric ring shape, but the 3D failure modes are very different. Same results can be seen from comparison between Figure 6.6B and Figure 6.17 too. Figure 6.18 summarizes commonly shapes (cross-section and three-dimensional) of failure zones near wellbore under different in-situ stress and well-pressure conditions.

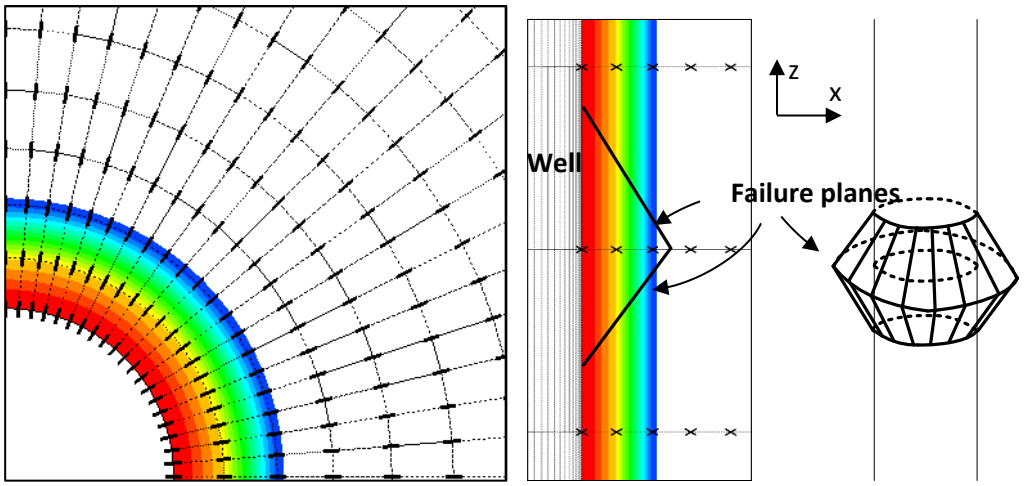

Figure 6.16 Sketch of vertical failure planes. σ_v = 50 MPa, σ_H = 30 MPa, σ_h =30 MPa, p_{ini} = 19 MPa, p_{mud} = 10 MPa. Color zones indicating $f_{mc} > 0$.

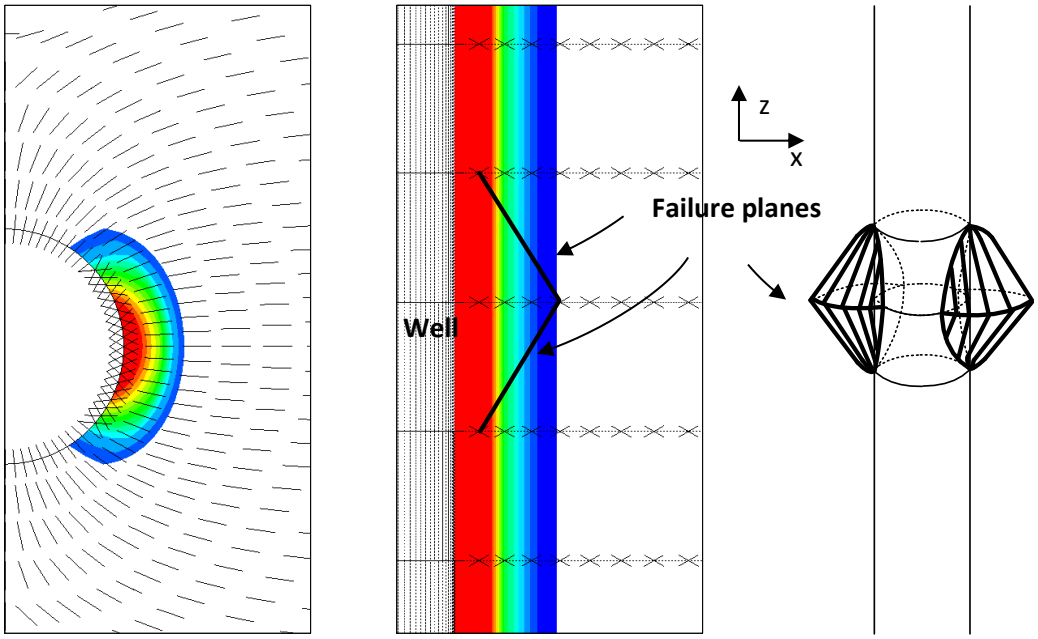

Figure 6.17 Sketch of vertical failure planes. σ_v = 50 MPa, σ_H = 35 MPa, σ_h =25 MPa, p_{ini} = 19 MPa, p_{mud} = 10 MPa. Undrained boundary condition. Color zones indicating $f_{mc} > 0$.

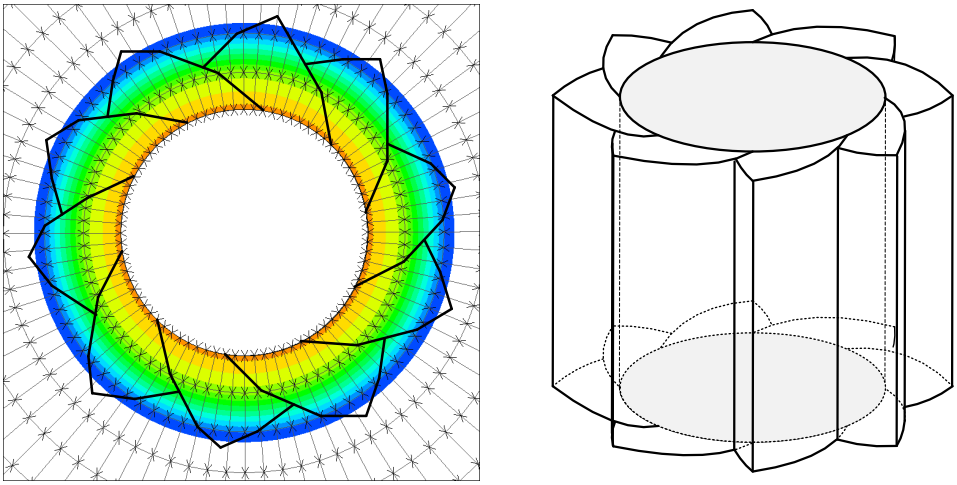

a) *Normal faulting stress regime:* σ_v *= 30 MPa,* σ_H *= 25 MPa,* σ_h *= 25 MPa,* p_{well}*= 0 MPa.; isotropic horizontal stresses; low well pressure;* $\sigma_2 = \sigma_v$ *near wellbore. (Figure 6.6A)*

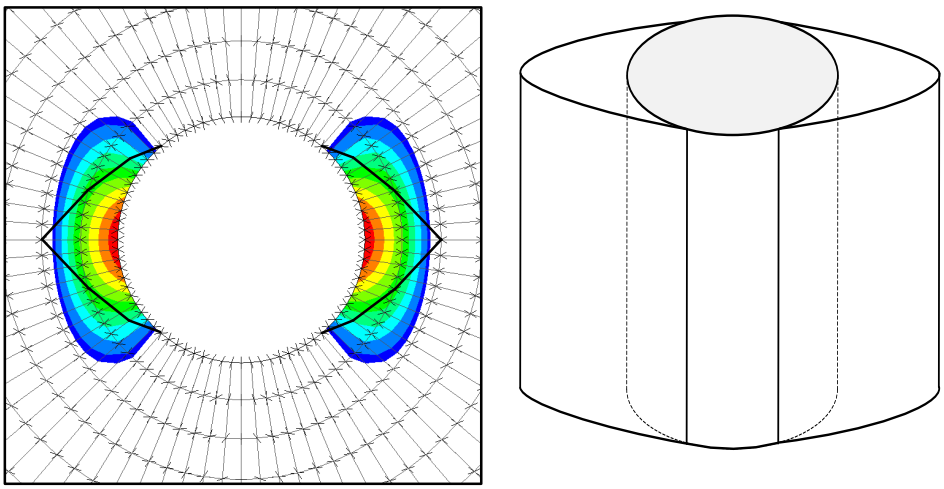

b) *Reverse faulting stress regime:* σ_v *= 30 MPa,* σ_H *= 40 MPa,* σ_h *= 10 MPa,* p_{well}*= 0 MPa.; anisotropic horizontal stresses; low well pressure;* $\sigma_2 = \sigma_v$ *near wellbore. (Figure 6.6B)*

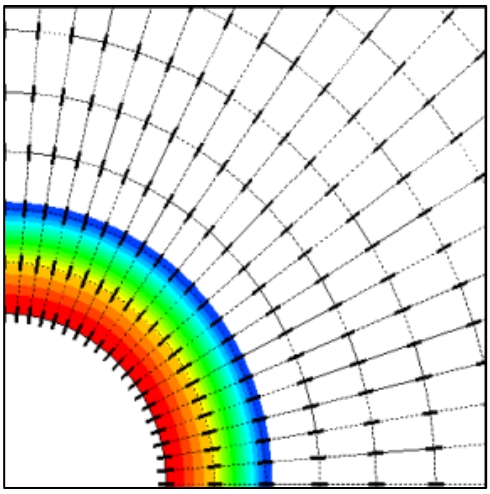

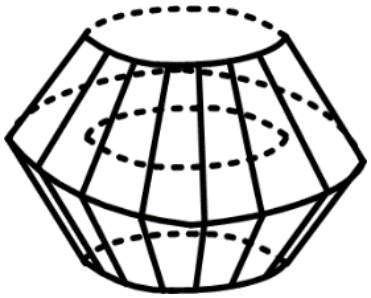

c) *Normal faulting stress regime:* σ_v *= 50 MPa,* σ_H *= 30 MPa,* σ_h *= 30 MPa,* p_{well}*= 19 MPa.; isotropic horizontal stresses; medium well pressure;* $\sigma_2 = \sigma_\theta$ *near wellbore.(Figure 6.16)*

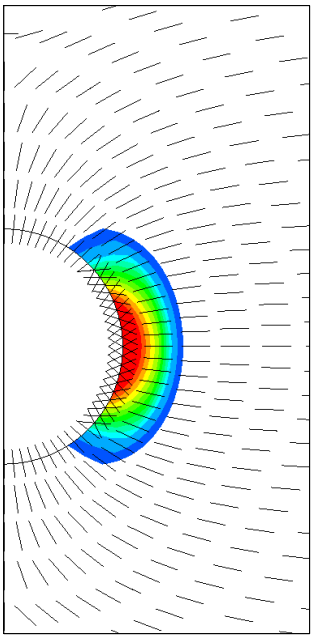

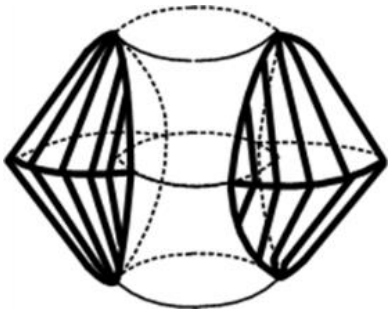

d) *Normal faulting stress regime:* σ_v *= 50 MPa,* σ_H *= 35 MPa,* σ_h *= 25 MPa,* p_{well}*= 19 MPa.; anisotropic horizontal stresses; medium well pressure; near wellbore.* σ_2 *rotates from vertical to tangential. (Figure 6.17)*

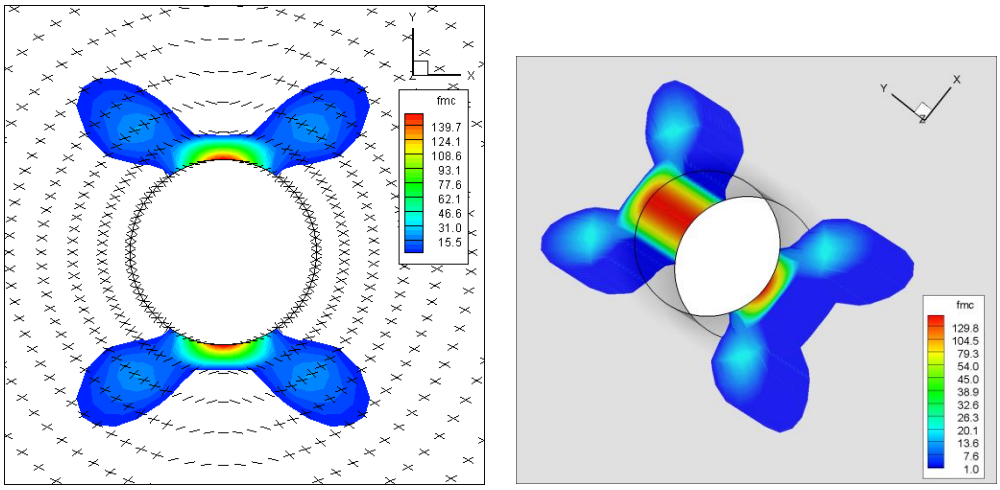

e) *Reverse faulting stress regime:* σ_v *= 50 MPa,* σ_H *= 56 MPa,* σ_h *= 30 MPa,* p_{well}*= 28 MPa.; anisotropic horizontal stresses; high well pressure; near wellbore* $\sigma_2 = \sigma_v$*. (Figure 6.15B)*

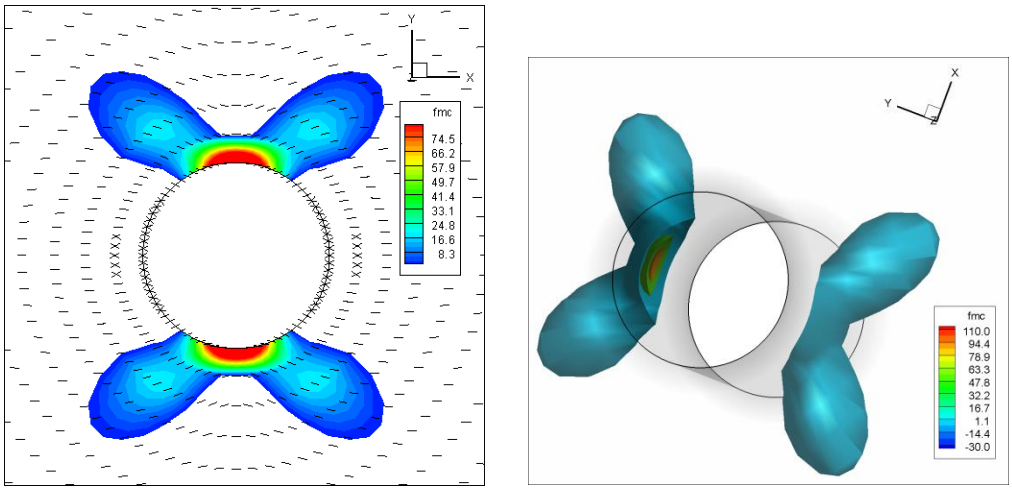

f) *Normal faulting stress regime:* σ_v *= 60 MPa,* σ_H *= 40 MPa,* σ_h *= 20 MPa,* p_{well}*= 19 MPa.; anisotropic horizontal stresses; high well pressure; near wellbore* σ_2 *rotates from vertical to tangential. (Figure 6.15A)*

Figure 6.18 Cross-sectional and three-dimensional view of failure zone shapes near wellbore under different in-situ stress regimes and well pressure.

6.4. Fully-coupled THM Analysis

Thermal stress can be significant even if the thermal effect on wellbore deformation is not obvious, as can be seen from the comparison between the deformation results (Figure 6.19 and Figure 6.11B) and thermal stress results (Figure 6.12B, 6.13B, and Figure 6.20A-B) of poroelastic and THM analysis. Lower mud temperature than formation temperature will decrease the stress concentration at wellbore wall in minimum horizontal stress direction. Therefore, the wellbore is temporarily stable at the beginning. This hydrostatic reduction of wellbore stress may lead to tensile failure in the maximum horizontal stress direction (Figure 6.20A). With time, the cooling effect will go further into the formation, which will induce higher failure tendency to the tensile zones (Figure 6.20B). On the another hand, if the well is shut-down and mud is heated up by the formation with time, the compressive stress concentration in minimum horizontal stress direction will appear again. Figure 21-23 compare the effects of different temperature differences under same in-situ stresses and mud pressure. We can see from Figure 6.22 that for short term, at t = 1 hour, the near wellbore failure tendency is much lower for Δt = -55 ℃ than Δt = 0 ℃. For both cases, failure zones switched from x- direction (t =1 hour) to y- direction (t = 33.8 hour) after 34 hours. The slight decrease of failure tendency for no temperature change case at 33.8 hour is caused by the decrease of pore pressure in the compression zone with time (x-direction), which moves the Mohr-circle away from the

failure envelope. The significant increase of failure tendency for Δt = -55 ℃ at 33.8 hour is due to the diffusion of cooling effect. Although with different failure mechanisms, both simulation examples show small failure zones in y-direction at 33.8 hour (Figure 6.23). Δt = -55 ℃ plot shows slight larger failure zone than Δt = 0 ℃ plot. For the current simulation conditions, a lower mud pressure and small temperature difference will maintain the well bore stability.

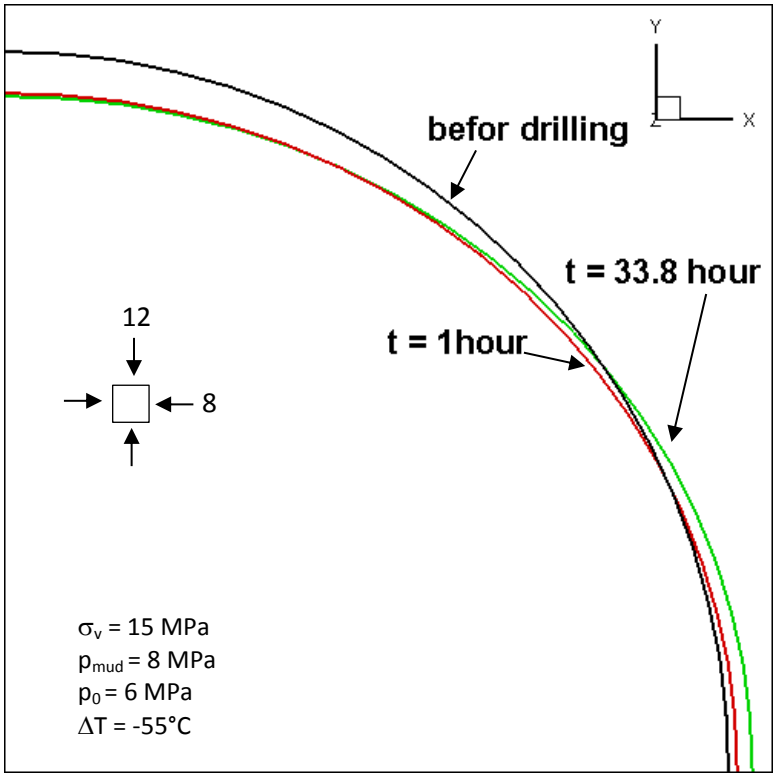

Figure 6.19 THM analysis: Illustration of wellbore deformation in 34 hours after drilling. p_{mud} = 8 MPa, p_{ini} = 6 MPa, ΔT = -55 ℃.

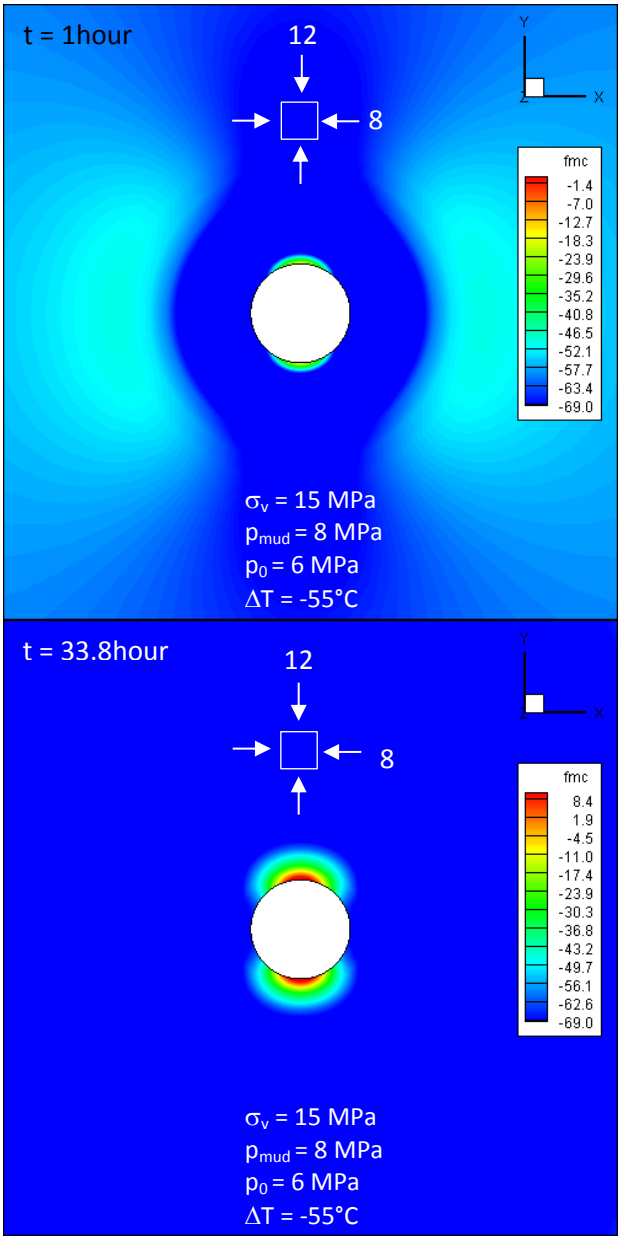

Figure 6.20 THM analysis: Development of failure tendency in 34 hours after drilling. p_{mud} = 8 MPa, p_{ini} = 6 MPa, ΔT = -55 ℃. f_{mc} is the value of Mohr-Coulomb failure function. Positive value indicates failure.

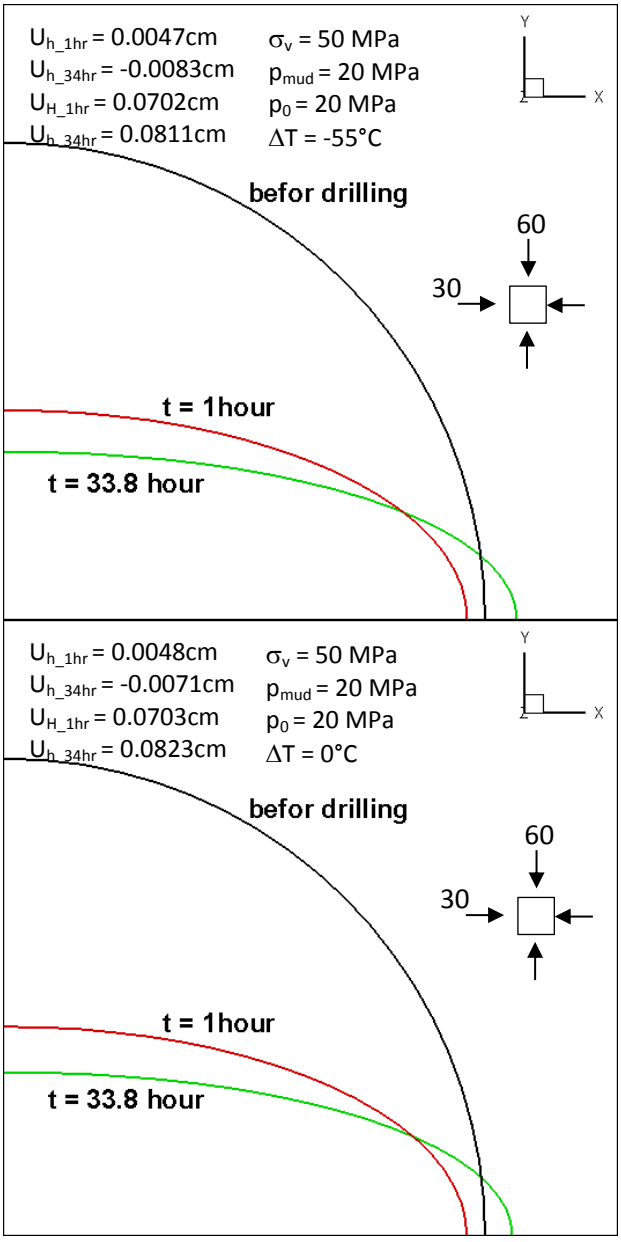

Figure 6.21 THM analysis: Wellbore deformation under different temperature boundary conditions. Left: -55 ℃ temperature difference between drilling mud and formation. Right: No temperature difference between drilling mud and formation.

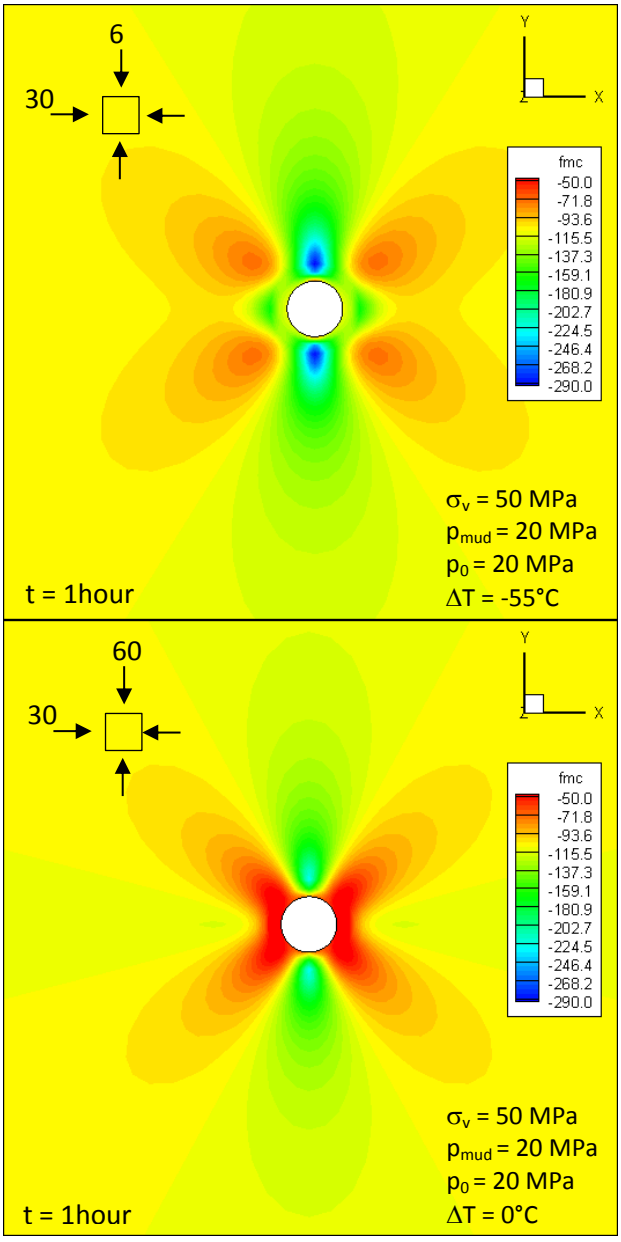
6
30
Y
X
fmc
-50.0
-71.8
-93.6
-115.5
-137.3
-159.1
-180.9
-202.7
-224.5
-246.4
-268.2
-290.0
σv = 50 MPa
pmud = 20 MPa
p0 = 20 MPa
ΔT = -55°C
t = 1hour
60
30
Y
X
fmc
-50.0
-71.8
-93.6
-115.5
-137.3
-159.1
-180.9
-202.7
-224.5
-246.4
-268.2
-290.0
σv = 50 MPa
pmud = 20 MPa
p0 = 20 MPa
ΔT = 0°C
t = 1hour

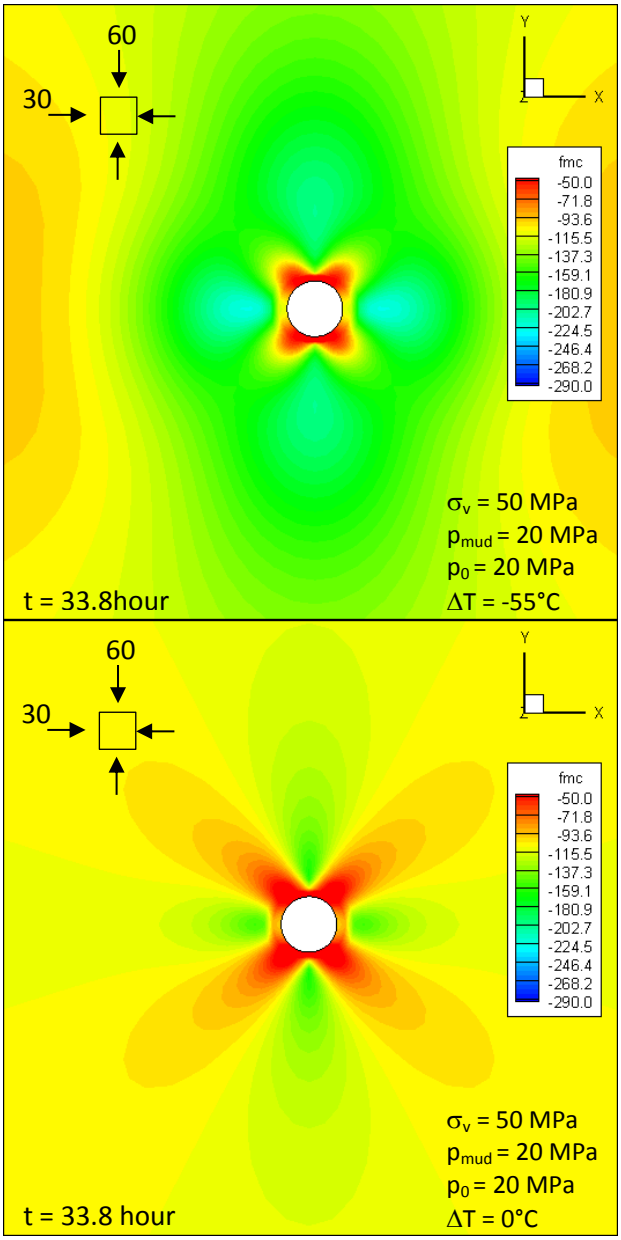

Figure 6.22 THM analysis: Development of failure tendency under different temperature boundary conditions in 34 hour after drilling. Left: -55 ℃ temperature difference between drilling mud and formation. Right: No temperature difference between drilling mud and formation.

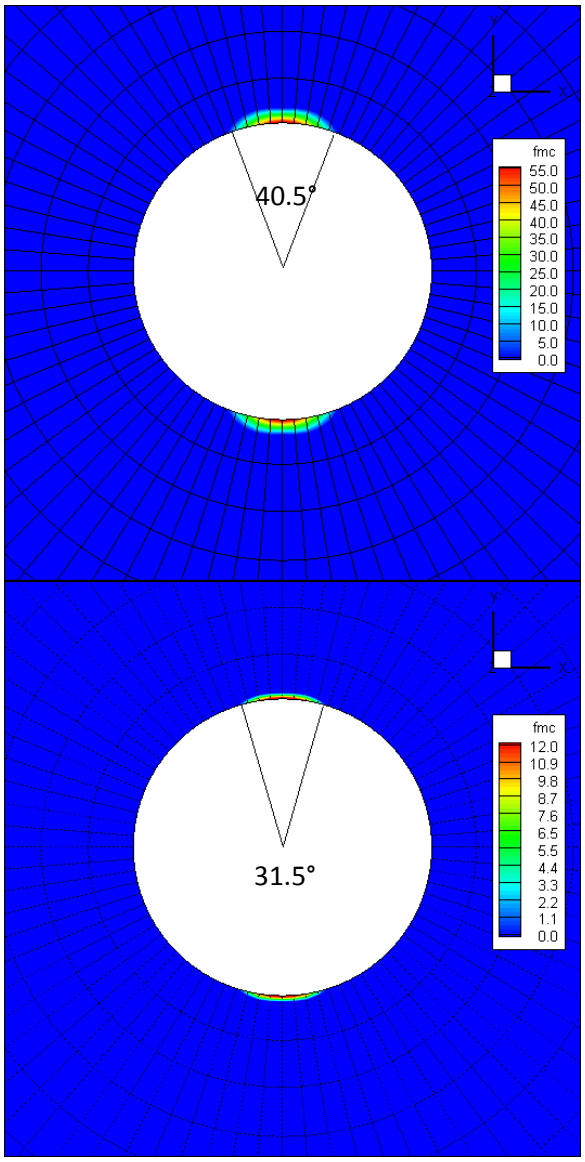

Figure 6.23 THM analyses: ranges of failure zone under different temperature boundary conditions at 34 hour after drilling. Left: -55 ℃ temperature difference between drilling mud and formation. Right: No temperature difference between drilling mud and formation.

6.5. Effect of rock heterogeneity

Heterogeneity of rock properties is one of the essential factors that should be considered in stability analysis. Rocks are normally heterogeneous and moreover, properties in the stressed zone can be altered from original values, which will introduce induced heterogeneity in the rock. Rock properties can be time and stress dependent. In another world, non-linear stability analysis is necessary. Weibull distribution as discussed in Chapter 3 is used in this section to model the rock heterogeneity and provide simulation examples that show the effect of heterogeneity on borehole stability. The distributions of every rock properties should be compactable to each other. This section is not aimed to explain the correlation among different rock properties. Therefore, in the following simulation, only Young's modulus is set to be heterogeneous for illustration simplicity. Other properties, such as Poisson's ratio, porosity, strengths, and so on, can be introduced to the model using same method, as in next section. To prepare a numerical rock sample, we first assume the distribution of Young's modulus follows Weibull's distribution with parameter λ = 10 GPa and m = 5 (Equation 6.4):

$$f(x) = \frac{m}{\lambda}(\frac{x}{\lambda})^{k-1} e^{-(\frac{x}{\lambda})^{m}} \tag{6.4}$$

The simulation domain is divided to 16000 grid blocks, and the unit grid size is 0.4 m x 0.4 m x 0.2 m. 16000 random numbers following Equation 6.4 is generated and distributed to these grid blocks. Then, the Young's modulus for each element of the mesh is obtained using numerical interpolation. Here, it is ensured that the wellbore does not cut through blocks with different Young's modulus in each layer of mesh. The distribution of Young's modulus in FEM mesh is shown in Figure 6.24. All other properties are kept uniform as listed in Table 6.1. Elastic response of wellbore under in-situ stress σ_v = 15 MPa, σ_H = 28 MPa, σ_h = 2 MPa is calculated. The in-situ stresses are same as the simulation case shown in Figure 6.9. Three slices (top, middle, and bottom) of failure tendency plot and Young's modulus distribution plot are shown in Figure 6.25. Warm color represents higher Young's modulus. It is noticed from the result that the failure tendency is higher for larger Young's modulus at wellbore wall. Some failure zones show discontinuity. Although the general distribution of failure zone is along the maximum horizontal direction, the heterogeneity influences the local development of failure zone. Figure 6.26 shows a 3D view of the failure zone and the types of failure in the failure zone. Red color represents compressive failure, and blue color represents tensile failure. Tensile failure is observed in far distance comparing to Figure 6.9 where tensile failure only occurs at wellbore wall.

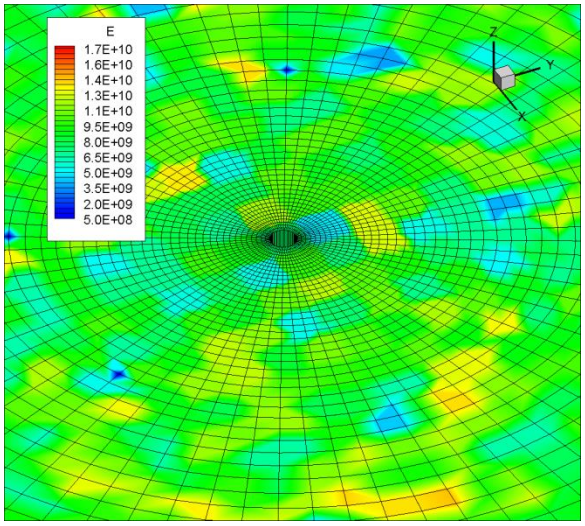

Figure 6.24 Heterogeneous distribution of Young's modulus. Weibull's distribution: λ = 10 GPa, m = 5. Element size for distribution is 0.4 m × 0.4 m × 0.2 m.

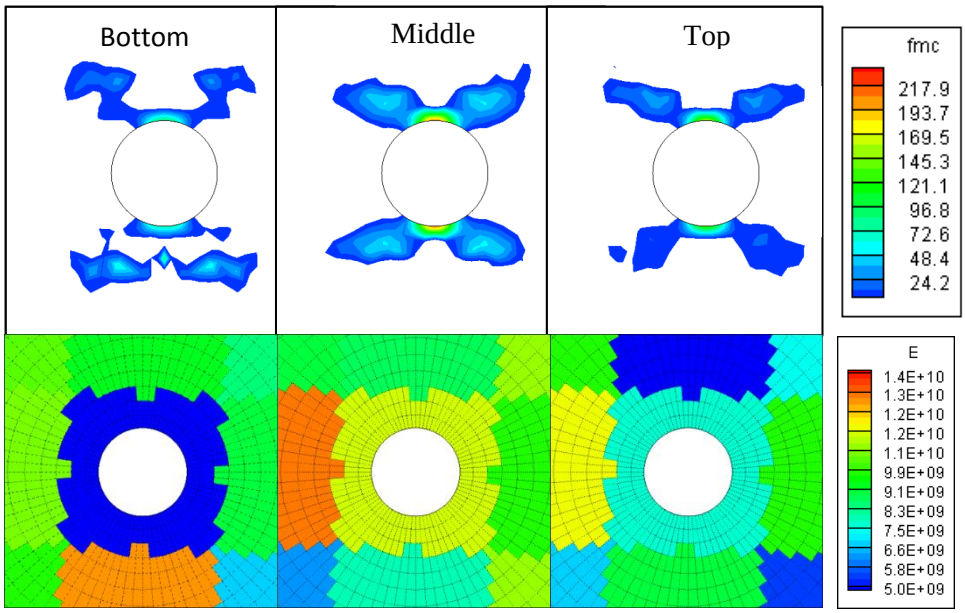

Figure 6.25 Top: Views of bottom, middle, and top slices of failure zones. Bottom: distribution of Young's modulus of bottom, middle, and top layer of matrix corresponding to failure zone slices.

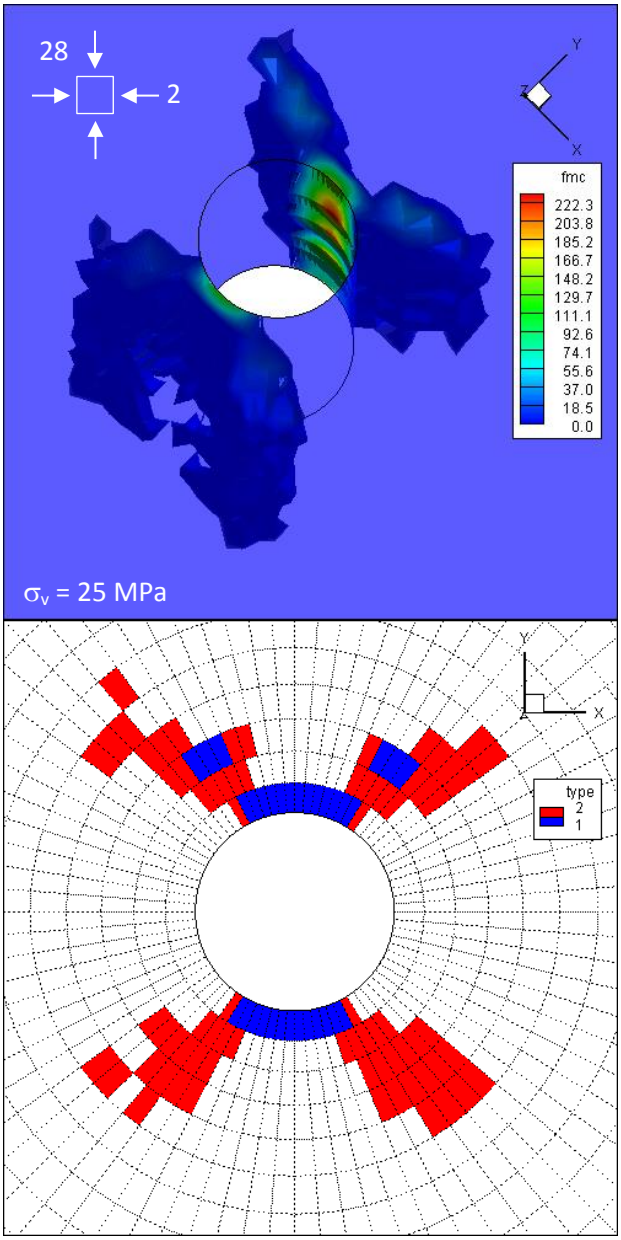

Figure 6.26 Left: 3-dimension view of failure zones. Color represents the Mohr-Coulomb function value. Right: Failure types. Red zones represent compressive failure, and blue zones represent tensile failure.

6.6. Case summary

Borehole behavior has been analyzed using current three-dimensional finite element model. Numerical simulations for cases with different stress states and well conditions have been done. The results show effects of pore pressure, temperature difference, drainage condition, and stress regimes on wellbore instability. Failure modes, type, orientation of failure plane have also been calculated. Mohr-coulomb theory is used to show the failure tendency under difference conditions.

High mud pressure and cool mud temperature will reduce the compression stress concentration at wellbore in minimum horizontal stress direction, but increase the tensile failure tendency in maximum horizontal stress direction. The increase of tensile failure tendency grows with time. Drainage of fluid will lower the failure tendency at wellbore uniformly. Uncouple analysis results in different failure zone than coupled poroelastic analysis. Failure zones of normal and reverse stress regime have similar cross-section shape but different three-dimensional shape. For low permeability reservoir, thermal effect is significant comparing to pore pressure effect. Rock heterogeneity will alter the local failure tendency, but the general failure behavior is mainly depends on stress condition.

7

THREE-DIMENSIONAL FULLY COUPLED FEM ANALYSIS OF HETEROGENEOUS RESERVOIR CONSIDERING ROCK DAMAGE AND PERMEABILITY ENHANCEMENT

Fluid injection is a commonly used stimulation approach in geothermal and oil/gas reservoirs development. The injection process involves coupled rock deformation and fluid flow as described in poroelastic theory (Biot 1946). The effect of thermal stresses and thermally-driven flow can also be significant in some cases. These physical processes in the reservoir will result in stress state, pore pressure, and temperature changes. The variations of these state variables are inter-related and their interaction needs to be considered. These changes can also lead to rock failure, fracture slippage, and changes in both fluid and heat flow, which are critical when planning the exploration strategy. In this chapter, the result of application of the FEM model of Chapter 5 are presented to study the influence of thermo-poro-mechanical coupling and rock heterogeneity on rock failure evolution, permeability variation and potential for occurrence of micro-seismicity. The modeling and interpretation of injection induced micro-

seismicity is important as it can be used to assess the stimulation results and to also perform risk analysis.

The influence of stress alteration and damage evolution on permeability has been studied by many researchers (Kiyama et al. 1996; Shipping et al. 1994; Tang et al. 2002; Li et al 2005). In this section, a non-linear FEM formula (Equation 5.41) is used to model the stress-dependent permeability. In addition, micro-seismicity which is often observed during or after fluid stimulation is considered. The occurrence and locations of potential induced-seismic events are related to the failure process of reservoir rock. After description of the theoretical basis and modeling strategy, we present a few example simulations to illustrate the THM coupled response of a heterogeneous reservoir to fluid injection under different in-situ stresses and with different injection plans.

As stress state changes, micro-cracks and voids can form inside the rock, and irreversible damage occurs. In this work, permeability and elastic modulus of the rock are also considered to depend on the damage level. Continuum damage mechanics is used to capture the rock post-peak softening behavior observed in triaxial tests (Tang et al. 2002) and bi-linear damage evolution law is applied to every rock element in the simulation zone. The continuum damage model is based on the assumption that the strength characteristics of rock follows Weibull distribution, which relates the damage evolution with degradation of rock due to

micro-crack initiation, micro-void growth, and micro-fracture propagation, i.e., the process which depend on the heterogeneity distribution. The distribution of rock heterogeneity here consists of "weak" zones, "soft" zones, and "high-permeability" zones, expressed in terms of rock properties used in this model, i.e., rock strength, elastic modulus, and permeability. The parameters of heterogeneity distribution are calibrated using stress-strain constitutive law obtained from lab test results of reservoir rock samples (Li et al. 2011) and previous work (Fujii et al. 1999) on constitutive relations for brittle rocks. The same laboratory-derived rock mechanical parameters are also used to build the damage evolution law. Damage variable "*d*" is introduced in to the context, which represents the damage level of the material, and has a value between 0 and 1.

7.1. Elemental damage evolution for triaxial test condition

When the elemental block is under uniaxial stress, the constitutive law presented in Figure 7.1 is adopted. The degraded Young's modulus after damage is assumed to be (Tang et al. 2002):

$$E = (1-d)E_o \tag{7.1}$$

where d is the damage variable, and E_0 is the original Young's modulus of undamaged material.

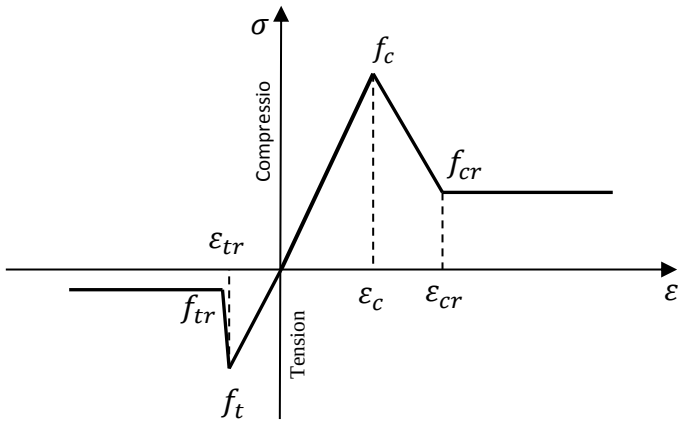

Figure 7.1 Elastic-brittle tensile damage and elastic-softening compression damage constitutive law of element subject to uniaxial stress.

Using Hooke's law, stress-strain relationship of triaxial state under principal stresses can be written as:

$$\sigma_i = \frac{E}{1+\nu}[\varepsilon_i + \frac{\nu}{1-2\nu}\varepsilon_{jj}], \quad i, j = 1,2,3 \tag{7.2}$$

The maximum tensile stress criterion is adopted for tensile failure, that is, failure occurs when the largest principal stress exceed the uniaxial tensile strength. The maximum principal tensile stress and strain are denoted by σ_3 and ε_3 in this model. The constitutive relationship (Equation 7.2) in terms of σ_3 and ε_3 can be written as:

$$\sigma_3 = \frac{E}{1+\nu}[\varepsilon_3 + \frac{\nu}{1-2\nu}\varepsilon_v] \tag{7.3}$$

It is assumed that isotropic degradation of the elemental block and the change of Poisson's ratio after degradation are small for isotropic material. Therefore, during the failure process, Poisson's ratio is kept constant. Rearranging Equation (7.3) one obtains the Young's modulus for a triaxial stress state:

$$E = \sigma_3(1+\nu)/(\varepsilon_3 + \frac{\nu}{1-2\nu}\varepsilon_v) \tag{7.4}$$

Then, the damage variable can be calculated as:

$$d = 1 - \frac{E}{E_0} = 1 - f_{tr}(1+\nu)/(\varepsilon_3 E_0 + \frac{\nu}{1-2\nu}\varepsilon_v E_0); \quad \varepsilon_3 > \varepsilon_{tr} \tag{7.5}$$

where f_t is the uniaxial tensile strength and f_{tr} is the residual strength after complete failure. And ε_{tr} is the tensile strain at complete failure.

The Mohr-Coulomb criterion is used for compression failure criterion:

$$\sigma_1 - \psi\sigma_3 + C = f_{mc} \tag{7.6}$$

$$\text{where } C = \frac{2c_f \cos\phi_f}{1-\sin\phi_f}; \text{ and } \psi = \frac{1+\sin\phi_f}{1-\sin\phi_f} \tag{7.7}$$

c_f is the uniaxial compressive strength. Substituting generalized Hook's law into Equation (7.6), yields

$$E = \frac{(\sigma_1 - \psi\sigma_3 + C)(1+\nu)}{\varepsilon_1 + \frac{\nu}{1-2\nu}\varepsilon_v - (\varepsilon_3 + \frac{\nu}{1-2\nu}\varepsilon_v)\psi} \tag{7.8}$$

Consider equivalent stress as $\bar{\sigma} = \sigma_1 - \psi\sigma_3 + C$, the equivalent strain can then be expressed as:

$$\bar{\varepsilon} = \frac{\varepsilon_1}{1+\nu} + \frac{\nu}{(1-2\nu)(1+\nu)}\varepsilon_v - (\frac{\varepsilon_3}{1+\nu} + \frac{\nu}{(1-2\nu)(1+\nu)}\varepsilon_v)\psi \tag{7.9}$$

Therefore, damage variable becomes:

$$d = 1 - [\left(\frac{f_{cr} - f_c}{\varepsilon_{cr} - \varepsilon_c}\right)(\bar{\varepsilon} - \varepsilon_c) + f_c]/(\sigma_1 - \psi\sigma_3 + C);\ \varepsilon_c < \bar{\varepsilon} < \varepsilon_{cr} \tag{7.10}$$

$$d = 1 - f_{cr}/(\sigma_1 - \psi\sigma_3 + C);\ \varepsilon_{cr} < \bar{\varepsilon} \tag{7.11}$$

where f_c is the uniaxial compression strength and f_{cr} is the residual stress after complete failure. ε_c is the compressive strain at peak stress and ε_{cr} is the compression strain at complete failure.

As explained in Chapter 5, an iterative method is used to solve the non-linear system of equations (5.41). The iteration continues until d is close enough to those obtained in last iteration within a prescribed tolerance (0.01), i.e.:

$\left\| \frac{d_{i+1} - d_i}{(1 - d_i)} \right\| < \varepsilon$ where i = number of iteration step. (1-d_i) is used in the denominator due to the fact that d can be zero at some data points.

7.2. Stress dependent permeability evolution

Permeability is a stress dependent variable, and develops with damage evolution. Before failure, the stress dependent permeability is calculated as (Tang et al. 2002):

$$k = k_0 \exp(-\beta(\sigma_{ii}/3 - \alpha p)) \tag{7.12}$$

It is assumed that the volumetric change (ΔV) of a damaged element leads to three orthogonal fractures that have parallel walls (Li et al. 2012). The aperture of each fracture can be approximated as:

$a = \frac{\Delta V}{3A} \approx \frac{\varepsilon_v V}{3\sqrt[3]{V^2}} = \frac{\varepsilon_v \sqrt[3]{V}}{3}$, V is the element volume, A is surface area. (7.13)

According to cubic law, permeability of a parallel plate fracture as described above (Equation 7.13) can be calculated as:

$$k_d = \frac{a^2}{12\mu} = \frac{(\varepsilon_v{}^2)(\sqrt[3]{V^2})}{108\mu} \tag{7.14}$$

7.3. Distribution of heterogeneity

In this simulation, the distribution of elemental strength, elastic modulus, and permeability is assumed to follow Weibull's distribution (Weibull, 1961), and it is assumed all three distributions have the same Weibull's shape factor. To determine the shape factor of Weibull distribution, a heterogeneous sample (40 cm × 40 cm × 40 cm) is considered for numerical uniaxial compression experiments. The mean values of the uniaxial compressive strength, elastic modulus, and Poisson's ratio are 50 MPa, 10 GPa, and 0.25, respectively (Table 6.2), which are the scale parameters of Weibull distributions. Figure 7.2 shows the comparison of the complete stress-strain curves obtained from numerical simulation and experimental work. The shape parameter for numerical simulation in Figure 7.2 is 5.0. The damage model (Figure 7.1) is applied to each element in the numerical model. And the following experimentally determined values are used in the simulations: f_c = 50 MPa, f_{cr} = 40% f_c, ε_c = 0.0005, $\varepsilon_{cr} = 2.5\varepsilon_c$. It can be seen that the numerical result agree well with the experimental results. One should notice here the complete stress-strain curve (solid line) is a representative curve processed from lab test results of reservoir rock samples (Li et al. 2011) and Fujii et al. research on constitutive relations for brittle rocks (Fujii et al. 1999).

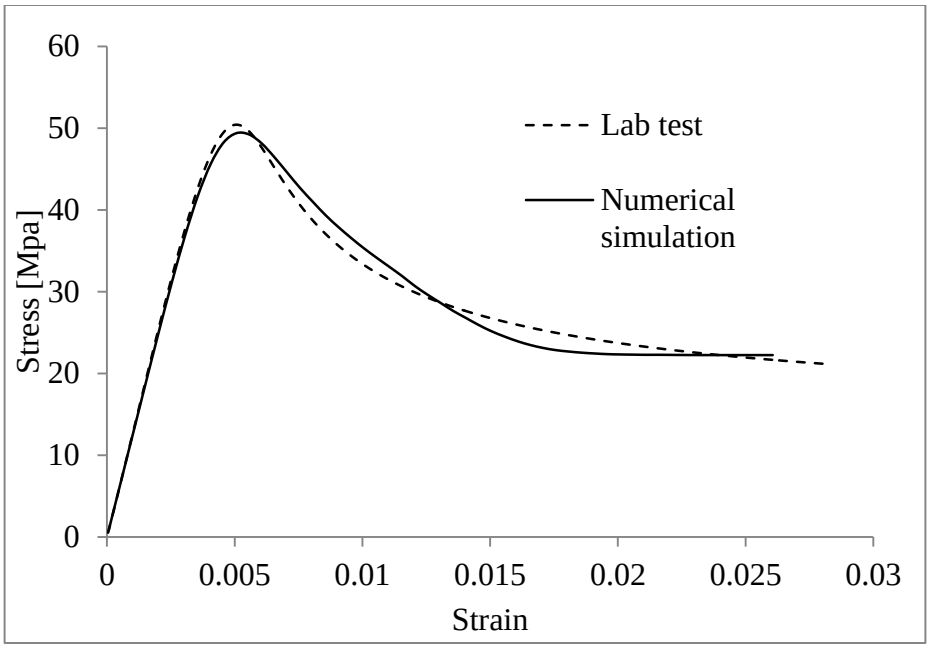

Figure 7.2 Comparison between simulated complete stress-strain curve and experimental results.

7.4. Simulation setup

The numerical model has previously been verified by analytical solutions (Chapter 5). Therefore, the focus of this section is on some case studies. A simulation domain of 1000 m × 1000 m × 500 m (Figure 7.3) is used to represent an EGS. The domain is discretized into 32000 eight-node brick elements and 35301 element nodes. A point injection source is used in this study, which is located in the center of the domain at coordinates x = 512.5 m, y = 512.5 m, z = 262.5 m. The volumetric injection rate is 3.125 x10^{-2} m^3/s, that is, 8.25 gal/s of fluid come out from the injection element into the reservoir. The viscosity of water is 3.0×10^{-4} Pa s and is assumed to be constant during the

simulation. The injection time is 48 hours. The rock heterogeneity, including Young's modulus, permeability, tensile and compression strengths, is distributed using Weibull function with a shape parameter of 5.0. The mean value for the distributions are E = 10 GPa (Young's modulus), k = 1 md (permeability), f_{tr} = 5 MPa (tensile strength), and f_{cr} = 50 MPa (compression strength). The domain is large enough so that the injection induced disturbances do not reach the boundary within the computation time period. A zero displacement and no fluid and heat flux boundary conditions are used in this study. The injection temperature is set to 25 ℃, but this restriction is removed and the well fluid is allowed to be warmed up in the shut-in phase. The initial temperature of the domain is 115 ℃, and the initial pore pressure is 10 MPa.

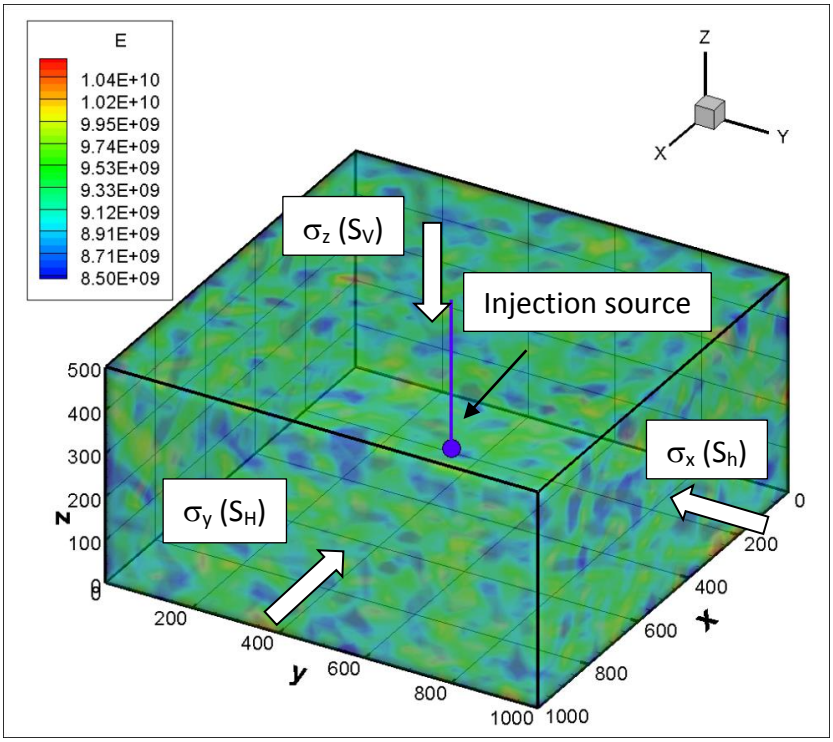

Figure 7.3 Model set-up for the heterogeneous reservoir. Unit: Young's modulus in Pascal (Pa), length in meter (m).

Table 7.1 Parameters used in the heterogeneous rock simulation.

Rock and fluid properties	
Young's modulus, E (mean)	10 GPa
Fluid viscosity, μ	3.0×10^{-4} Pa s
Permeability, k (mean)	1 md
Rock density	2400 kg/m^3
Porosity	0.2989
Poisson's ratio, ν	0.25
Undrained Poisson's ratio	0.461
Skempton coefficient, B	0.915
Fluid density	1000kg/m^3
Thermal expansion coefficient of solid, α_m	1.8×10^{-5} K^{-1}
Thermal expansion coefficient of fluid, α_f	3.0×10^{-4} K^{-1}
Thermal diffusivity, c^T	1.6×10^{-6} m^2/s

7.5. Influence of rock heterogeneity

A normal faulting in-situ stress regime is used for calculation in this section: σ_{xx} = 15 MPa (σ_h), σ_{yy} = 45 MPa (σ_H), and σ_{zz} = 50 MPa (σv), p_{ini} = 10 MPa. There are 8 data points (Gauss point) for each element, and the failure events at these points are recorded and reported as a potential micro-seismic event.

First consider the profiles of injection pressure and failure events with time, resulting from injection into a homogeneous rock as shown in Figure 7.4 and 7.5. The damage magnitude is shown by the value of damage variable, *d*. Events for a homogeneous rock occur only during several time steps, with similar damage magnitude for each time step. The number in brackets in Figure 7.4 indicates the

number of events which occurred at the corresponding time. One can notice that, failure occurs when the pore pressure at a point is greater than ~15 MPa, which is the critical pressure at which the rock element experiences tension (S_h = 15 MPa).

The failure events for homogeneous rock form two layers of circular zones in the y-z plane. This is to be expected when rock properties are assumed to be isotropic. When plotted on y-z plane, these two layers will overlap as shown in Figure 7.5. Colors distinguish time steps when events occur. The centered gray square indicates the location of the injection point. A regular pattern of failure evolution can be observed. The circles in Figure 7.5 can be viewed as the critical pressure front, which is the pore pressure to cause failure. Therefore, one can predict the failure locations at any time based on the arrival time of the critical pore pressure (black circle) front. For homogeneous rock under isotropic in-situ stresses, the pore pressure diffusion length is a function of the rock diffusivity and time, and can be analytically calculated. There are also studies on relations between the location and time of the failure events for anisotropic stress state (Schoenball et al. 2010). However, these analytical relations do not apply in real situations where rock damage, stress variation and rock heterogeneity are the norm. As can been seen from Figure 7.6-7.7, the distribution of events in a heterogeneous reservoir spreads in time and space in an irregular fashion. Also, the damage magnitude varies much in the process (Figure 7.6). According to the

failure criteria used in this study, the initiation of a failure event is governed by the local strength and effective stress changes. Therefore, locations at a long distance from the injection source with low local strength can fail prior to those stronger elements located closer to the source. Also, since the effective stress values at short distances experience a large pore pressure and stress disturbances, a higher strength zones near the source can fail earlier than a weak zone far from the source.

The results show that because of the heterogeneity and rock damage evolution, analytical resolution of pore pressure diffusion and failure initiation is not adequate and numerical modeling of heterogeneity and failure process is necessary. As can be seen from the result, the location and initiation of failure events is more influenced by local heterogeneity, rather than the overall diffusivity and time. Due to the small contrast between vertical stress and the maximum horizontal stress (5 MPa) and the isotropy of permeability ($k_h = k_V$), the failure zone does not display an elliptical shape often reported for homogeneous models.

By comparing Figures 7.4-7.7, it can be seen that the distributions of failure events for the two cases develop differently; in the homogeneous isotropic case, the event distribution is symmetric around the injection source. Events only occur at t = 5, 6, 20 hour, when the injection induced pore pressure increment is

sufficient to initiate a failure. Examination of the failure types reveals that all events at t = 5 hrs. and t = 20 hrs. are tensile failures, and all events at t = 6 hrs. are shear failures. Also, all events at t = 40 hrs. are also of the tensile type. This phenomenon shows that, for the homogeneous isotropic rock, elements reaching a critical state will fail in the same manner given the same pore pressure increment. The events distribution for heterogeneous rock in Figure 7.7 is more disseminated. As described previously, there are weak zones distributed in the simulation domain. Thus, the potential of both failure types also varies element by element. Both failure types occur during the same time step. More tensile type failure is observed from the results. The ratio is 34(tensile):11(shear) in the two-stage injection case (Figure 7.15), 48 (tensile):15(shear)) in 48 hour non-stop injection case (Figure 7.6), 60(tensile):33(shear) in 48 hour non-stop injection case for large in-situ stresses (section 7.7). It is reasonable to have more tensile failure events in this simulation. The tensile strength of modeled rock is much smaller than the compression strength. Also, the σ_h stress is relatively small and it is easy to create tensile stress by a small pore pressure increase.

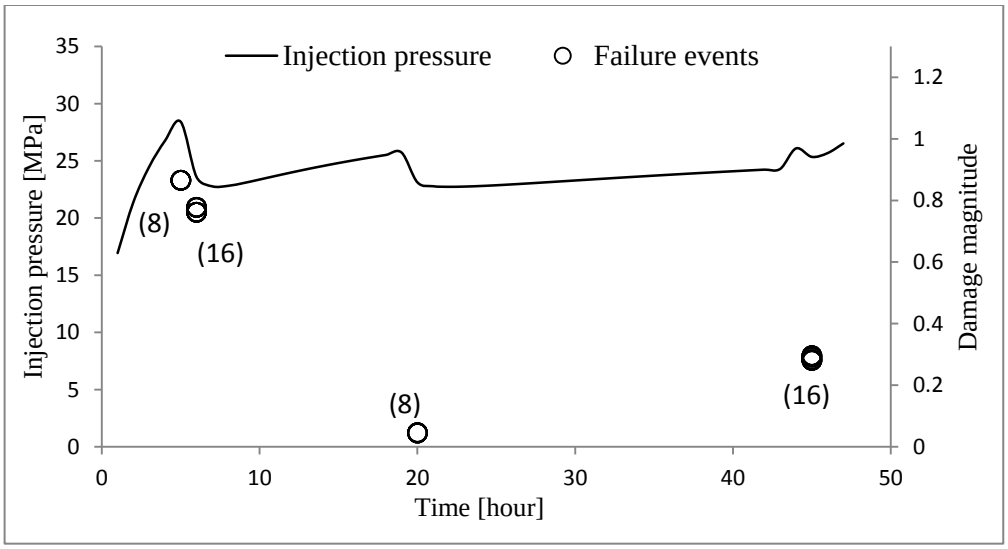

Figure 7.4 Profile of pressure at injection source and failure events for homogeneous model. Numbers in brackets show the number of events occur at corresponding time step.

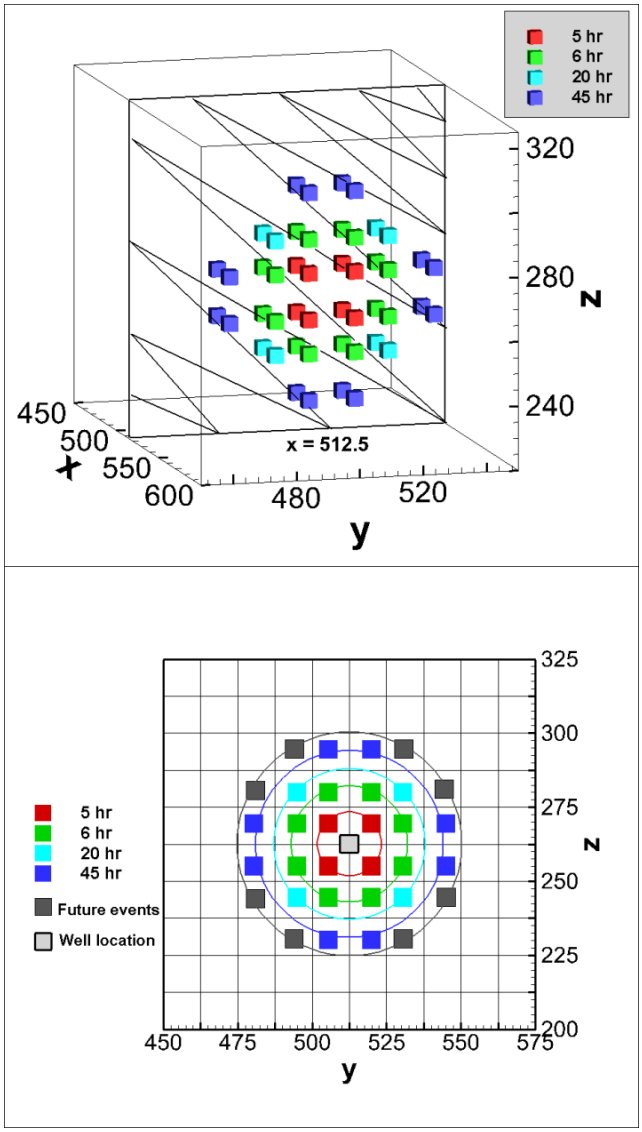

Figure 7.5 Distribution of failure events in space of homogeneous model. x = 512.5 plane indicates the plane on which the failure events are distributed.

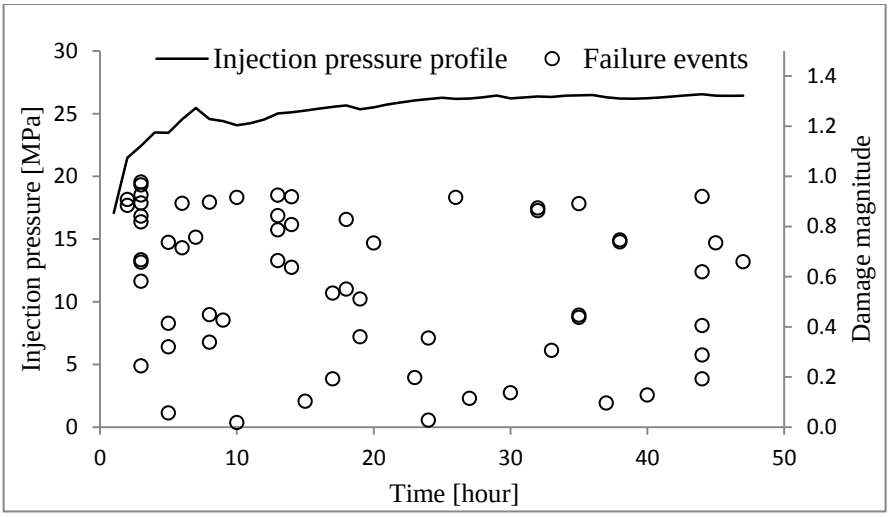

Figure 7.6 Profile of pressure at injection source and failure events for heterogeneous model.

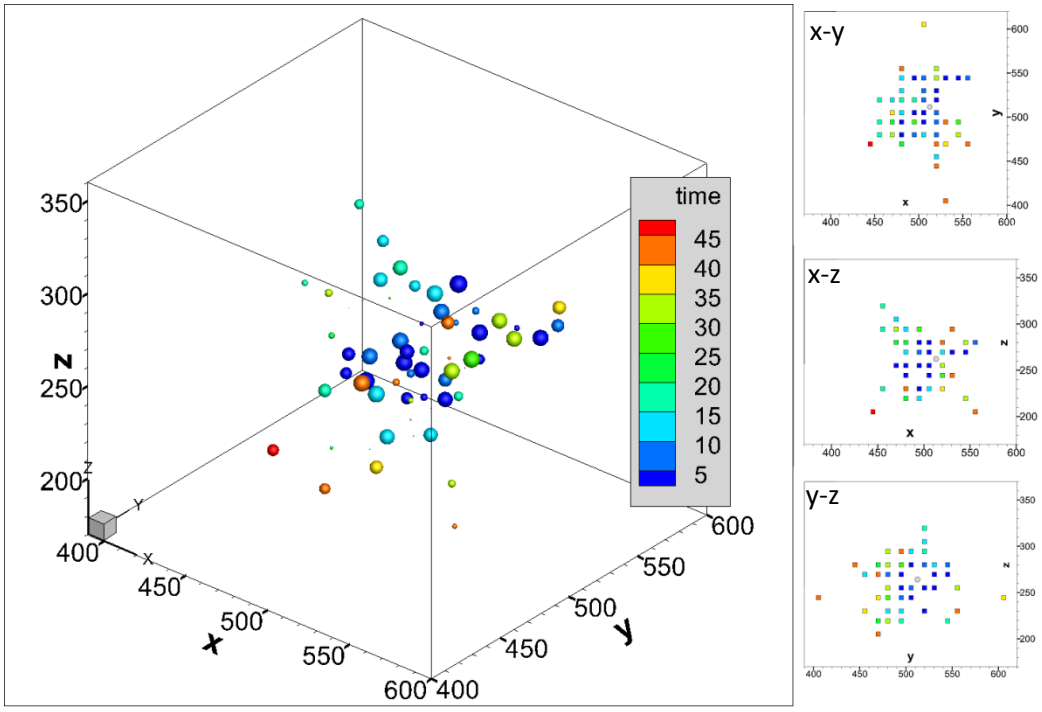

Figure 7.7 Distribution of failure events in space of heterogeneous model, and different direction of views of the distributions.

The preferred orientation of damage evolution and permeability development along the maximum horizontal stress can be observed in Figure 7.8-7.9. The tendency is more obvious for the homogeneous case. The gray circles in Figure 7.8-7.9 indicate the location of injection source. For homogeneous case, both permeability and damage develop symmetrically, which is not the case for the heterogeneous case, underscoring the importance of stress and rock heterogeneity in stimulation.

For the case a heterogeneous reservoir, the center of the contours or the highest values of permeability increment and damage variable are not located at or very near the injection point. This is because there is a weak zone around (x = 500 m, y = 500 m). The threshold tensile strain of this zone is 0.29×10^{-3}, while, the average threshold strain is 0.5×10^{-3}. Tensile failure at t = 2 hour in this weak zone (x = 505 m, y = 505 m) is observed as can be seen from the failure events plot (Figure 7.7). Another observation is that the damage is more spread from the injection source in the heterogeneous case, which causes a slightly larger permeability enhancement zone compared to the homogeneous case. However, the maximum permeability enhancement is slightly higher in homogeneous case.

Figure 7.10 plots failure events with permeability development. The rock failure increases the permeability directly by forming micro-fracture (Equation 7.14), and will change the stress-strain correlation of the rock which indirectly affects

the stress dependent permeability. Because the peak strength and Young's modulus of rock will decrease with damage, rock will subsequently experience larger strains at lower stresses. Large strain and further failure will lead to higher permeability enhancement. The location of failure is consistent with the stimulated zone distribution for both cases in Figure 7.10.

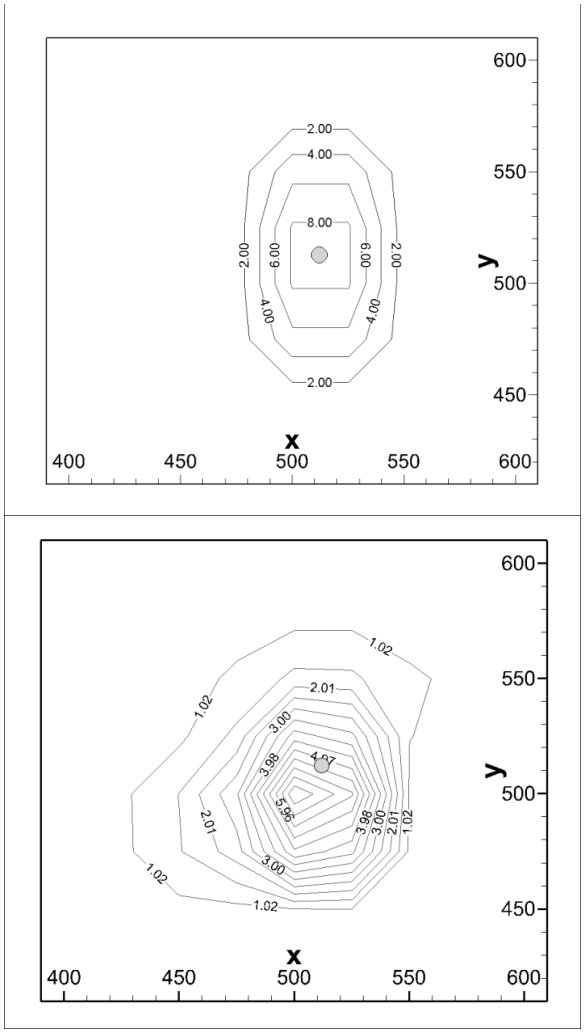

Figure 7.8 The distribution of stimulated permeability at t = 40 hour for homogeneous model (left) and heterogeneous model (right).

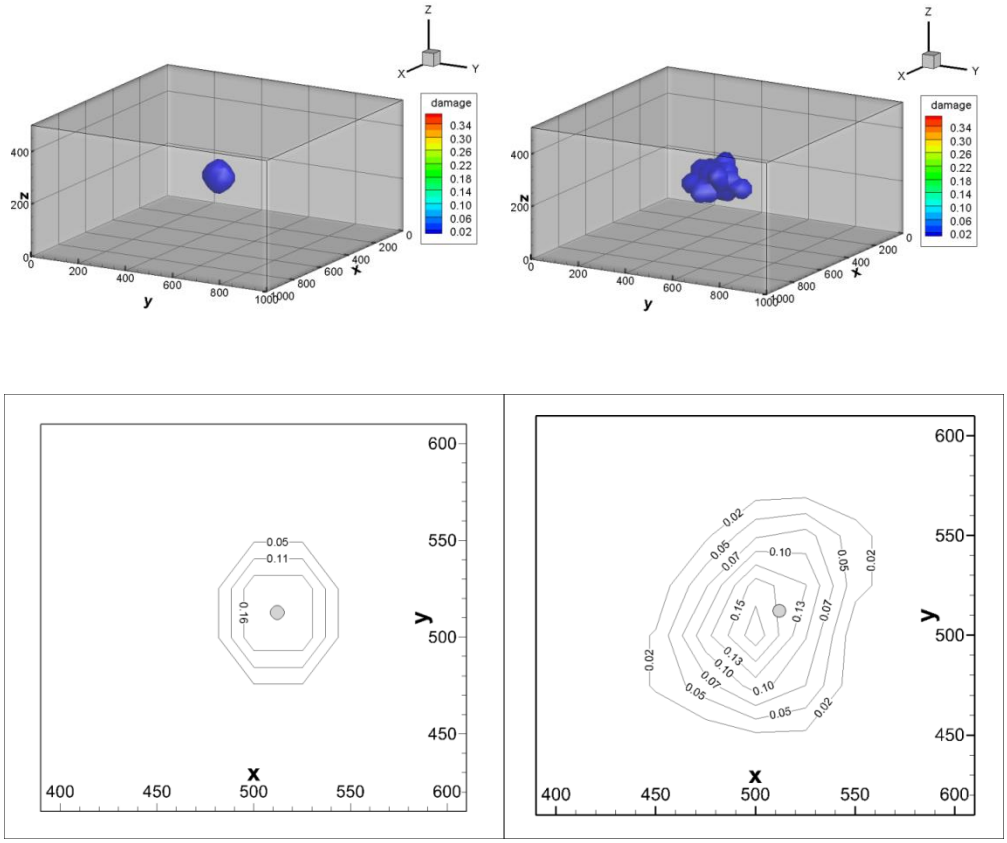

Figure 7.9 The distribution of damage variable at t = 48 hour for homogeneous model (left) and heterogeneous model (right). Slices are made at z = 250 m.

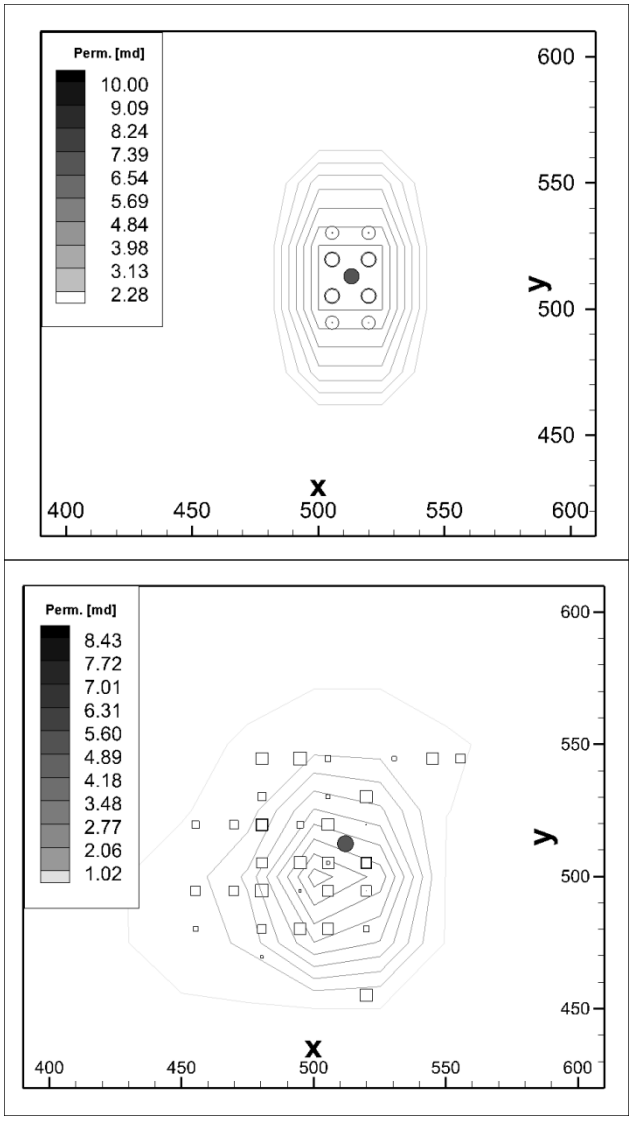

Figure 7.10 Stimulated permeability distribution and failure event locations at the end of injection for homogeneous model (left) and heterogeneous model (right). Slices are made at z = 250 m.

7.6. Rock response after shut-in and re-injection

Micro-seismic events have been observed after shut-in in some field injection tests (e.g., Schoenball and Kohl 2013). To simulate this phenomenon, the injection is stopped at t = 24 hour for both cases reservoir stimulation considered. The bottom-hole pressure and failure event profiles are shown in Figure 7.11 and 7.12. In these simulations, no failure events are observed during 24 – 48 hours after shut-in in either homogeneous or heterogeneous cases. For the homogeneous case, it is reasonable to not have failure events after shut-in. Because the diffused pore pressure cannot exceed the shut-in pressure that initiated failure events, unless the shut-in pressure is higher than the critical pore pressure due to high viscosity or existence of natural fractures which have lower shear strength. The maximum pore pressure change during shut-in hour in diffusion area is less than 0.5 MPa (Figure 7.13). The maximum absolute pore pressure in the diffusion area after shut in is 14.33 MPa when t = 25 hour at 50 m from the injection source (Figure 7.13). Accordingly, the failure function (f_{mc}, Equation 7.6) at 50 m attains the highest values (nearest value to the failure envelop) at t = 25 hour (Figure 7.14). The value of f_{mc} is -1.05 with an incremental of 0.2 after shut-in. The f_{mc} has increased from initial value of -3.08 to -1.25 during 24 hour of injection with ≈ 5 MPa of pore pressure increment. By comparison of these quantities, the diffused pore pressure increment is far from sufficient to initiate an event.

The post shut-in failure and seismicity that has been observed in the field could be attributed to slip on joints and faults. In numerical simulations, post shut-in failure could happen in a heterogeneous rock when a weak zone is present along the pore pressure diffusion path. The strength of the weak zone should be high enough so as to not fail before shut-in, but should be low enough to fail by a small pore pressure increase after shut-in (i.e., it should be critically-stressed). Another possible cause of post shut-in events can be the induced poroelastic stress in small distance ahead the pressure front immediately after shut-in. Also, in current simulations, failure will not happen in a previously pressurized zone, because after shut-in, the pore pressure in the pressurized zone will decrease and the Mohr-Column circle will move away from the failure envelope.

When injection re-starts at the same injection rate, new failure events occur several hours later when the induced pore pressure reaches the critical level (Figure 7.15). It is found that the new events (after re-injection) occur at the same locations as those when the injection is continuous, but at a later time than the non-stop injection case. For example, black circles in Figure 7.16B occur at times = 41, 44, 45, 46, and 48 hour for the two-stage injection test, while they occur at 20, 23, 24, 26, and 27 hours for the of non-stop 48 hour injection test (the two groups of events occur at the same locations). This is because the damage model and constitutive law used in this study are elastic (Chapter 3). The gray middle-size events in Figure 7.16A are events from a later time step

when t > 27 hour. We see no failure after shut–in and re-injection (at the same rate).

The damage evolution history depends on the induced pore pressure. It is observed that the damage zone of the two-stage test at 48 hour has the same shape as the damage zone of non-stop test at 27 hour, as shown in Figure 7.17. It is reasonable to predict the future events in the two-stage test will tend to occur at locations indicated by gray middle-size events in Figure 7.16A.

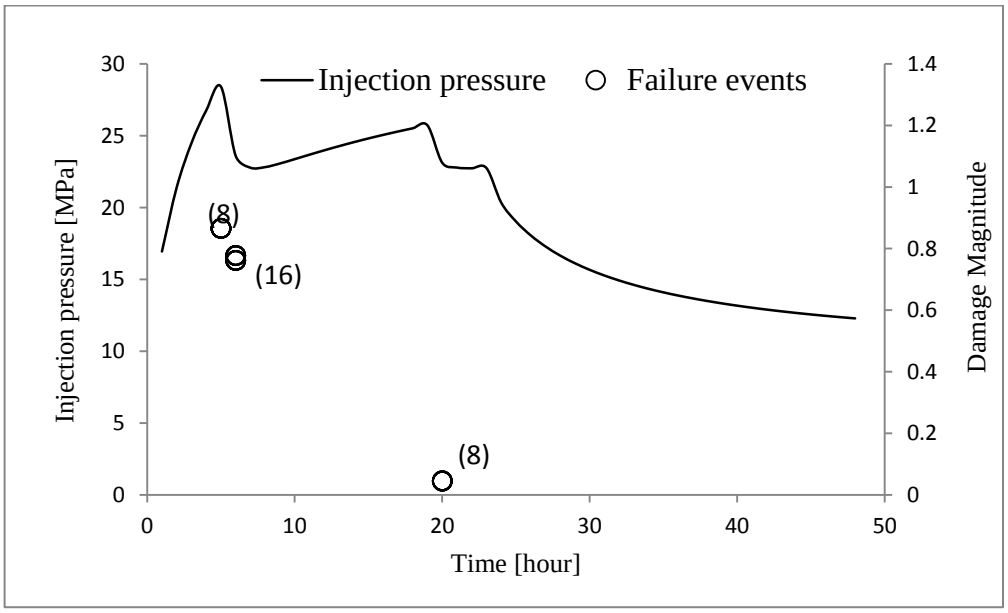

Figure 7.11 Profile of pressure at injection source and failure events for homogeneous model. The injection is shut down at t = 24 hour.

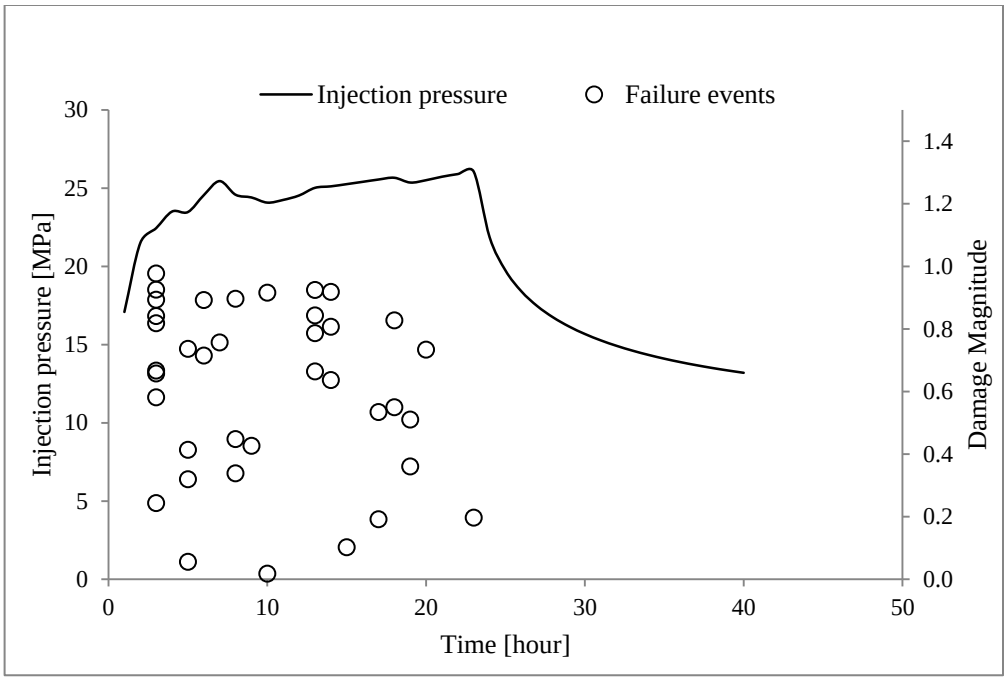

Figure 7.12 Profile of pressure at injection source and failure events for heterogeneous model. The injection is shut down at t = 24 hour.

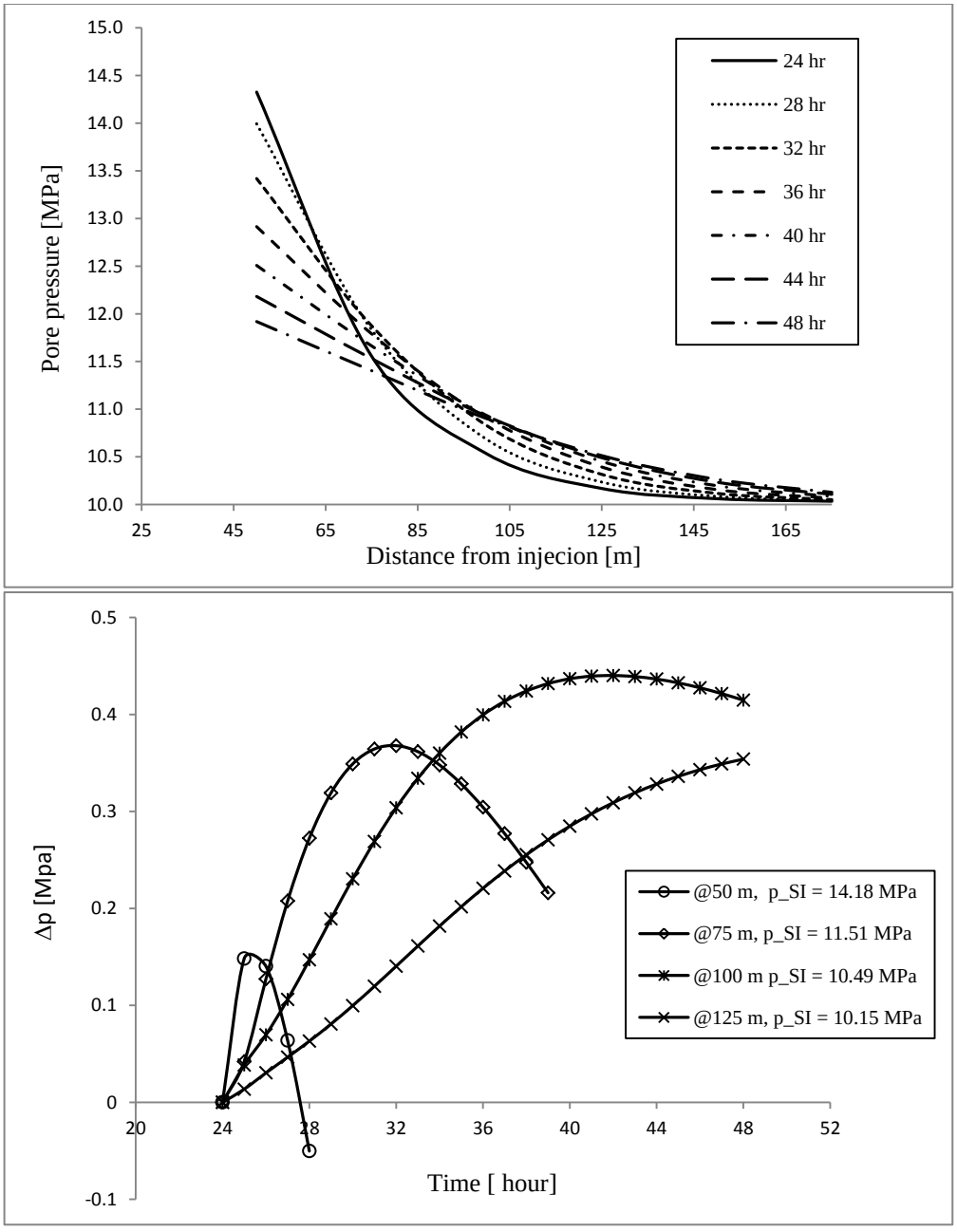

Figure 7.13 Pore pressure diffusion after shut in for homogeneous model.

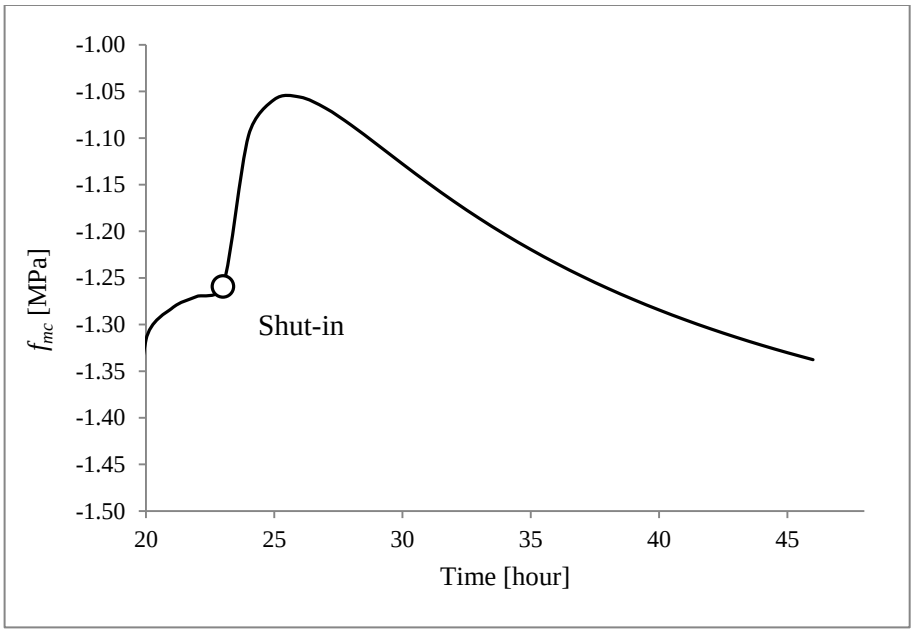

Figure 7.14 Variation of Mohr-Column function value f_{mc} at 50 m from injection source. Initial value of f_{mc} is -3.08 MPa under in-situ stress.

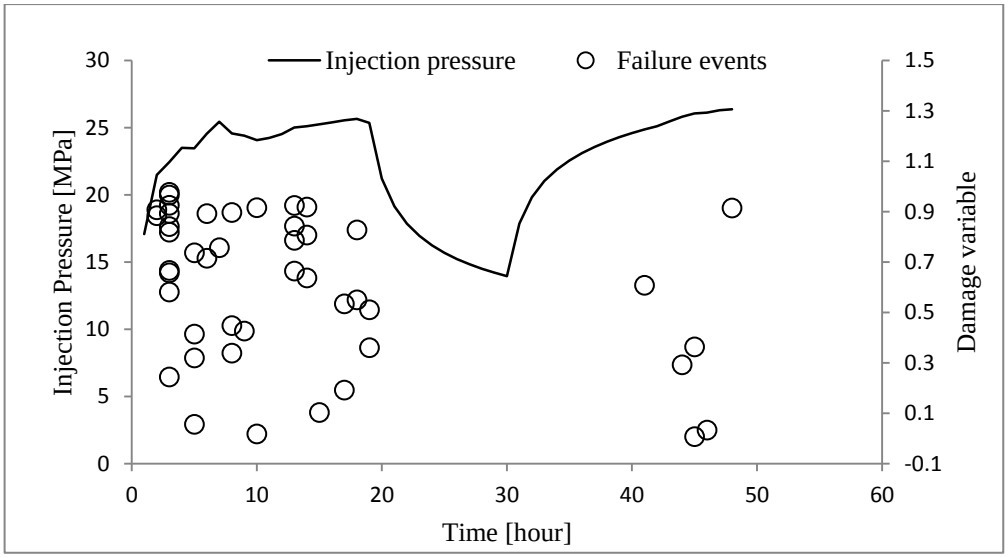

Figure 7.15 Profile of pressure at injection source and failure events for heterogeneous model. The injection is stopped at t = 20 hour, and re-inject starts at t = 30 hour

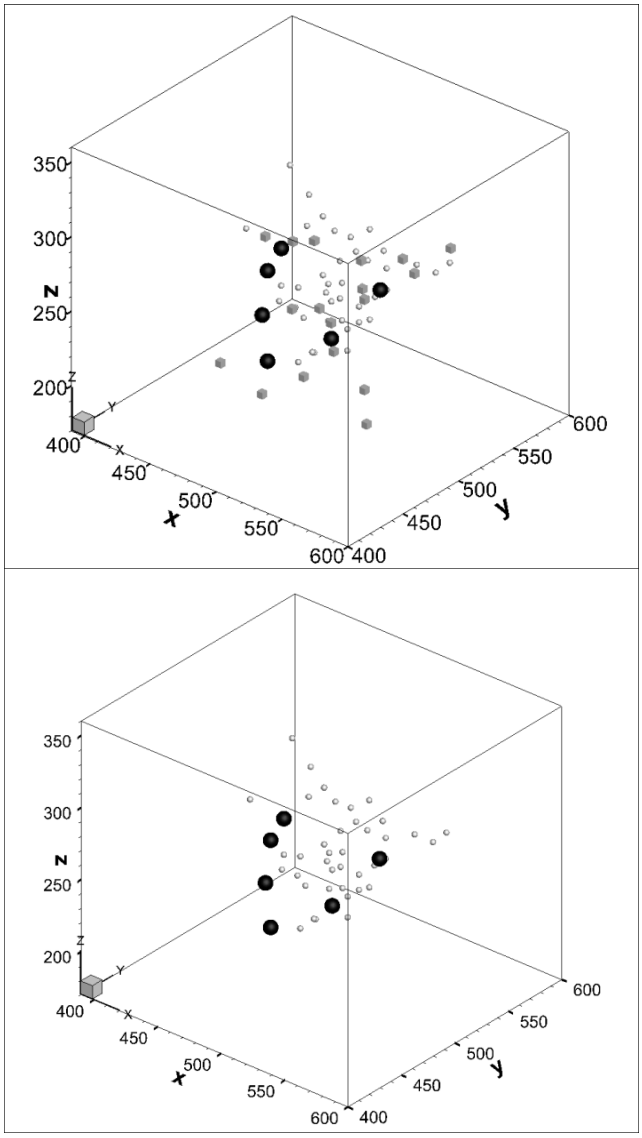

Figure 7.16 Comparison between failure events distribution of 48 hour non-stop injection (left) and of two-stage injection (shut-in at 20 hour and re-injection at 30 hour) (right).

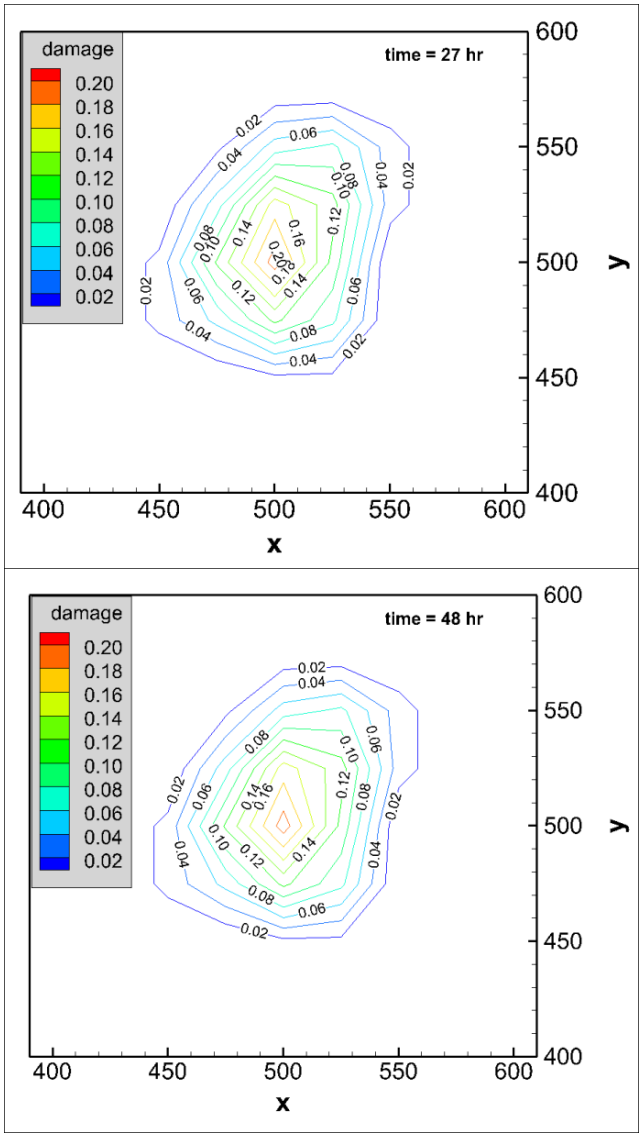

Figure 7.17 Comparison between damage distribution at 27 hour of 48 hour non-stop injection (left) and at 40 hour of two-stage injection (shut-in at 20 hour and re-injection at 30 hour) (right). Slices are made at z = 250 m.

7.7. Influence of different in-situ stresses

Damage zone development for three in-situ stress states has been simulated. The three in-situ stresses sets are: a normal faulting regime as used in previous simulations (σ_v = 50 MPa, σ_H = 45 MPa, σ_h = 15 MPa); a normal faulting regime with higher stress values (σ_v = 65 MPa, σ_H = 50 MPa, and σ_h = 35 MPa); and a strike-slip regime (σ_v = 50 MPa, σ_H = 65 MPa, and σ_h = 35 MPa). For comparison, the middle horizontal slices of damage zones for low (set I) and high (set II) in-situ stress magnitudes are plotted in Figure 7.18. It can be seen that the damage level is higher and damage zone is larger for the high magnitude normal regime in-situ stresses. However, similar pattern of damage evolution can be observed in both cases. When comparing failure zones of normal faulting regime (set II) and strike-slip faulting regime (set III), the difference of damage evolution pattern is found to be more significant (Figure 7.19). These results shows that given the same heterogeneous distribution and injection rate, the shape of the damage zone is mainly controlled by in-situ stress orientation, and the size of the damage zone is mainly controlled by the magnitude of in-situ stresses. A comparison of permeability enhancement between two different in-situ stresses regimes (set II and set III) is shown in Figure 7.20. The enhanced permeability zone has the similar shape as damage zone.

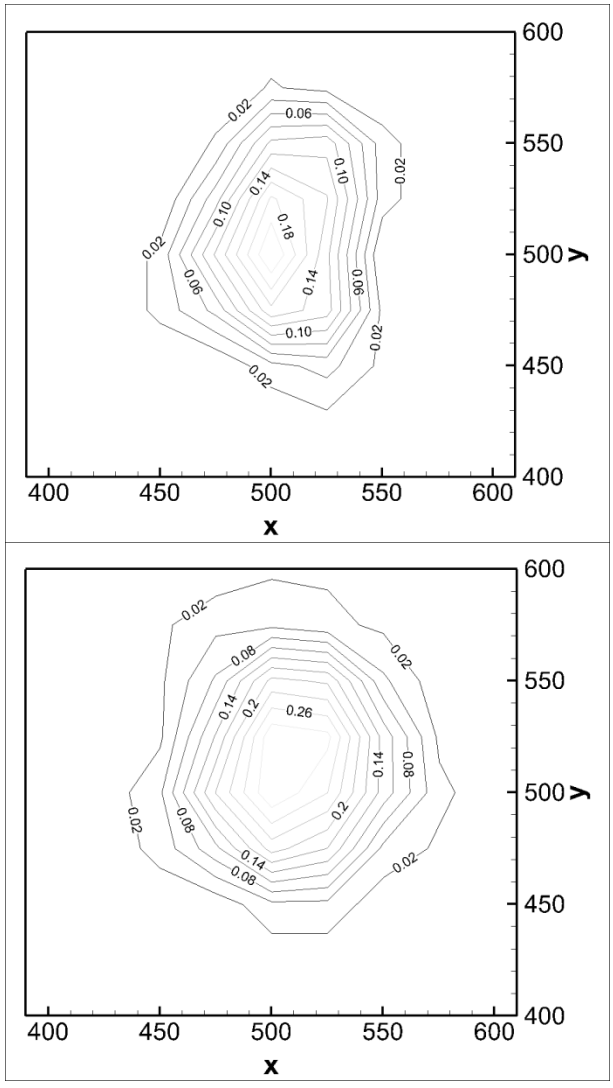
600
550
500
450
400
y
400
450
500
550
600
x
0.02
0.06
0.10
0.14
0.18
0.02
0.10
0.14
0.06
0.02
0.06
0.10
0.02
0.02
0.08
0.14
0.2
0.26
0.14
0.08
0.02
0.02
0.08
0.14
0.2
0.08
0.02

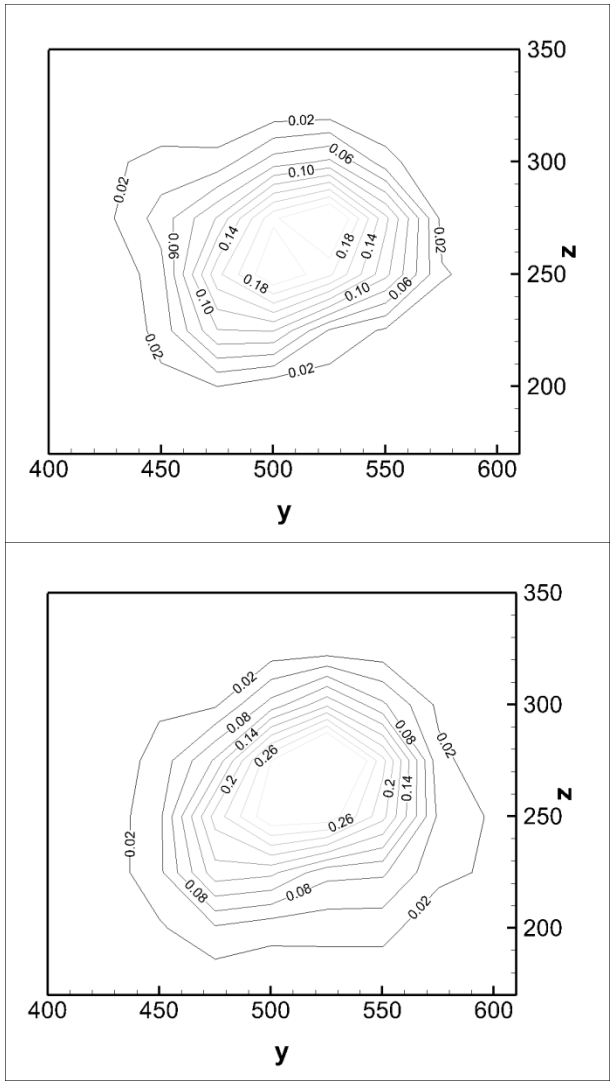
350
300
250
200
z
400
450
500
550
600
y
0.02
0.06
0.10
0.14
0.18
0.26
0.2
0.08

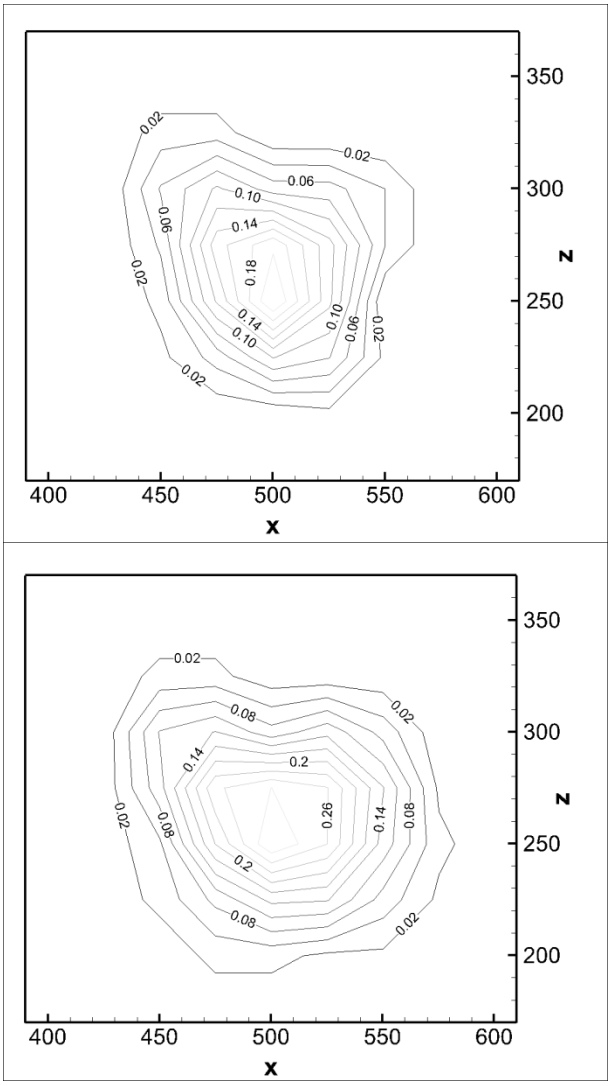

Figure 7.18 Comparison between damage distributions of different in-situ stresses (σ_x = 15 (σ_h), σ_y = 45 (σ_H), σ_z = 50 MPa (σ_V)) (left) and (σ_x = 35 (σ_h), σ_y = 50 (σ_H), and σ_z = 65 MPa (σ_V)) (right). Slices are made at z = 250 m.

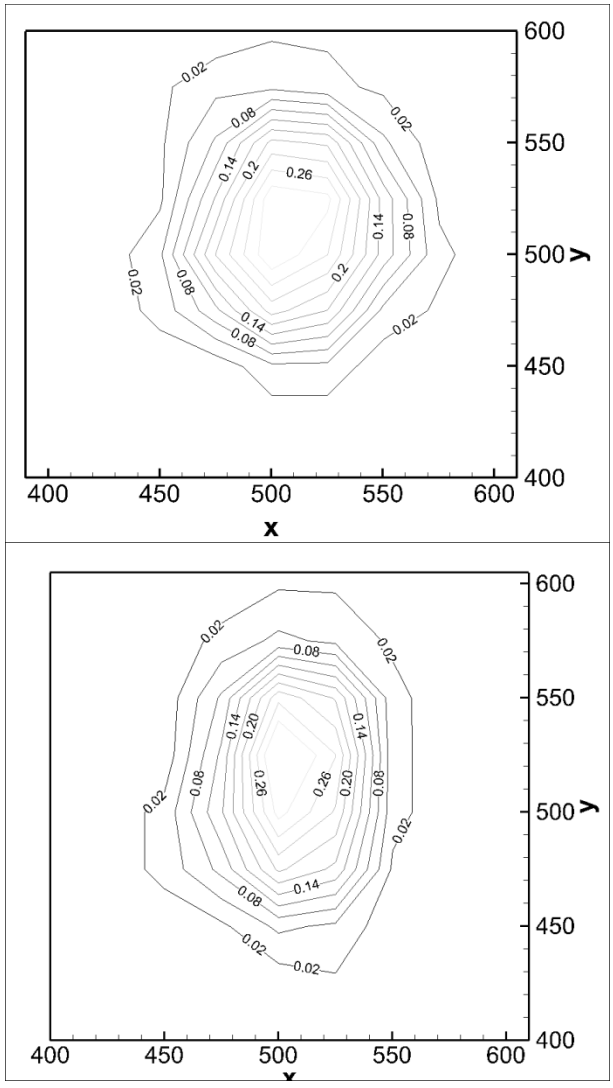
600
550
500
450
400
y
400
450
500
550
600
x
0.02
0.08
0.14
0.2
0.26
0.14
0.08
0.02
0.02
0.08
0.14
0.08
0.2
0.02
600
550
500
450
400
y
0.02
0.08
0.02
0.14
0.20
0.14
0.26
0.20
0.08
0.02
0.02
0.08
0.14
0.08
0.02
0.02

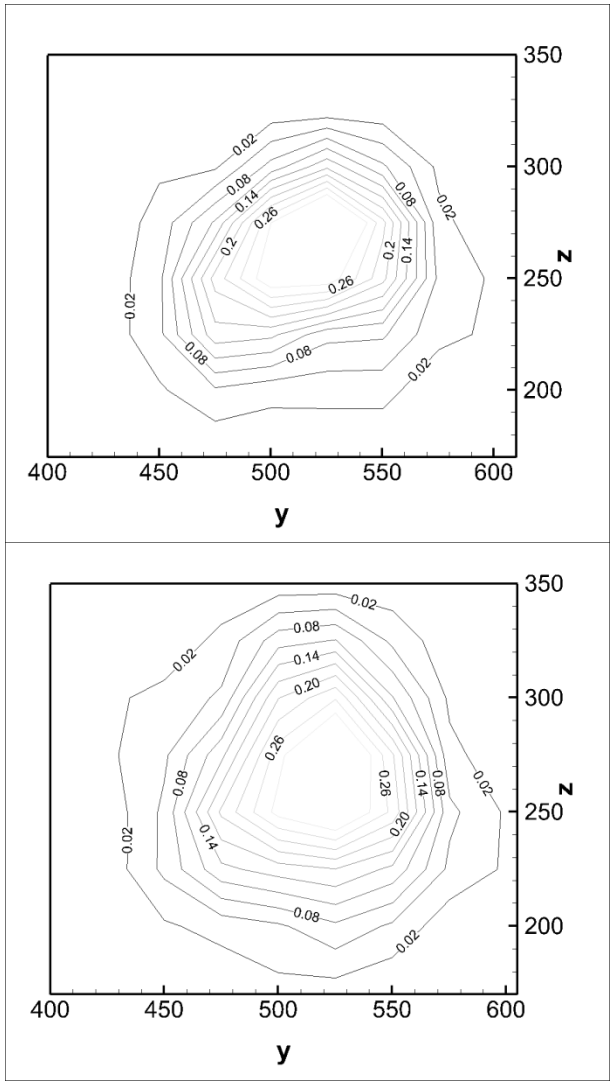
350
300
250
200
z
400
450
500
550
600
y
0.02
0.08
0.14
0.2
0.26
0.20

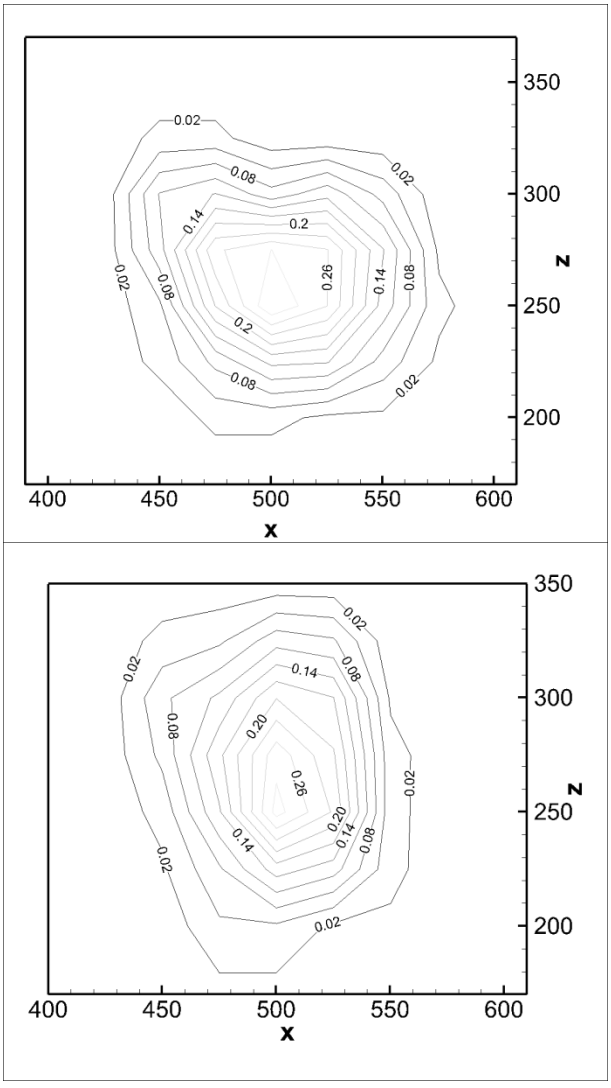

Figure 7.19 Comparison between damage distributions of different in-situ stresses (σ_x = 35 (σ_h), σ_y = 50 (σ_H), σ_z = 65 MPa (σ_V)) (left) and (σ_x = 35 (σ_h), σ_y = 65 (σ_H), and σ_z = 50 MPa (σ_V)) (right). Slices are made at z = 250 m.

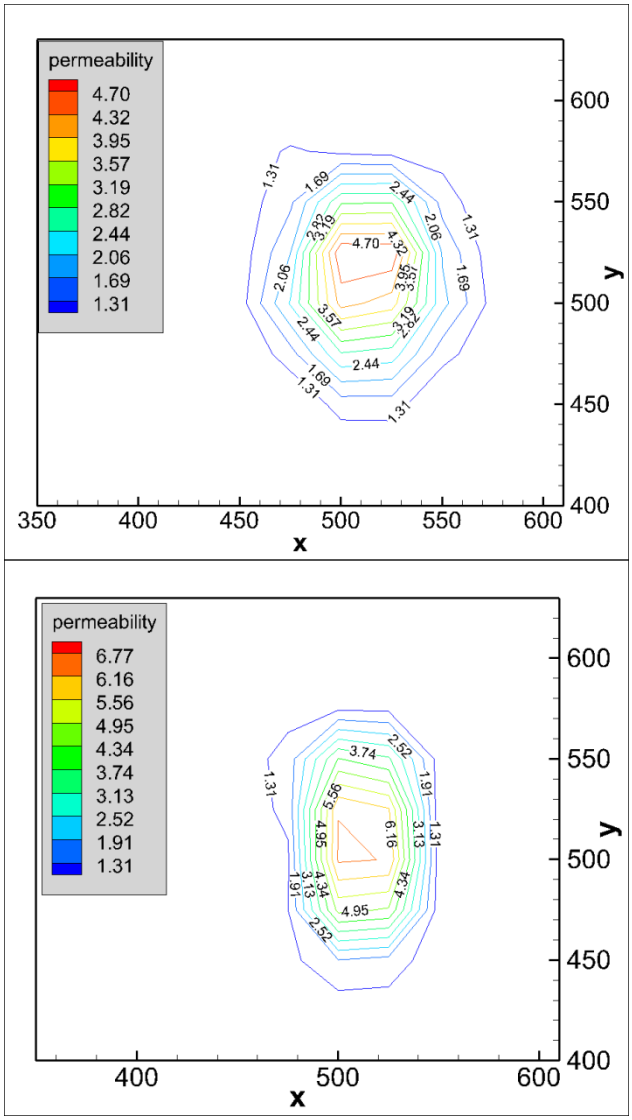

Figure 7.20 Comparison between permeability distributions of different in-situ stresses (σ_x = 35 (σ_h), σ_y = 50 (σ_H), σ_z = 65 (σ_V) MPa) (left) and (σ_x = 35 (σ_h), σ_y = 65 (σ_H), and σ_z = 50 (σ_V) MPa) (right). Slices are made at z = 250 m.

7.8. Thermal effect in point injection case

The temperature results for the current case show that the temperature changes will not develop at long distances within the simulation time period (Figure 7.21). Note that flow and transport is based in equivalent permeability and fracture flow and transport is not exclusively considered. For rock mass has a thermal diffusivity of 1.6×10^{-6} m^2/s, the characteristic time of 10 meter diffusion distance is 2 years. Although, heat convection within the rock matrix is considered in this work, the heat transfer within injection period is not very large.

7.9. Case summary

A finite element model has been developed to implement the fully coupled thermal-poroelastic response of homogeneous and heterogeneous rock to injection. In this model, the nodal displacement, pore pressure and temperature are taken as primary variables. The stress and strain fields are calculated after finite element analysis, and damage evolution is evaluated using the stress and strain results. In the finite element analysis, stiffness matrix is stress dependent and subject to change with time. The resulting damage zone and enhanced permeability of different stimulation cases are compared to study the influence of in-situ stresses, heterogeneity, and injection plan on stimulation result.

The numerical results show that rock transport and mechanical heterogeneity has significant influence on the location and initiation of failure events. The

distribution of failure events in heterogeneous reservoir is scattered and depends on the local heterogeneity distribution, other than symmetrically distributing around the injection source for homogeneous reservoir. For the injection plan and heterogeneity distribution used in this study, no failure event has been observed after shut-in. It is found that after re-injection the failure event profile follows the history of non-stop injection when the pore pressure restored up to critical value. The stimulation result is also influenced by in-situ stresses. It is found that the in-situ stress orientation has major control on the shape of stimulated zone, and the magnitude of in-situ stresses has influence on stimulated volume. Higher in-situ stresses tend to result into high level damage. The stimulated zone is smaller and the average damage level is lower under low in-situ stresses. Heat conduction and convection are considered in this work. However, the thermal effect is not obvious for this tight reservoir during the computation time period (48 hour).

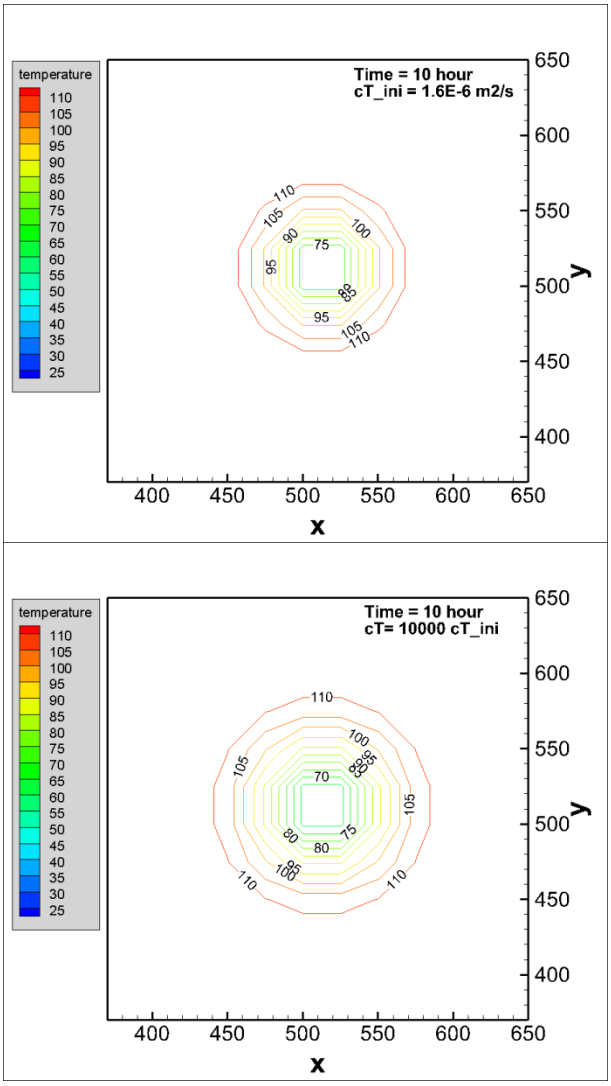

Figure 7.21 Comparison between temperature distributions of rocks with different thermal conductivities. Slices are made at z = 250 m.

8

THREE-DIMENSIONAL FULLY COUPLED FEM ANALYSIS OF GEOTHERMAL RESERVOIRS WITH STOCHASTIC FRACTURE NETWORKS

Simulation of the response of an engineered geothermal system (EGS) requires analyzing the THM response of the reservoir rock, which are generally fractured and to some extent have heterogeneous properties. The THM response of the reservoir rock includes the opening, slip, and possibly propagation of natural fractures, and the failure process of intact rock. To assess the mechanical (deformation) and hydraulic (permeability enhancement) response of fractured rock during stimulation, three sub-models are required: a fracture network model, a rock heterogeneity model, and a coupled THM model. The rock heterogeneity model and the FEM THM model have been explained in detail previously (Chapter 5 and Chapter 6). This chapter will focus on the fracture network model and its implementation in the current FEM model.

As discussed in Chapter 2, there are generally two classes of fracture models, stochastic fracture models and deterministic models. There are also works that

utilize combined deterministic and stochastic fracture networks. In most reservoir stimulation and fracture modeling, the thermo-poroelastic coupling process has been either neglected or simplified to empirical correlations (Cladouhos et al. 2001; Willis-Richards et al. 1996; Bruel, 2002). Three-dimensional THM models have been developed and applied to reservoir stimulation, development, and well bore stability analyses (Zhou and Ghassemi 2009; Lee and Ghassemi 2011). However, the reservoir rock was modeled as continuous porous media with possibly a few major fractures.

In this work, a fracture network is introduced into a coupled poroelastic model with heat transport. Poroelastic stresses in the rock matrix are computed at each time step, and are interpolated onto the natural fracture faces when calculation the fracture apertures change. The overall permeability of fractured rock is estimated using the equivalent permeability (Tezuka and Watanabe 2000). An iterative method is employed to retrieve the stress-dependent permeability at each time step. Considering the problem complexity and the computational cost, the rock strain and fracture geometry changes are considered independent from the thermal response. The heat transport in the reservoir is assumed to occur via fluid flow within the fractures, and the heat conduction from the rock matrix to the fracture fluid. Compared to heat convection via fracture flow, heat convection within the rock matrix is insignificant in early stage of injection and

is neglect in this work (Delaney 1982). The heat conduction from rock matrix to the fracture fluid is assumed to be linear and governed by 1-D diffusive equation.

8.1. Fracture deformation and induced permeability enhancement

Fracture dilates during shear slippage. As the shear stress acting on fracture surface exceeds fracture shear strength, shear failure occurs and induces rock deformation of the surface of rupture. This permanent displacement is referred as shear displacement which has significant influence on permeability improvement of natural fractures. Shear slippage criterion can be derived from the theory of shear failure using the linear Mohr-Coulomb criterion. Using Patton's method (Patton 1966), the shear strength of the fracture can be calculated as:

$$\tau_p = \sigma' \tan\left(\varphi_{basic} + \varphi_{dil}^{eff}\right) \tag{8.1}$$

where σ' is the effective normal stress acting on fracture surface. φ_{basic} is the basic friction angle which is a material property of the fracture surface, usually varies between 30˚ and 40˚ (Barton and Choubey 1977). φ_{dil}^{eff} is the effective shear dilation angle which is related to the roughness of fractures, can be calculate from laboratory-measured dilation angle, φ_{dil} as:

$$\varphi_{dil}^{eff} = \frac{\varphi_{dil}}{1+9\sigma'/\sigma_{nref}} \tag{8.2}$$

σ_{nref} is the effective normal stress which causes 90% closure of the compliant aperture. When the shear stress on fracture surface exceeds the shear strength, shear slippage occurs. And the resulted shear displacement can be estimated by:

$$U_s = \frac{\tau_n - \tau_p}{K_s} \tag{8.3}$$

τ_n is the shear stress applied on fracture surface. τ_p is the shear strength described above. K_s is the fracture shear stiffness, can be expressed as:

$$K_s = \gamma \frac{G}{r} \tag{8.4}$$

γ is a geometric parameter that can be treat as an measure of the ability of the matrix to accommodate the deformation, which is used as $\frac{7\pi}{24}$ in this model (Eshelby 1957). r is the penny shape fracture radius. G is the surrounding material shear modulus.

The change in aperture (dilation) due to excess shear stress can be calculated from shear displacement, as (Willis-Richards et al. 1996):

$$a_s = U_s \tan(\varphi_{dil}^{eff}) \tag{8.5}$$

When the fracture surfaces are in contact, the "in contact" fracture aperture is given by:

$$a = \frac{a_0}{1 + 9\sigma'/\sigma_{nref}} + a_s + a_{res} \tag{8.6}$$

where a_{res} represents the residual aperture at high effective stress, taken to be zero in this model. a_0 is the initial total compliant aperture of the fracture. And a_s is the aperture change due to shear slippage, as discussed above.

For fully open fractures, the opening aperture is the normal displacement (of one face) multiplied by 2. For a circular shape fracture of radius *R* under normal stress σ_n, the normal displacement of any point of the crack surface is given by (Jaeger and Cook 1969):

$$u(r) = \frac{2(1-\upsilon)}{\pi G}\sqrt{R^2 - r^2} \tag{8.7}$$

Resulting in the maximum width at the center

$$a = \frac{4(1-\upsilon)R}{\pi G} \tag{8.8}$$

The volume of the penny shaped crack is obtained from:

$$V = \int_0^R 2\pi r\left(\frac{4(1-\upsilon)R}{\pi G}\right)dr = \frac{8(1-\upsilon)R^3\sigma_n}{3G} \tag{8.9}$$

Indicating an average aperture of:

$$\bar{a} = V/\pi R^2 = \frac{8(1-\upsilon)R\sigma_n}{3\pi G} \tag{8.10}$$

The new aperture due to updated stress distribution will be input for the equivalent permeability calculation of next time step as described previously.

To estimate the scale of the micro-earthquake (MEQ) caused by fracture slip, the methodology of McGarr et al. 1979 and Hanks and Kanamori 1979 is used to calculate the magnitude of radiated elastic energy. The seismic moment due to slip "U_s" over the slip area, can be obtained from

$$M_0 = \int_{\Sigma} G U_s dA \tag{8.11}$$

G is the shear modulus of the rock. The magnitude of a micro-earthquake generated by the slippage can then be estimated as:

$$M = (\frac{2}{3}) \log_{10} M_0 - 10.7 \tag{8.12}$$

8.2. Analysis of near wellbore reservoir response

This simulation focuses on utilizing a stochastic fracture network and poroelasticity to simulate the thermal-hydro-mechanical response of a near wellbore fractured zone during the fluid injection process, and to assess the permeability enhancement in the stimulated zone. In order to investigate the near wellbore reaction to injection, a small scale reservoir model of size 40 m $\times$ 40 m $\times$ 20 m is considered. The fractured geothermal reservoir is modeled using a system of rock blocks some of which contain stochastically-distributed fractures and fractured zones. The effect of the fractures on permeability is introduced into the model by using the equivalent permeability approach (Chapter 2). The

rock matrix is assumed to be poroelastic and the fractures are allowed to deform and to slip. Heat transport within the fractured rock and the associated thermal stress on the rock is also considered (fully-coupled analysis, Chapter 5). A series of simulations are carried out to analyze the rock mechanical response and permeability evolution for a Newberry-type reservoir. In fractured reservoirs, like Newberry tuff, the overall fluid flow pattern is dominated by flow within the interconnected natural fracture network, since the conductivity of fractures is much higher than intact rock. However, the heat energy is stored in the rock mass surrounding the fractures, and it takes time to heat-up the fracture fluid to a desirable temperature. Therefore, to engineer a geothermal system, one need to enhance the permeability/connectivity of the pre-existing natural fractures without creating massive hydraulic fractures.

8.2.1. Stochastic fracture network

A natural fracture network of 500 penny-shape cracks is introduced into the poroelastic model (Figure 8.1). The 3D hydraulically conductive fracture network is generated using stochastic descriptions of its characteristics (Chapter 2) namely, Poisson distribution for fracture location, log-normal distribution for fracture size, and Fisher von-Mises distribution for fracture orientation. The parameters of these distributions are usually found from field tests or experimental data. The fracture data can be complied to form a network by defining location, size, and orientation of the fractures. One of such stochastic

fracture network (Table 8.1) is shown in Figure 8.1. The parameters of the fracture distribution used herein are from fracture analysis of Newbery field (AltaRock 2011), and from empirical suggestions (Cacas et al. 1990). Fracture apertures are assigned following the relationship with the fracture size (Tezuka 2005):

$$a = \alpha\sqrt{r} \tag{8.13}$$

where a is the initial aperture. α can be estimated from average virgin permeability (Willis-Richards 1996), which is evaluated to be 0.004 in this study. α is a field dependent factor and requires careful evaluation. The power n is decided to be ½ in this study, adopted from Tezuka and Watanabe (2000).

Table 8.1 Parameters of the probability functions of stochastic fractures in Figure 8.1

Density [m^{-1}]	1.0
Mean of the log(radius) [radius in meters]	0
Standard deviation of the log(radius) [radius in meters]	0.7
Fisher von Mises distribution parameter	2.8
α	4.0 X10^{-3}
Number of fractures	500

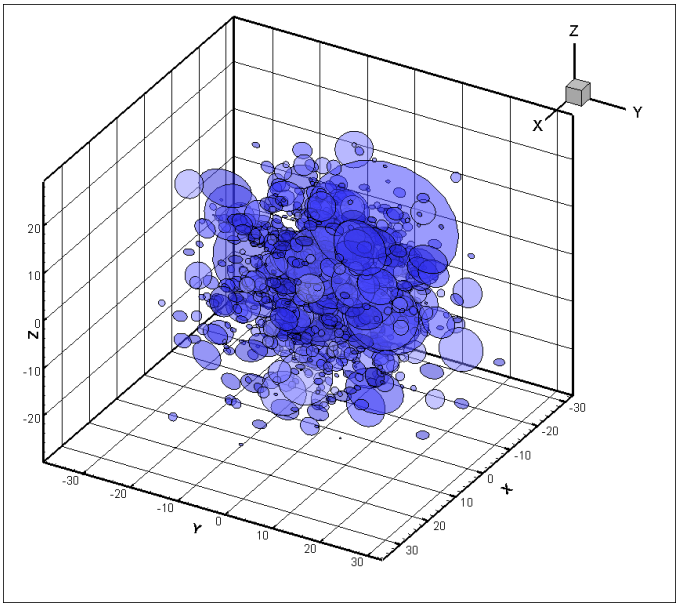

Figure 8.1 A stochastic fracture network.

8.2.2. Model set-up

Figure 8.2 shows the simulation domain with selected finite element mesh, and Figure 8.3 shows the fractured zone that contains 500 stochastic fractures (half domain). Rock properties are from experiment conducted on Newbery tuff core plugs (Li et al. 2012). A constant wellbore pressure boundary condition is applied to this model. The outer boundary of the reservoir block is assumed to be a no flow boundary.

Table 8.2 Parameters used in near wellbore simulation.

Rock properties		**Fracture properties**	
Model size (m^3)	40 x 40 x 20	Fracture density(m^{-1})	1
Young's modulus(GPa)	27.24	Fisher parameter, κ	2.8
Poisson's ratio	0.4	Mean fracture radial (lognormal)	0
Skempton's coefficient	1	Standard deviation of fracture radial, *s*	0.7
Matrix permeability (md)	5		
Porosity	0.025	Fracture basic friction angle (˚)	50.2
Fluid density (kg/m^3)	1000	**Stress State**	
Fluid bulk modulus (MPa)	3291	Vertical stress (MPa)	67
Fluid viscosity (Pa s)	1.0×10^{-4}	Maximum horizontal stress (MPa)	62
Fluid viscosity (Pa s)	1.0×10^{-4}	Minimum horizontal stress (MPa)	41
Shear dilation angle (˚)	3.0	In-situ pore pressure (MPa)	25
90% closure stress (MPa)	100	Injection pressure (MPa)	5

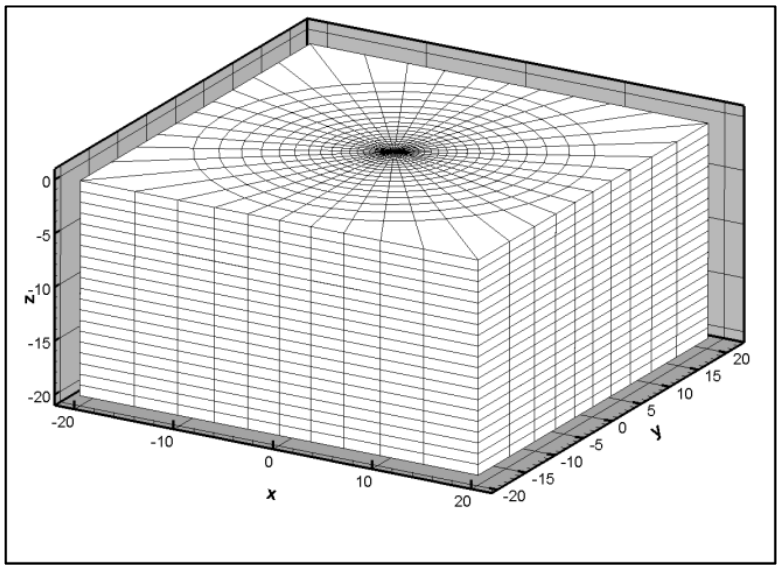

Figure 8.2 Finite Element mesh of a small scale reservoir model.

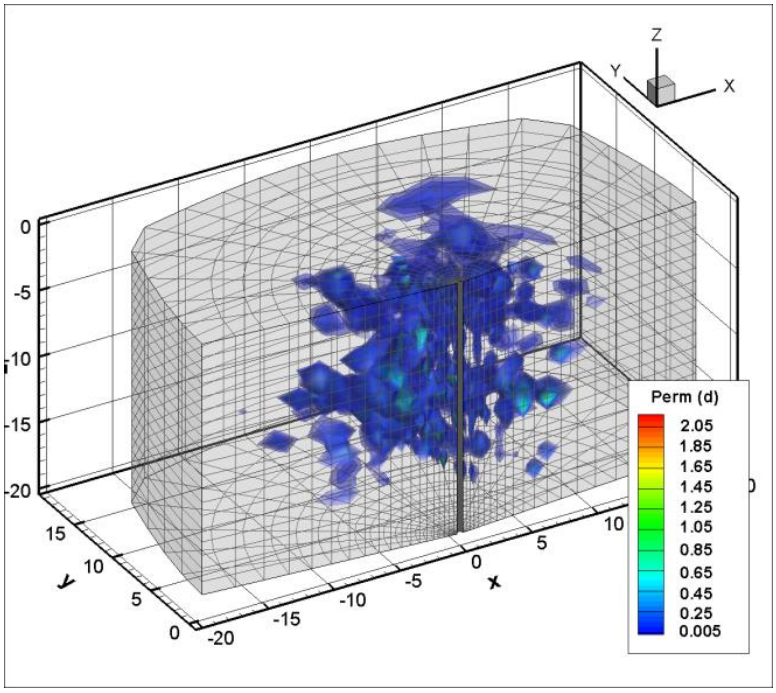

Figure 8.3 Fractured zones shown in half domain. Color bar shows the equivalent permeability of the fractured zone in Darcy units.

8.2.3. Simulations and results

Pore pressure development after 2 hours of injection, and the corresponding micro-seismic events are plotted in Figures 8.4 and 8.5, respectively. Figure 8.4 shows the pore pressure distribution of three fracture networks with different stochastic parameters. In these figures, κ is the fracture orientation parameter and s is the fracture size parameter (Table 8.2). We can see from both the pore pressure and the seismic clouds that the fracture properties dramatically influence the stimulation results. The seismic events of the fracture network with fisher von Mises orientation distribution are limited near the injection well. The

randomly distributed fracture network has a larger zone of micro-seismic events and higher pore pressure build up. The fracture size also has influence on the permeability improvement result (Figure 8.5B and C). The location of shear slippage is different from each case. This phenomenon indicates the important role of characterizing fracture properties for reservoir stimulation modeling and design.

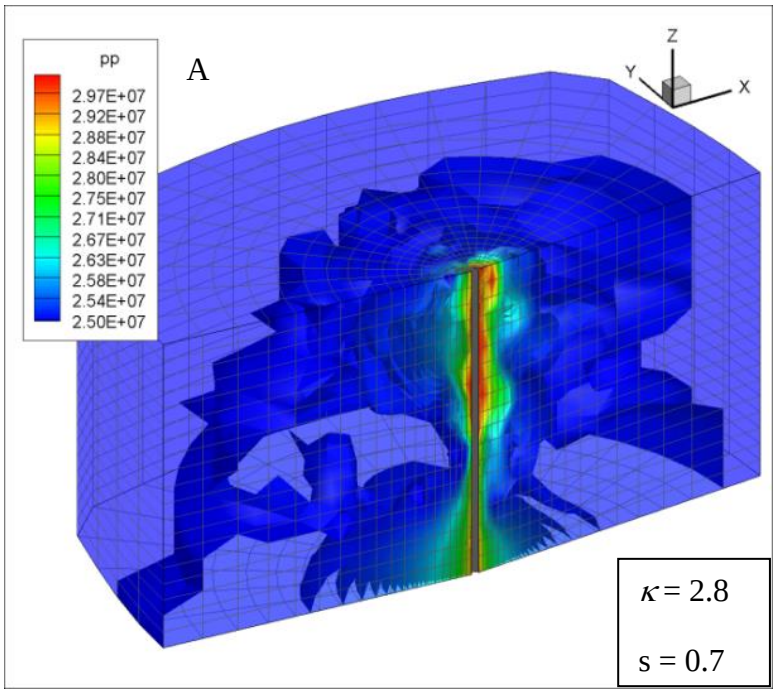

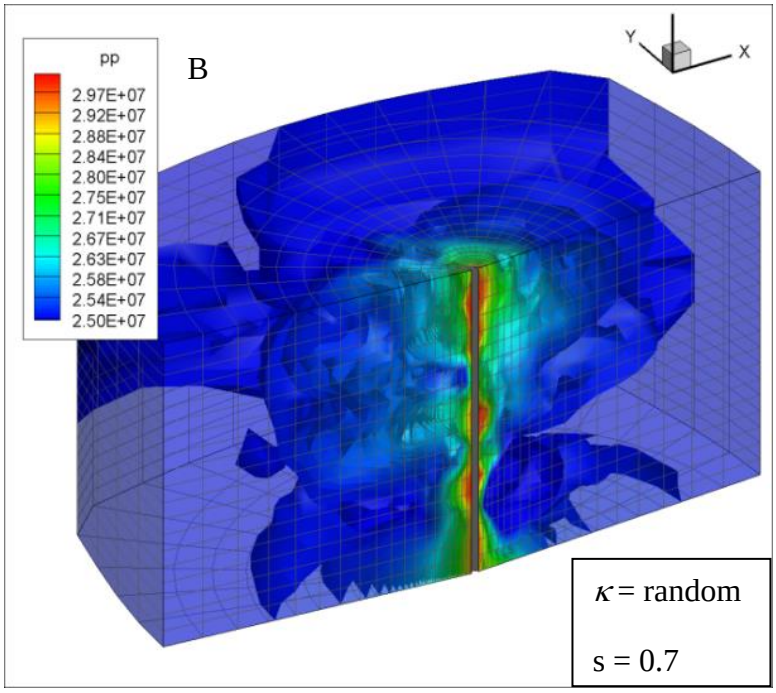

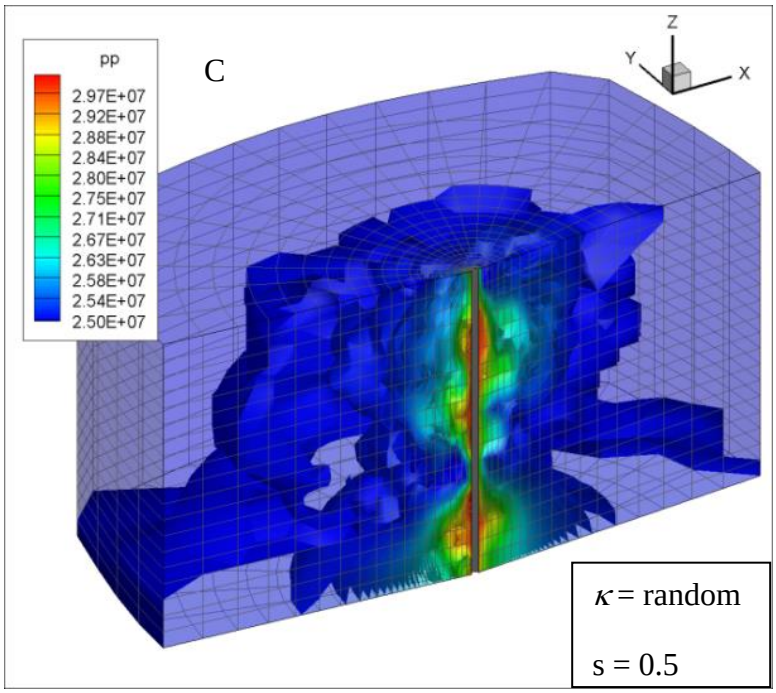

Figure 8.4 Pore pressure development at t = 2 hour in the fractured reservoir.

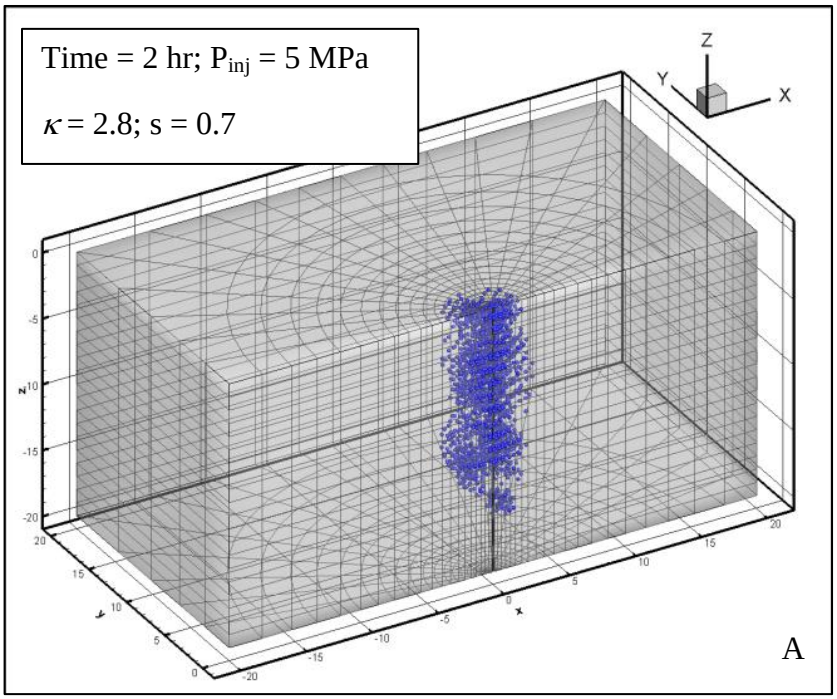
Time = 2 hr; P_{inj} = 5 MPa
κ = 2.8; s = 0.7
Z
Y
X
A

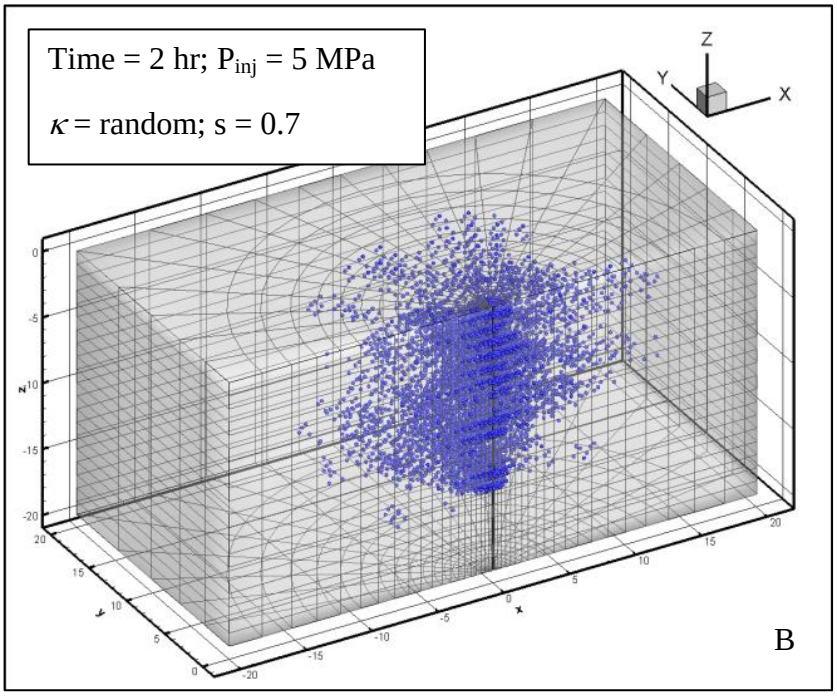
Time = 2 hr; P_{inj} = 5 MPa
κ = random; s = 0.7
Z
Y
X
B

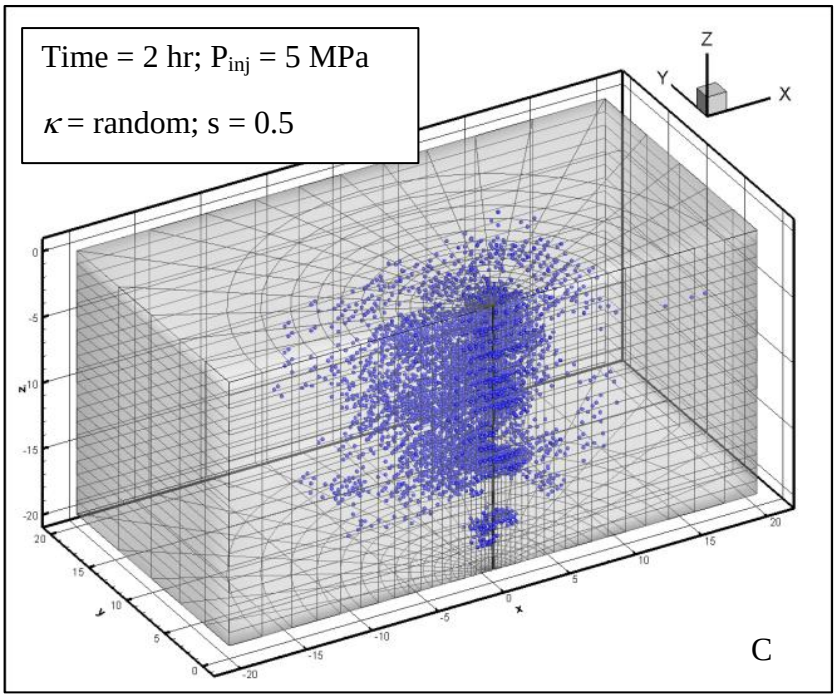

Figure 8.5 Micro-seismic events at t = 2 hour of three blocks with different fracture properties.

To illustrate the permeability improvement, Figure 8.6 shows the comparison of injection in two reservoirs having the same fracture networks, but with different rock type. One of them (group B) is assumed to consist of a rigid rock matrix which does not easily fail during the injection. The other one (group A) has the same rock type as used in previous simulation (Table 8.2) and is weaker. We can see that before shear dilation, the pore pressure distributions are the same in both reservoirs. After shear dilation, the pore pressure distribution in rock A is affected by the updated permeability, and higher pore pressure is shown in the upper zone (Figure 8.6 A2). We can see from Figure 8.6 A3 and B3, after 10

hours of injection, the pore pressure built-up in reservoir A has been delayed. Higher reservoir pressure is shown in Figure 8.6 B3. This observation resulted from the fracture opening and permeability increasing in reservoir A.

A1

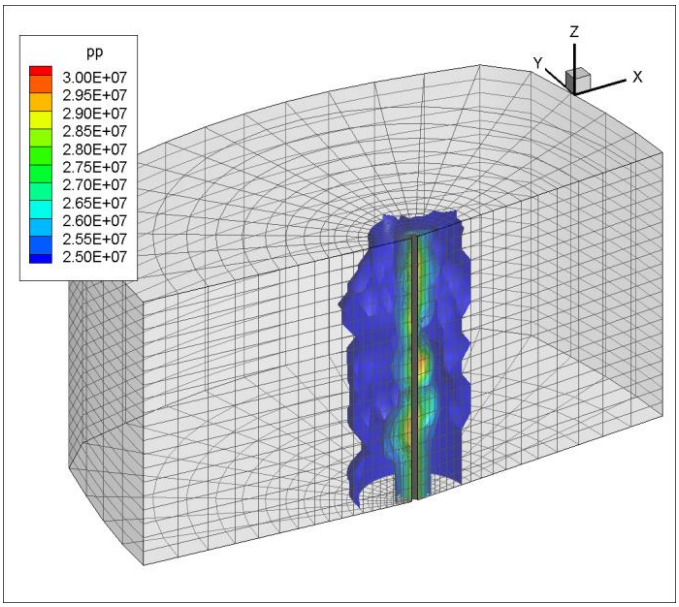

B1

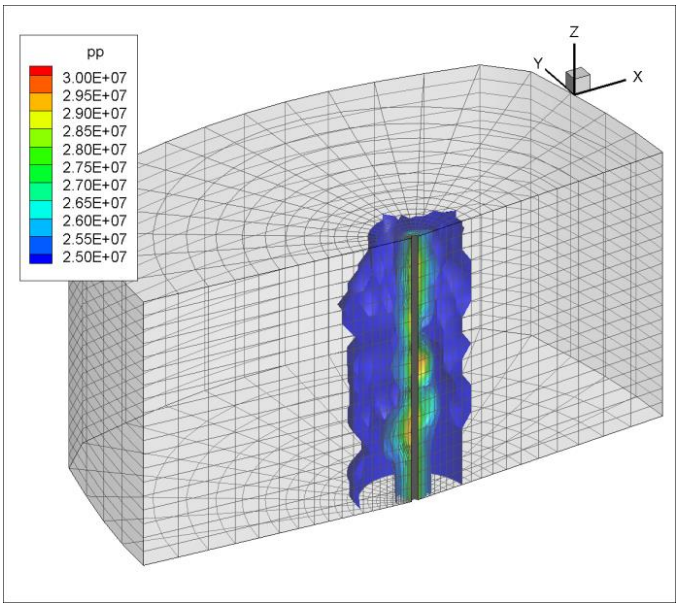

A2

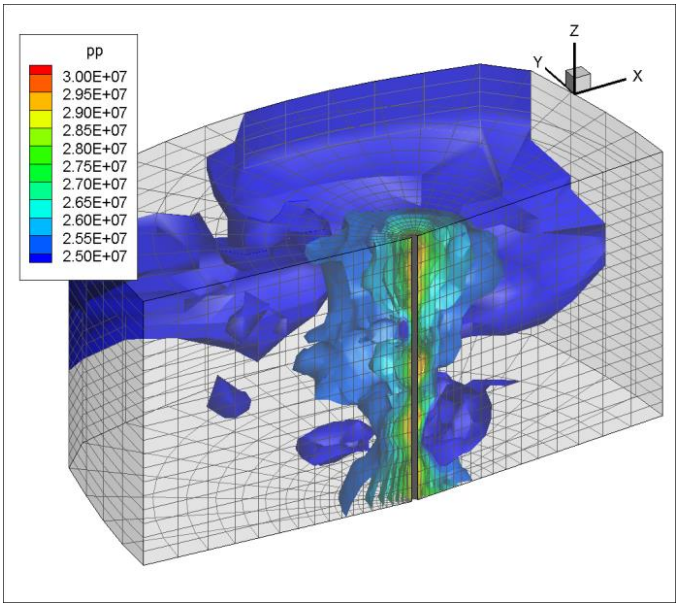
pp
3.00E+07
2.95E+07
2.90E+07
2.85E+07
2.80E+07
2.75E+07
2.70E+07
2.65E+07
2.60E+07
2.55E+07
2.50E+07
Z
Y
X

B2

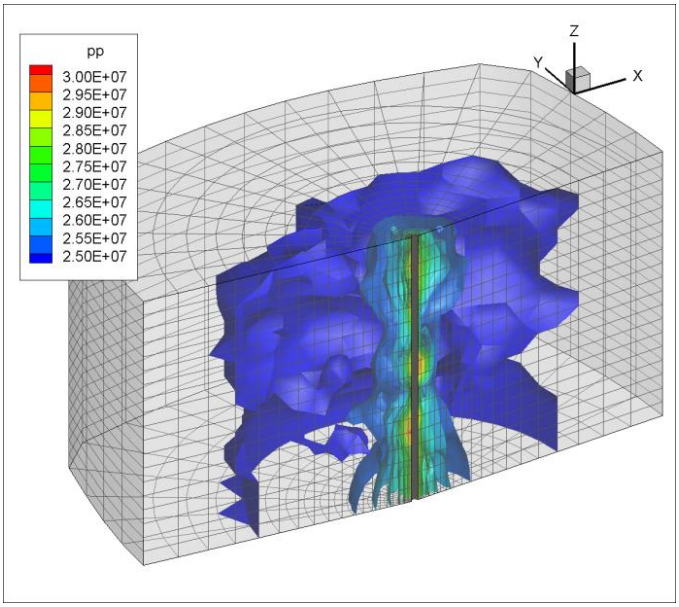
pp
3.00E+07
2.95E+07
2.90E+07
2.85E+07
2.80E+07
2.75E+07
2.70E+07
2.65E+07
2.60E+07
2.55E+07
2.50E+07
Z
Y
X

A3

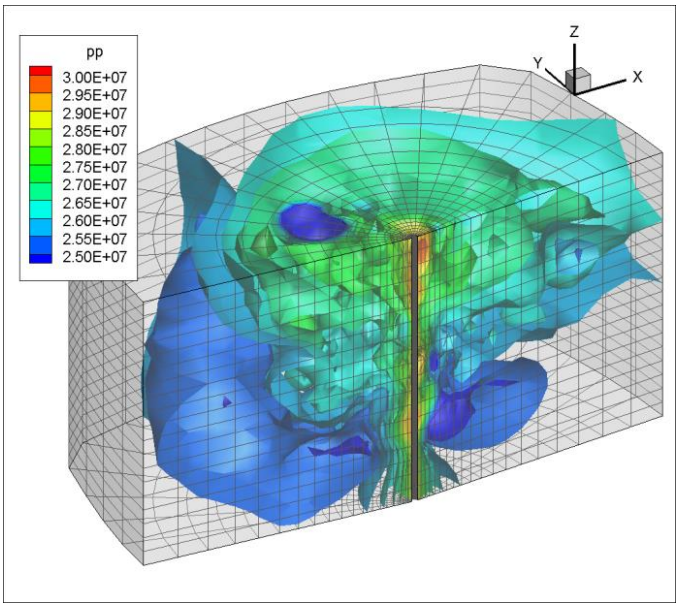

B3

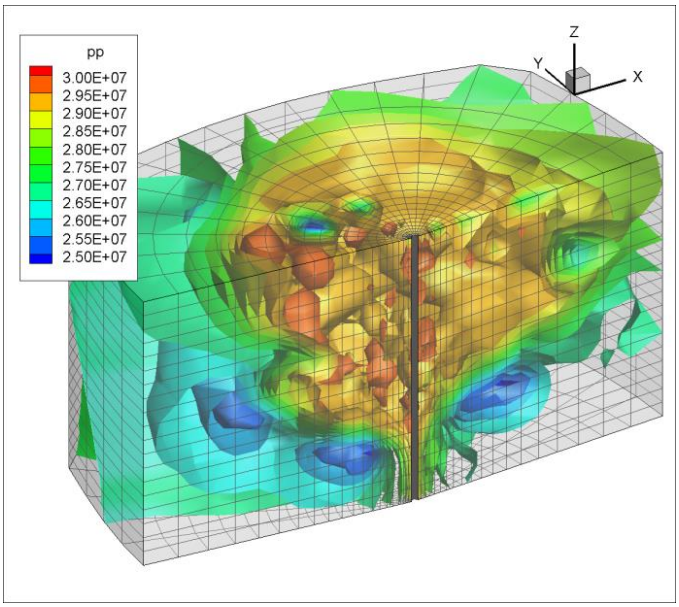

Figure 8.6 Iso-surfaces of pore pressure distribution for reservoirs with (A) and without (B) permeability improvement at (1) t = 0 hour, (2) t = 2 hour, and (3) t = 10 hour of injection.

The flow rate vs. time profile of the above two reservoirs is shown in Figure 8.7. The green line shows the flow rate profile of the reservoir with improved permeability caused by fracture aperture increase. Red line shows the flow rate profile of stronger reservoir. We can see that, in the stimulated reservoir, the flow rate increases quickly after the shear dilation.

Figure 8.8 shows the seismic events at t = 5 hour, when a large of flow rate is observed in Figure 8.7. Large shear slippages are recorded, which is one of the reasons for the large increase of flow rate at t = 5 hour (the well pressure is maintained constant during injection). The flow rate will also increase when the injection fluid front reaches the higher permeability zones. Therefore, we can see periodic increase of flow rate from both curves. To show the permeability improvement, slices of permeability contours of the reservoir A at t = 4 hour and t = 5 hour are plotted in Figure 8.9. Permeability changes at all locations of shear slippage shown in Figure 8.8. But, all the change cannot be shown in a single contour map because of the rather broad range of permeability values (5×10^{-16} m^2 to 6.2×10^{-8} m^2) with the simulation domain. Therefore, only the values in the range of 2.5×10^{-13} m^2 to 8.5×10^{-11} m^2 are plotted in Figure 8.9 for illustration purpose. We can observe permeability increase in various locations in Figure 8.9. The results show the correlations between seismic events, permeability improvement, and flow rate increase.

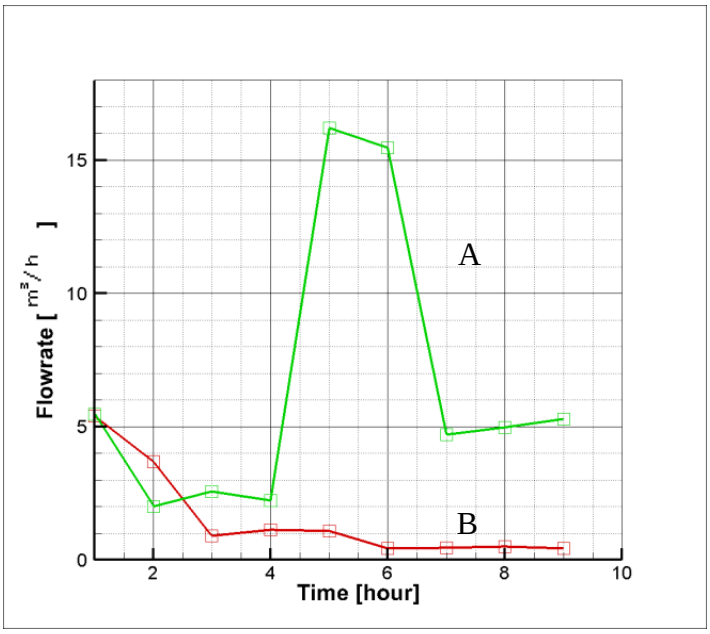

Figure 8.7 Wellbore flow rate profiles with time for reservoirs with (A) and without (B) permeability improvement.

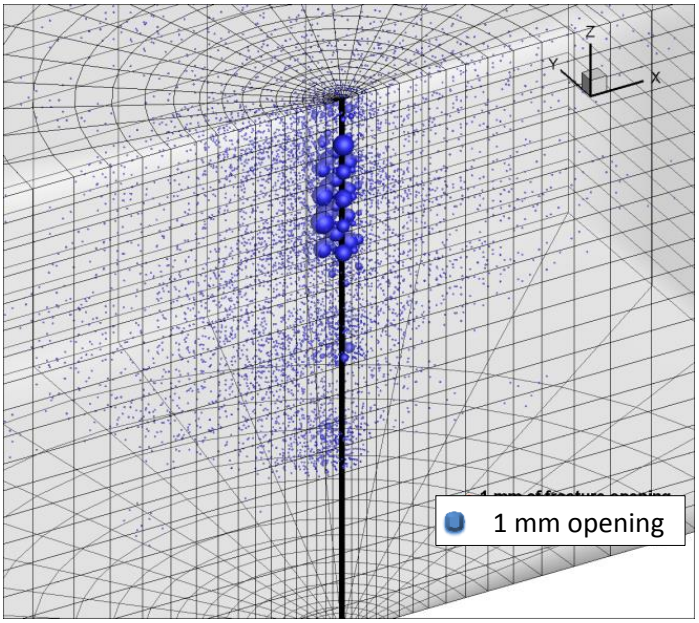

Figure 8.8 Micro-seismic events plot at t = 5 hours. Bubble size indicates the shear slippage value.

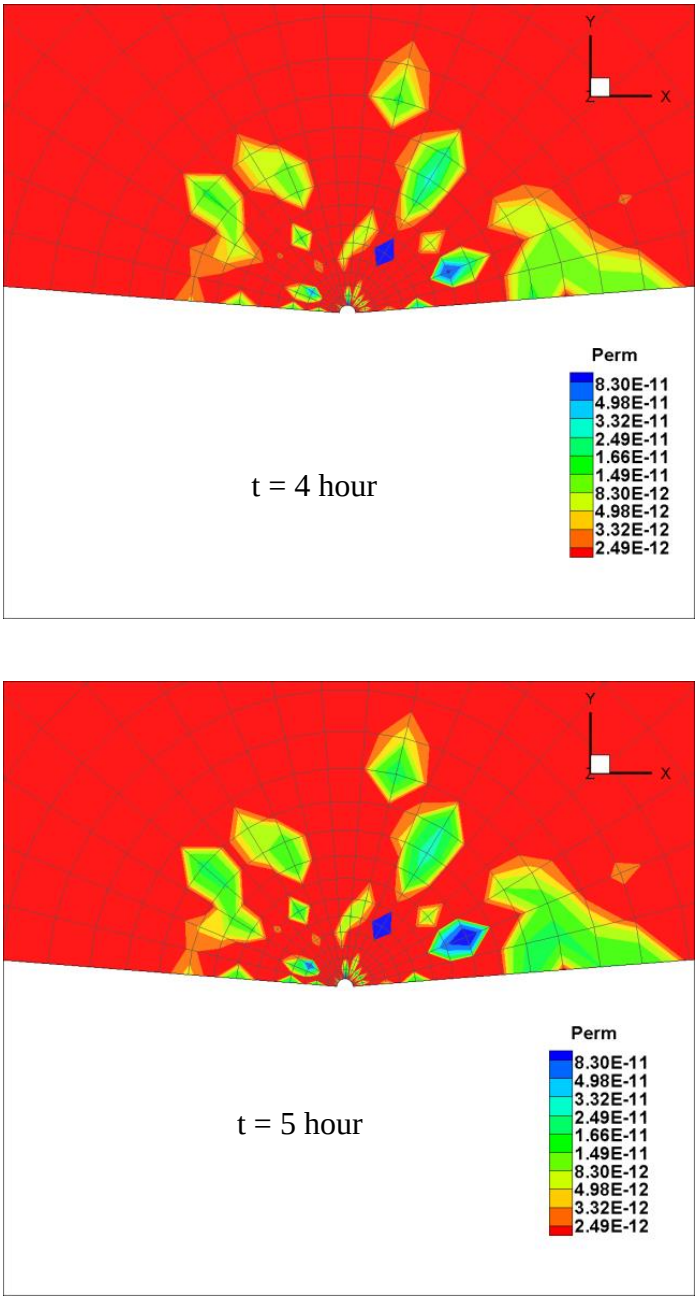

Figure 8.9 Near-well permeability development, showing the center layer at t = 4 hours and t = 5 hours. Only 25 Darcy to 850 Darcy permeability range is plotted for the best illustration.

8.2.4. Near well response using line injection source

Larger scale stimulation cases are also carried out to obtain a general view of the stimulation outcome. The reservoir domain is 100 m ×100 m ×100 m size. Considering the scale of the simulation domain and the computational cost, the injection well section is represented as three vertical injection elements serving as a line source (15 m vertical interval) (Figure 8.10). Instead of using a wellbore mesh, a mesh with a uniform grid mesh 50 × 50 ×50 is used. The far field boundary is set to be no flow, and traction specified boundary. The injection rate of the line source is specified (per unit volume) and well pressure during the injection will be calculated. The far field tractions are equal to the in-situ stresses. The rock properties are the same as Table 8.2. The fracture properties are as Table 8.3. And one of the fracture geometry is shown in Figure 8.11. Figure 8.12 shows the resulting high permeability fractured zone.

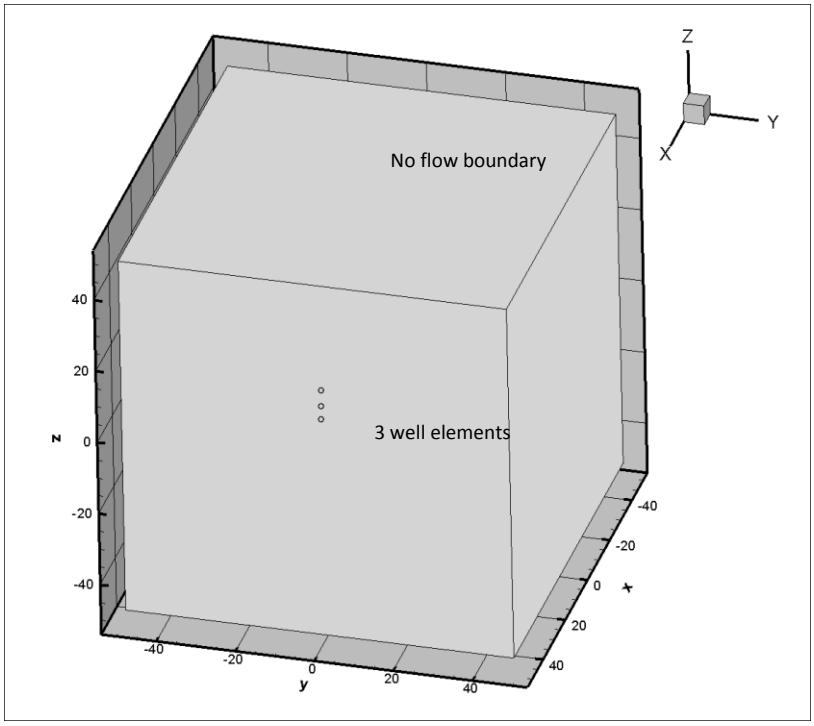

Figure 8.10 Model size and setup for large scale simulation test.

Table 8.3 Parameters used in line source simulation.

Fracture properties	
Fracture density(m^{-1})	1
Fisher parameter, κ	1.7
Mean fracture radial (lognormal)	0
Standard deviation of fracture radial, *s*	0.7

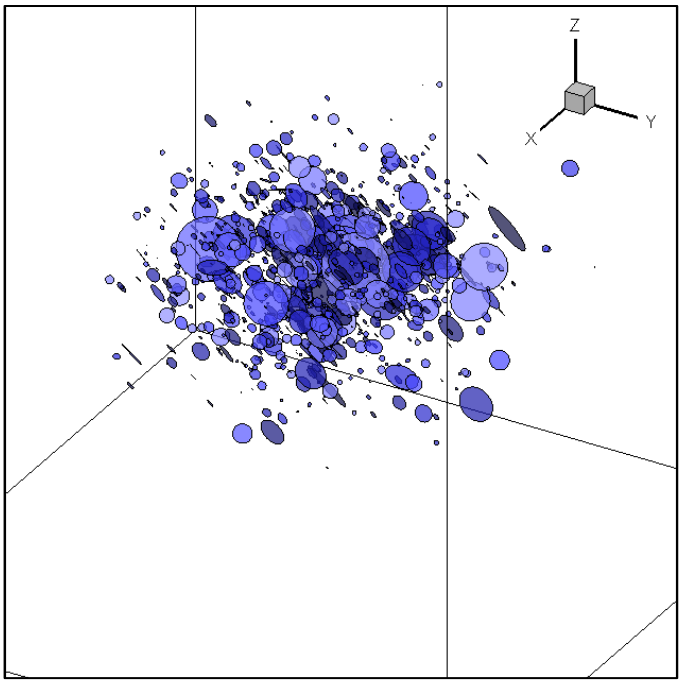

Figure 8.11 Fracture geometry of a fracture network with 1000 fractures.

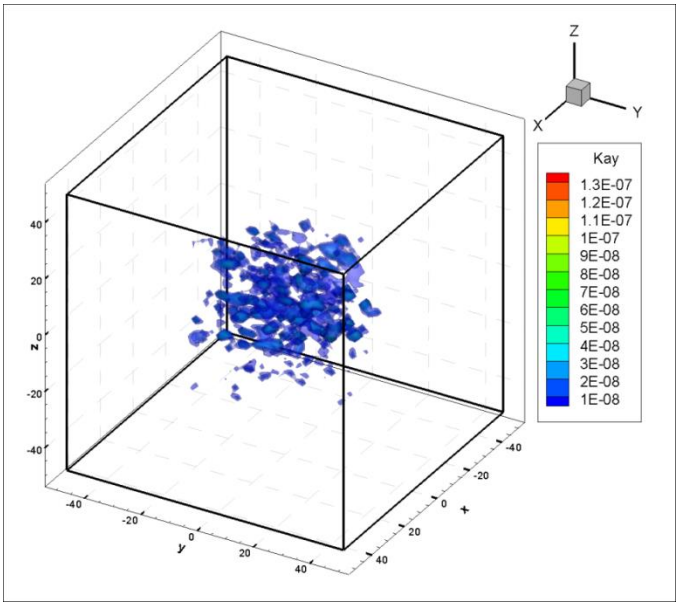

Figure 8.12 Fractured zone permeability heterogeneity due to the fracture network shown in Figure 8.11.

Figure 8.13 shows the pore pressure distribution development at 1 hr., 3 hr., 6 hr., and 9 hr. during the stimulation of 12 hours. Figure 8.14 shows the injection well pressure profile with prescribed injection rate. The results show that in this case the shear slip of natural fractures do not have significant influence on the injection pressure vs. injection rate profile. This is reasonable, considering the size disparity of reservoir and injection source, as well as the highly fractured nature of the reservoir. Figure 8.15 shoes the pressure distribution and shear slippage failure location at time = 9 hour on the center slice (z = 0). We can see that the stimulated zone indicated by micro-seismicity cloud shows similar shape as pore-pressure developed zone. In this model, the injection pore pressure, which will induce poroelastic stress in the domain, is the only disturbance to the initially balanced in-situ state. Therefore, the stress changes and hence the displacement of the fractures can only happen where the pore pressure develops. Figure 8.16 gives a 3D view of the potential micro-seismicity cloud at 9 hours, which indicates the stimulated zone volume at that time.

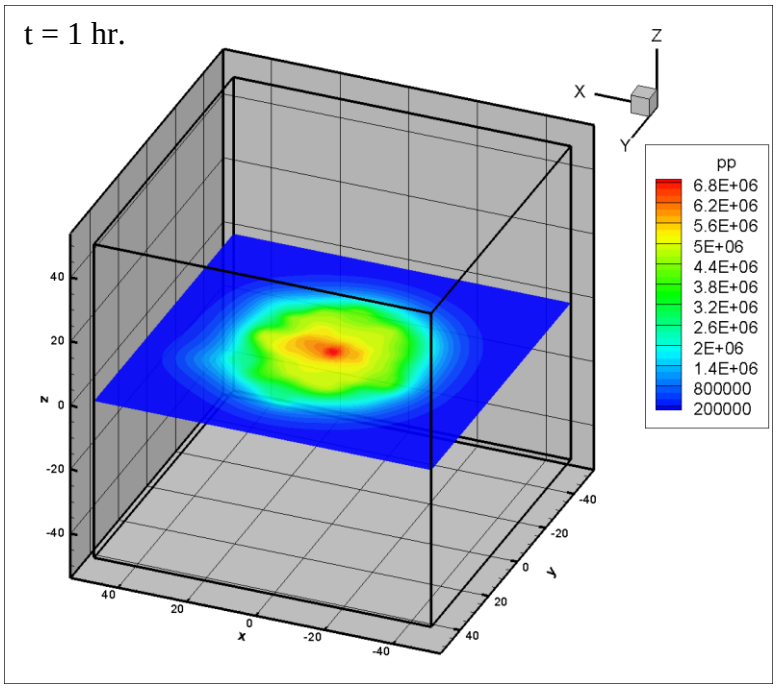
t = 1 hr.
Z
X
Y
pp
6.8E+06
6.2E+06
5.6E+06
5E+06
4.4E+06
3.8E+06
3.2E+06
2.6E+06
2E+06
1.4E+06
800000
200000
40
20
0
-20
-40
z
x
y

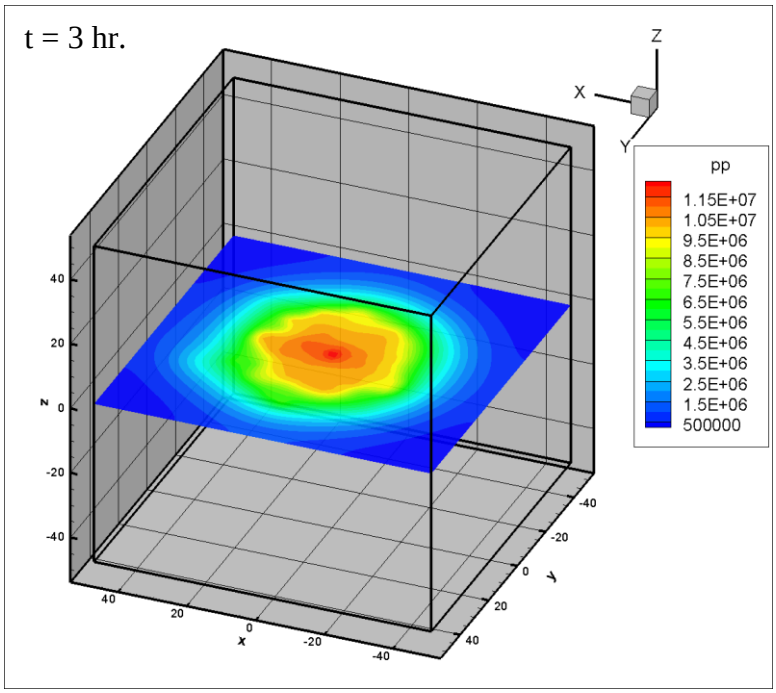
t = 3 hr.
Z
X
Y
pp
1.15E+07
1.05E+07
9.5E+06
8.5E+06
7.5E+06
6.5E+06
5.5E+06
4.5E+06
3.5E+06
2.5E+06
1.5E+06
500000
40
20
0
-20
-40
z
x
y

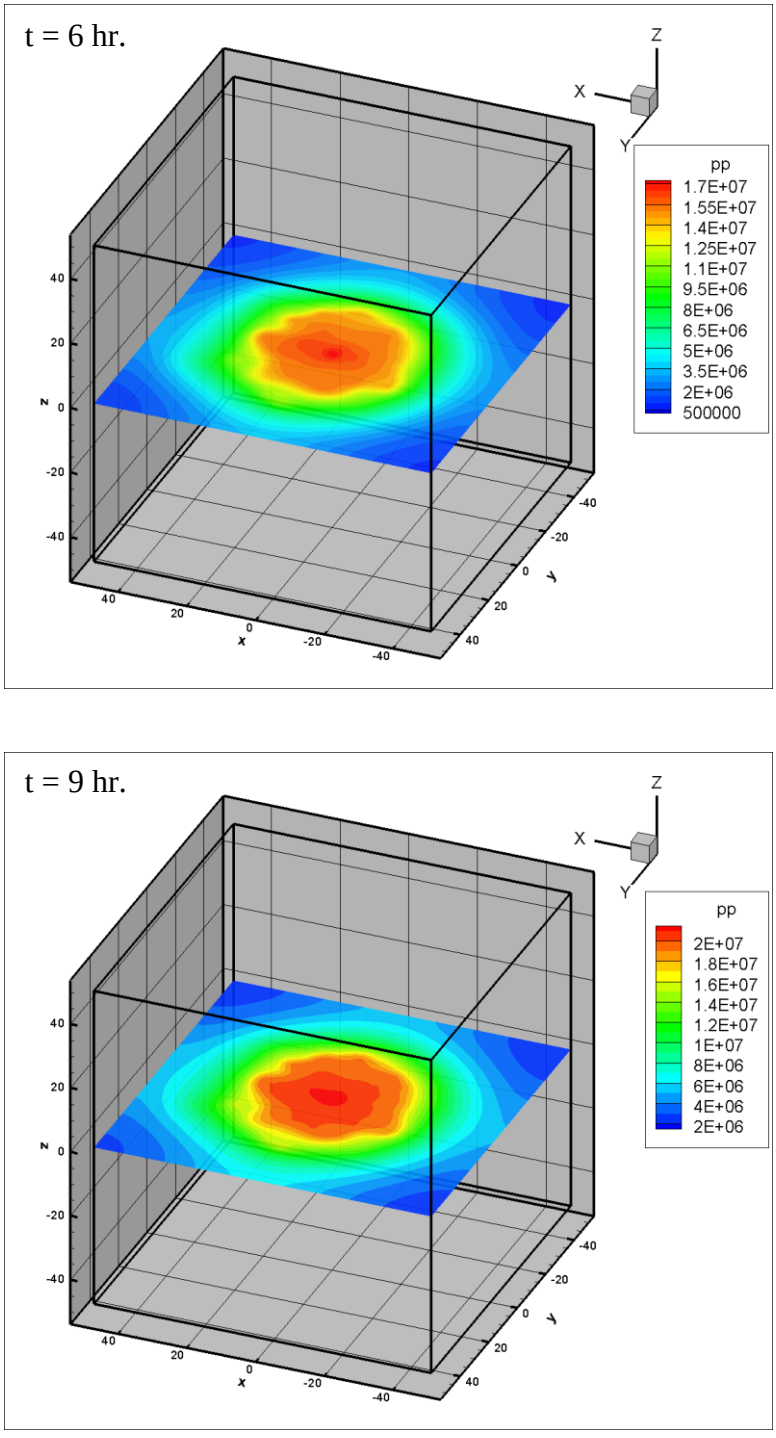

Figure 8.13 Development of excess pore pressure due to stimulation.

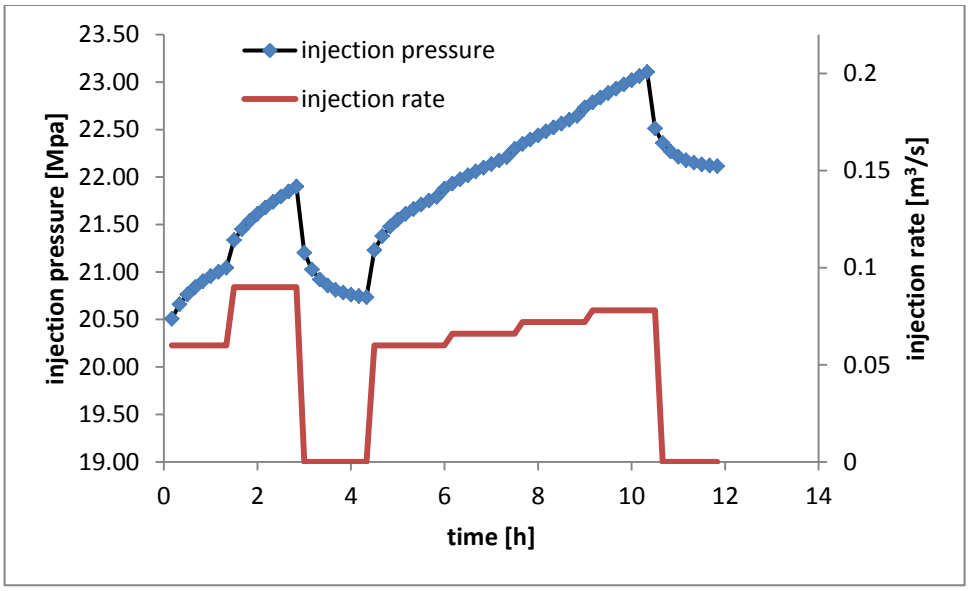

Figure 8.14 Injection pressure vs. injection rate profile.

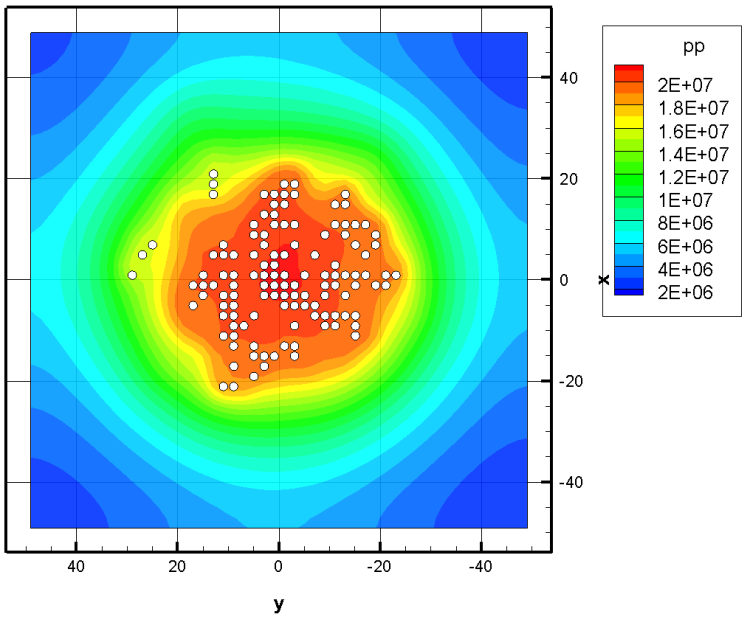

Figure 8.15 Pressure distribution and shear slippage failure location at time = 9 hour on the center slice (z = 0).

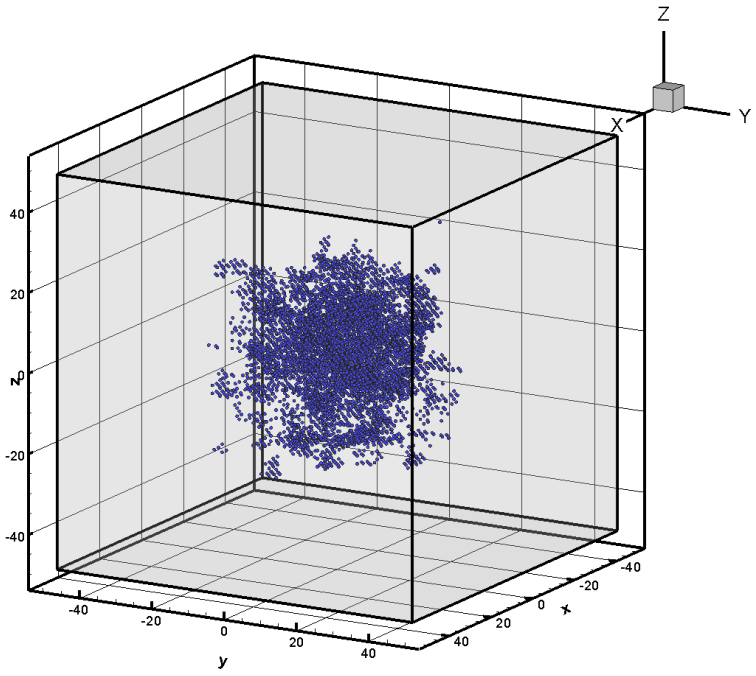

Figure 8.16 Shear slippage failure events (accumulative) at time = 9 hour.

Monte- Carlo tests are usually required for models using stochastic distributions, because different random data set can deliver varying results. Stochastic data analysis is out of the scope of this study, but it is necessary to verify that the influence of data set selection on the simulation results. Figure 8.17 shows the pore pressure distributions at 9 hours for two models, in which the fracture networks are generated using the same stochastic parameters but different random seeds. We can see that the overall results, such as induced pore pressure, pressurized zone shape and stimulated volume, show consistency. Local inconsistencies can be caused by the different distribution of fractures in the two

networks. Figure 8.17 compares the well pressure profiles of two sets. The overall patterns of the profiles are similar. The fact that set 1 has slightly higher well pressure (0.38 MPa) than set 2 (0.34 MPa) indicates set 1 has smaller overall fracture conductivity, because fluid is difficult to diffuse to the reservoir and builds up higher well pressure. However, the difference is with-in practical error tolerance.

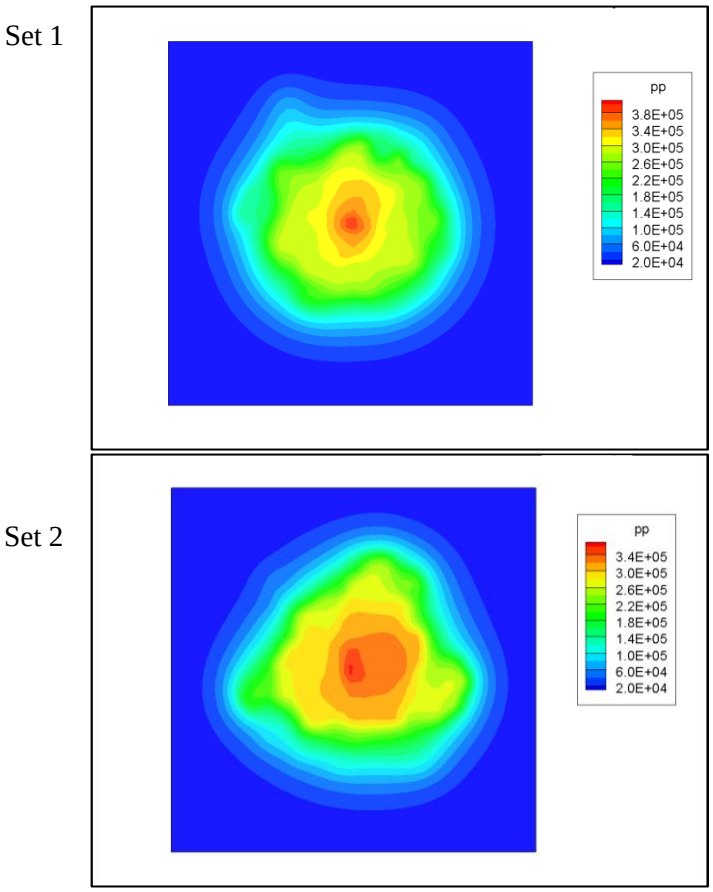

Figure 8.17 Pore pressure distributions of fractured reservoirs, in which natural fractures are generated from different random data sets with same stochastic parameters.

8.2.5. case summary

This simulation example shows different aspects of permeability enhancement in EGS. The model is shown to be capable of analyzing the stress variations, pore pressure distributions, and potential injection induced micro-seismicity. From the results, we have seen the important role of fracture network properties (fracture distribution, orientation, and fracture network connectivity) in geothermal reservoir design and development. The fracture aperture changes with stress variations associated with injection, and directly influence the reservoir permeability evolution. The orientation of the fractures in the reservoir dramatically influences the fracture network connectivity, hence the permeability development. In a fractured reservoir, properties of fracture network have a significant impact on pore pressure and seismic events distribution. Results also show a correlation between pore pressure increase, fractures slip and MEQs. A comparison with field/lab test needs to be conducted in the future work. Calibration of fracture distribution parameters and damage induced permeability change will be reported in the following context.

8.3. Large scale reservoir response analysis

8.3.1. Model set up

This model is also applied to a fractured geothermal reservoir, in which the natural fracture network is to be connected to the injection well via a hydraulic fracture, as shown in Figure 8.18. A one-wing elliptical hydraulic fracture on x-z

plane is centered at coordinates (670.0 m, 242.5 m, 250.0 m). The elliptical crack has a major axis (x-direction) of 300 meters and a miner axis (z-direction) of 150 meters. The elliptical fracture has a uniform width of 5 mm. The modeled reservoir has a length of 1000 meters in x-direction, a width of 500 meters in y-direction, and a thickness of 500 meters in z-direction. The injection well is set vertically along the minor axis of hydraulic fracture, and the open-hole injection section is 160 m (140 m-300 m). The injection rate is held at 26.56 l/s for 40 hours. The injection water temperature is set to be 50℃ and the reservoir temperature is 115℃. The whole domain is selected large enough to eliminate boundary effects. We assume fixed displacement and no flow boundary condition at far field. This domain is discretized into 20,000 uniform finite element bricks and subject into the fully coupled FEM model. The in-situ stress state is indicated in Figure 8.18A also. The maximum horizontal stress is in x-direction, and this is a normal regime stress state where the largest in-situ stress is vertical. A cluster of 1000 natural fractures is located in front of the hydraulic fracture. The coordinates of the center of the natural fracture network is (450 m, 250.0 m, 250.0 m), and the fractured zone is 500 m X 500 m X 500 m. Figure 8.18B shows more details about natural fracture network and hydraulic fracture. Rock properties and fracture network parameters are listed in Table 8.4. Rock and fracture properties are from AltaRock (2011) Newberry reservoir and Li et al. 2012.

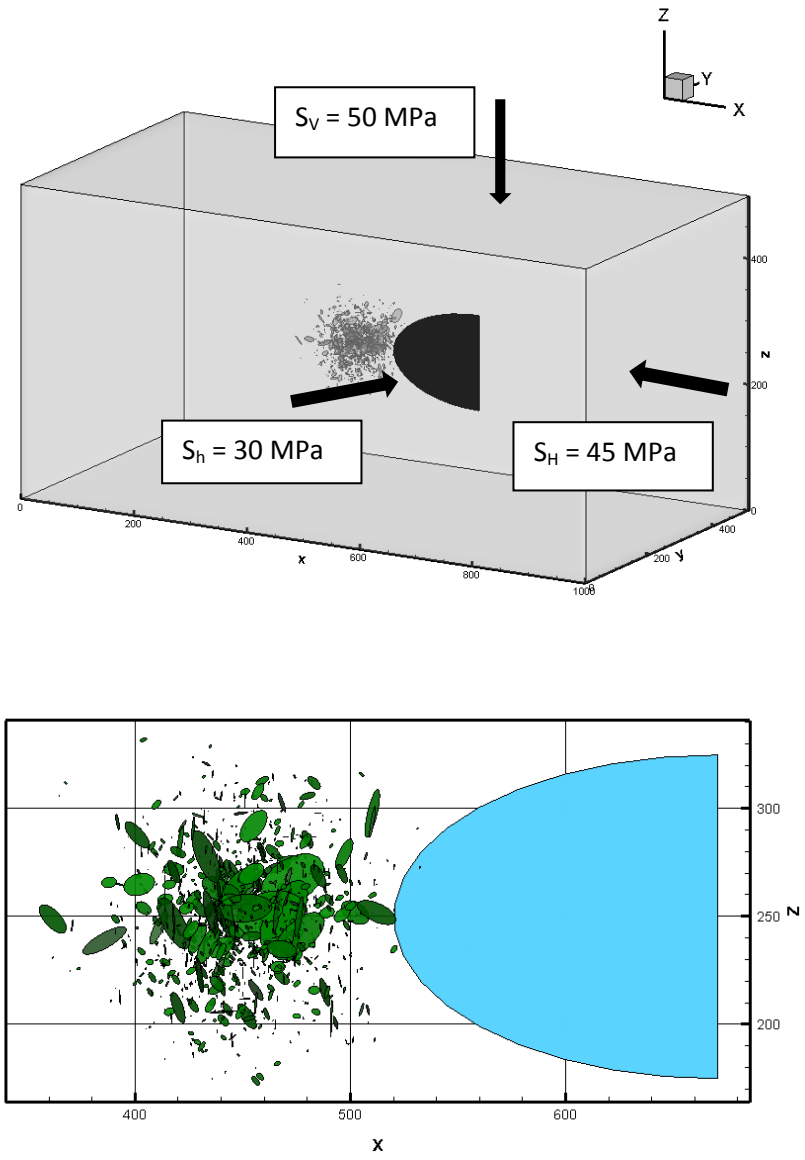

Figure 8.18 a) Reservoir geometry and in-situ stress state. b) Details of natural fracture network and hydraulic fracture.

Table 8.4 Rock and natural fracture properties used in large scale simulation.

Rock density	2700 kg/m^3
Fluid density	1000 kg/m^3
Rock permeability	3.24 X 10^{-12} m^2/s
Rock porosity	0.2989
Young's Modulus	10 GPa
Boit's coefficient	0.915
Poisson's ratio	0.219 (drain), 0.461(undrain)
Bulk Modulus (fluid)	3.291GPa
Number of fractures	1000
Fracture size (Log EX)	0.0
Fracture orientation, κ	2.8
Fluid viscosity	3.0X10^{-4} Pa s
Basic friction angle	0.698
Dilation angle	0.052
90% closure stress	100 MPa
Thermal expansion coefficient (solid)	1.8 X 10^{-5} K^{-1}
Thermal expansion coefficient (fluid)	3.0 X10^{-4} K^{-1}
Thermal diffusivity	6.0 X 10^{-12} m^2/s
Fracture density	1.5 m^{-1}
Fracture size (Log SD)	1.0
size-aperture coefficient	4.0 X 10^{-3}

8.3.2. Simulations and results

The response of natural fracture network to injection is analyzed. At first, two sets of fractures are tested individually. These two sets of fractures have the

same distribution and orientations, with different sizes and apertures. The resulting micro-seismic events location is the same for both sets. This shows the significant influence of fracture orientation on the occurrence of shear slippage. Figure 8.19 is a plot of the normal to the slipped fractures and their corresponding MEQ events at time = 10 hour. Gray circles represent all the fractures, while color rectangles are the slipped fractures. The color bar gives the magnitude of slippage induced micro-seismicity. It can be seen that shear slippage happens on fractures whose normal orientations fall into a certain range as indicated in the plot. The direction cosines of a fracture plane can be written in terms of its fracture dip and azimuth. From Figure 8.19, we can see that most fractures with azimuth between (-30°, 30°) slip after 10 hours of injection. Slipped fractures are sorted and plotted in Figure 8.20. Colors on fractures indicate the magnitude of MEQ events. It is evident from the figure that the event magnitudes are not strongly related to the fracture orientation, size, or the distance to the injection source. We observe the same magnitude of events on different size of fractures. We also observe higher magnitude of events on fracture far from the injection source than the near ones. And from Figure 8.19, we can see the same magnitude events occur on fractures with large range of azimuth angles. However, due to our assumption of the dependency of fracture aperture and size (aperture is 10^{-4} of fracture size, Equation 8.13), the correlation between the fracture aperture and event magnitude is not evident. In order to

characterize the sensitivity of fracture slip to injection, fluid gravity and vertical stress gradient are ignored in this work, and we can see slippage occur on shallower fractures (Figure 8.20). By adding fluid gravity, the lower part of reservoir would be pressurized first, as discussed in Wang and Ghassemi 2012b.

Pore pressure distributions within fracture network from time = 1 hour and time = 10 hour are shown in Figure 8.21. It can be seen that injection fluid mainly pressurizes the interconnected fractures, and only a small amount of fluid is transported through the low permeability matrix. We can see from the results that the pore pressure development is mostly controlled by the connectivity, and there is less pore pressure development in some isolated fractures near the injection source (hydraulic fracture). This is reasonable because the rock permeability is much lower (two orders of magnitude) than fracture permeability, and injected fluid mostly goes into high permeable zones.

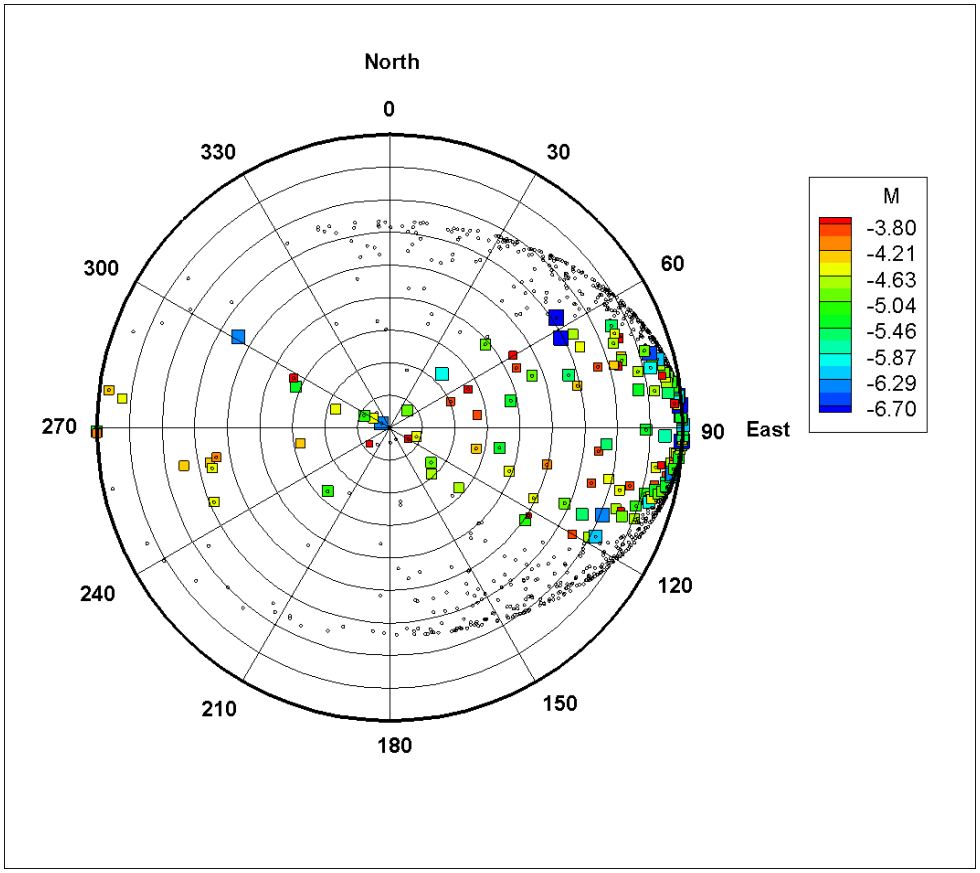

Figure 8.19 Slipped fractures' normal directions are plotted as colored squares. Gray circles show all the normal directions of natural fractures.

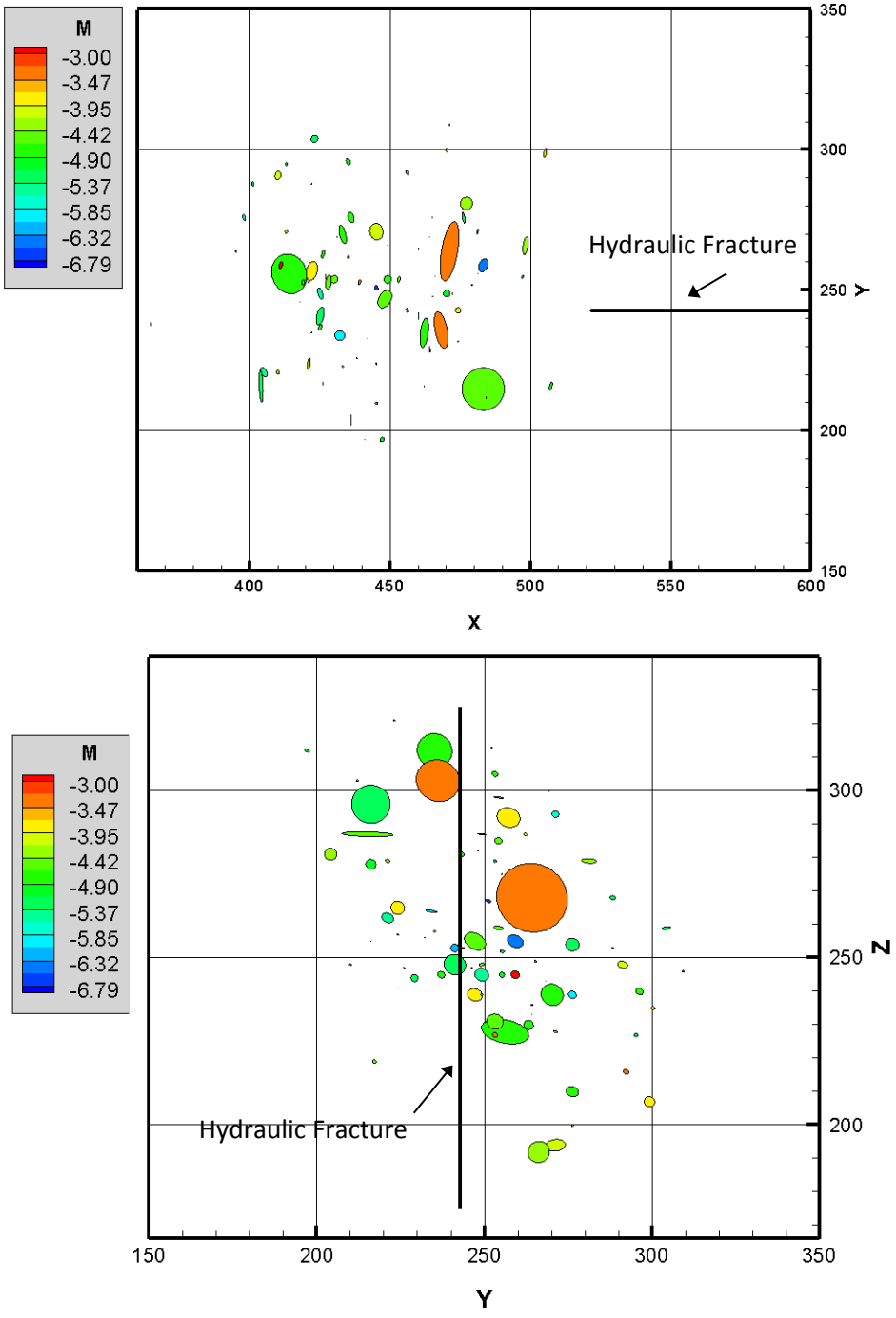

Figure 8.20 Slipped fractures and magnitude of the induced micro seismicity. a) x-y plane view. b) y-z plane view.

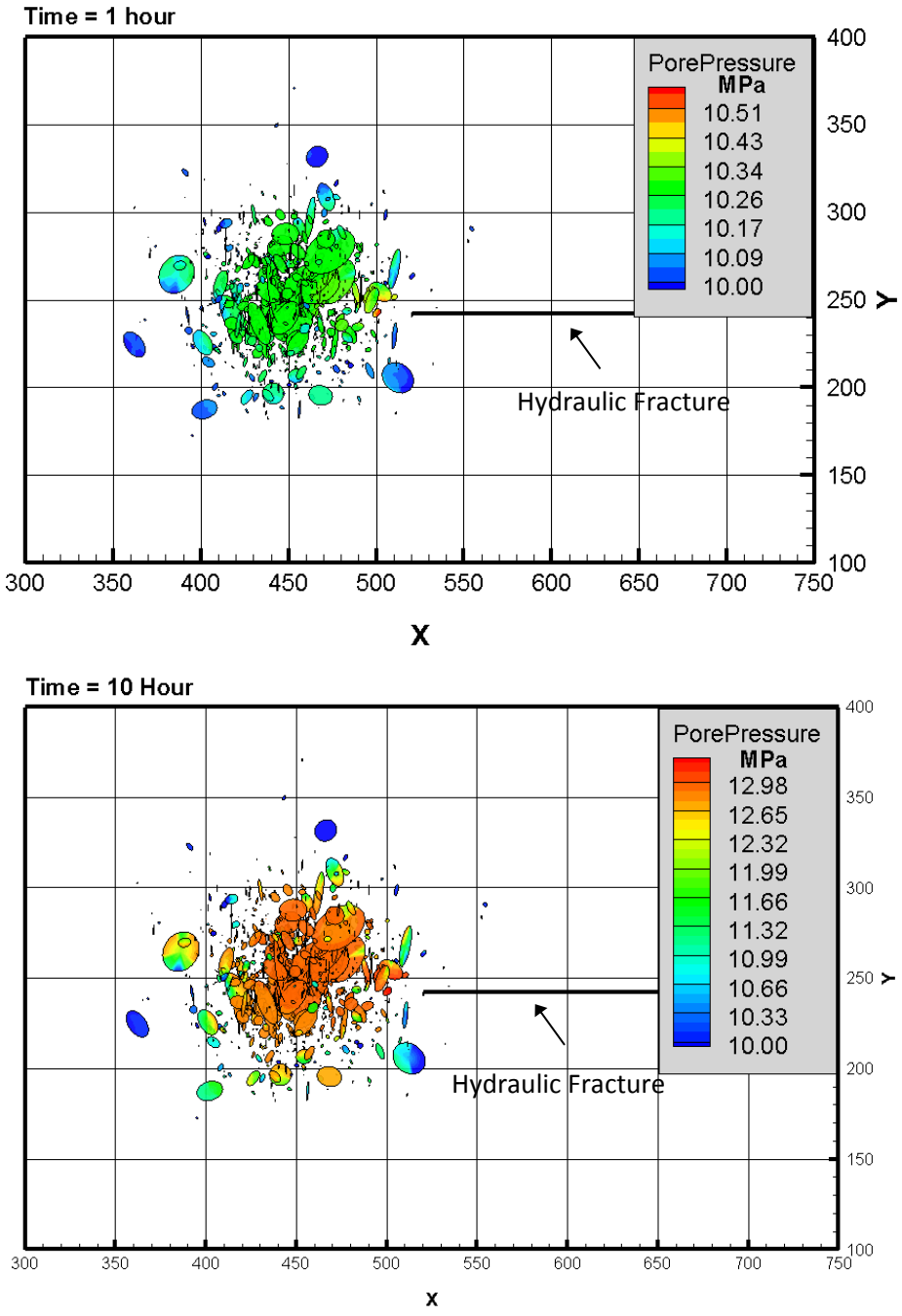

Figure 8.21 Pore pressure distributions in individual fractures at time = 1 hour and time = 10 hour.

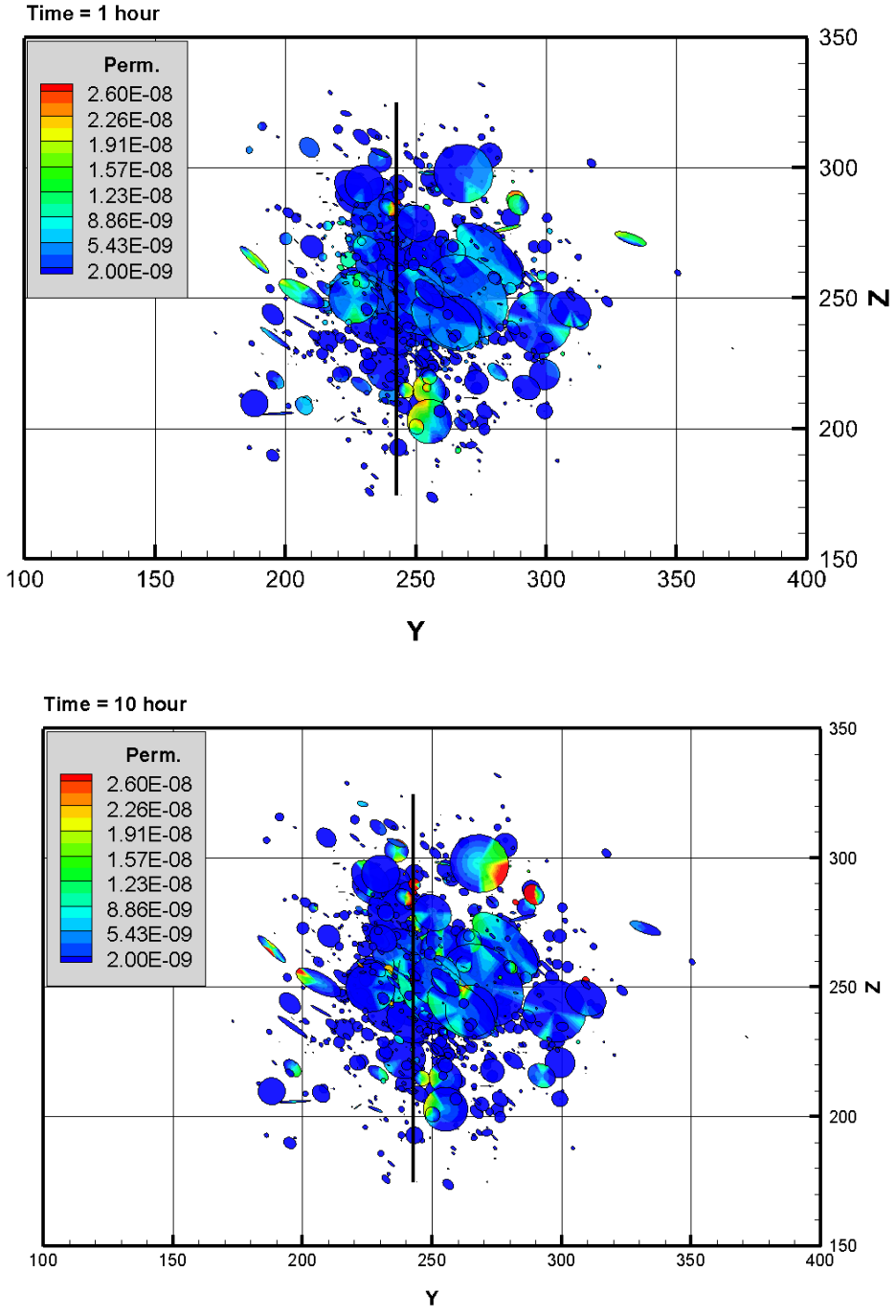

Figure 8.22 The permeability enhancement of fracture network. y-z plane view. Thick black line indicates location of the hydraulic fracture.

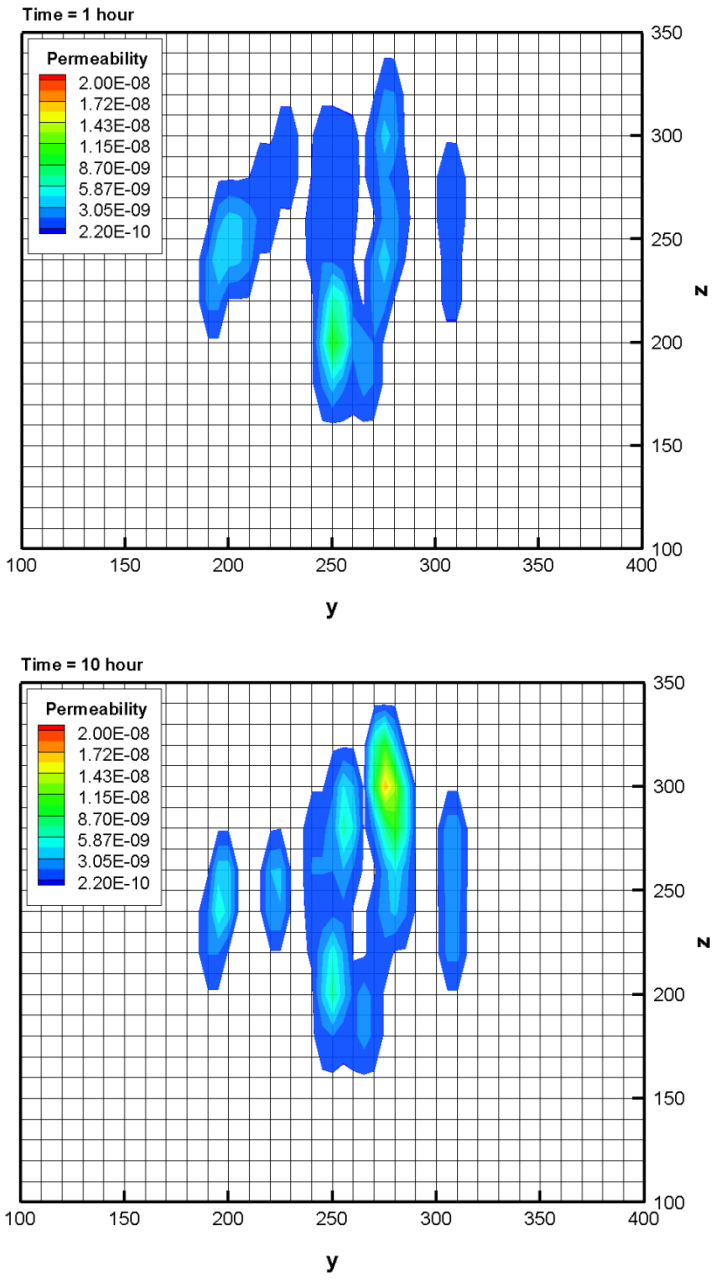

Figure 8.23 Improvement of averaged permeability of elements, low permeability zone (< 2.0×10^{-10} m^2/s) has been blank out. y-z plane slice at x = 450.0 m (center of fracture network).

In the fracture deformation mechanism, there are two sources of permeability improvement: fracture opening and shear dilation. By comparing slipped fractures in Figure 8.20 and fracture permeability enhancement in Figure 8.22, much of the large permeability increases occur where no slippage is observed. For example, the permeability of the fracture located on 270Y-300Z in Figure 8.22B, has been enhanced by approximately one order of magnitude. No shear slippage events are observed on this fracture in Figure 8.20B. Therefore, it can be concluded the permeability enhancement of this fracture is caused by fracture opening by pressurization (and thus eventual mode I propagation). There are also fractures where permeability decreases near the lower part of the hydraulic fracture zone. This decrease can be caused by fracture closing or "shear squeezing", which could lead to aperture reduction.

In this model, not all the natural fractures have been utilized in calculation (when small fractures are contained totally within one element their attribution of the permeability is not take into account). As discussed previously, only fractures that intersect the finite element mesh faces are considered for permeability evaluation. Figure 8.23 shows the permeability improvement in terms of equivalent permeability of finite elements at time = 1 hour and time = 10 hour, respectively. It can be seen that there are zones where permeability is increased after injection. Also, there are zones where permeability is decreasing during injection. In this study, the fracture deformation is assumed to be elastic

and reversible. As can be seen in the figures, the maximum accumulate permeability enhancement is approximately four fold.

The thermal effects during injection are also examined. The results show that during stimulation, the temperature variation in the stimulation time period (~2 days) is very little due to low thermal conductivity of the rock material, as can be seen from Figure 8.24. The reservoir temperature is 115 ℃, and the injection fluid temperature is 20 ℃.

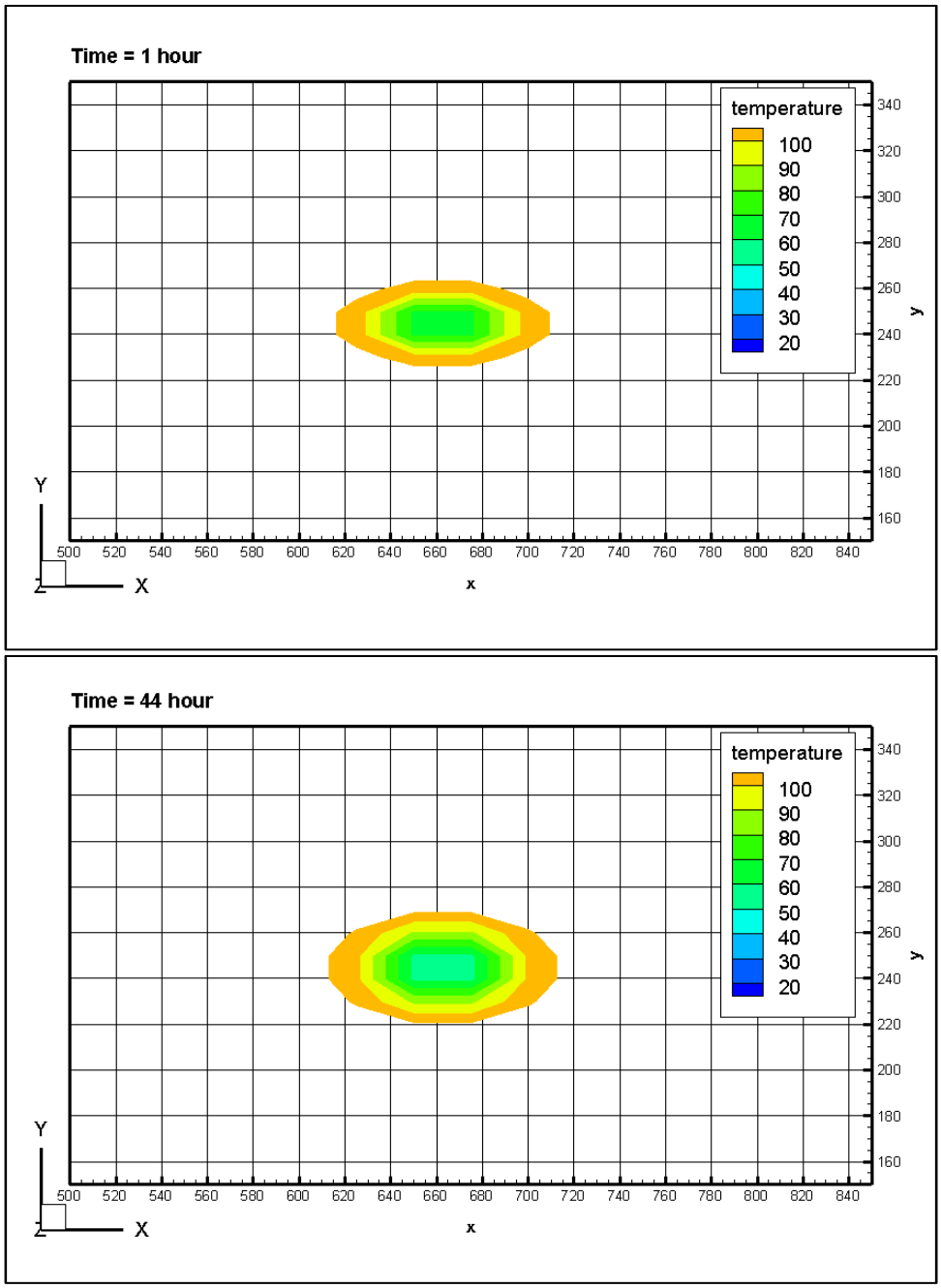

Figure 8.24 Temperature variation during injection at Time = 1 hour and Time = 44 hour.

8.3.3. case summary

The 3D thermal and poroelastic model developed in this work calculates the performance of fractured reservoir during stimulation. The permeability enhancement of the natural fracture network and the corresponding slippage-induced MEQ events has been analyzed. The results show that fractures orientations have a major influence on the initiation of shear slippage. From permeability improvement, we can conclude that as the pressure field changes during injection, fracture permeability can be enhanced. Also, induced effective stress change on fracture surface can also cause fracture closure, hence decrease the local permeability. Shear slippage does not necessary indicates permeability enhancement according to the simulation results. Some fractures' aperture decreases while shear slipping. Since the zone of temperature disturbance is so small (does not even reach the fractured zone as shown in Figure 8.21) for the given injection rate, and permeability, we do not observe cooling effect in this case study.

This model is useful to analyze the geothermal reservoir response during stimulation. It can give assistance when design an injection schedule and to predict the effects of the stimulation. By comparing simulation result and field observations, this model can also be used to evaluate the fracture network models.

9

SUMMARY

9.1.Conclusions

The coupling THM process of rocks is one of the most important phenomena in unconventional reservoir development. In order to properly interpret the coupling behavior during injection and production, this dissertation has employed a finite element method (FEM) in developing a fully-coupled thermo-poroelastic model, which considers the effect of heterogeneous rock damage and natural fracture deformation. The current method has been used to study the near wellbore rock instability/failure. The important role of the variation and reorientation of principle stresses in determining the wellbore failure mode has been presented in Chapter 6. The cooling effect on wellbore stability is illustrated too. The current method has also been applied to heterogeneous, naturally fractured reservoir stimulations for evaluating the permeability enhancement and understanding the injection induced micro-seismicity. The important influences of heterogeneity, rock damage, and natural fracture deformation on the reservoir response during stimulation have been illustrated through several numerical examples. The results show that:

- The current model is capable of predicting different aspects of reservoir response to fluid injection. Given the robust functionality of the well-established FEM formulation, this numerical model is compatible with various concept models, such as fully-coupled reservoir simulation model, decoupled fluid flow and heat transfer model, wellbore stability model, rock damage evolution model, and natural fracture network model.

- Rock failure and fracture deformation induced permeability development and rock degradation have significant impact on the mechanical and flow behavior of the reservoir. Simulation examples in this dissertation have shown the correlation among pore pressure distribution, stress alternation, rock damage evolution, and stimulated volume development. The non-linear FEM model is capable of predict the real-time stimulation results, such as stress-dependent permeability and injection induced micro-seismicity.

- Redistribution and reorientation of stresses after drilling mostly control the failure tendency and failure mode of the near wellbore rock. The variation of the magnitude and orientation of stresses can be resulted from excavation (mechanical loading/unloading), higher/lower than formation well pressure (fluid loading), or cooling effect (thermal

loading). The in-situ stress state also has significant influence on the borehole stability. Simulation examples in Chapter 6 comprehensively reveal the ability of current model in predicting the rock failure under various different conditions.

- Distributions of initial heterogeneous properties are very important in the determination of rock degradation ratio and the initiation of local failure. It also plays important role in the redistribution of stress and pressure field during injection. Results in Chapter 7 also show the effect of heterogeneity on real-time development of stresses, pore pressure, permeability enhancement, and induced MEQ in the reservoir during injection.

- Natural fractures have important roles in the development of pore-pressure fields, stimulated zones, and the induced MEQ during fluid injection and their important impact has been captured using this FEM model combining with fracture deformation model, as shown in detail in Chapter 8. The hydraulic conductivity of the natural fractures highly depends on fracture distribution parameters. The selection of FEM also has influence on the fracture network conductivity evaluation. Fracture orientation plays a major role in the shear slippage and dilation of natural fractures, as shown in Chapter 8. Another result is that the natural

fractures dominant the fluid flow pattern and stimulated volume development in the reservoir.

- Micro-seismic events are related to rock failure, fracture slippage, and permeability enhancement, from which the stimulated reservoir volume can be calculated. Each event is related to one failed finite element, and the event magnitude is calculated according to the damage level of the element. For slippage induced MEQ events, the magnitude is related to the shear displacement of the fracture. Rock failure and fracture deformation induced permeability enhancement has been studied in Chapter 7 and 8. The results show consistency among MEQ events, enhanced permeability zone, and stimulated reservoir volume.

9.2.Contributions

This dissertation combines discrete fracture model and equivalent continuum model to develop a hybrid model, which use discrete stochastic network in building a continuum approximation. The implantation of stochastic fracture network into the existing thermo-poroelastic model extends the capability of current thermo-poroelastic model into predicting the coupling behavior of naturally fractured reservoirs, in both oil/gas and geothermal energy. Applications and limitations of the natural fracture network model have been illustrated in this dissertation, providing useful guidance when the consideration

of natural fractures is essential in reservoir modeling. The deformation of fractures has been related to reservoir permeability enhancement and the induced micro-seismic events. Both shear dilation and opening of the fractures have been considered, where joint model and penny shape fracture model are used.

Continuum damage mechanics binding with rock heterogeneity distribution are utilized to modeling the rock failure process. The failure induced rock degradation and permeability enhancement have been used in the THM model to simulate the non-linearity of coupled process. Weibull theory is used for distributing rock heterogeneity, the parameters of which is related to the damage evolution curve of continuum damage mechanics. Combing these two theories, this dissertation is able to reproduce complete stress-strain curves of heterogeneous rock samples under triaxial test condition, which implies a more applicable modeling of rock heterogeneity.

This dissertation provides various examples to illustrate the different shapes and types of wellbore failure zones, and emphasizes the role of rotation and magnitude of induced principal stresses in determining wellbore failure modes. The importance of poroelastic effect and thermal effect is also pointed out. Three-dimensional comprehensive description of failure conditions is provided in Chapter 6, which explains typical failure modes observed in practice.

Influence of rock heterogeneity on stimulation response has been extensively studied in Chapter 7, which gives an integrated interpretation on different aspects of heterogeneous rock's behavior during fluid injection. The permeability enhancement and occurrence of micro-seismicity have been related to the damage of rock mass. Effects of different injection plans are also presented.

Models of reservoirs with both fractures and heterogeneous rock mass are presented in Chapter 8, which shows the dominating role of fracture flow in fluid diffusion in unconventional reservoir. Most of the fluid goes in to fractured zone by penetrating the intact rock between fractures and the injection source. The result also shows the significance of fracture network connectivity and fracture orientation for shear slippage induced permeability enhancement. The observation is that fluid is mostly confined in interconnected fractures, and only fractures whose orientation falls into certain range may have shear slippage.

9.3.Recommendations

The natural fracture model needs to be valid case by case for its accuracy in representing the in-situ local connectivity, since stochastic models simulate the fracture network in a way of representing the overall conductivity behavior of the reservoir.

Multiple simulations of random samples from the same distribution need to be conducted for statistical modeling approaches, due to the non-unique nature of the random data set. Simulation conclusions should always be drawn from cases using representative date set(s). The concept model will need to be re-examined when conflicting results are obtained from different random samples.

Conditional statistical distributions of heterogeneous rock properties and natural fractures would lead the current model to be more realistic. High quality and adequate interpretation of field data will also increase the accuracy of the model prediction.

Development of a mature damage model based on 3D stress-strain constitutive relations considering the plastic strain during the failure process is recommended. Most of current continuum damage models are based on observations of constitutive relations from uniaxial test.

Robust methods for modeling the propagation and interaction of large amount of fractures is required to depict more realistic geothermal reservoir simulation. A more sophisticated fracture deformation and propagation model is needed. The efficiency of using finite element method to simulate fractures and its propagation, comparing to boundary element method, needs to be improved.

REFERENCES

ALTAROCK. 2011. Newberry volcano EGS demonstration stimulation planning. *GRC Annual Meeting, San Diego, CA, October 25, 2011*.

Barton N., S. Bandis, and K. Bakhtar. 1985. Strength, deformation and conductivity coupling of rock joints. *International Journal of Rock Mechanics and Mining Sciences & Geomechanics, Abstracts* 22(3): 121-140.

Biot, M.A. 1941. General theory of three-dimensional consolidation. *Journal of Applied Physics* 12(2): 155-164.

Bruel, D. 2002. Impact of induced thermal stresses during circulation tests in an engineered fractured geothermal reservoir. *Oil & Gas Science and Technology* 57(5): 459-470.

Bruel, D., M.C. Cacas, E. Ledoux, and G. Marsily. 1994. Modeling storage behaviour in a fractured rock mass. *Journal of Hydrology* 162: 267-278.

Cacas M.C., E.Ledoux, G. De Marsily, and B. Tillie. 1990. Modeling fracture flow with a stochastic discrete fracture network: calibration and validation 1. the flow model. *Water Resources Research* 26(3): 479-489.

Carrera, J., J. Heredia, S. Vomvoris, and P. Hufschmied. 1990. Modeling of flow on a small fractured monzonitic gneiss block. *Selected Papers in Hydrogeology of Low Permeability Environments, International Association of Hydrogeologists, Hydrogeology:* 2: 115-167.

Carter, J.P. and J.R. Booker 1982. Elastic consolidation around a deep circular tunnel. *International Journal of Solids Structures*18(12): 1059-1074.

Chen, Z.H., L.G. Tham, M.R. Yeung, and H. Xie. 2006. Confinement effects for damage and failure of brittle rocks. International Journal of Rock Mechanics and Mining Sciences 43(8):1262-1269

Cheng, A.H.D. and E. Detournay. 1988. A direct boundary element method for plane strain poroelasticity. International Journal for Numerical and Analytical Methods in Geomechanics 12(5): 551-572.

Cladouhos, T.T., M. Clyne, M. Nichols, S. Petty, W. Osborn, and L. Nofziger. 2011. Newberry volcano EGS demonstration stimulation modeling. GRC Transactions 35: 317-322.

Delaney, P. T., 1982. Rapid intrusion of magma into wet rock: ground water flow due to pressure increases. J. Geophys. Res. 87 : 7739–7756.

Dershowitz, W.S. 1984. Rock joint systems. Ph.D. thesis, Massachusetts Institute of Technology, Cambridge.

Detournay, E. and A. H-D. Cheng. 1988. Poroelastic response of a borehole in a non-hydrostatic stress field. International Journal for Numerical and Analytical Methods in Geomechanics 25(3): 171-182.

Dhondt, G. 2004. The finite element method for three-dimensional thermomechanical applications. John Wiley & Sons, Ltd.

Ekbote, S. and Y. Abousleiman. 2006. Porochemoelastic solution for an inclined borehole in a transversely isotropic formation. Journal of Engineering Mechanics 132(7): 754-763.

Eshelby, J.D. 1957. The determination of the elastic field of an ellipsoidal inclusion, and related problems. Proceddings of the Royal Society of London. Series A, Mathematical and Physical Sciences 241(1226): 376-396.

Fujii, Y., Y. Ishijima and T. Kiyama. 1999. Confining pressure-dependency of coefficients in the simple constitutive equations for brittle rock. Processing 1999 Japan-Korea Joint symposium on Rock Engineering. 323-330.

Ghassemi, A. and A. Diek. 2003. Linear chemo-poroelasticity for swelling shales: theory and application. Journal of Petroleum Science and Engineering 38(3-4): 199-212.

Ghassemi, A. and G.S. Kurma. 2007. Changes in fracture aperture and fluid pressure due to thermal stress and silica dissolution/precipitation induced by heat extraction from subsurface rocks. Geothermics 36(2): 115-140.

Ghassemi, A., Q. Tao, and A. Diek. 2009. Influence of coupled chemo-poro-thermoelastic processes on pore pressure and stress distributions around a wellbore in swelling shale. Journal of Petroleum Science and Engineering 67(1-2): 57-64.

Griffiths, D.V. and I.M. Smith. 1991. Numerical methods for engineers. Oxford: Blackwell Scientific Publications Ltd.

Hallinan Jr., A. 1993. A review of the Weibull distribution. Journal of Quality Technology 25(2): 85-93.

Hanks, T.C. and H. Kanamori. 1979. A moment magnitude scale. Journal of Geophysical Research: Solid Earth 84(B5) 2248-2350.

Heidug, W.K. and S.W. Wong. 1996. Hydration swelling of water-absorbing rocks: a conostitutive model. International Journal for Numerical and Analytical Methods in Geomechanics 20(6): 403-430.

Hristopulos, D.T. and G. Christakos. 1999. Renormalization group analysis of permeability upscaling. Stochastic Environmental Research and Risk Assessment 13(1-2): 131-160.

Hudson, J.A. and P.R. La Pointe. 1980. Printed circuits for studying rock mass permeability. International Journal of Rock Mechanics and Mining Science and Geomechanics Abstracts 17(5): 297-301.

Jaeger, J.C. and N.G.W. Cook. 1969. Fundamentals of rock mechanics. New York: Chapman and Hall.

Jaeger, J.C., N.G.W. Cook, and R.W. Zimmerman. 2007. Foundamentals of rock mechanics.4th edn. Blackwell Publishing.

Johnson, N.L., S. Kotz, and N. Balakrishnan. 1994. Continuous univariate distributions, Vol. 1, 2nd Edn. New York: Wiley.

Kachanov, L.M. 1958. On the creep fracture time. Izv Akad, Nauk USSR Otd. Tech. 8: 26-31.

Kachanov, L.M. 1986. Introduction to continuum damage mechanics. The Netherlands: Martinus Nijhoff Publishers.

Kolditz, O. and C. Clauser. 1998. Numerical simulation of flow and heat transfer in fractured crystalline rocks: application to the hot dry rock site in rosemanowes (U.K.). Geothermics 27(1):1-23.

Krempl, E. 1977. On phenomenological failure laws for metals under repeated and sustained loading (fatigue and creep). Conf. on Environmental Degradation of Engineering Materials, Blaksburg, VA.

Kurashige, M. 1989. A thermaoelastic theory of fluid-filled porous materials. International Journal of Solids Structures 25(9): 1039-1052.

Lee, S-H, and A. Ghassemi. 2011. Three-dimensional thermo-poro-mechanical modeling of reservoir stimulation and induced microseismicity in geothermal reservoir. Proceedings, Thirty-sixth Workshop on Geothermal Reservoir Engineering, Stanford University, Stanford, California, 31 January – 2 Feburary, 2011.

Lemaitre, J. 1985. A continuous damage mechanics model for ductile fracture. Journal of Engineering Materials and Technology 107(1): 83-89.

Li, L.C., C.A. Tang, G. Li, S.Y. Wang, Z.Z. Liang, and Y.B. Zhang. 2012. Numerical simulation of 3D hydraulic fracturing based on an improved flow-stress-damage model and a parallel FEM technique. Rock Mechanics and Rock Engineering 45(5): 801-818.

Li, X., L. Cui, J-C. Roegiers. 1998. Thermoporoelastic modeling of wellbore stability in non-hydrostatic tress field. International Journal of Rock Mechanics and Mining Sciences & Geomechanics, Abstracts 35(4): 584-588.

Li, Y., J. Wong, and A. Ghassemi. 2012. Mechanical properties of intact and jointed welded tuff from Newberry volcano. Proceedings of Thirty-Seventh Workshop on Geothermal Reservoir Engineering, Stanford University, Stanford, California, 30 January – 1 Feburary, 2012.

Liang Z.Z. 2005. Three-dimensional numerical modelling of rock failure process. Ph.D. Thesis. Dalian University of Technology, Dalian, China.

Mandel, J. 1953. Consolidation des sols (etude mathematique). Geotechnique 3: 287-299.

Marin, E. 2010. Characteristic dimensions for heat transfer. Latin-American Journal of Physics Education 4(1): 56-60

Maury, V.M. and J-M. Sauzay. 1987. Borehole instability: case histories, rock mechanics approach, and results. SPE/IADC Drilling Conference, New Orleans, LA, March 15-18, 1987.

McGarr, A., A.M. Spottiswoode, N.C. Gay, and W.D. Ortlepp. 1979. Observations relevant to seismic driving stress, stress drop, and

efficiency. Journal of Geophysical Research: Solid Earth 84(B5) 2251-2261.

McTigue, D. 1986. Thermoelastic response of fluid-saturated porous media. Journal of Geophysical Research 91(B9): 9533-9542.

Mody, F.K. and A.H. Hale. 1993. Borehole stability model to couple the mechanics and chemistry of drilling fluid shale interaction. Proceedings, SPE/IADC Drilling Conference, Amsterdam, 23-25 Feburary 1993.

Muller A.L., E.D.A. Vargas Jr., L.E. Vaz, and C.J. Goncalves. 2008. Borehole stability analysis considering spatial vairiability and poroelastoplasticity. International Journal of Rock Mechanics and Mining Sciences 46(1): 90-96.

Murakami, S. and N. Ohno. 1980. A continuum theory of creep and creep damage. 3rd IUTAM Symposium on Creep in Structures, Leicester.

Murthy, D.N.P., M. Xie, and R, Jiang. 2003. Weibull models. New York: Wiley.

National Research Council. 1996. Rock fractures and fluid flow. Washington, D.C.: National Academy Press.

Noetinger, B. 1994. The effective permeability of a heterogeneous medium. Transport in Porous Media 15(2): 99-127.

Rahman, M.K., M.M. Hossain, and S.S. Rahman. 2002. A shear-dilation-based model for evaluation of hydraulically stimulated naturally fractured reservoirs. International Journal for Numerical and Analytical Methods in Geomechanics 26 (5): 469-497.

Rice, J.R. and M.P. Cleary. 1976. Some basic stress-diffusion solutions for fluid-saturated elastic porous media with compressible constituents. Reviews of Geophysics and Space Physics 14(2): 227-241.

Robinson, P. 1984. Connectivity, flow and transport in network models of fractured media. Ph.D. thesis. Oxford University, Oxford, UK.

Robotnov, Y.N. 1969. Creep problems in structural members. North-Holland.

Rosso, R.S. 1976. A comparison of joint stiffness measurements in direct shear, triaxial compression, and in situ. International Journal of Rock

Mechanics and Mining Sciences & Geomechanics, Abstracts 13(6): 167-172.

Rubin, Y. 2003. Applied stochastic hydrogeology. Oxford: Oxiford University Press.

Safari, M.R. and A. Ghassemi. 2011. 3d analysis of huff and puff and injection tests in geothermal reservoirs. Proceedings 36th Workshop on Geothermal Reservoir Engineering, Stanford University, Stanford, California, Jan. 31- Feb. 2, 2011.

Schoenball, M. and T. Kohl. 2013. The peculiar shut-in behavior of the well GPK2 at Soultz-sous-Forets. GRC Transactions 37: 217-220.

Schoenball, M., T.M. Muller, B.I.R. Muller, and O. Heidbach. 2010. Fluid-induced microseismicity in pre-stressed rock masses. Geophysical Journal International 180(2): 813-819.

Shapiro, S.A., P. Audigane, and J.J. Royer. 1999. Large-scale in situ permeability tensor of rocks from induced microseismicity. Geophysical Journal International 137(2): 207-213.

Smith I.M. and D.V. Griffiths. 2004. Programming the finite element method, fourth ed. New York: John Wiley.

Smith, L. and F.W. Schwartz. 1984. An analysis of the influence of fracture geometry on mass transport in fractured media. Water Resources Research 20(9): 1241-1252.

Sneddon, I.N. 1946. The distribution of stress in the neighborhood of a crack in an elastic solid. Proceedings of the Royal Society of London. Series A, Mathematical and Physical Sciences 187: 229-260.

Tang, C.A., L.G. Tham, P.K.K. Lee, T.H. Yang, and L.C. Li. 2002. Coupled analysis of flow, stress and damage (FSD) in rock failure. International Journal of Rock Mechanics and Mining Sciences 39(4): 477-489.

Terzaghi, K. 1923. Die Berechnung des durchlassigkeitsziffer des tones aus dem verlauf der hydrodynamischen spannungserscheinungen. Sitz. Akad. Wiss. Wien, Abt.IIa. 132: 125– 38.

Tezuka, K. and K. Watanabe. 2000. Fracture network modeling of hijiori hot dry rock reservoir by deterministic crack network simulator (D/SC). In

proceedings of World Geothermal Congress, Kyushu-Tohoku, Japan, 28 May – 10 June, 2000.

Tezuka, K., T. Tamagawa, and K. Watanabe. 2005. Numerical simulation of hydraulic shearing in fracture reservoir. In proceedings of World Geothermal Congress, Antalya, Turkey, 24 –29 April 2005.

Warren, J.E. and H.S. Price. 1961. Flow in heterogeneous porous media. SPE Journal 1(3): 153-169.

Weibull, W. 1939. A statistical theory of the strength of material. Ing. Betenskapa Acad. Handlingar. Stockholm. 151.

Weibull, W. 1951. A statistical distribution function of wide applicability. Journal of Applied Mechanics 18: 293-297.

Westmann, R.A. 1965. Asymmetric mixed boundary-value problems of the elastic half-space. Journal of Applied Mechanics 32(2): 411-417.

Willis-Richards, J., K. Watanabe, and H. Takahashi. 1996. Progress toward a stochastic rock mechanics model of engineered geothermal systems. Journal of Geophysical Research 101(B8): 481-496.

Zhou, X. and A. Ghassemi.2009, Finite element analysis of coupled chemo-poro-thermo-mechanical effects around a wellbore in swelling shale. International Journal of Rock Mechanics and Mining Science 46(4), 769-778.

APPENDIX

A1. Algorisms of introducing fracture network into finite element mesh

When numerically embed penny shaped fractures into finite element mesh, one need to superpose properties of penny shaped fractures onto finite elements, and interpolate results from finite element node to fracture surface. Fundamental routines of computational geometry is needed in, for instance, 1) determination and visualization of the fracture network pattern; 2) algorisms of finding intersection lines between fractures and element interfaces; 3) searching for conductive channels assembled by interconnected fractures and excluding isolated fractures from fracture network. In this section, a library of geometry recipes used in this work is gathered. And all methods are explained in a manner likely to be adopted in FORTRAN programming, or most likely to find an available FORTRAN subroutine.

Geometrical figures in three dimensions in three-dimensional space can be described using a series of points defined by a set of rectangular coordinates (x, y, z) with respect to a set of orthogonal axes. The point can also be represented by cylindrical coordinates (ρ, ϕ, z) or spherical coordinates (r, θ, ϕ) under the circumstances. The main task of the recipes shown in this section is to represents the target geometry using points coordinates.

A1.1. Intersection line between a circle and a quadrilateral in space

In equivalent permeability calculation, the length of intersection line (L) between the penny shape fracture (F) and finite element interface (A) is required (Figure A1). To calculate the length of a line segment, we need to find the coordinates of two end points $P_a(x_1, y_1, z_1)$ and $P_b(x_2, y_2, z_2)$.

$$Length = \sqrt{(x_1 - x_2)^2 + (y_1 - y_2)^2 + (z_1 - z_2)^2} \quad \text{(A1)}$$

Several steps need to be followed to obtain the coordinates of two end points. 1) The quadrilateral is dissembled into two triangles. 2) Intersect-line (l) between the plane of 3D circle (F) (fracture) and each triangle (T_1) is obtained. 3) Intersection points (P_1, P_2) of the line (l) and three edges of the triangle (T_1) can be found. 4) Intersection points (P_3, P_4) of the intersection line and the circle can also be found. 5) Determining the two end points (P_2, P_3) out of four intersect-points (P_1, P_2, P_3, and P_4), and calculate $length_1$ in first triangle (T_1). 6) Do step 2-5 for another triangle, and calculate $length_2$ in second triangle. 7) Adding $length_1$ and $length_2$ up will yield *length* of the target line segment, which we looked for in the beginning.

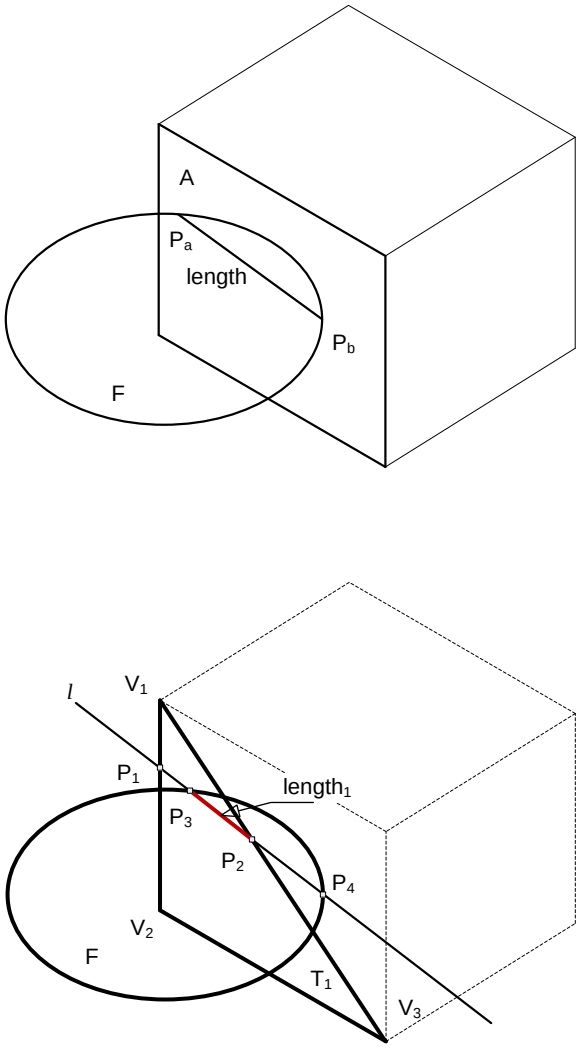

Figure A1 Schematic of intersection line calculation between fracture and FEM element surface.

A1.2. Intersection between a plane and a triangle in 3D

It is convenient to take the normal form of the fracture plane, since one point on the plane (the fracture center) (x_p, y_p, z_p) and normal vector to the plane (x_n, y_n, z_n) are given. Let V_1 (x_1, y_1, z_1), V_2(x_2, y_2, z_2) and V_3(x_3, y_3, z_3) be the coordinates of

the vertices of the triangle. We can first calculate the signed distances between the vertices and the plane in the following way:

$$d = -x_n x_p - y_n y_p - z_n z_p$$

$$dist_1 = x_n x_1 + y_n y_1 + z_n z_1 + d$$

$$dist_2 = x_n x_1 + y_n y_2 + z_n z_2 + d$$

$$dist_3 = x_n x_3 + y_n y_3 + z_n z_3 + d \qquad \text{(A2)}$$

We can examine these distances two by two. If the signed distances of the two vertices have opposite signs, and then there is a point of intersection between them. There are special cases that one or both of the vertices is on the plane, which can be identified by having a zero distance. If an intersection point exists, we can find its coordinates (x, y, z) by using the following linear interpolation. Take $dist_1$ and $dist_2$ as example:

$$\alpha = dist_2 / (dist_2 - dist_1)$$

$$x = \alpha x_1 + (1-\alpha) x_2$$

$$y = \alpha y_1 + (1-\alpha) y_2$$

$$z = \alpha z_1 + (1-\alpha) z_2 \qquad \text{(A3)}$$

Repeat above procedure three times, we can find 0, 1, 2, or 3 points of intersection between the triangle and the plane. Three points of intersection indicates the plane and the triangle are co-planer. One point of intersection indicates that one and only one of the vertices is on the plane. When two points of intersection return, we can write out the parametric form of the intersection line (Equation A4).

$$x = x_1 + Ft$$

$$y = y_1 + Gt$$

$$z = z_1 + Kt$$

$$F = (x_1 - x_2) / \sqrt{(x_1 - x_2)^2 + (y_1 - y_2)^2 + (z_1 - z_2)^2}$$

$$G = (y_1 - y_2) / \sqrt{(x_1 - x_2)^2 + (y_1 - y_2)^2 + (z_1 - z_2)^2}$$

$$K = (z_1 - z_2) / \sqrt{(x_1 - x_2)^2 + (y_1 - y_2)^2 + (z_1 - z_2)^2} \quad \text{(A4)}$$

A1.3. Intersection between a line and a circle in 3D

In this part, it is convenience to write the equation of a circle in implicit form using its center (x_c, y_c, z_c) and radius (r) as:

$$(x - x_c)^2 + (y - y_c)^2 + (z - z_c)^2 = r^2 \quad \text{(A5)}$$

And from above we have the parametric form of the line as

$$x = x_1 + Ft$$

$$y = y_1 + Gt$$

$$z = z_1 + Kt \tag{A6}$$

There can be 0, 1, or 2 intersection points. We will look at the 2 intersection point case only, because other two cases indicate no communication between the fracture and the element interface. The coordinates of the two intersection points can be calculated as follows.

$$\begin{aligned} root = r^2(F^2 + G^2 + K^2) - [&(F(y_c - y_1) - G(x_c - x_1))^2 \\ &+ (G(z_c - z_1) - K(y_c - y_1))^2 \\ &+ (K(x_c - x_1) - F(z_c - z_1))^2] \end{aligned}$$

$$t = \frac{[F(x_c - x_1) + G(y_c - y_1) + K(z_c - z_1)] \pm \sqrt{root}}{F^2 + G^2 + K^2}$$

$$x = x_1 + Ft$$

$$y = y_1 + Gt$$

$$z = z_1 + Kt \tag{A7}$$

A1.4. Determination of two intersection point between a circle and a triangle in 3D

We have obtained four points previously, which are intersection points of one line to a circle (p_3, p_4), and to a triangle (p_1, p_2). It is to solve an overlapping problem of line segments in this situation. There are seven possible relative locations of four end points of two line segments as shown in the following.

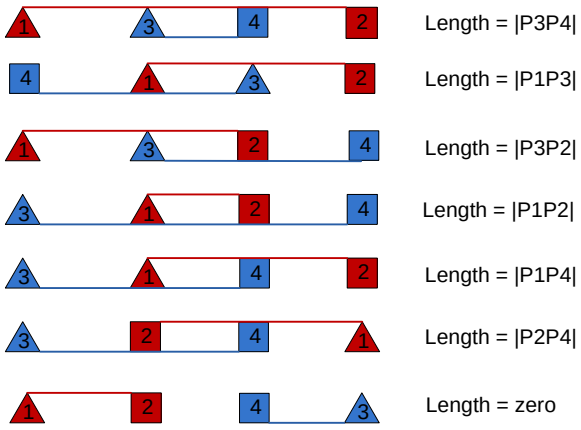

Figure A2 Possible relative locations for line segment overlapping calculation.

The relative position of these four points can be determined by the value of four angles: $\angle 132$, $\angle 142$, $\angle 314$, and $\angle 324$. For example, case 1 in above figure stands when both $\angle 132$ and $\angle 142$ equals to π. After two intersection points are determined, the intersection length can be calculated. Repeat same procedure for all six element interfaces, we can obtain the intersection lengths of a fracture to finite element surfaces.

A2. Visualization of fracture network

Most of the commonly used image processing software does not provide a function to plot massive number of 3D circles in space. Usually, the user need to explicitly input coordinates of points on 3D circles. On the other hand, coordinates of points on fractures are also required when interpolating elemental stresses onto fractures' surface. The procedure of defining a point on a circle in space is basically a coordinate transformation. Consider a unit circle (black) and a point (P_0) on the circle, as shown in Figure A3.

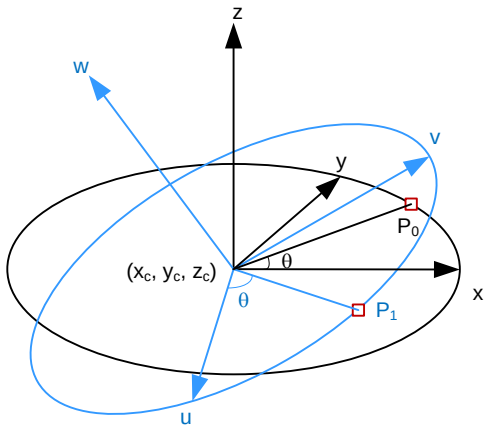

Figure A3 Illustration of circular area in 3-dimension space.

First, one needs to find three orthogonal vectors to define the transformed coordinate system (Blue). Since the normal of the fracture (*w*) is given and can serve as one of the orthogonal axes of the fracture plane, the other two vectors (*u* and *v*) can be calculated using *w* and *x*, as:

$$u = \frac{x \times w}{\|u\|}, \text{ and } v = \frac{w \times u}{\|v\|} \quad \text{(A8)}$$

Having unit vectors *u*, *v*, and *w* in hand, the new coordinates of any known point P_0 after rotation can be calculated as

$$P_1 = u\cos\theta + v\sin\theta \quad \text{(A9)}$$

The last step is resizing the unit circle to a circle with radius *r*, and relocating the center from (0, 0, 0) to *C* (x_c, y_c, z_c). The coordinate of the point P_F transformed from P_0 can be calculated as:

$$P_F = ur\cos\theta + vr\sin\theta + C \quad \text{(A10)}$$

It is not difficult to define points on a unit circular area in 2D. Therefore, using above algorism can easily list out the coordinates of necessary points in a circular area (fracture surface) in space. When plotting fractures, one can treat the circles as polygons by defining limit number of points on circle to approximate the fractures. Figure A4 shows a meshed out unit circle for stress interpolation. Figure A5 shows a fracture network, in which each of the fracture is approximated by a 20-sides polygon.

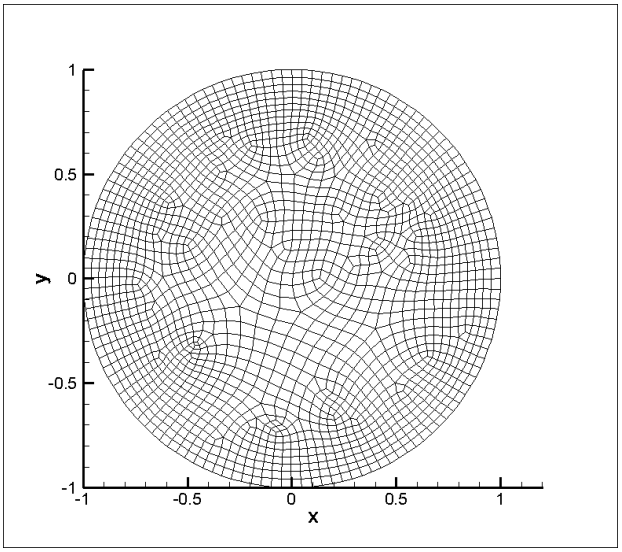

Figure A4 A sample of FEM mesh for a circular area

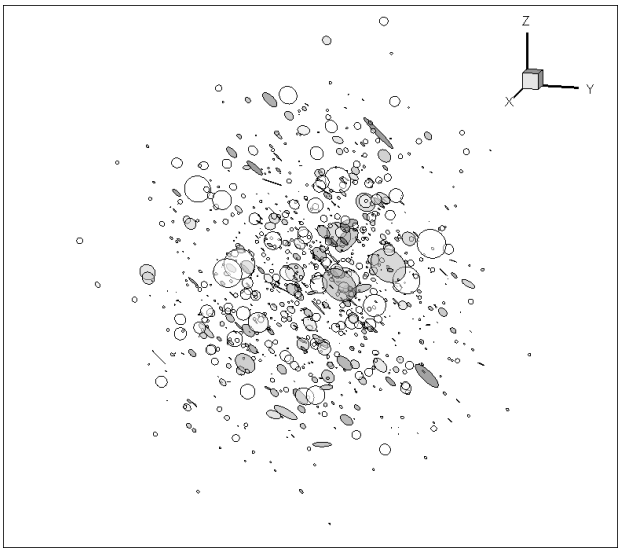

Figure A5 A sample of penny shape fracture network.

A3. Determination of inter-connected fracture channels

The algorism of searching for inter-connected fractures in a network includes a series of determination of intersection between two fractures (circular areas) in space. A circle in space is formed by a plane cutting a sphere. The normal of the plane is identical to the fracture normal, the center and radius of the sphere are the same as the fracture center and radius (Figure A6).

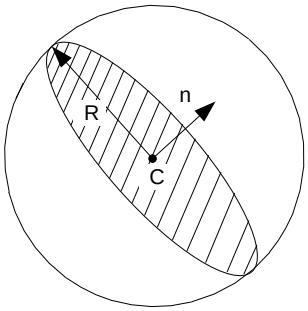

Figure A6 A circular area in space is formed by a plane cutting a sphere.

The first step is to determine if two spheres intersect, by calculating the distance between the two centers, and comparing it to the sum of the two radiuses. The two spheres intersect when the following relation (Equation A11) is valid.

$$|d| \le |R_1| + |R_2| \tag{A11}$$

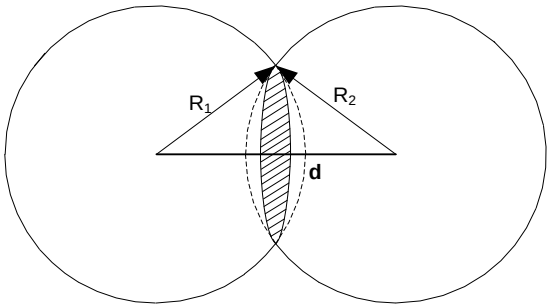

Figure A7 Intersection of two spheres.

There are three possible relative locations of two fractures in space, given the two spheres intersect: 1) two fractures are parallel; 2) two fractures are co-planar; 3) two fractures are Non-coplanar and non-parallel.

1). Two fractures are parallel

If two fractures have same or opposite normal, and the distance from one fracture center to another fracture plane is not equal to zero, they are parallel. There will be no intersection point in this situation.

$$n_1 \cdot n_2 = \pm 1, \text{ and } d > 0 \qquad \text{(A12)}$$

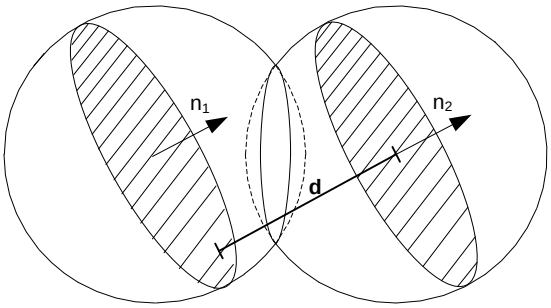

Figure A8 Two parallel fractures.

2). Two fractures are co-planar

If two fractures have same or opposite normal and the distance of the center of one fracture to another plane is equal to zero, they are co-plane. There will be one or two intersection points, which can be determined by comparing the distance between two centers to the sum of their radius.

$$n_1 \cdot n_2 = \pm 1, \text{ and } d = 0 \tag{A13}$$

There will be one intersection points, if $|d'| = |R_1| + |R_2|$, and two intersection points, if $|d'| < |R_1| + |R_2|$.

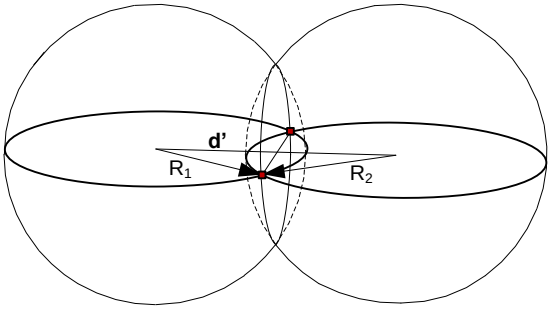

Figure A9 Two co-planner fractures.

To find the mid-point of the intersection line segment, let us consider the following figure in 2D.

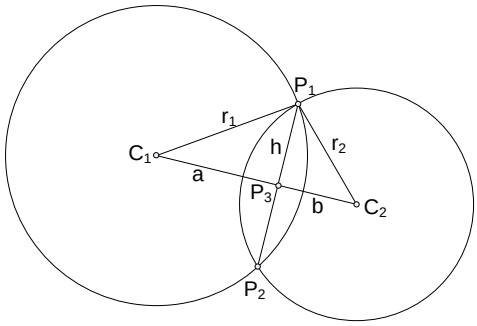

Figure A10 Intersection line between two co-planner circles.

In Figure A10, a = $|C_1P_3|$, b = $|C_2P_3|$, h = $|P_1P_3|$, and d' = $|C_1C_2|$. Considering the two triangles $C_1P_1P_3$ and $C_2P_1P_3$, we can write

$$a^2 + h^2 = r_1^2 \text{ and } b^2 + h^2 = r_2^2 \quad \text{(A14)}$$

And using $d = a + b$, we can solve for a,

$$a = (r_1^2 - r_2^2 + d^2)/(2d) \tag{A15}$$

And finally, we can solve for P_3

$$P_3 = C_1 + a(C_2 - C_1)/d \tag{A16}$$

3). Two fractures are Non-coplanar and non-parallel

In this case the problem reduces to find the intersection points of a line (intersection line between two fracture planes) and a circle (section A1.3), and then calculate the line segment overlapping as previous (section A1.4).

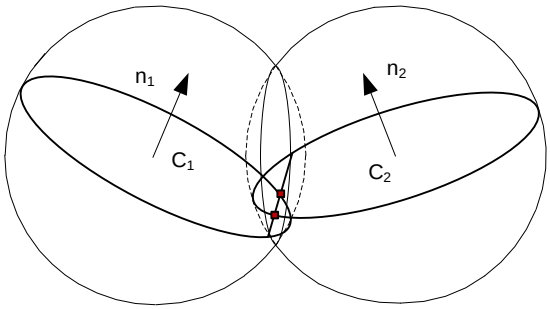

Figure A11 Intersection line of two 3D circles.

Here, the method used in this work to determine the intersection line between two fracture planes is explained. The implicit functions of two fracture planes can be written as:

$$n_{1x}x + n_{1y}y + n_{1z}z + d_1 = 0 \tag{A17}$$

$$n_{2x}x + n_{2y}y + n_{2z}z + d_2 = 0 \tag{A18}$$

where

$$d_1 = -(n_{1x}x_{c1} + n_{1y}y_{c1} + n_{1z}z_{c1})$$

$$d_2 = -(n_{2x}x_{c2} + n_{2y}y_{c2} + n_{2z}z_{c2})$$

And the line of intersection that we want to find is (in parametric form):

$$\begin{cases} x = x_0 + ft \\ y = y_0 + gt \\ z = z_0 + ht \end{cases} \tag{A19}$$

where the parameter coefficients, f, g, and h, and one point (x_0, y_0, z_0) on the line are given by:

$$\begin{aligned} f &= y_{c1}z_{c2} - y_{c2}z_{c1} \\ g &= z_{c1}x_{c2} - z_{c2}x_{c1} \quad \text{, and} \\ h &= x_{c1}y_{c2} - x_{c2}y_{c1} \end{aligned}$$

$$\begin{aligned} x_0 &= (g(d_1z_{c2} - z_{c1}d_2) - h(d_1y_{c2} - y_{c1}d_2))/(f^2 + g^2 + h^2) \\ y_0 &= -(f(d_1z_{c2} - z_{c1}d_2) + h(d_2x_{c1} - x_{c2}d_1))/(f^2 + g^2 + h^2) \\ z_0 &= (f(d_1y_{c2} - y_{c1}d_2) + g(d_2x_{c1} - x_{c2}d_1))/(f^2 + g^2 + h^2) \end{aligned} \tag{A20}$$

Then follow section (A1.3) and (A1.4), two intersection points of two fractures can be found. Finally, the mid-point can be located. The resulted channel-

networks are 1-D pipes connected by fracture centers and mid-points (Figure A12).

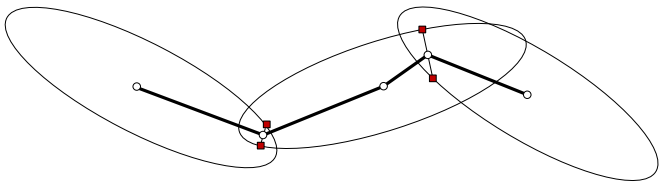

Figure A12 1-D channel formed by interconnected fractures.

A4. Efficient method of computing polygon area and polyhedron volume

Depending on the simulated domain, irregular polygon elements (triangle and quadrilateral for most of the time) and polyhedron elements (tetrahedron and hexahedron for most of the time) are always used to make the FEM meshing more flexible. The following introduces an efficient way to compute the polygon area and polyhedron volume during numerical programming.

A4.1. polygon area

The area computation use the facts that 1) the norm of the cross product vector is the area of the parallelogram they from, 2) the triangle they form has half of that area, and 3) The polygon area (N nodes) is the sum of the signed areas (area vector, Allen Van Gelder 1995) of the triangles formed by consecutive pairs of nodes and the origin. The following sketch illustrates the geometry in detail (Figure A13).

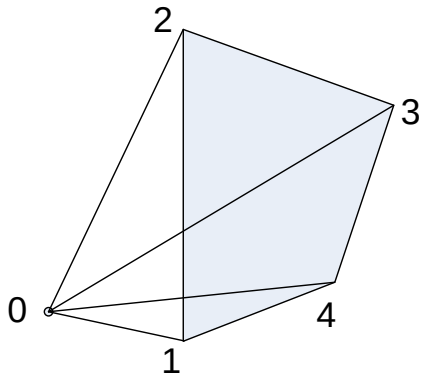

Figure A13 Illustration of area vector.

$$A_{1234} = A_{120} + A_{230} + A_{340} + A_{410} \tag{A21}$$

$$A_{abc} = \frac{1}{2} \times v_{ba} \times v_{bc}$$

After translating the origin to node N (e.g. node 4 for quadrilateral), the formula then reduces to (Figure A14)

$$A_{1234} = A_{124} + A_{234} \tag{A22}$$

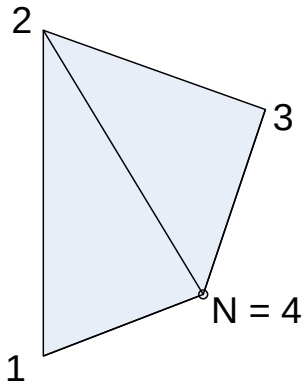

Figure A14 Orientations of vertices for polygon area calculation.

The area of the triangles in Figure A14 can be calculated as $A_{124} = 1/2\|v_{21} \times v_{24}\|$, and only the coordinates of four vertices are required then.

A4.2. Polyhedron volume

Using the similar concept as used in polygon area calculation, the volume of a polyhedron can be expressed as signed volume of pyramids formed by the surfaces of the polygon and the origin (Figure A15).

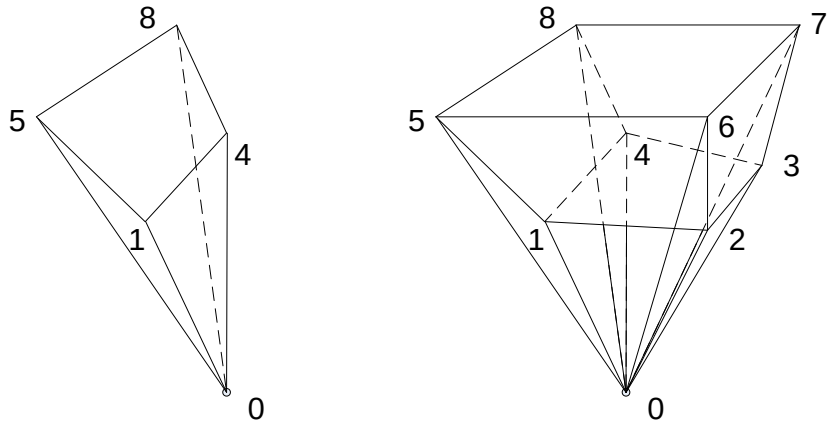

Figure A15 An illustration of the signed volume for polyhedron volume calculation.

$$V = V_{4321} + V_{5841} + V_{5678} + V_{1265} + V_{2376} + V_{3487} \tag{A23}$$

$$V_{abcd} = \frac{1}{6} A_{abcd} \cdot v_{a0} \tag{A24}$$

$$A_{abcd} = A_{abd} + A_{bcd} \tag{A25}$$

The volume is positive when v_{a0} points to the same side as the normal vector which is collinear with area vector of the surface.

In the same way, after translating the origin to one of the vertices (e.g. point 1), the formula will be simplified, only pyramids contains point 7 will be taken into account. One should notice that the order of nodes has been changed.

$$V = \frac{1}{6}\left[(A_{5876} + A_{3267} + A_{4378}) \cdot v_{71}\right] \tag{A26}$$

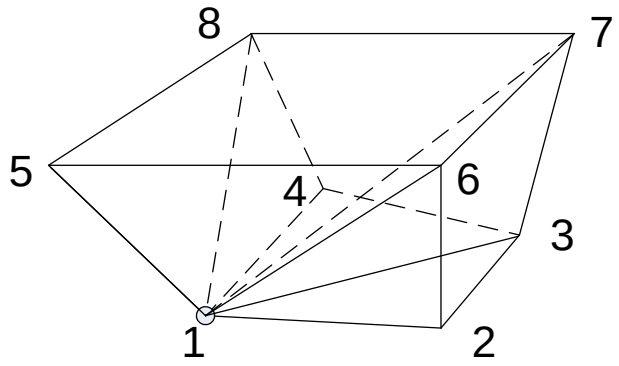

Figure A16 Orientations of vertices for hexahedron volume calculation.

A5. Analytical solutions for stress field in the vicinity of a penny shape crack

A5.1. Sneddon 1946 solution

In Sneddon's work, he defined new variables (ζ and ρ) in cylindrical coordinate system due to the axisymmetric of the problem. And three un-vanished stresses (σ_z, σ_r, and σ_θ) can be expressed in terms of these two variables, as follows.

$$\zeta = z/c\,;\ \rho = r/c \tag{A27}$$

$$\sigma_z = \frac{2p_0}{\pi}[C_1^0 - S_0^0 + \zeta C_2^0 - \zeta S_1^0]$$

$$\sigma_r + \sigma_\theta + \sigma_z = \frac{4(1+\sigma)}{\pi} p_0 [C_1^0 - S_0^0]$$

$$\sigma_\theta - \sigma_r = \frac{2p_0}{\pi}[(1-2\sigma)[C_1^2 - S_0^2 - \zeta(C_2^2 - S_1^2)] \qquad \text{(A28)}$$

Define following:

$$r^2 = 1+\zeta^2;\ \cot\theta = \zeta;\ 2\zeta\cot\phi = \rho^2 + \zeta^2 - 1;\ R^2 = (\rho^2 + \zeta^2 - 1)^2 + 4\zeta^2$$

Terms used in above can be written out as:

$$C_1^0 = R^{-\frac{1}{2}}\cos\frac{1}{2}\phi; C_2^0 = rR^{-\frac{3}{2}}\cos(\frac{3}{2}\phi - \theta); C_0^1 = \frac{1}{\rho}(R^{-\frac{1}{2}}\cos\frac{1}{2}\phi - \zeta);$$

$$C_1^1 = \frac{1}{\rho} - \frac{r}{\rho}R^{-\frac{1}{2}}\cos(\theta - \frac{1}{2}\phi)\ ; C_2^1 = \rho R^{-\frac{3}{2}}\cos\frac{3}{2}\phi;\ C_1^2 = \frac{2}{\rho}C_0^1 - C_1^0;$$

$$C_2^2 = \frac{2}{\rho}C_1^1 - C_2^0$$

$$S_0^0 = \tan^{-1}\frac{R^{\frac{1}{2}}\sin\frac{1}{2}\phi + r\sin\theta}{R^{\frac{1}{2}}\cos\frac{1}{2}\phi + r\cos\theta}$$

$$S_1^0 = R^{-\frac{1}{2}}\sin\frac{1}{2}\phi; S_2^0 = rR^{-\frac{3}{2}}\sin(\frac{3}{2}\phi - \theta);$$

$$S_0^1 = \frac{1}{\rho}(1 - R^{-\frac{1}{2}}\sin\frac{1}{2}\phi); S_1^1 = \frac{r}{\rho}R^{-\frac{1}{2}}\sin(\theta - \frac{1}{2}\phi);\ S_2^1 = \rho R^{-\frac{3}{2}}\sin\frac{3}{2}\phi;$$

$$S_0^2 = \frac{1}{\rho}(C_0^1 - \zeta S_0^1)\,;\; S_1^2 = \frac{2}{\rho}S_0^1 - S_1^0\,;$$

A5.2. Westmann 1965 solution

In Westmann 1965, a half-space is considered, on which the surface interior to the circle $r = a$ is subjected to a uniform shearing stress S in the $\theta = \pi$ - direction. Exterior to the circle the surface displacements u and v are zero; the entire surface is assumed to be free from normal tractions (pure shear). The solution for stresses in cylindrical coordinates when $z \neq 0$ is:

$$\frac{\sigma_r}{S} = \frac{4}{\pi}\frac{1}{2-\nu}[2I_1^1 - \frac{z}{a}(I_2^1 - \frac{1}{r/a}I_1^2)]\cos\theta$$

$$\frac{\sigma_\theta}{S} = \frac{4}{\pi}\frac{1}{2-\nu}[2\nu I_1^1 - \frac{z}{a}\frac{1}{r/a}I_1^2]\cos\theta$$

$$\frac{\sigma_z}{S} = \frac{4}{\pi}\frac{1}{2-\nu}\frac{z}{a}I_2^1\cos\theta$$

$$\frac{\sigma_{r\theta}}{S} = \frac{4}{\pi}\frac{1}{2-\nu}[-(1-\nu)I_1^1 + \frac{z}{a}\frac{1}{r/a}I_1^2]\sin\theta$$

$$\frac{\sigma_{\theta z}}{S} = \frac{2}{\pi}\frac{1}{2-\nu}[-\nu I_1^2 - (2-\nu)I_1^0 + \frac{z}{a}(I_2^2 + I_2^0)]\sin\theta$$

$$\frac{\sigma_{zr}}{S} = \frac{2}{\pi}\frac{1}{2-\nu}[-\nu I_1^2 + (2-\nu)I_1^0 + \frac{z}{a}(I_2^2 - I_2^0)]\cos\theta \qquad \text{(A29)}$$

When z = 0, adopting Heaviside step function *H(x)*:

$$H = \begin{cases} 0 & x < 0 \\ \frac{1}{2} & x = 0 \\ 1 & x > 0 \end{cases} \qquad \text{(A30)}$$

$$\frac{\sigma_r}{S}=\frac{8}{\pi}\frac{1}{2-\nu}\frac{(r/a)H(1-r/a)}{[1-(r/a)^2]^{\frac{1}{2}}}\cos\theta$$

$$\frac{\sigma_\theta}{S}=\frac{8}{\pi}\frac{\nu}{2-\nu}\frac{(r/a)H(1-r/a)}{[1-(r/a)^2]^{\frac{1}{2}}}\cos\theta$$

$$\sigma_z=0$$

$$\frac{\sigma_{r\theta}}{S}=-\frac{4}{\pi}\frac{(1-\nu)}{2-\nu}\frac{(r/a)H(1-r/a)}{[1-(r/a)^2]^{\frac{1}{2}}}\sin\theta$$

$$\frac{\sigma_{\theta z}}{S}=-\{H(1-\frac{r}{a})+\frac{2}{\pi}(\frac{-1}{[(r/a)^2-1]^{\frac{1}{2}}}+\sin^{-1}(\frac{a}{r})$$
$$+\frac{\nu}{2-\nu}\frac{1}{(r/a)^2[(r/a)^2-1]^{\frac{1}{2}}})H(\frac{r}{a}-1)\}\sin\theta$$

$$\frac{\sigma_{zr}}{S}=\{H(1-\frac{r}{a})+\frac{2}{\pi}(\frac{-1}{[(r/a)^2-1]^{\frac{1}{2}}}+\sin^{-1}(\frac{a}{r})$$
$$-\frac{\nu}{2-\nu}\frac{1}{(r/a)^2[(r/a)^2-1]^{\frac{1}{2}}})H(\frac{r}{a}-1)\}\cos\theta \qquad \text{(A31)}$$

Define following:

$$\rho^2=1+(\frac{z}{a})^2;\ \frac{z}{a}\tan\Theta=1;\ 2\frac{z}{a}\cot\phi=(\frac{r}{a})^2+(\frac{z}{a})^2-1;$$

$$R^2=\left[\left(\frac{r}{a}\right)^2+\left(\frac{z}{a}\right)^2-1\right]^2+4\left(\frac{z}{a}\right)^2$$

Terms used above can be finding as:

$$J_0^0 = \tan^{-1}\frac{R^{\frac{1}{2}}\sin\frac{1}{2}\phi + \rho\sin\Theta}{R^{\frac{1}{2}}\cos\frac{1}{2}\phi + \rho\cos\Theta}; J_1^0 = R^{-\frac{1}{2}}\sin\frac{1}{2}\phi \;;\; J_2^0 = \rho R^{-\frac{3}{2}}\sin(\frac{3}{2}\phi - \Theta);$$

$$J_0^1 = \frac{1}{r/a}(1 - R^{\frac{1}{2}}\sin\frac{1}{2}\phi);\; J_1^1 = \frac{\rho}{r/a}R^{-\frac{1}{2}}\sin(\Theta - \frac{1}{2}\phi) \;;\; J_2^1 = \frac{r}{a}R^{-\frac{3}{2}}\sin\frac{3}{2}\phi;$$

$$J_0^2 = \frac{1}{r/a}\{\frac{1}{r/a}(R^{\frac{1}{2}}\cos\frac{1}{2}\phi - \frac{z}{a}) - \frac{z}{a}J_1^0\};\; J_1^2 = \frac{2}{r/a}J_0^1 - J_1^0;\; J_2^2 = \frac{2}{r/a}J_1^1 - J_2^0;$$

$$I_0^0 = -\frac{z}{a}J_0^0 + R^{\frac{1}{2}}\sin\frac{1}{2}\phi;\; I_1^0 = J_0^0 - R^{-\frac{1}{2}}\cos\frac{1}{2}\phi;\; I_2^0 = J_1^0 - \rho R^{-\frac{3}{2}}\cos(\frac{3}{2}\phi - \Theta);$$

$$I_0^1 = -\frac{1}{2}\frac{z/a}{r/a}R^{\frac{1}{2}}\sin\frac{1}{2}\phi + \frac{1}{2}\frac{r}{a}J_0^0 - \frac{1}{2}\frac{1}{r/a}R^{\frac{1}{2}}\cos\frac{1}{2}\phi;$$

$$I_1^1 = \frac{1}{r/a}(\rho R^{-\frac{1}{2}}\cos(\Theta - \frac{1}{2}\phi) - R^{\frac{1}{2}}\sin\frac{1}{2}\phi);$$

$$I_2^1 = \frac{\rho}{r/a}R^{-\frac{1}{2}}\sin(\Theta - \frac{1}{2}\phi) - \frac{r}{a}R^{-\frac{3}{2}}\cos\frac{3}{2}\phi;$$

$$I_1^2 = -\frac{1}{(r/a)^2}(R^{\frac{1}{2}}\cos\frac{1}{2}\phi - \frac{z}{a}R^{\frac{1}{2}}\sin\frac{1}{2}\phi) + R^{-\frac{1}{2}}\cos\frac{1}{2}\phi;$$

$$I_2^2 = \frac{2}{(r/a)^2}(\rho R^{-\frac{1}{2}}\cos(\Theta - \frac{1}{2}\phi) - R^{\frac{1}{2}}\sin\frac{1}{2}\phi) - I_2^0;$$